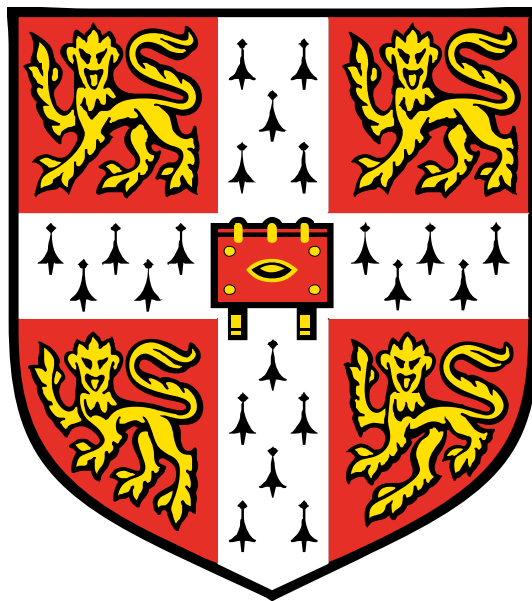# The Effect of Superimposed Stress on High Temperature Degradation of Single Crystal Superalloys during Exposure to Various Sulphur and Sea Salt Environments

## Noel Glaenzer

Downing College

University of Cambridge

This thesis is submitted for the degree of Doctor of Philosophy

September 2019

*This thesis is dedicated to my wife, my daughters and my parents.*

*Quidvis recte factum quamvis humile praeclarum.*

Sir Henry Royce (1863-1933)

# I Preface

This thesis is the result of my own work and includes nothing which is the outcome of work done in collaboration, except as declared in the Preface and specified in the text.

It is not substantially the same as any that I have submitted, or is being concurrently submitted for a degree, diploma or other qualification at the University of Cambridge or any other University or similar institution, except as declared in the Preface and specified in the text. I further state that no substantial part of my dissertation has already been submitted, or is being concurrently submitted for any such degree, diploma or other qualification at the University of Cambridge or any other University or similar institution except as declared in the Preface and specified in the text

It is less than 60,000 words in length.

Noel Glaenzer, September 2019

The Effect of Superimposed Stress on High Temperature Degradation of Single Crystal Superalloys during Exposure to Various Sulphur and Sea Salt Environments

## II Abstract

Alternative fuels and novel cycles are increasingly used to supply the world growing demand in energy whilst reducing the carbon emission. Such cycles include the integrated gasification combined cycle (IGCC) with carbon capture, which uses coal as fuel. In such situations however, sulphur and sodium chloride, contained in the coal, are known to form sodium sulphate that, if deposited at the root of the single crystal turbine blades, can initiate hot corrosion. Low temperature Type II corrosion consists of the formation of a fused salt melt, which interacts with the combustion gases and causes other constituents of the alloy to dissolve. The resulting melt prevents the oxide to be protective. Simultaneously, the large centrifugal stresses in the blade attachment area can cause the substrate to crack. If undetected, such cracks will grow and result in catastrophic failure.

The current work consisted in the construction and commissioning of a customised test bench reproducing the environments experienced at the root of the turbine blades. The investigation compared a first-generation Ni-based superalloy with 12.2 wt% Cr (SCRY-83) commonly referred to as "$Cr_2O_3$-former" in regard to its oxide composition, to a second generation one with 6.5 wt% Cr (SCRY-4) also referred to as "$Al_2O_3$-former". A mixture of NaCl and $Na_2SO_4$ is often used in the literature to reproduce hot corrosion. The effect of each deposits was first analysed independently. It was found that NaCl caused scale damage, via the formation of high vapor pressure compounds for the $Al_2O_3$-former, or via the transport of Cr to the gas interface for the SCRY-83. In contrast, $Na_2SO_4$ formed a liquid phase at the surface of both alloys, but initiated damage only when in contact with the $Al_2O_3$-former. Sulphur ingress was the largest on sample coated with NaCl and exposed to a mixture of air and $SO_2/SO_3$, affecting particularly the $Al_2O_3$-former. The simultaneous application of force in these environments always resulted in a larger reaction layer, and was thought to originate from the flow of liquid phases ($NaCl$-$NiCl_2$ when coated with NaCl, or $Ni_3S_2$ when exposed to air+$SO_2/SO_3$, or $Na_2SO_4$-$NiSO_4$ when coated with NaCl and exposed to air+$SO_2/SO_3$). The type II environment with applied force was the most aggressive and it initiated two cracks on the $Al_2O_3$-former, and a 40 μm thick damaged region was detected on the $Cr_2O_3$-former. Proven and novel methods of damage characterisation were assessed throughout this work, and their suitability was found to depend on the harshness of the environment. The high Cr alloy always outperform the $Al_2O_3$-former or exhibited similar depth of attack (when coated with NaCl).

Noel Glaenzer

# III Acknowledgements

This work could not have been possible without the unconditional support of my thesis supervisor, T.W. Clyne. His experience in building experimental rigs was paramount to the success of this work. In addition, he showed endless patience for teaching and repeating basic material science.

Also critical to this work was the contribution of Richard G. Finding money for a research project is not an easy task and he has been defending this case to the top! Prabhakar also spent a lot of time with me, making sure I got the chemistry of hot corrosion right. To both of you, I hope this work is a small payback of your initial time investment, though I still owe you a lot. Still within Solar, but in the customer services, Emmanuel S. deserves a medal! He helped me to convince Eddy to start a PhD part-time and further supported my application to replace a very experienced colleague.

My wife has always been next to me, providing an ocean of calm, making sure I did not become insane (not sure she succeeded though!). To my family (Remi, Magali, Annie and Louis), thank you for being there when I needed it.

I must not forget my lab friends, making research pleasant and helping with their skills: Maya and Erika for their kindness, Kevin Robert and Bob Stearn for their technical skills, SuKi for showing his creep rig, Veronica for taking me to Salathong, Tom and Fernando for the coffees and comforting me when I broke the Camscan, Stella for the very useful discussion on hot corrosion and for shutting the water off to save the rig (but not the furnace). More generously, all the members of the Gordon lab making it a nice place to do research.

# IV Contents

# V Nomenclature

| Symbol | Description | Units |
|--------|-------------|-------|
| $\mathcal{A}$ | Area | $m^2$ |
| $\alpha$ | Misorientation angle between {001} and tensile axis | ° |
| $\beta$ | Compression ratio | – |
| δ | Fork vertical displacement | mm |
| $\Delta G_0$ | Gibbs free energy of reaction | kJ mol$^{-1}$ |
| $\Delta H_f^0$ | Heat of formation at 298.15K | kJ mol$^{-1}$ |
| duct | Ductility | – |
| ε | Strain | – |
| E | Young's modulus | GPa |
| F | Force | N |
| G | Shear modulus | GPa |
| $\gamma$ | Shear strain | – |
| $h$ | Height of the blade | m |
| $H^0$ | Enthalpy in standard state | kJ mol$^{-1}$ |
| $I$ | Second moment of area | $m^4$ |
| k | Material dependant oxidation constant | g m$^2$ h$^{-x}$ |
| $\kappa$ | Ratio of specific heat | – |
| $m$ | Mass of the sample | g |
| $M$ | Moment | N m |
| $Mi$ | Molecular weight of gas i | g.mol$^{-1}$ |
| $\mu$ | Linear attenuation coefficient | cm$^{-1}$ |
| n | Mass gain exponent | – |
| $\nu$ | Poisson ratio | – |
| $\eta$ | Thermal efficiency | % |
| $\omega$ | Angular speed | Rad s$^{-1}$ |
| R | Radius blade to the shaft | m |

| Symbol | Description | Units |
|--------|-------------|-------|
| $\rho$ | Density | kg m$^{-3}$ |
| S | Surface area | m² |
| $\Sigma$ | Beam stiffness | N mm$^{-1}$ |
| $\sigma$ | Stress | MPa |
| t | time | h |
| $T_i$ | Temperature at station i | °C (K) |
| $T\varepsilon$ | Temperature of eutectic point | °C |
| $T_m$ | Melting temperature | °K |
| $\theta$ | Diffraction angle | ° |
| UTS | Ultimate tensile strength | MPa |
| $Vi$ | Concentration per volume of gas i | – |
| $x$ | Distance along the beam | m |
| $y$ | Distance to neutral axis | m |
| $z$ | Width of the beam | m |

# Chapter 1　General Introduction

## 1.1　Overview

"India will add the equivalent of today's European Union to its electricity generation by 2040, while China will add the equivalent of today's United States" [1]. This quote, from the International Energy Agency (made in 2017), puts in plain words the incredible energy challenge faced by developing countries, whilst trying to reduce greenhouses gas emission.

In this context of energy growth and conventional gas field depletion (ie: North Sea), there is a need for newer resources, able to supplement intermittent renewable energies, whether these are conventional, like deeper and further offshore oil and gas, or unconventional, like shale gas or biomass. However, in these situations the risk arises to encounter contaminants (HCl, $SO_3$, $V_2O_5$, $CdSO_4$, $PbSO_4$, $Na_2NO_3$... [2]–[5]) able to damage nickel-based superalloys turbine blades, which in turn reduces the gas turbine life or increases the risk, resulting in increasing costs. This study is primarily focused at the operation of industrial gas turbines on offshore platforms, but the mechanisms and reactions are also applicable to biomass industry, shale gas and aero gas turbines operating offshore.

Industrial gas turbines are often installed on offshore oil and gas platforms, for their compactness and power-to-weight ratio. Crude oil is often extracted with the inclusion of dissolved raw natural gas. The gas is then separated and, if there is no pipeline to the shore, it is used locally as fuel on the platform. If there is not enough consumption, the excess is flared. There is a clear economic advantage to using it as fuel for the gas turbines; however, the gas is not necessarily "clean". In such environments, degradation of the turbine blades is common in the hot section. It often originates from the presence of sea salt (NaCl) in the air and sulphur from the fuel. In general, this is in the form of $H_2S$, although elemental sulphur $S_8$ is also possible.

When sulphur-rich fuel is burned, sulphur dioxide and trioxide ($SO_2$ and $SO_3$) are produced, together with other combustion products. The latter gases can combine with sea

salt (NaCl) to form hydrogen chloride (HCl) and sodium sulphate ($Na_2SO_4$). The salts can deposit at the root of the nickel-based superalloys blade and can damage the thermally-grown oxide that protects the blade from its environment. A distinction is often made as to whether the contaminant is in its liquid form (Type I hot corrosion, from 850 to 950°C) or in its solid form (Type II hot corrosion, from 600 to 800°C) when it first deposits onto the blade. The mechanisms, kinetics and nature of the attacks are different between the two types.

Type I hot corrosion typically occurs at the tip or trailing edge of the blade (where the temperature is highest). As a result, in case of failure, a loss in performance will be experienced, with a possible small increase in vibration. Unless there is important secondary damage by the following rotating stages, the gas turbine will keep running until the next planned downtime.

However, Type II hot corrosion affects the (air-cooled) root of the blade, where the temperature is lower, but the stresses are higher than those at the tip. If there is enough degradation to create a crack that can propagate, it may cause fracture of the blade. In this case, a major rotor imbalance will occur and the complete turbine would be damaged.

Hot corrosion is not the only degradation that can occur in the turbine section. Due to the high temperature and large centrifugal load, creep is also a concern. It can result in blades rubbing against the casing. This problem has been overcome over the years, mainly by alloy development. Unfortunately, modifying material composition to optimise for creep resistance has reduced resistance to hot corrosion.

The first three chapters of this work consist of a literature review on the thermo-mechanical performance of nickel-superalloys and the environmental degradation occurring in the turbine section.


## 1.2   Life-limited components in gas turbines

Good reliability and high thermal efficiency are paramount criteria for the operation of a gas turbine. The ideal cycle used by gas turbines is the "Brayton" or "Froude" cycle. Assuming isentropic compression of air between stages 1 and 2, isobaric fuel addition between stages 2 and 3 and isentropic expansion taking place between stages 3 and 4, the thermal efficiency, $\eta$, can be related to the firing temperature and the pressure ratio, $\beta$, as follows [6]:

$$\eta = 1 - \frac{T_4}{T_3} = 1 - \frac{1}{\beta^{\frac{\kappa-1}{\kappa}}}$$ 

<div align="right">Equation 1.1</div>

where $\kappa$ is the ratio of specific heats (specific heat at constant pressure over the one at constant volume)

It is noted in Equation 1.1 that, to increase thermal efficiency, the firing temperature ($T_3$) needs to be increased, as well as the pressure ratio ($\beta$). These increases are unfortunately subject to limits arising from material properties. Development of new materials, casting techniques and cooling technologies permitted recent progress, shown in Figure 1.1, in raising both the pressure ratio (in green) and the turbine entry temperature (in blue), for industrial (dashed lines) and aero-engine gas turbines (solid lines).
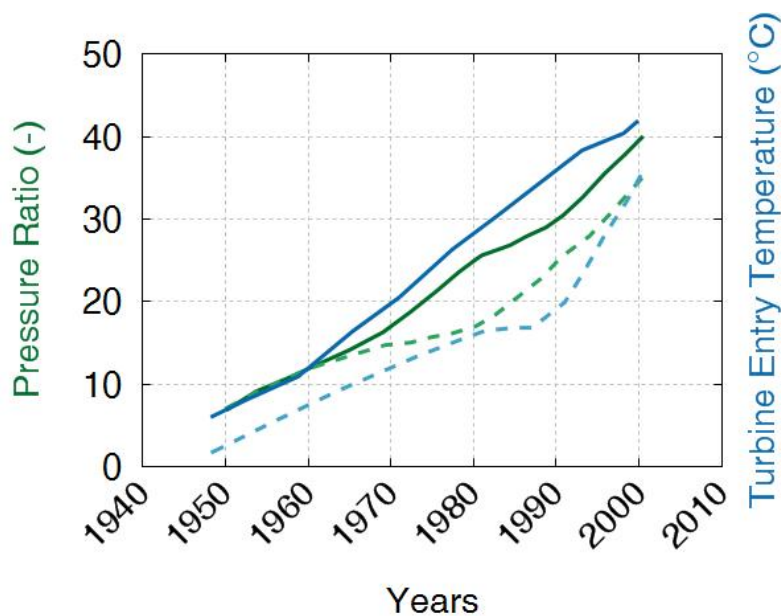


Figure 1.1: Increases in pressure ratio and turbine entry temperature against the years, solid line for aero and dashed for industrial gas turbines (data from Boyce [7])

Rotating components such as blades or disks have a maximum allowable creep strain (also termed "creep life") before getting into contact of nearby parts. This requires the gas turbine to be overhauled or repaired after a certain amount of time (currently of the order of 30,000 hours under full load conditions).

## 1.3   Environment of the turbine blade

In addition to undergoing extreme temperature and pressure, turbine blades are exposed to aggressive gases. Figure 1.2, obtained with chemical equilibrium with application [8] and gas turbines performances data, shows the exhaust gases composition. It is noted that there

is a large amount of nitrogen and oxygen. At higher load, $O_2$ is consumed turning into $CO_2$ and $H_2O$.
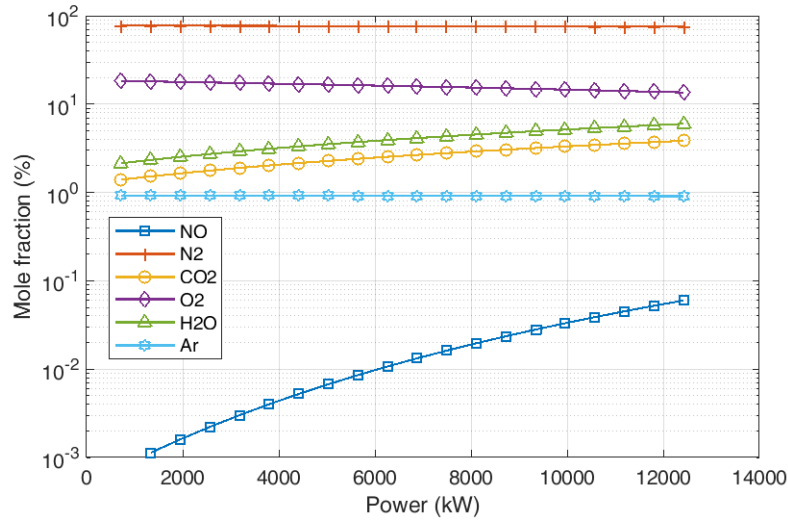


Figure 1.2: Effect of power on the exhaust gas composition of a 13 MW generator (inlet & exhaust duct loss=101 mmH$_2$O, $\eta_{GB}$=97%, $\eta_{Gen}$=98.5%, LHV=46,206 kJ/kg, model: T130 20501)

## 1.4   Single crystal turbine blades

Investment casting developments in the 1950s permitted a gain in turbine entry temperature by switching from wrought to cast blades. Figure 1.3 (a) shows the evolution of manufacturing techniques over the years.

Figure 1.3: Evolution of creep life and chromium content of newly developed superalloys from Reed [9]

In the temperature range of interest ($T > 0.5\ T_m$), creep mechanisms on polycrystalline metals can be divided in two majors groups: boundary mechanisms and lattice mechanisms [10]. Because creep strain rate is a function of $d^{-2}$ for Nabarro-Herring and $d^{-3}$ for Coble (with $d$ being the grain diameter), a superior (Nabarro-Herring and Coble) creep resistance is therefore achieved by having large grain size. The removal of transverse grain boundaries by introduction of directionally solidified blade (Figure 1.4) therefore assisted with this, giving an advantage of either a stress increase of ~200 MPa or a temperature increase of ~30°C [11].

5

The oriented grain growth arises by maintaining a moderate thermal gradient of 10–100 °C cm$^{-1}$ associated with a withdrawal rate of the furnace 5 to 40 cm hr$^{-1}$ [12]. Thanks to the cubic symmetry (FCC), it encourages the growth along the <001> crystallographic orientations, resulting in a number of grains aligned parallel to the solidification direction. Finally, the selection of the growth of only one grain was made with a grain selector, that has a spiral shape, resulting in a blade made of a single crystal (with a selected orientation). The elimination of grain boundary again permitted a stress or temperature increase.

Unfortunately, defects are sometimes present in the form of dendritic microsegragation, resulting in compositional gradients or porosity due to the freezing contraction [12]. Post-casting heat treatments are therefore done to promote the right microstructure and remove as many defects as possible from the casting. For example, for CMSX-4, a solution treatment is first applied to remove microsegregation associated with the dendritic growth for 8 h at 1314 °C and then air cooled. This is followed by two ageing treatments, the first for 4 h at 1140 °C for the γ and the final for 16 h at 871 °C, which when it is done result in a γ' size of ~ 0.45 µm [9], [13].

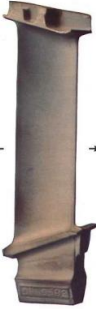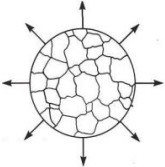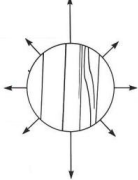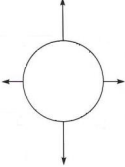| Equiaxed crystal structure, good mechanical properties in all directions | Columnar crystal structure, improved mechanical properties in longitudinal axis | Single crystal, excellent mechanical properties in longitudinal axis and heat resistance |
|---|---|---|
| (a) Conventionally cast turbine blade | (b) Directionally solidified turbine blade | (c) Single crystal turbine blade |

Figure 1.4: Turbine blade manufacturing technique and effect on crystal structure and properties copied from [14]

## 1.5   Objective of the research

The research objective is threefold:

(i) To understand how contaminants affect gas turbine blade material at high temperature,

(ii) To explore the effect of superimposed stress on harsh environments with varying amounts of sulphur dioxide/trioxide and sodium chloride (an area in which there has been very little previous work),

(iii) To examine the influence of chromium content on these environments (in view of the expected importance of the presence of a protective chromia layer).

# Chapter 2    Thermo-mechanical performance of Nickel superalloys

## 2.1   Centrifugal forces and stresses

The stress in a rotating blade, arising from the centrifugal force, for a given rotational speed, is readily obtained from the density and section area of the blade. Assuming a mean blade radius of 0.7 m and a rotation of 5100 rpm, Poursaeidi et al. [15] found a value of 230 MPa at the root, decreasing toward the tip, as shown in Figure 2.1. Reed et al. [16], with slightly different values from those above and a constant section, found a value of 180 MPa.
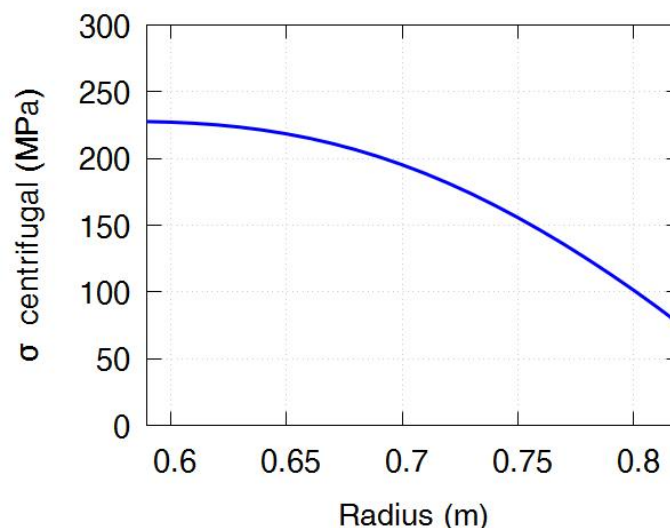


Figure 2.1: Centrifugal stress as a function of blade radius from Poursaeidi et al. [15] (assumptions: Blade height=20cm, 5100 rpm, ρ=8110 kg m$^{-3}$)

## 2.2   Stresses exerted by the gases on the blades

The stresses arising in the blade, from the forces exerted on it by the impingement of the gas, are less simple to calculate than those arising from centrifugal load. Poursaedi et al. [15] have estimated that, at full power, the net force acting on a blade (contributing to the rotation of the shaft and normal to the radial direction of the turbine) is approximately 1000 N, while the axial force is much smaller (~ 200 N).

The situation of the blade is like a cantilever subjected to a uniformly distributed load (although both gas velocity and effective projected area of the blade do vary with the radial position). By approximating the blade geometry to a cylinder of 25 mm diameter, and applying the moment to the mid-span of the blade, the stress can be calculated as per Equation 2.1.

$$\sigma = \frac{M}{I} y \qquad \text{Equation 2.1}$$

With the moment exerted at the root $M = Fh = 100$ Nm

$I$ the second moment of area (m⁴) $I = \frac{\pi}{4} r^4$

$y$ the distance from the neutral axis (m)

With the assumptions made above, a stress of around 60 MPa is predicted. The assumption of cylindrical geometry is a (rather simple) approximation, but helps to understand that the stress arising from the gases impinging into the blade is relatively small compared to the centrifugal force.

## 2.3   Thermal stress

Due to turbine blade cooling, the difference of temperature between the inner side exposed to cooling air and the outer side exposed to combustion gases, creates significant thermal stress. This thermal stress peaks during transients (shutdown, start-up, load change etc). Figure 2.2 shows the Von Mises thermal stress calculated using COMSOL [17] during steady state for a nozzle made of M-152 alloy (composition of this alloy is available in appendix § 9.2). (The thermal barrier coating has been neglected, but the combustion gases temperature is relatively low). This steady-state value results in a thermal stress in the order of 150 to 200 MPa, with spikes during transients.

This affects mainly the air foil and the stress value will be smaller for the root of the blade. This confirms that thermal stress can be significant.
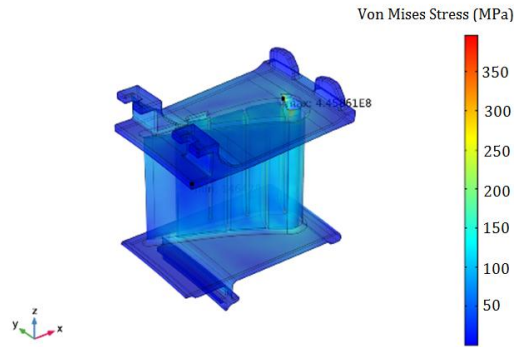
Figure 2.2: Visualization of a nozzle showing the predicted Von Mises stresses arising from thermal gradient under steady-state operating conditions reproduced from Comsol [17] (M-152 alloy with boundary conditions: cooling air at P=30 bar an T=600 K, combustion gases P=30 bar T=1100 K, airfoil=0.7 Mach on pressure side and 0.45 Mach on suction side)

## 2.4   Crystal structure and slip systems

Nickel-based superalloys single crystals are composed of a solid solution phase (γ shown in Figure 2.3 (a) and an ordered phase (γ') made of $Ni_3Al$ (b).
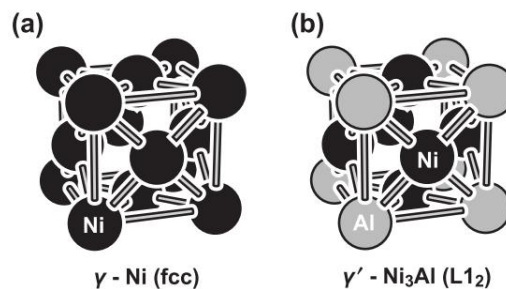


Figure 2.3: Illustration of the crystal structures (a) nickel based FCC and (b) nickel and aluminium in the ordered lattice of a $Ni_3Al$ compound copied from Reed and Rae [18]

The mechanical properties (E, UTS, µ…) of single crystals are anisotropic (see Figure 2.4). Since both phases have face centred cubic structures and coherent interfaces, so with three principal orientations, the material can be considered approximately orthotropic [19]. This property will be used to build an orthotropic elastic finite element model (§ 4.5).

In order to model their plastic deformation, two main approaches were envisaged by Meric and Cailletaud [20]. The first is to be considered at the macroscopic level and to define an anisotropic yield criterion, while the second is to transpose the macro stress level into the crystal shear stress and see if the slip system has been activated. If it has been activated, then the shear strain can be calculated. Both cases require a user subroutine to be written in Abaqus to model their behaviour.

The effect of the misorientation on Young's modulus is shown in Figure 2.4 (a). The UTS, yield and elongation value as a function of misorientation are shown in Figure 2.4 (b) for PWA1483. The Young's modulus is low in the <001> direction and rises to a maximum noted in the <111> direction. However, the UTS and yield value decrease away from <001>.



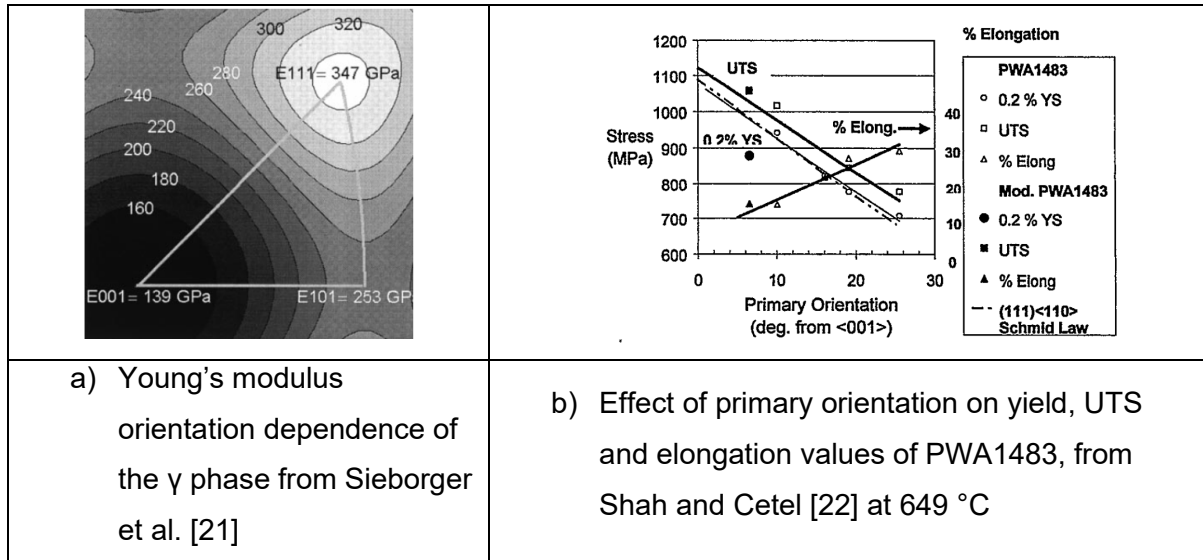| a) Young's modulus orientation dependence of the γ phase from Sieborger et al. [21] | b) Effect of primary orientation on yield, UTS and elongation values of PWA1483, from Shah and Cetel [22] at 649 °C |
|---|---|

Figure 2.4: Effect of misorientation on the Young's modulus, UTS, yield and ductility

Deformation of single crystals material occur on a specific set of slip planes (usually with high atomic density and in the closely packed direction [23]). The four octahedral {111} slip planes have three directions resulting in 12 possible slip systems {111}<110>. Alternatively, the three cubic planes {001} have two directions resulting in a total of 6 possible slip system {100}<110>. OILS rule applied to a tensile test performed in the <001> direction results in slip occurring either in the ($\bar{1}11$) plane in the [101] direction or in the ($1\bar{1}1$) plane in the [011] direction. Images confirming slip traces on {111} planes were captured by Meric et al. [20] during a tensile test in the [001] direction.

## 2.5 Creep

During normal operation the turbine blades grow slowly in length due to a phenomenon known as creep. The rate of creep increases if temperature or stress is increased. Equation 1.1 shows that there is an interest for a low creep material to achieve better thermal efficiency (via a higher turbine entry temperature).

Nickel-based alloys (with a FCC crystal structure), have been developed for these applications over a long time, with various factors being relevant to this choice. Self-diffusion is, for example, lower in FCC than in BCC or HCP [9]. It is not appropriate to go into greater

detail here on their creep characteristics, but it may be noted that Ni-Ru and Ni-Re form directional bonds that do not favour solute-vacancy exchanges [9]. This is thought to be the explanation as to why 4d and 5d of the d-block transition metals exhibit relatively low interdiffusion coefficients. These elements (refractory metals) have high melting points (>1800 °C), mechanical strength and hardness. The family includes molybdenum, tungsten, niobium, tantalum and rhenium[1].

The improvements in creep performance that have been achieved via the introduction of such elements and via other developments are illustrated by the data shown in Figure 1.3 (a). The evolution of composition, with a reduction in chromium content, is highlighted in Figure 1.3 (b). This reduction is partly due to it being displaced by these refractory elements and partly because it is a γ-stabiliser and creep resistance usually requires a high γ' content [9]. However, as detailed later (§ 3.4.2.2), this reduction and enhanced refractory metal content tends to impair corrosion resistance (including resistance to type II corrosion).

Thanks to air cooling, the root of the blade is kept below 700 °C permitting operation at higher stress. Creep data at 750 °C for CMSX-4 is shown in Figure 2.5. It is observed that significant creep strain occurs above 600 MPa. The root of the blade being kept much cooler is therefore not expected to undergo significant creep.



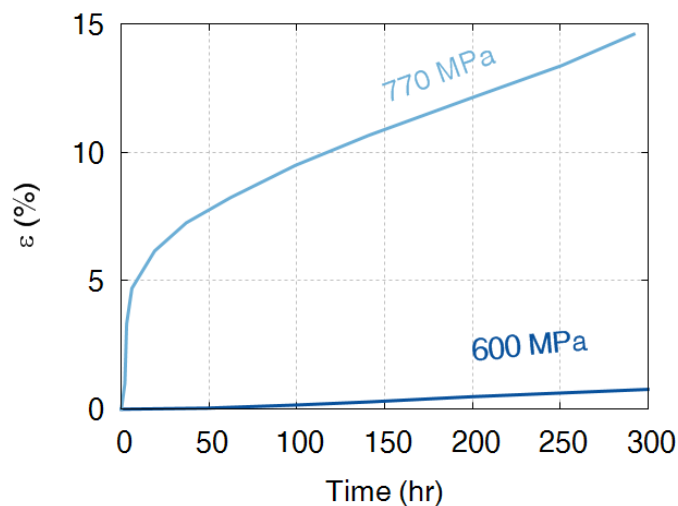Figure 2.5: Creep curve of CMSX-4 at 750 °C – for sample orientated within 10° of <001> reproduced from Matan et al. [24]

---

[1] Other metals are sometimes included and are parts of the wider refractory metals family (hafnium, ruthenium...) [131]

# Chapter 3   Environmental degradation of the turbine blade

It was seen in the previous chapter that turbine blades are operating at extreme temperatures with substantial mechanical loading. In addition, turbine blades are subjected to an aggressive environment. Air is causing oxidation while various contaminants can come into contact with the blades and cause damage.

## 3.1   Introduction

Superalloys are made of several elements, and knowing which compounds is going to form requires a thermodynamic assessment as shown in Figure 3.1. If this chemical reaction is likely to occur, its rate of production or consumption becomes significant (both are assessed in this work with $\Delta G_0$). Finally, stability of the compound is important to ascertain its abundance.
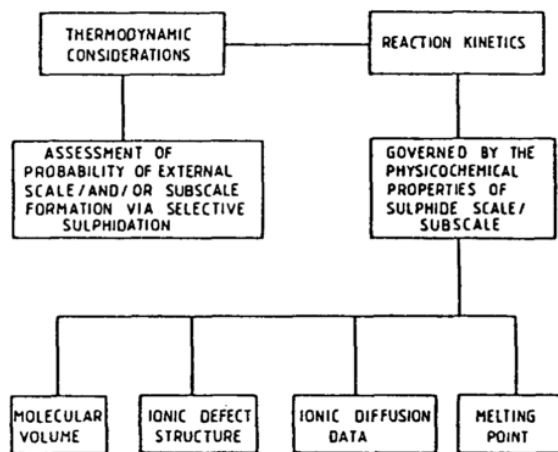
Figure 3.1: Factors influencing the development of superalloys protection from Strafford and Datta [25]

## 3.2   Oxidation of superalloys

Oxidation is a chemical reaction between the turbine blade material and the oxygen from the flue gases. A good oxidation resistance is observed when the oxide formed is dense, creating a barrier to oxygen diffusion, is adherent and stable [26]. At constant temperature and pressure, the stability of the oxides, formed by nickel-superalloys, can be ranked by its Gibbs free energy [27], shown in Figure 3.2.

Since reactions equilibrium are dependent on temperature, it is useful to calculate the Gibbs energy of formation as a function of temperature. Jacobson [28] detailed in Equation 3.1 how to calculate the Gibbs free energy. The overall $\Delta G°$ for the reaction is calculated as per Equation 3.2.

| | |
|---|---|
| $$G°(T) = \{\Delta_f H°(298) + [H°(T) - H°(298)]\} - TS°(T)$$ | Equation 3.1 from [29] |
| $$\Delta G°(T) = \sum_{j}^{product} \chi(j)G°(T,j) - \sum_{j}^{reactant} \chi(i)G°(T,i)$$ | Equation 3.2 from [28] |

Whether the compounds are in their condensed (liquid) or gas phases the $\Delta G°$ is unchanged.

When the $\Delta G°$ is positive the reaction goes backwards. When it is negative the reaction goes forwards. The further away from the *x*-axis, the faster is the kinetic of this reaction. For example, it is noted that there is a larger (more negative) Gibbs free energy of formation for Al oxidation than Ni. If both compounds are present in equal quantity (leading to a similar activity) $Al_2O_3$ would react more readily and be more abundant than NiO.
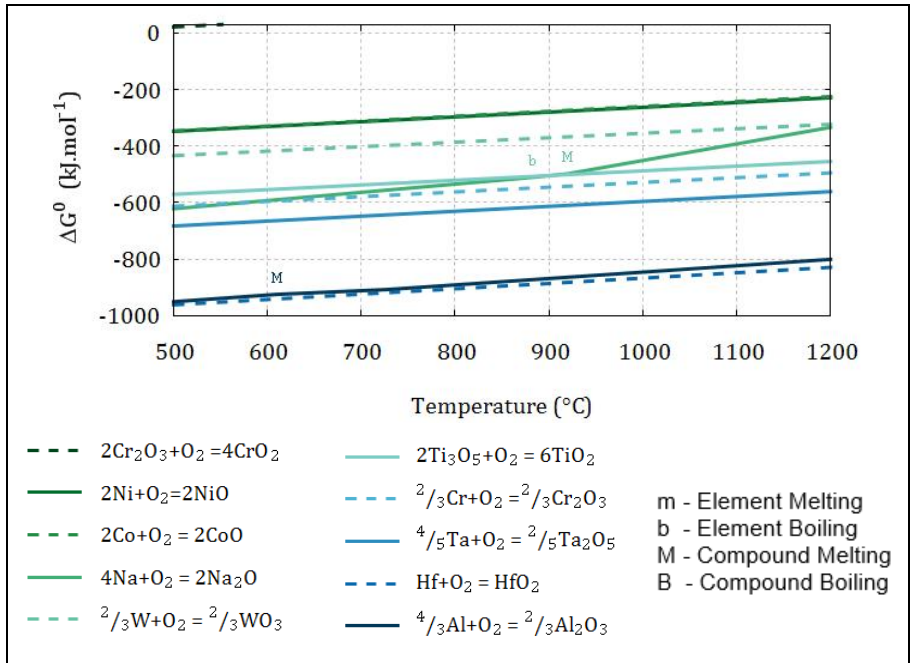
Figure 3.2: Free Gibbs energy of formation ($\Delta G_0$) of various oxides. Data from [30] and [31]

In addition to stability, oxide resistance to high temperature is also important. For instance, $Cr_2O_3$ converts to $CrO_3$ at 1000 °C [26]. This compound is volatile, resulting in oxide loss compromising the protection of the turbine blade. Vapour pressure of various oxides relevant to nickel superalloys are shown in Figure 3.3. Aluminium oxide, for example, is preferred at high temperature due its very low vapour pressure.
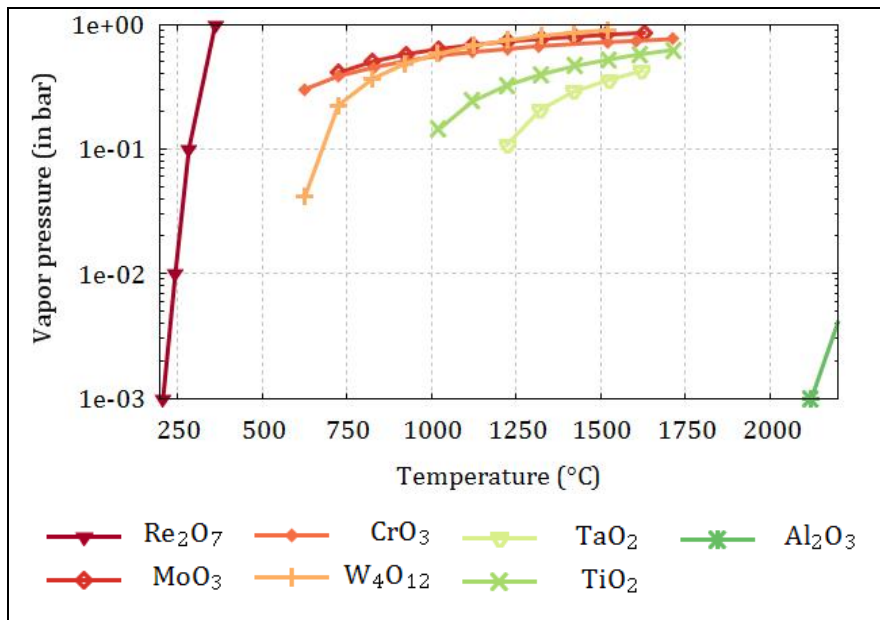


Figure 3.3: Vapour pressure against temperature of various oxides relevant to superalloys. Data for $Re_2O_7$, $MoO_3$ and $Al_2O_3$ from Lide [32], remaining data from Ramberg et al. [33]

15

Fick's first law, in one dimension, states that a flux of mobile species would flow from the region of high concentration to a region of low concentration, at a rate governed by the diffusion coefficient [27]. Kinetics of oxidation is often studied through gravimetric change.

$$\frac{\Delta m}{\mathcal{A}} = k \, \log t \qquad \text{Equation 3.3}$$

$$\frac{\Delta m}{\mathcal{A}} = k \, t^n \qquad \text{Equation 3.4}$$

With $\mathcal{A}$ sample surface, $k$ the temperature and material dependent rate constant, $t$ the time and $n$ the exponent material dependent

At a low temperature (500 °C), oxides on Al or Cu exhibit logarithmic growth rates (Equation 3.3). Thus, very thin oxides are found. They are formed rapidly and grow slowly with time. The logarithmic rate was explained by transport controlled by electronic effects [34].

At higher temperature (>500 °C), a linear rate can be observed (n=1 in Equation 3.4). This is observed on low-carbon, low-silicon steel in $N_2$-$O_2$ (1–16 %vol) environments. The linear rate was explained by gas phase diffusion [27].

Most often the kinetic growth rate has a parabolic behaviour (n=0.5). Wagner's theory of scale, building on Fick's first law (see above), was fundamental in providing an understanding of this behaviour [35], [36]. The theory assumes that each interface is at a local chemical equilibrium and that gas phase transport (through pores and microcrack, for example) is neglectable. It does not account for transport occurring at the grain boundaries and due to dislocations. In such situation, the scaling rate is controlled by diffusional mass transport of cations or anions through the oxide film, resulting in a parabolic oxide growth. If the transport of metal cations is predominant, the scale grows outwardly, and inwardly if the metal anions are dominant ($O^{2-}$). If there is an equivalent transport rate, then a growing double layer is observed [37].

Oxide growth for alloys is more complex than pure metals due to competing and synergistic effects [26]. To illustrate this, Figure 3.4 shows which oxides form on a ternary alloy made of Ni-Cr-Al at 1000°C. Three regions are distinguished: the first with NiO and internal oxide, the second with $Cr_2O_3$ and internal oxide and the third with $Al_2O_3$ [38].
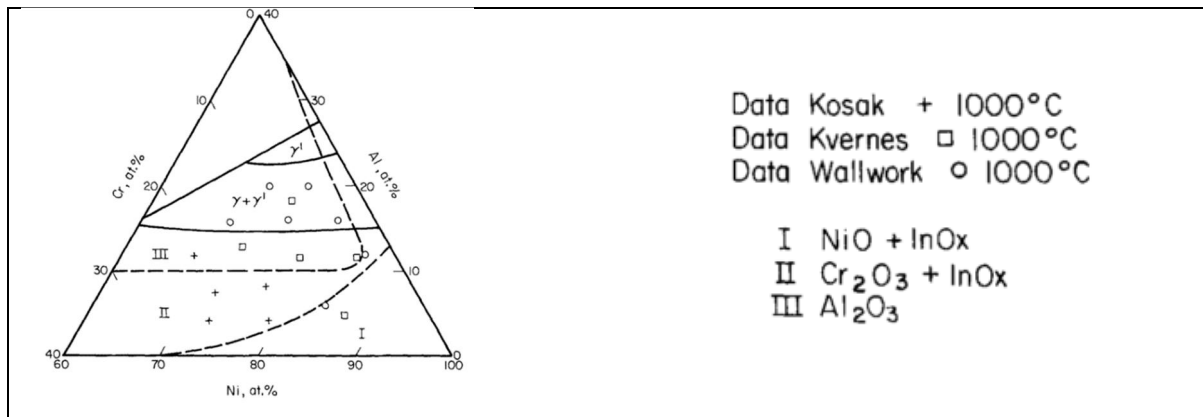
Figure 3.4: Oxide map of the ternary system Ni-Cr-Al at 1000°C, from Wallwork and Hed [38]

Sudbrack et al [39] studied CMSX-4 (with 115 ppm Y) and cycled it 440 times, between 815 °C and 27 °C. The oxide layer was made of 4 varying thickness layers. The first was made of NiO, followed by a $Cr_2O_3$ and spinel, followed by a Cr-Ta rich layer and the last layer was made of $Al_2O_3$. This is in agreement with the work from Onal et al. [40] and more recently from Li et al. [41]. Li et al. performed isothermal exposure at 800 °C with varying times. Their samples were made of single crystals with composition close to CMSX-4 (6.3 wt% Al, 6 wt% Cr and Co, Ti, Mo, W and Ta). They observed that after 5 h a thin NiO layer had formed followed by the $Cr_2O_3$ and spinel. After 750 h the same 4 layers described above were also found. The NiO formed first because of its abundance in the base material (60 wt%). In addition, since it is a p-type conductor, it induces growth by outward diffusion of cations, while (to balance) oxygen is diffusing inward. The development of the $Al_2O_3$ layer stops the diffusion of Ni and the NiO layer also stops growing [41].

Obigodi-Ddjeng [42] studied the oxidation of PW1483 (with very similar composition/treatment as SCRY-83). His XRD results show, after an exposure of 24 h at 800 °C, peaks matching NiO, $Cr_2O_3$ and mixed oxide ($NiCr_2O_4$ and $CoCr_2O_4$). The weight gain was around 0.4 mg/cm$^2$ after 20 h.

## 3.3  Fuel contaminants

Contaminants can enter the turbine carried by air and fuel (and its additives) required by the turbine, but also by water (from compressor wash).

### 3.3.1 Salts deposition

The fuel and air are mixed and burned in the combustion chamber. It was noted by McCreath [43] that salt particles and small particles (lower than 5 µm size) passing through

the primary zone would evaporate. However, larger droplets (bigger than 6 µm) passing through combustion dilution zone would survive the residence time.

Deposition of salts on a turbine blade can occur by three mechanisms. First, submicron aerosol particles can deposit onto the blade. The second possibility is as a result of impact of larger particles being shed [44] or due to a poor liquid fuel atomisation [45]. Sodium chloride and sodium sulphate vaporise at high temperatures (T>1413 °C & 1429 °C), and vapour condensation onto colder blades (due to the internal air cooling) [46] could also occur.

The phase of the sodium chloride and sodium sulphate is also indicated at atmospheric pressure in Figure 3.5.

The effect of pressure would increase the melting point of the various salts, for example at 15 bar (which is roughly the pressure in the combustor) the NaCl melting point is 1090 °C [47] while it is 801 °C at atmospheric pressure.



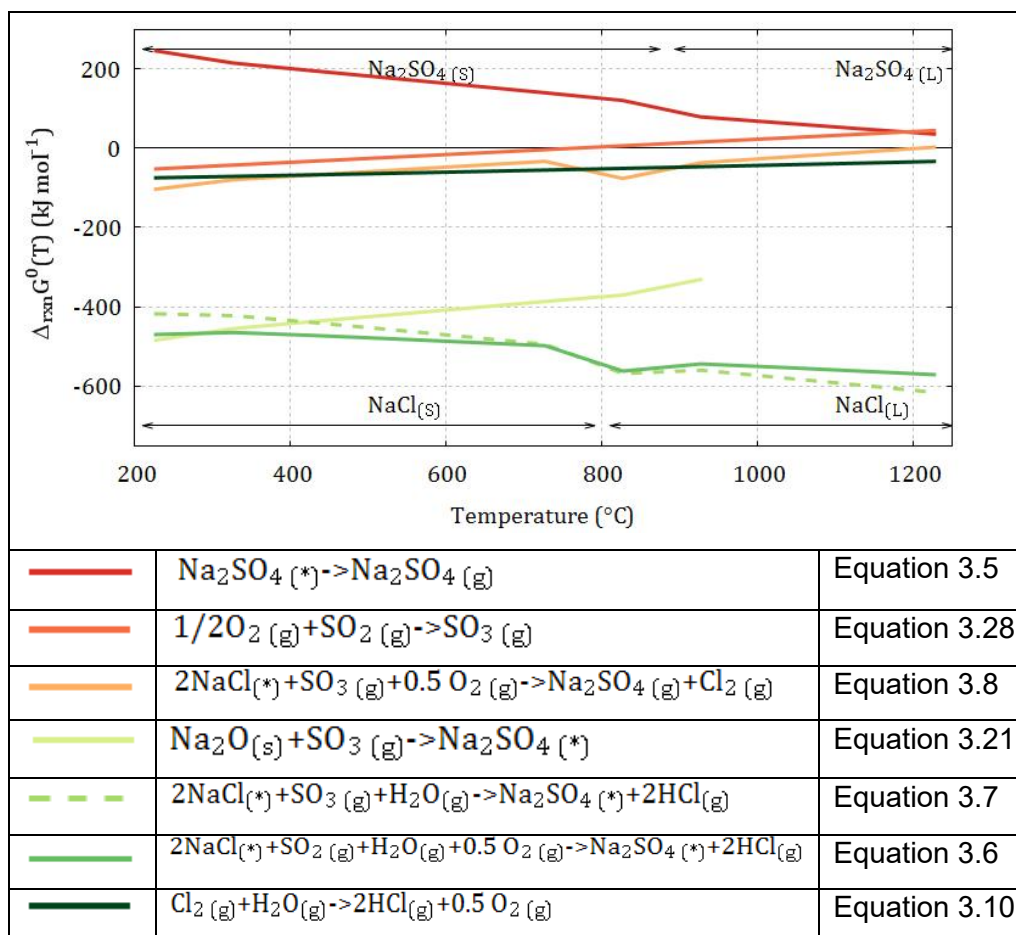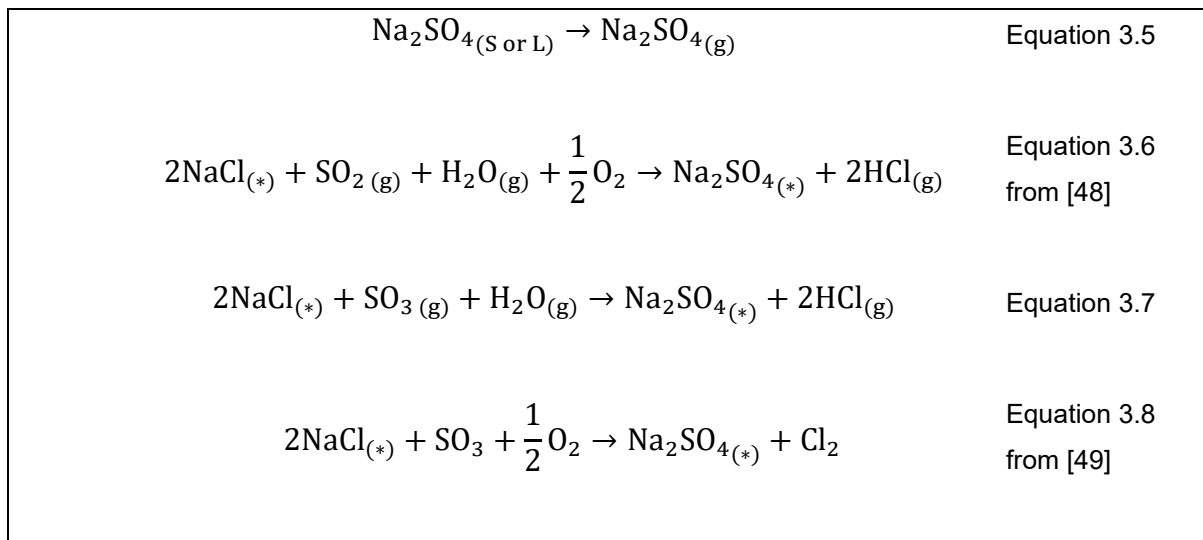| | | |
|---|---|---|
| ——— | $Na_2SO_{4\,(*)} \rightarrow Na_2SO_{4\,(g)}$ | Equation 3.5 |
| ——— | $1/2O_{2\,(g)} + SO_{2\,(g)} \rightarrow SO_{3\,(g)}$ | Equation 3.28 |
| ——— | $2NaCl_{(*)} + SO_{3\,(g)} + 0.5\,O_{2\,(g)} \rightarrow Na_2SO_{4\,(g)} + Cl_{2\,(g)}$ | Equation 3.8 |
| ——— | $Na_2O_{(s)} + SO_{3\,(g)} \rightarrow Na_2SO_{4\,(*)}$ | Equation 3.21 |
| – – – | $2NaCl_{(*)} + SO_{3\,(g)} + H_2O_{(g)} \rightarrow Na_2SO_{4\,(*)} + 2HCl_{(g)}$ | Equation 3.7 |
| ——— | $2NaCl_{(*)} + SO_{2\,(g)} + H_2O_{(g)} + 0.5\,O_{2\,(g)} \rightarrow Na_2SO_{4\,(*)} + 2HCl_{(g)}$ | Equation 3.6 |
| ——— | $Cl_{2\,(g)} + H_2O_{(g)} \rightarrow 2HCl_{(g)} + 0.5\,O_{2\,(g)}$ | Equation 3.10 |

Figure 3.5: Gibbs free energy calculated with data from [29] at atmospheric pressure, every 100°C

At the combustor exit, DeCrescente and Bornstein [48] found that sodium chloride will combine with sodium dioxide to form sodium sulphate (and hydro-chlorine) as per Equation 3.6. The relatively low value of the $\Delta G°$ means that sodium chloride slowly turns into sodium

sulphate and hydrogen chloride. Equation 3.7 and Equation 3.8 can go forward either with $SO_2$ or $SO_3$, with the latter reaction promoted at low temperatures (<800 °C). However, a comparison between the two equations (meaning all reactants are present), shows in Figure 3.5 a lower $\Delta G°$ for Equation 3.7, that has a faster kinetic rate.

$$Na_2SO_{4(S\,or\,L)} \rightarrow Na_2SO_{4(g)}$$ 
Equation 3.5

$$2NaCl_{(*)} + SO_{2\,(g)} + H_2O_{(g)} + \frac{1}{2}O_2 \rightarrow Na_2SO_{4(*)} + 2HCl_{(g)}$$ 
Equation 3.6 from [48]

$$2NaCl_{(*)} + SO_{3\,(g)} + H_2O_{(g)} \rightarrow Na_2SO_{4(*)} + 2HCl_{(g)}$$ 
Equation 3.7

$$2NaCl_{(*)} + SO_3 + \frac{1}{2}O_2 \rightarrow Na_2SO_{4(*)} + Cl_2$$ 
Equation 3.8 from [49]

The production of sulphate was studied by Glarborg and Marshall [50]. They estimated the rate of production and consumption of each reaction, which is displayed schematically in Figure 3.6.
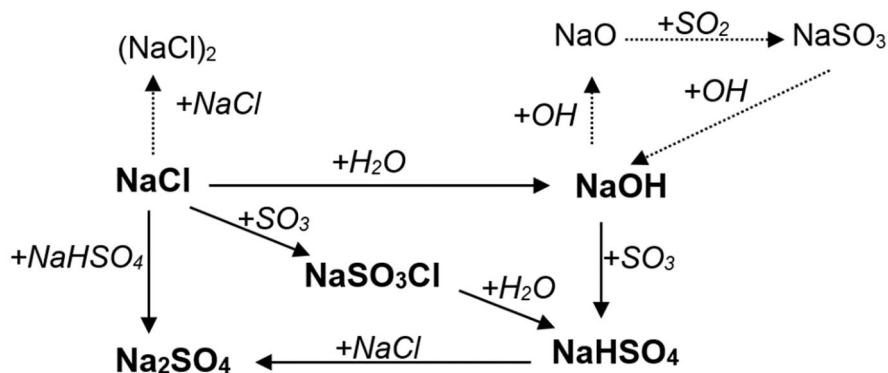


Figure 3.6: Pathway from NaCl to $Na_2SO_4$ showing the importance of $SO_3$. Adapted from Glarborg and Marshall [50]

### 3.3.2 Effect of chlorine-based contaminants

Sea salt is often present in air (as spray particles) near the sea and ocean shore. Atmospheric models developed by Cotton et al. [51] have shown that significant concentration is retained up to an altitude of 1 km. The solute weight fraction of the sea salt was linked to the ambient relative humidity by Zhang et al. [52]. They found that increasing humidity is linked to lower solute weight fraction.



| (a) Before water wash | (b) After water wash |

Figure 3.7: Top sections of compressor EGV of a turbine located in the north Atlantic Ocean before and after water wash

On offshore platforms, sea salt quantity ingested by the gas turbine is decreased using air inlet filtration. However, as the air is assumed clean offshore, and as space is at a premium, air filtration is sometimes coarse and undersized (with the use of high-velocity filters) and may allow a small amount of sea salt to be ingested. Also, despite the use of the best filtration, a draught of air opposite to the flow direction may occur when the turbine is shut down, depositing salt inside the turbine (chimney effects). Water wash should be performed after an extended outage.

NaCl melts at 801°C and boils at 1465°C (see Table 3.1). It is therefore expected to be in either in its liquid or solid form as it crosses the turbine stages.
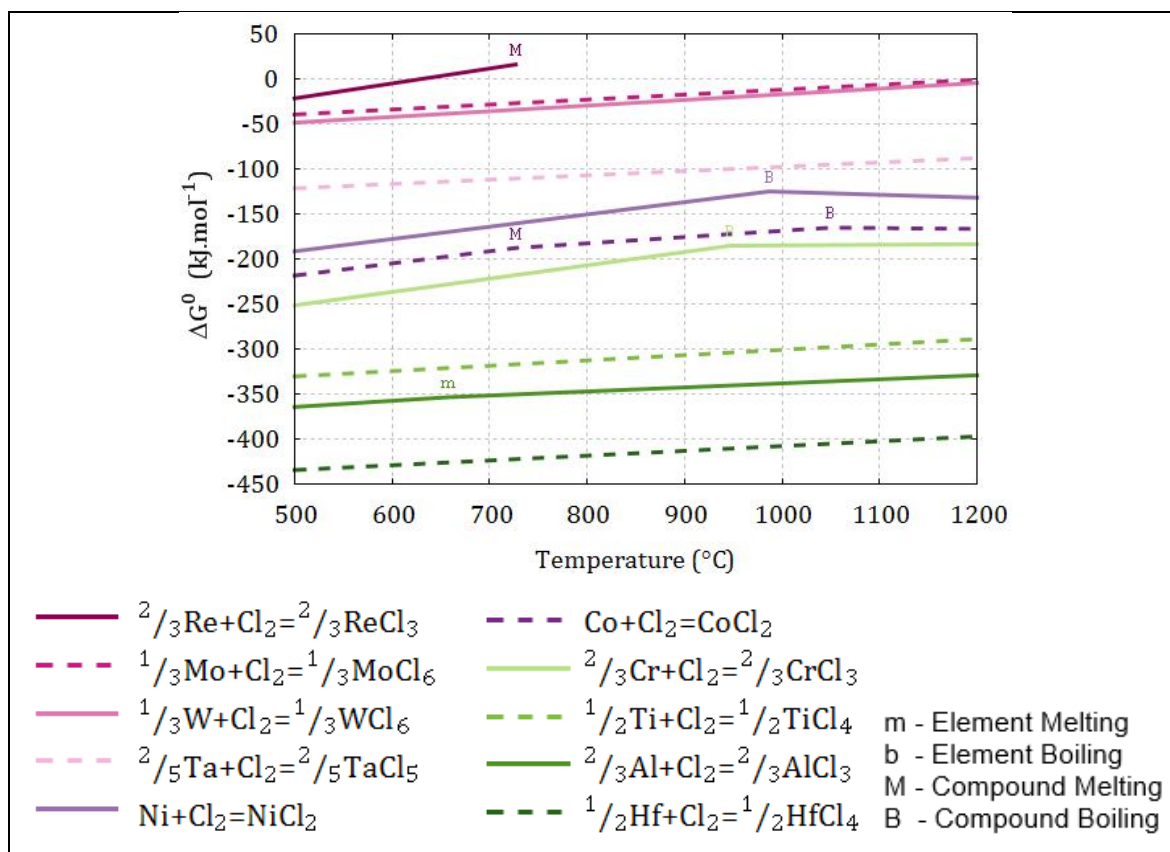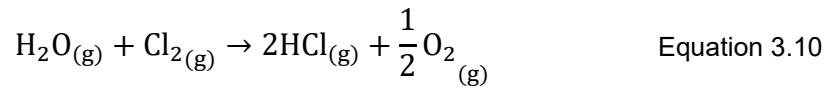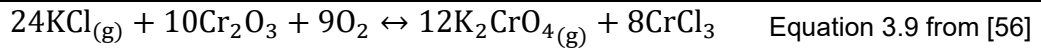
Figure 3.8: Gibbs free energy calculated for chloride compounds relevant to superalloys. Data from [53], [54]

Chlorine gas recombines into hydrogen chloride in the presence of steam (Equation 3.10 with $\Delta G°$ calculated in Figure 3.5). Both compounds can cause significant harm to the turbine. Hurst et al. [55] undertook hot-stage microscopy of Nimonic 90 (composition available in appendix § 9.2), sprayed with sodium chloride at 700 °C. The author found that the thermally grown oxide would crack in the presence of sea salt. McKee et al. [49] repeated the same experiment on IN738 (composition also available in appendix) at 800 °C, and found the same result. To determine which of the sodium or the chloride was cracking the oxide, they exposed the sample to an environment made of $O_2$ and 60 ppm HCl and a different sample in an environment made of $O_2$ and 1% $Cl_2$. Both samples experienced a very rapid attack with features identical to the ones seen in a sample sprayed with NaCl. The author suspected an NaCl/$NiCl_2$ and/or NaCl/$CoCl_2$ eutectics, (respective phases diagram available in appendix § 9.4.7 and § 9.4.8) as possibility. Alexander [56] (reported by [57]), while working on stainless steel alloys, suspected a $CrCl_3$ with low vapour pressure would form, per Equation 3.9, cracking the protective chromium oxide.

21

$$24KCl_{(g)} + 10Cr_2O_3 + 9O_2 \leftrightarrow 12K_2CrO_{4(g)} + 8CrCl_3 \qquad \text{Equation 3.9 from [56]}$$

$$H_2O_{(g)} + Cl_{2(g)} \rightarrow 2HCl_{(g)} + \frac{1}{2}O_{2(g)} \qquad \text{Equation 3.10}$$

To confirm this hypothesis, the vapour pressure of several compounds was plotted in Figure 3.9. Data from Lide [32] also included $Cl_2S$, $Cl_2S_2$, $Cl_2OS$ and $Cl_2O_2S$ with temperatures below 140 °C, at 1 bar, meaning these compounds are very volatile. It can also be seen that $AlCl_3$ is the compound with the highest partial pressure.
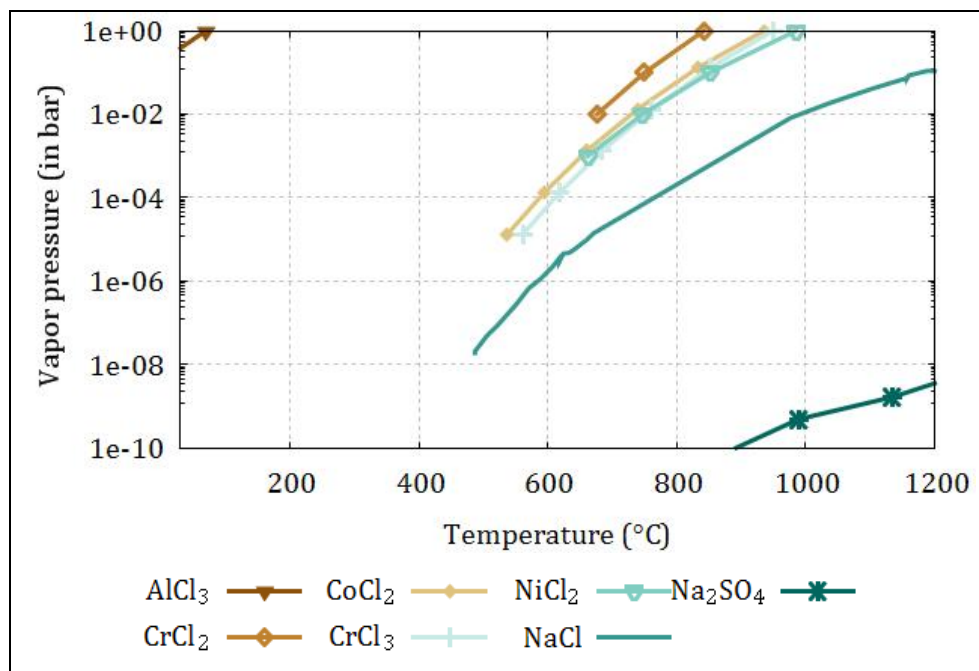


Figure 3.9: Vapour pressure of compounds relevant to sodium chloride and nickel-based superalloys. Data from Lide [32] for $AlCl_3$, $NiCl_2$ and $CoCl_2$ compiled from authors [58], [59] for NaCl and $Na_2SO_4$ and from Hancock [60] for $CrCl_2$, and $CrCl_3$

Electron probe microanalysis (EDMA), performed by Hurst et al. [55], found the chlorine just below the oxide scale and on top of the substrate. The authors mentioned that the oxide was ready to spall. In addition to the test above, NaCl was introduced, but as a vapour instead of condensed salt. Despite the same amount of reactant in the environment, the vapour form was less aggressive than the condensed form.

### 3.3.3  Effect of sulphur-based contaminants

The fuel may carry sulphur, either in the form of elemental sulphur ($S_8$) or mixed with the gas as hydrogen sulphide ($H_2S$). As described earlier, a remote platform doing gas re-injection has not enough space to separate sulphur from the gaseous fuel. Similarly, the cost of low sulphur diesel (automotive grade oil – AGO) is much higher than marine grade oil (factor 2 or even higher in remote regions). To give an order of magnitude, a 4.2 MW gas turbine generator will consume 35 m$^3$ of diesel per day or $31t$. Given the large amount of fuel consumption, the difference in price becomes significant. Independently from this economic observation, a longer logistic chain also means more chance of contamination.

Investigation on the effect of sulphur are made with sulphur containing gases mixed either with inert gases or with air. In the second case, oxidation is competing with sulphides formation. The Gibbs free energy was calculated for several reactions and is shown in Figure 3.10. A comparison with $\Delta G°$ value of oxide (Figure 3.2) and chloride (Figure 3.8) formation, shows a relatively low value for sulphide formation. However, the exposition of pure nickel samples to air mixed with sulphur (at 700°C) was found to promote the formation of nickel sulphide at a much faster rate than oxide [61], [62]. This was explained by a faster diffusion in sulphides, due to a higher lattice defect (than oxides) promoted by a higher deviation from stoichiometry (ie: for chromium it can range from $CrS_{1.3}$ to $CrS_{1.54}$). Finally, a $Ni/Ni_3S_2$ eutectic exists with Tε=635°C ($Co_4S_3$ at Tε=880°C) [63] (Ni-S phase diagram is also available in appendix § 9.4.5). The reactions, often relying in the transport of species through scales, will be faster in a liquid than in a solid.
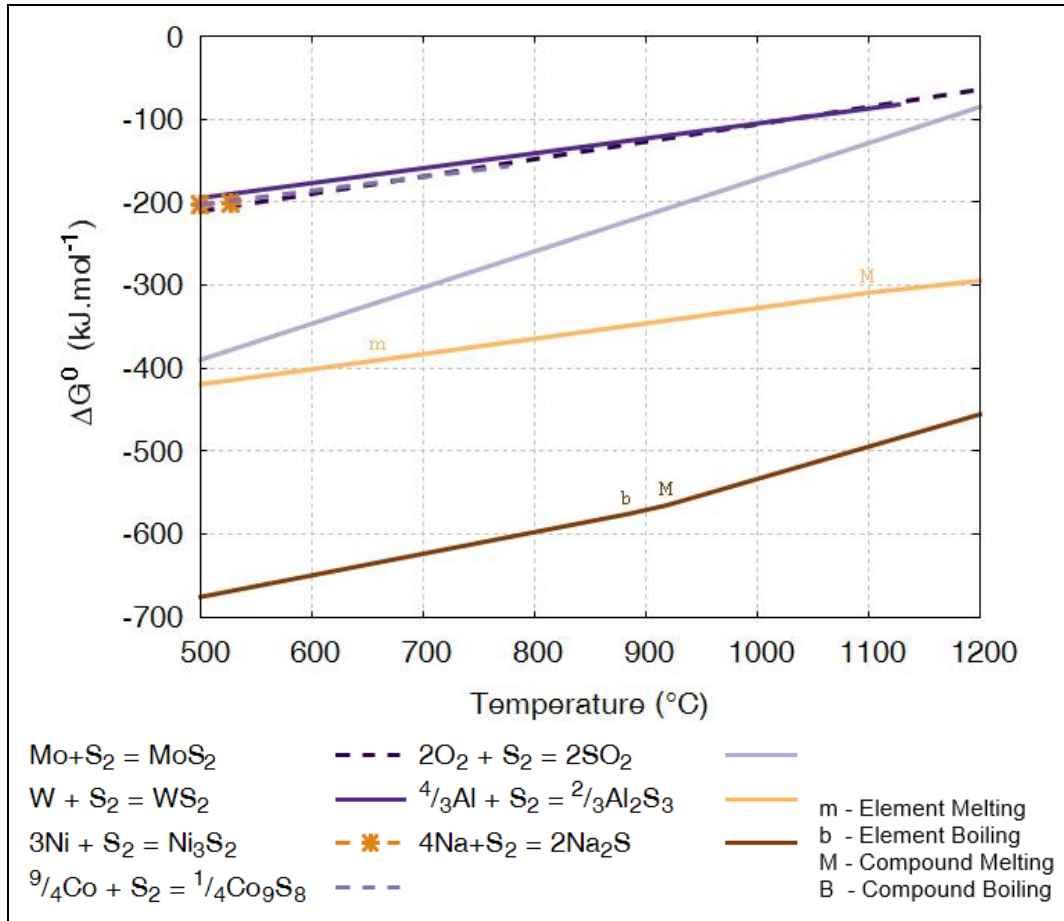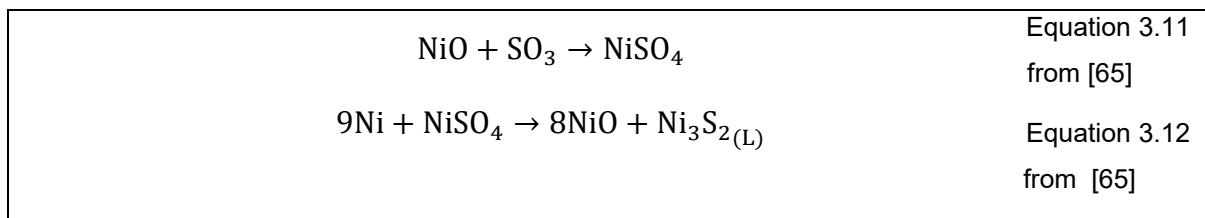
Figure 3.10: Gibbs free energy of formation calculated for several superalloys elements reacting with sulphur. Data from [53], [54]

Sulphides will therefore form despite being thermodynamically unfavoured. Floreen and Kane [64] studied crack growth characteristics in $He+SO_2$ and in $Air+SO_2$. They found that air inhibited sulphide formation (compared to He environment). The mechanisms by which air does so is worth studying. Haflan and Kofstad [65] studied, between 500 and 900 °C, the effect of exposure of pure nickel, to environments of $SO_2/SO_3+O_2$. Equation 3.11 and Equation 3.12 were the proposed mechanisms in their study.

| | |
|---|---|
| $$NiO + SO_3 \rightarrow NiSO_4$$ | Equation 3.11 from [65] |
| $$9Ni + NiSO_4 \rightarrow 8NiO + Ni_3S_{2\,(L)}$$ | Equation 3.12 from [65] |

These mechanisms are schematically represented in Figure 3.11 in their concentration ranges (the blue cross indicates the concentration expected in the rig). These mechanisms were found to give rise to a parabolic mass gain [66] (between 500 and 600°C, with an $SO_2$ concentration of 100 Pa).
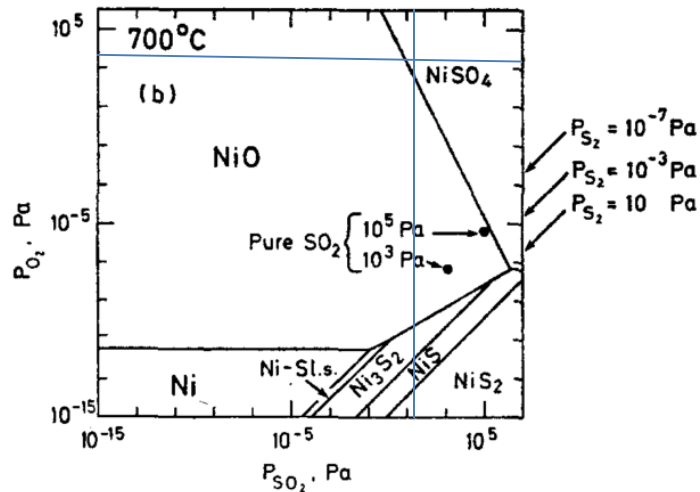
24

Figure 3.11: Phase stability diagrams for the Ni-S-O system constructed with $\Delta G°$ taken at 700°C, from Siersten and Kofstad [66]

Sulphur protection is achieved with specific alloy composition or with pre-oxidation. Vanadium addition (up to 20 wt%) to Co-20Cr-3.5Al-Y was found to result in the lowest weight gain, compared to alloy made of various composition (0.5–5 Ta, 1–10 Mo, 1–5 Zr) during exposure of 240 h at 750 °C in an environment depleted in oxygen ($pS_2 = 10^{-1}$ Pa, $pO_2 = 10^{-16}$ Pa) [25].

Natesan [67] pre-oxidised at 875 °C and 1100 °C samples made of $Ni_3Al$, and exposed them at 875 °C, to an environment of air and 0.1–4.7% $H_2$–$H_2S$. He observed that samples pre-oxidised at 875 °C experienced an additional mass gain, while those that were pre-oxidised at 1100°C did not. He concluded that the alumina layer formed at 875 °C was not protective. A continuous protective layer requires a high concentration of Al (to increase the activity) and/or a high temperature (to raise the lattice diffusion coefficient).

### 3.3.4 Alkali sulphate induced damage

Alkali salts, often present as contaminants, react with sulphur to form alkali sulphate (Equation 3.6 and Equation 3.7). Hot corrosion Type I and II share commonality that will be presented in this section. For example, both types rely on the formation of a liquid phase to initiate. This is generally possible due to the presence of several low temperature eutectic.

### *3.3.4.1     Liquid formation*

The condensation of sodium sulphate onto the blade is possible by the relatively low temperature of the blade, for example, due to film cooling [68]. Upon contact of sodium sulphate, the nickel oxide is sulphated and a liquid is formed.

Table 3.1: Melting point and boiling point of several compounds relevant to hot corrosion ordered by increasing temperature

| Product | Melting point (°C) | Boiling point (°C) | Reference |
|---|---|---|---|
| 50% $Na_2SO_4$ + 50% $CoSO_4$ | 565 | | [46] |
| 47% NaCl + 53% $Na_2SO_4$ | 618 | | [69] |
| 62% $Na_2SO_4$+38% $NiSO_4$ | 631 | | [70] |
| NaCl | 801 | 1465 | [69] [71] |
| 30% $K_2SO_4$ + 70% $Na_2SO_4$ | 831 | | [69] |
| $Na_2SO_4$ | 884 | 1404 | [69] [19] |
| $K_2SO_4$ | 1069 | | [69] |

It is noted that Ni and Co are both liquid at 700°C. This is critical to initiate the fluxing mechanism.

## 3.3.5 Fluxing mechanism

More species can dissolve in the liquid ($NiSO_4$/$CoSO_4$/$Na_2SO_4$) and this lead to the formation of an ionic melt. This ionic melt can dissolve the protective oxides either through acididic or basic dissolution. (It is, in some aspects, similar to the amphoteric behaviour of aqueous atmospheric corrosion [72]).

### *3.3.5.1     Basic dissolution*

The thermally grown oxide (TGO) can go through a basic dissolution, as per the general Equation 3.13 (written specifically for nickel oxide in Equation 3.14, and for alumina oxide in Equation 3.15).

| | | |
|---|---|---|
| M: Metal | $MO + O^{2-} \leftrightarrow MO^{2-}$ | Equation 3.13 |
| | $2NiO + \dfrac{1}{2}O_2 + O^{2-} \leftrightarrow 2NiO_2{}^{2-}$ | Equation 3.14 from [72] |
| | $Al_2O_3 + O^{2-} \leftrightarrow 2AlO_2{}^{-}$ | Equation 3.15 from [9] |

In practice, Equation 3.21 can be combined with Equation 3.15 to give Equation 3.16.

$$2NiO + Na_2SO_4 + \frac{1}{2}O_2 \leftrightarrow 2NaNiO_2 + SO_3 \qquad \text{Equation 3.16 from [9]}$$

The basic dissolution of the oxide explained above is consuming the salt ($Na_2SO_4$) and producing the acid ($SO_3$) (in Equation 3.21). Therefore, basic dissolution of the oxide increases the melt acidity.

### 3.3.5.2    *Acidic dissolution*

Alternatively, the TGO can also go through acidic dissolution, as per the general Equation 3.17. An example is written for alumina oxide in Equation 3.18 and nickel oxide in Equation 3.19.

| | | |
|---|---|---|
| M: Metal | $MO \leftrightarrow M^{2+} + O^{2-}$ | Equation 3.17 |
| | $Al_2O_3 + 3SO_3 \leftrightarrow 2Al^{3+} + 3SO_4{}^{2-}$ | Equation 3.18 from [9] |
| | $NiO \leftrightarrow Ni^{2+} + O^{2-}$ | Equation 3.19 from [27] |

Similarly, the acidic dissolution increases the basicity of the melt, as per Equation 3.20.

$$NiO + Na_2SO_4 \leftrightarrow NiSO_4 + Na_2O \qquad \text{Equation 3.20 from [73]}$$

### 3.3.5.3    *Neutralization of the melt*

Equation 3.21 shows the equivalent of acid-base equation for sodium sulphate equilibrium. It can be re-written in an ionic form as Equation 3.22.

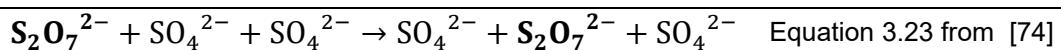| | |
|---|---|
| $Na_2O_{(s)} + SO_{3\,(g)} \leftrightarrow Na_2SO_{4\,(s)}$ | Equation 3.21 |
| Base + acid $\leftrightarrow$ Salt | |
| $O^{2-} + SO_3 \leftrightarrow SO_4{}^{2-}$ | Equation 3.22 |

The first step (mentioned above) is the formation of a liquid melt. In this melt, the protective oxide scale breaks down through an acidic dissolution [74], [75] and is usually termed

"initiation" or "incubation" as the alloy is behaving in the same way as if there was no deposit [34].

After the dissolution of the oxide, the second step of degradation is re-precipitation of the same oxide (ie: nickelate ions) into a porous oxide at the fused salt interface with the gas (grey blobs in Figure 3.13) [73]. Another species is travelling through the fused salt melt to retain the local electrical equilibrium.
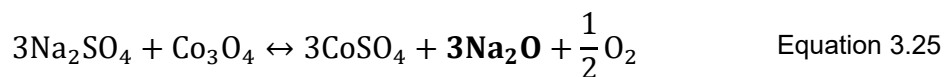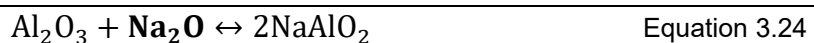
### *3.3.5.4      Transport mechanisms*

A first model was presented by DeCrescente and Bornstein [48] and further extended by Goebel and Pettit [76], who considered $O_2^-$ or $O_2^{2-}$ as the balancing transport species. However, it was calculated by Luthra [74], in cobalt alloys, that the transport rate of oxygen in ionic form $O_2^-$ and sulphur dioxide in ionic form ($SO_3^{2-}$) were much lower than the corrosion rate observed in his experiment. He therefore suggested that another transport mechanism could involve movement of $S_2O_7^{2-}$ inward balanced with $SO_4^{2-}$ outward in the melt. Instead of physical movement of the species, a rotation mechanism of the charge may occur (explained in Equation 3.23).

$$\mathbf{S_2O_7}^{2-} + SO_4^{2-} + SO_4^{2-} \rightarrow SO_4^{2-} + \mathbf{S_2O_7}^{2-} + SO_4^{2-} \quad \text{Equation 3.23 from  [74]}$$

In the presence of oxides made of different compositions, it is possible to have one oxide going through basic dissolution, while at the same location, another oxide going through acidic dissolution. This was named a "synergistic dissolution" and can be seen in Figure 3.12 (a). Since this phenomena does not depend on any transport, it accelerates greatly the dissolution, as reported by Rapp [73], [75].

Below is an example showing basic dissolution for $Al_2O_3$ and acidic dissolution for $Co_3O_4$ where the two curves cross in Figure 3.12.

$$Al_2O_3 + \mathbf{Na_2O} \leftrightarrow 2NaAlO_2 \quad \text{Equation 3.24}$$

$$3Na_2SO_4 + Co_3O_4 \leftrightarrow 3CoSO_4 + \mathbf{3Na_2O} + \frac{1}{2}O_2 \quad \text{Equation 3.25}$$

This synergistic dissolution is thought to be the reason for the rapid hot corrosion degradation and was recently reviewed by Alvarado-Orozco et al. [77]. If the negative solubility criteria is maintained, the hot corrosion is self-sustained.

## 3.3.6 Rapp-Goto "negative solubility criteria"

Rapp [72] first noted that solubility of nickel oxide in nickel sulphate varied with the basicity. This observation was extended to several oxides see Figure 3.12 (a). $SiO_2$ is an exception since there are no acidic dissolution possible in the range of the basicity studied.
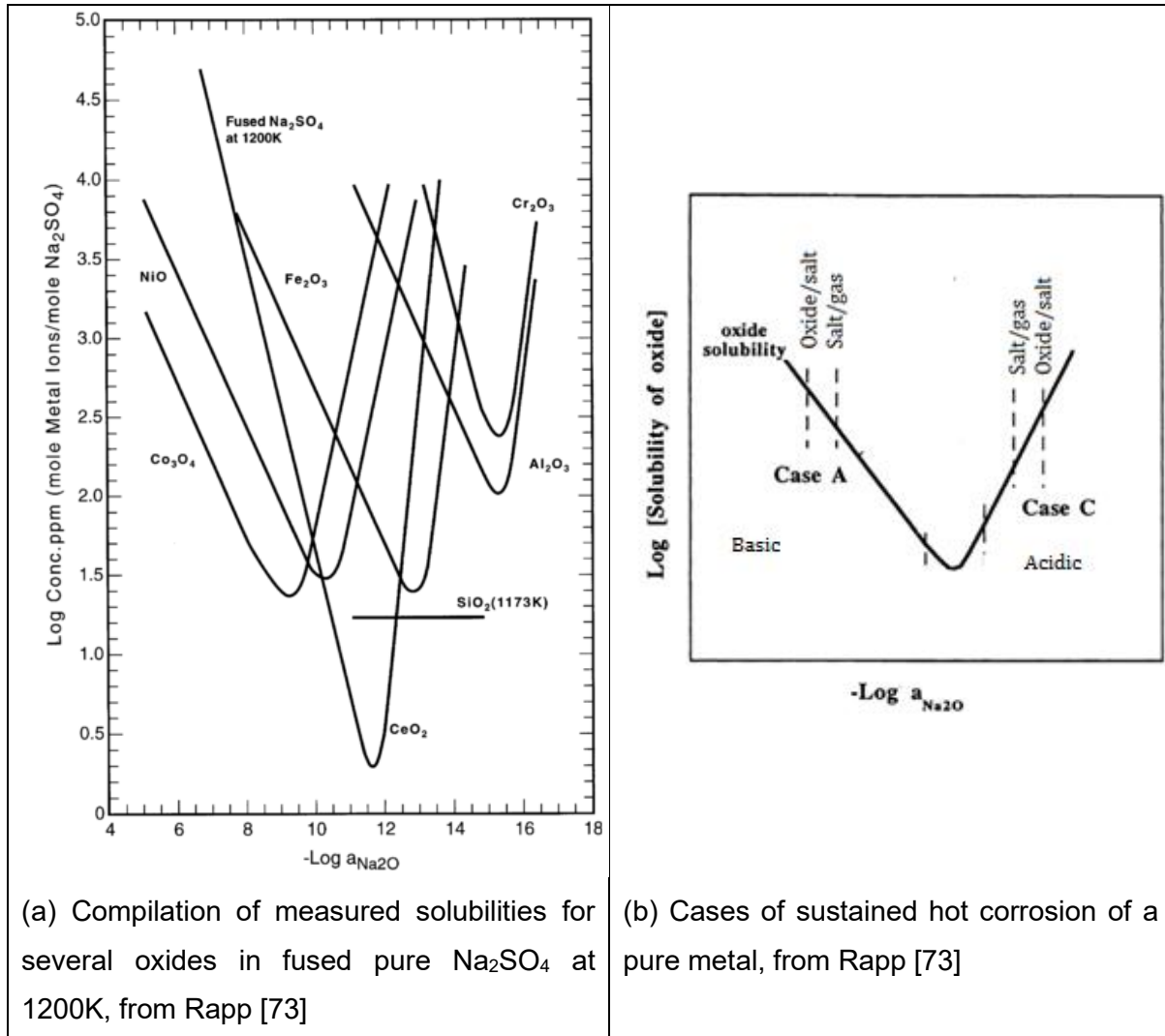
| | |
|---|---|
|  |  |
| (a) Compilation of measured solubilities for several oxides in fused pure $Na_2SO_4$ at 1200K, from Rapp [73] | (b) Cases of sustained hot corrosion of a pure metal, from Rapp [73] |

Figure 3.12: Solubities of several oxides plotted against liquid fused salt melt basicity

Therefore, by knowing the oxide solubility as a function of basicity, Rapp and Goto [78] devised a criterion to infer the sustainability of the dissolution. If the oxide solubility in the molten deposit is negative at the oxide–molten salt interface (as written in Equation 3.26), then the oxide will dissolve at the oxide–salt interface and re-precipitate at the salt–gas interface.

$$\left(\frac{d[Oxide\ Solubility]}{dx}\right)_{x=0} < 0$$

x=0 at the oxide/salt

x>0 in the salt melt

Equation 3.26 from [79]

This criterion is showing the oxide solubility in Figure 3.12 (b) for a basic dissolution, which is also shown schematically in Figure 3.13 (a). Acidic dissolution is shown in Figure 3.13 (b).

Note that in Figure 3.12 (b), the case at the bottom of the solubility curve was omitted for clarity but can also occur.
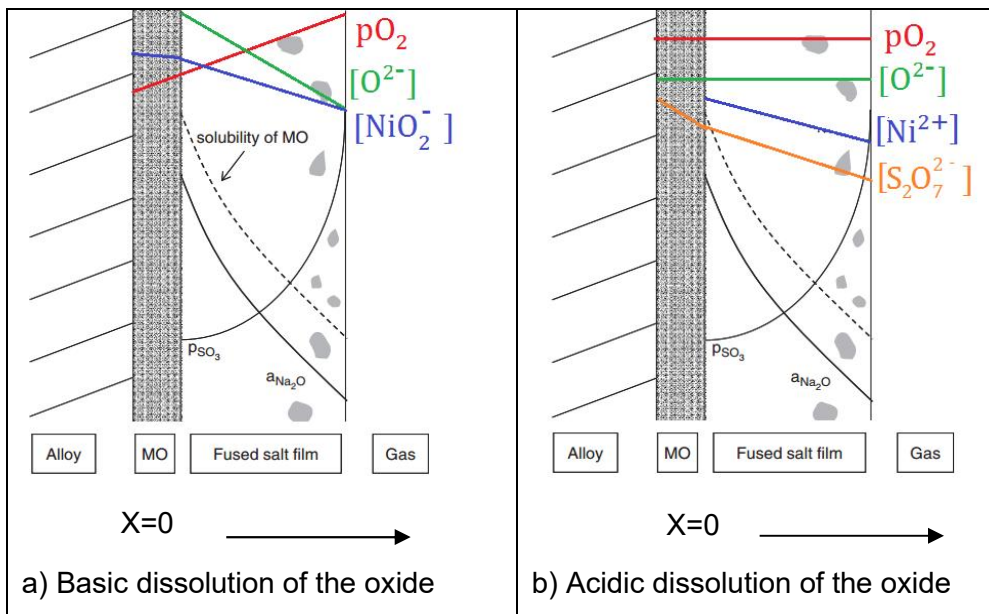


Figure 3.13: Schematic representation of hot corrosion dissolution and re-precipitation in a molten salt film, from Young [27]

## 3.4 Hot corrosion Type I and Type II

Hot corrosion has been divided into two different categories: Type I, named "high temperature hot corrosion" and Type II named "low temperature hot corrosion". The two types require sodium sulphate to initiate, and are sharing some of the mechanisms that have been shown above.

The distinction is often made on the failed parts due to the different microstructures of the attack that they exhibit. Figure 3.14 is helpful in explaining how the corrosion rate is reduced in between the two ranges and includes a schematic comparison with oxidation.
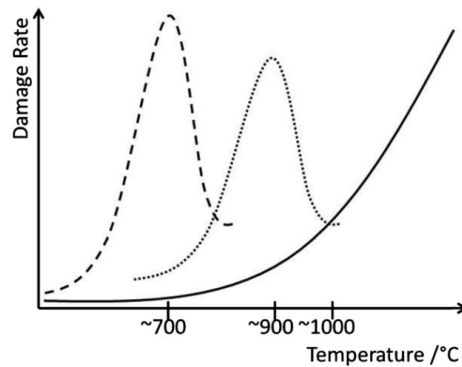


Figure 3.14: Degradation rate comparison of hot corrosion (Type II in dashed line and Type I in dotted line) and oxidation (full line) against temperature, from Sumner et al. [80]

## 3.4.1 Type I hot corrosion

The temperature range of Type I is 850–950 °C (above this range the $Na_2SO_4$ salts volatilizes and hot corrosion is not observed [34]).

The reaction layer microstructure of hot corrosion Type I is described as homogenous layer with a lower front of sulphide [81], [82].

Otsuka and Rapp [75] measured the acidity and the basicity of the melt at the surface of a pure Nickel sample coated with sodium sulphate undergoing hot corrosion. The probe results were plotted against time on the Ni-Na-S-O phase stability diagram and are shown in Figure 3.15.
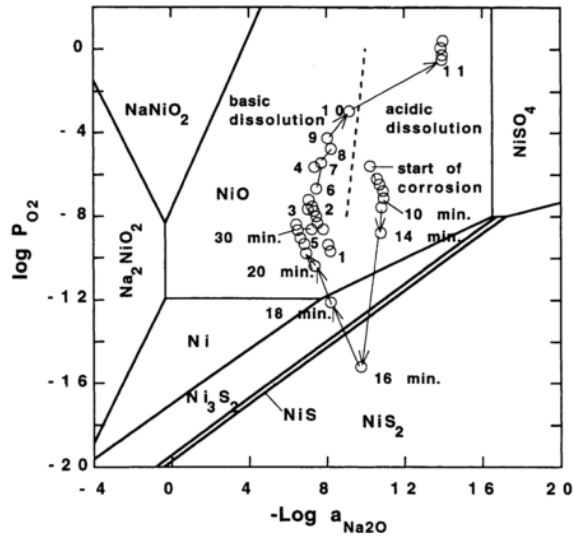
Figure 3.15: Basicity and oxygen activity measured on a pre-oxidised Nickel sample coated with sodium sulphate at 1173K on $O_2$-0.1% $SO_2$, from Rapp [72]

Figure 3.15 shows that the melt starts with an acidic dissolution of the oxide, then moving to basic dissolution and again acidic dissolution, etc. This model is in-line with the "self-sustaining" behaviour of hot corrosion, reported by Eliaz et al. [83], making it infamous. The explanation of hot corrosion Type I for pure nickel is, as explained above, also valid for other oxides, as shown in Figure 3.12 ($Cr_2O_3$, $Al_2O_3$, $Fe_2O_3$, $Co_3O_4$...).

## 3.4.2 Type II hot corrosion

The Type II hot corrosion temperature range starts at 600 °C and decreases substantially above 850 °C [49]. The kinetics and the reaction layer microstructure is different from Type I, in that it shares the acidic dissolution described above [74]. This acidic fluxing can be caused by the gas or by the alloy itself.

### *3.4.2.1 Gas phase acidic fluxing*

If the sulphur trioxide partial pressure is high enough (as shown in Figure 3.11), a formation of nickel sulphate becomes possible (as per Equation 3.27).

$$NiO + SO_3 \rightarrow NiSO_4 \qquad \text{Equation 3.27}$$
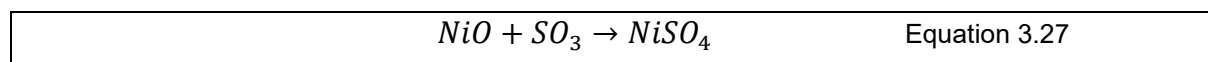
Nickel sulphate would readily mix with sodium sulphate and form a liquid (eutectic system $Na_2SO_4$/$NiSO_4$ $T\varepsilon$=671°C) that is at the origin of hot corrosion.

The minimum concentration of sulphur trioxide that would cause the nickel sulphate to form has been estimated by Lillerud and Koftsad [82] at 100 ppmv at 700°C Figure 3.16 shows that this minimum rises to 1000 ppmv at 800°C (note that these values are found in a mix of $O_2$ +4 %$SO_2$).
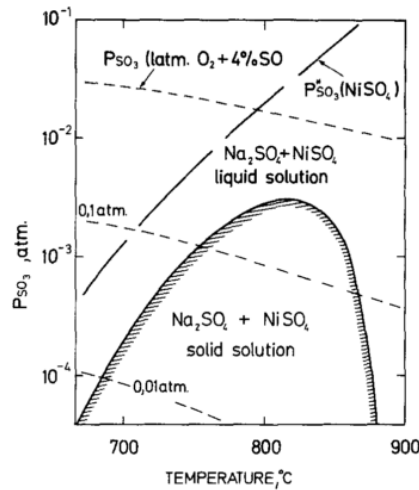


Figure 3.16: Estimation of the critical partial pressures of $SO_3$ for formation of sodium sulphate and nickel sulphate [82]

This relatively low value of sulphur trioxide required to form nickel sulphate means it is important to know the concentration of sulphur trioxide at the exit of the combustion chamber.

As it appears, sulphur dioxide first forms at the exit of the combustor, and requires a further oxidation to form sulphur trioxide (as per Equation 3.28). A kinetic dissociation model of sulphur dioxide into sulphur trioxide has been developed by Hindiyarti et al. [84]. Figure 3.17 (a) shows that $SO_3$ exists only at low temperatures, but the reaction is sluggish as shown in (b).
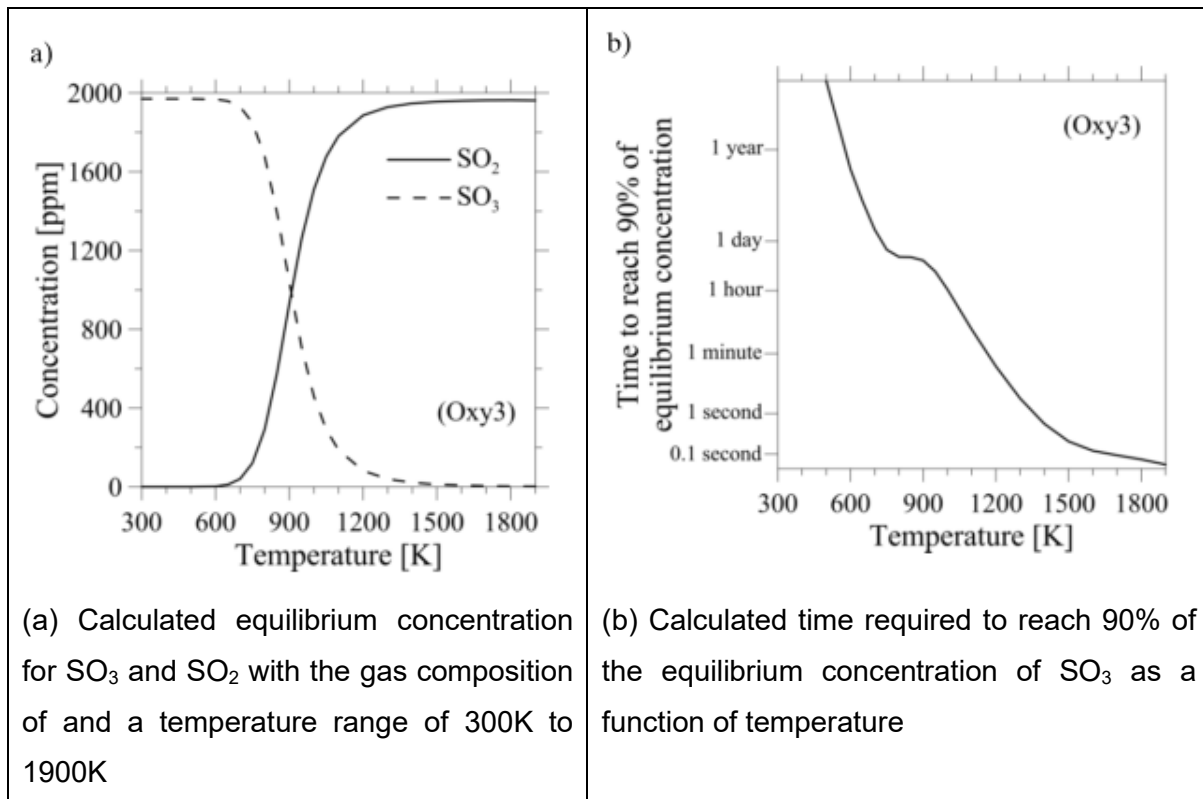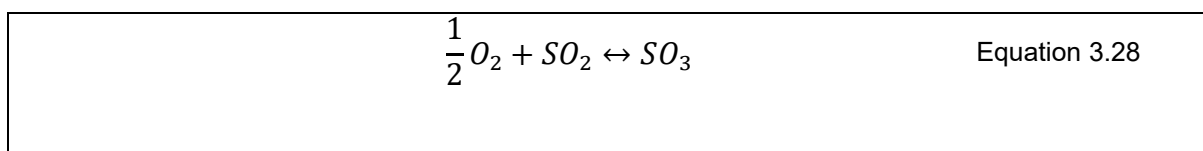
Figure 3.17: SO₂/SO₃ concentration in the following conditions: $SO_2$=1968ppm, $O_2$=2.8% vol, $H_2O$=9.1% vol, $N_2$=0.4% vol, from [85]

As seen in Figure 3.6, $SO_3$ is critical for the formation of $Na_2SO_4$. There is therefore interest to measure the concentration of $SO_3$ in the rig. Sulphur trioxide measurement methods have been listed and compared by Fleig et al. [86].

$$\frac{1}{2}O_2 + SO_2 \leftrightarrow SO_3 \qquad \text{Equation 3.28}$$

The rate of the reaction above (Equation 3.28) is slow ($\Delta G°$ available in Figure 3.5). That is why catalysts are seldom used in rig reproducing hot corrosion conditions. Garcia-Herrera et al. [87] have shown that the conversion rate is greatly affected by the type of catalyst. The platinum type seems to achieve the highest conversion rate; the type of catalyst used in this rig will be described in § 4.3.1.3.

### 3.4.2.2 Alloy induced acidic fluxing

Addition of refractories (Mo, W, Ta...) to nickel-based alloy has a great effect on matrix strengthening [88]. In addition, they also improve creep life resistance (as seen above in § 2.5). However, excessive quantities of Cr, Mo, W or Re promotes topologically close packed

phases to precipitate. These are brittle and deplete the matrix from key elements. Cr concentration in new generation single crystals is therefore much reduced (see Figure 1.3). The increase in refractories at the expense of Cr is particularly relevant for alloy-induced acidic fluxing.

The acidic fluxing is explained below with Mo (but the same mechanisms are assumed to occur for other refractories). When exposed to high temperatures, Mo oxidises, following Equation 3.29.

$$Mo + \frac{3}{2}O_2 \leftrightarrow MoO_3 \qquad\qquad \text{Equation 3.29}$$
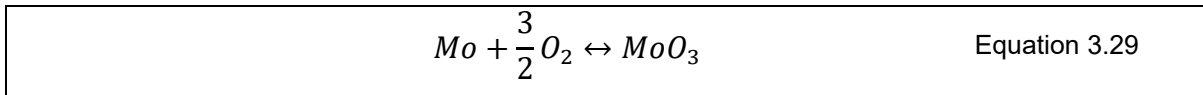
This compound has a high partial pressure that will cause scale damage (see Figure 3.9). Nonetheless, molybdenum oxide reacts with $Na_2O$ (see Equation 3.30).

$$MoO_3 + Na_2O \leftrightarrow Na_2MoO_4 \qquad\qquad \text{Equation 3.30}$$
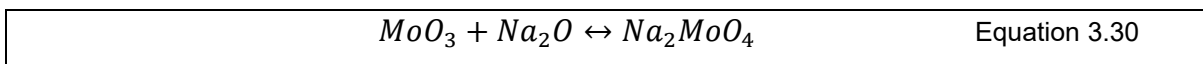
Two effects are then seen. First, the consumption of $Na_2O$ (the base of acid + base = salt in Equation 3.21) means excess acid ($SO_3$) is released in the fused salt melt, making it more acidic [89]. Second, Jones et al. [90] also describes Equation 3.30 as acid + base = salt, with $MoO_3$ being the acid. By comparing the different reactions progressing (against $Y_2O_3$, $CeO_2$, $ZrO_2$, $GeO_2$), $Ta_2O_5$ was found to be very reactive (hence very strongly acidic). (It is also noted that a eutectic $Na_2O.4MoO_3$-$MoO_3$ exists with Tε=510°C, as well as $Na_2WO_4$- $Na_2O.2WO_3$ with Tε=625°C both available in appendix § 9.4.10).

To further illustrate this, Stringer et al. [91] investigated Co-based alloys with 25 wt% Cr and 0, 2.5, 5, 7.5 and 10 wt% Mo. Stringer reported that upon exposure to air at 900°C, a reasonably protective scale was formed. However, when a different set of samples were exposed to $Na_2SO_4$, all the alloys had a layered scale structure displaying severe corrosion, except for the Co-25Cr. This shows that the $CoSO_4$/$Na_2SO_4$ eutectic melt reacted with Mo, lowering the $Na_2O$ activity, and shifting toward the acidic side of Figure 3.12 (a), allowing dissolution of the cobalt oxide.

### 3.4.2.3    Combined effect of NaCl and Na₂SO₄

Several authors mentioned that NaCl is required to trigger $Na_2SO_4$ attack [60], [91], [92]. Rosier et al. [93] investigated the effect of varying the salt quantity in a specimen solicitated in fatigue. The samples made of Udimet 720 Li (composition available in appendix § 9.2), were coated with 98% $Na_2SO_4$ + 2% NaCl and were exposed to flowing air + 300 ppm $SO_2$.

Figure 3.18 below suggests a minimum for which, life is reduced when sufficient $Na_2SO_4 + 2 \%$ NaCl is supplied. Below this optimum, too much $SO_2$ is supplied, converting all the NaCl into $Na_2SO_4$. Scale breakdown (mentioned above in § 3.3.2) is therefore not occurring. However, above this optimum, NaCl is abundant over $Na_2SO_4$, and the corrosion is again slowed down.
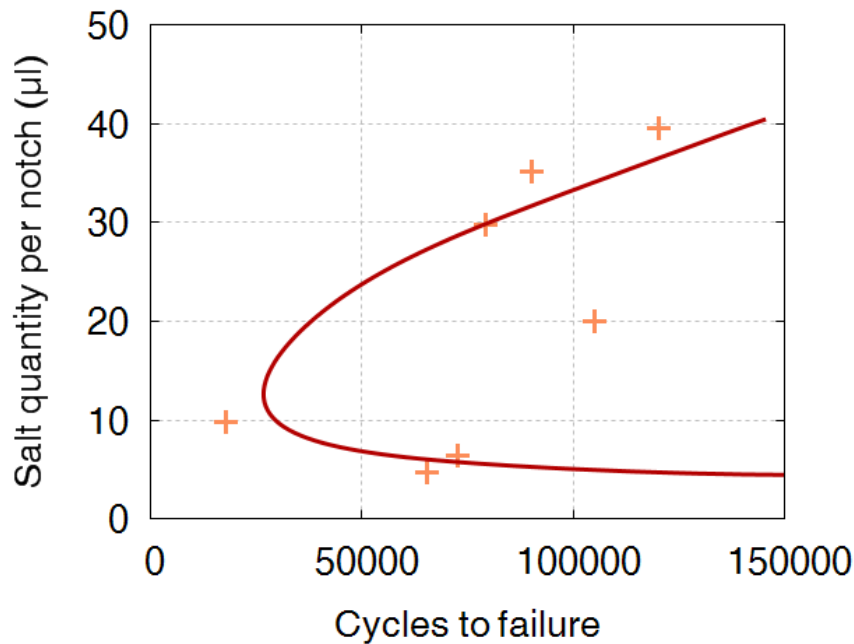
Figure 3.18: Effect of $Na_2SO_4$+2% NaCl deposition on the cycle to failure of Udimet 720 Li at 700°C, data from Rosier et al. [93]

### 3.4.2.4 Microstructure of the reaction layer

Lortrakul et al. [94] have observed, at 700°C, on sample pre-coated with $Na_2SO_4$, and flow with $O_2$-$SO_2$/$SO_3$ that, during exposure to a hot corrosion Type II environment (during 4 h), the γ matrix of the CMSX-4 single crystal was the first one to be attacked. This may be explained, since W, Mo, Re and Ru are partition to γ [9].

Figure 3.19 shows the cross-section of a CMSX-4 single crystal exposed during 15 min to a hot corrosion Type II environment. It shows an outermost layer rich in cobalt immediately followed by nickel-rich. The inner layer is depleted in nickel and rich in aluminium and chromium. Finally, just against the substrate a sulphur rich layer is observed. A bulge of the inner layer is also noticed [94].
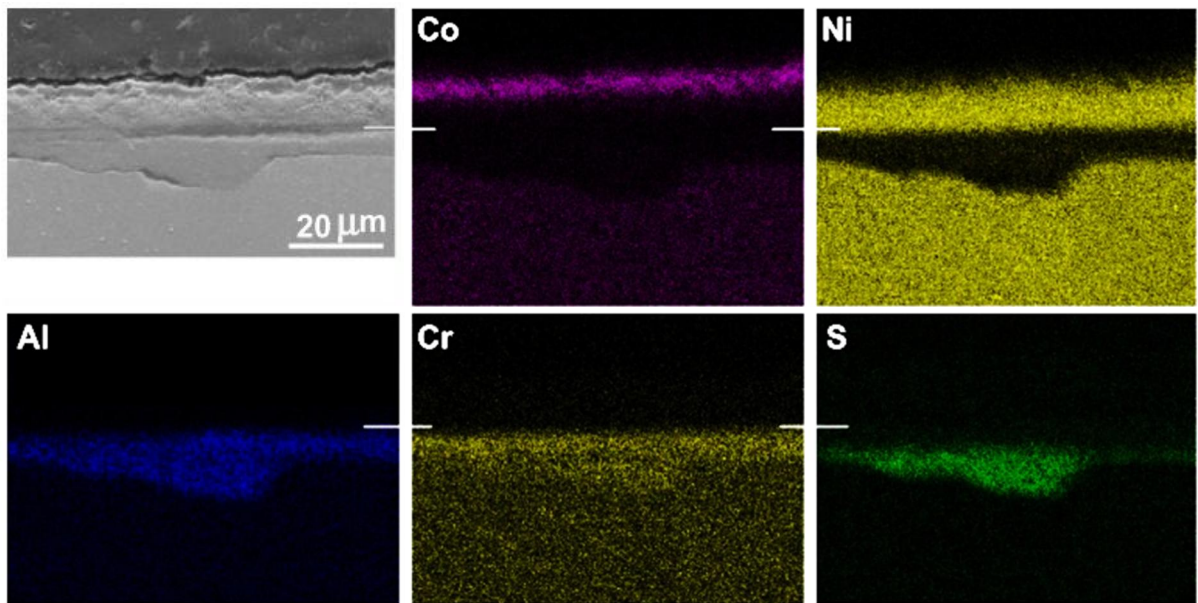
Figure 3.19: SEM image and EDX map of Type II hot corrosion scale on CSMX-4 at 700°C with the white line indicating the origin of the surface, from [94]

Hocking and Vasantree [95] describe visual observations of Ni-Cr (0.1–50 wt% of chrome). These observations report a "green and green tinted blister" [96] as being nickel oxide, while a light to dark grey is also detected at the surface and associated with nickel-sulphate eutectic. This visual observation will be used later to compare what is being seen on the rig.

## 3.5   Effect of stress on hot corrosion

One focus of the current work is to establish the absence or presence of a relationship between hot corrosion and stress. The importance of this coupling has been shown by Floreen and Kane [64] with polycrystalline alloy (IN718 with its composition also available in appendix § 9.2) exposed under various gases combination (relevant to this work are Air+0.5% $SO_2$, Air+5% $SO_2$, He+0.5% $SO_2$, He+5% $SO_2$). They concluded that both stress and a corrosive environment must be present to produce subsurface change. There are, however, significant differences between studies in terms of how the stress is applied.

### 3.5.1 Constant stress or constant strain

Single crystal sample of CMSX-4 under constant stress and under hot corrosion Type II environment (at 550 °C) were investigated by Brooking et al. [97], [98]. Different shapes of samples were coated with 80% $Na_2SO_4$–20% $K_2SO_4$ and left in an environment of air+300 ppm $SO_2/SO_3$ and re-coated every 100 h. It was found that samples with the largest stress gradient (here a C-ring shape under strain control load) were the worst affected. Stress and flux of contaminant were therefore found critical to crack initiation.

The interaction between *creep* and *hot corrosion* (Type I) has been studied by Homaeian and Alizadeh [99] at 850 °C for a polycrystalline alloy (IN617). They concluded that hot corrosion accelerated the secondary creep rate due to intergranular oxide and voids. Those voids were typical of creep and were related to stress concentration during testing, effectively moving vacancies into high tensile stress regions, at the transverse of grain boundaries and triple point. Ahead of these regions, the grain boundary oxidation was enhanced by precipitation of $M_{23}C_6$ creating further voids. Finally, the *hot corrosion effect* was explained by a flux of cations from the alloy to the oxide, creating further voids. The accumulation of these voids allowed the creep-crack initiation to reach a suitable propagation size, nearly suppressing the secondary creep regime. Yoshiba et al. [100] (working on 8 mm cylinders re-coated every 25 h with a mixture of 90% $Na_2SO_4$–10% NaCl, and made of IN751, exposed at 800 °C) found that in air, creep had the lowest time to failure compared to cyclic stress (with varying dwell times). However, in a corrosive environment, time to failure was lowered, but surprisingly cyclic stresses were found to be much worse than creep.

### 3.5.2 Cyclic stress

Applying stress through *thermo-mechanical fatigue* was a very popular way of investigating hot corrosion particularly around 1970–1990. This is done through a burner rig, cycling between two temperatures (typically ambient and ~1000°C) [45], [81], [101]–[108] . The interest of such methods lies in degradation, in the cyclic temperature rig, being similar to in-service harsh environment blades (ie: MC2 nickel-based single crystal superalloys [102]). However, since the stress of the sample is related to the temperature gradient, it is difficult to investigate the coupling of the two variables. Also, knowing exactly which mechanism is activated is difficult (due to the same gradient).

The interaction between *fatigue* and *hot corrosion* has been studied on polycrystalline alloy (IN718) at 650 °C by Mahobia et al. [109], on directionally solidified nickel-based superalloys (DZ125) with the <001> direction parallel to the loading axis, at 850 °C by Yang

et al. [110] and on a single crystal (CMSX-4) by Brooking et al. [98], [111] at 550 °C. In the first two cases, the alloys were coated with 75% $Na_2SO_4$+ 25% NaCl salt (target concentration between 2.5 and 5 mg/cm$^2$). In the third case, samples were coated with 80% $Na_2SO_4$/20% $K_2SO_4$ and left in an environment of air+300ppm $SO_2$/$SO_3$ and re-coated every 100 h. It was observed in the polycrystalline case [109] that fatigue cracks initiating at the bottom of the corrosion pits, with cracks propagating in a mixed transgranular and intergranular mode, significantly reduced the number of cycles compared to uncoated specimen (by a factor of 2 at $\Delta\epsilon t/2=\pm0.6$ %). In the directionally solidified case [110], recrystallisation of the grain close to the surface occurred, leading to a very similar attack with fatigue crack initiating at grain boundary. This recrystallisation was particularly significant at large stress and did not happen on uncoated sample. Finally, Brooking et al. [111] noted on single crystal samples that, at a relatively low contaminant rate (1.25 µg cm$^{-2}$ h$^{-1}$), the (111) slip plane would activate while at a higher contaminant rate (5 µg cm$^{-2}$ h$^{-1}$) the (100) plane would activate. It was proposed that a change in the mechanisms is happening and a more aggressive gas-induced propagation of species is occurring.

The variation of the *dwell period* was investigated by several authors [93], [98], [100], [111]. Yoshiba et al. [100] (working on 8 mm cylinders re-coated every 25 h with a mixture of 90% $Na_2SO_4$-10% NaCl, and made of IN751, exposed at 800°C) showed that at low stress (50 MPa), failure seemed to be corrosion driven and hence time-dependant (see region B in Figure 3.20). In this region, the number of cycles and the variation of dwell-time have both negligible effect. As the stress is increased, Rosier [93] indicated that an increase in the dwell period resulted in a reduction of the number of cycles before failure. This was also noted by Brooking et al. [98], [111] when changing a tension-compression sawtooth from 1-1-1-1 to 1-60-1-1 (seconds). In the case of the maximum stress held for 60 s, it took 3 times longer to fail the sample, but only a fifth of the cycles were required to fail the samples. The reduction was caused by multiple crack initiation. At very high stress, (region A in Figure 3.20) the corrosive environment joined the same time to failure than air. In this case, the environment has a minor effect and the failure is dominated by the stress.
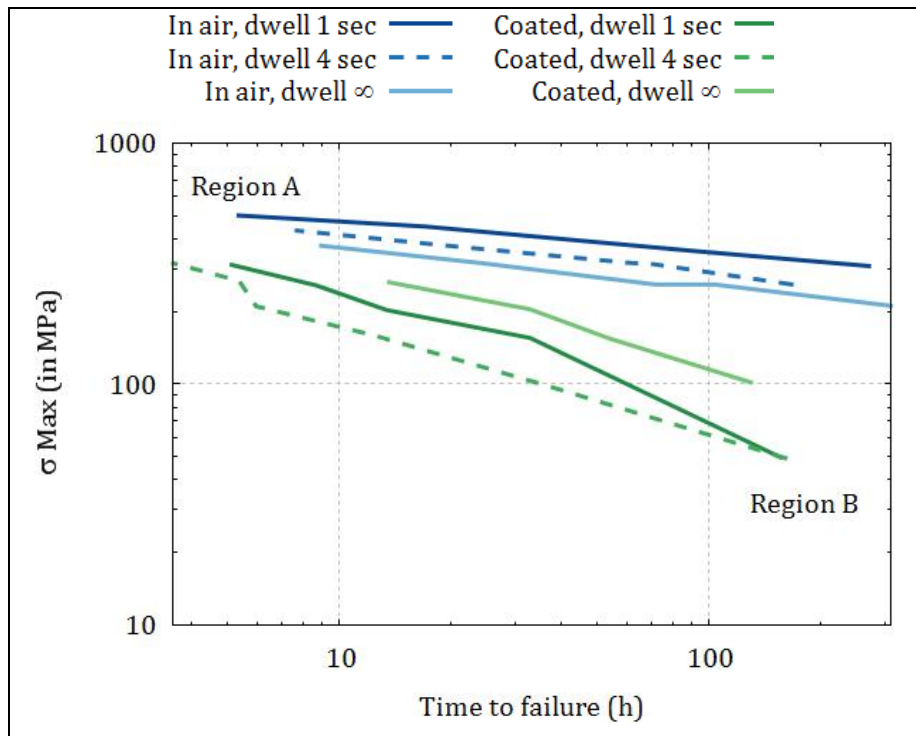
39

Figure 3.20: Effect of dwell time variation on the time to failure for samples made of IN751 exposed to air and samples coated with 90% $Na_2SO_4$-10% NaCl, data from Yoshiba [100]

The section above highlights a significant effect of stress on hot corrosion. Is this effect a feature of hot corrosion or is it also seen on samples contaminated with NaCl or exposed to $O_2$+$SO_2$/$SO_3$? Also, has the chromium content any effect on the effect of stress on hot corrosion? These questions could not be answered with the literature and prompted this work.

# Chapter 4   Experimental procedures

The preparation and treatment of the sample is made of several steps, summarised in Figure 4.1 and further detailed in this chapter.



Figure 4.1: Sample preparation steps

## 4.1   Sample preparation

Two alloys were used in the present work, SCRY-4 and SCRY-83, both in single crystal form.  Their nominal compositions are presented in appendix (9.2), where it can be seen that the main difference between them lies in the Cr levels (6.5 and 12.2 wt% respectively), although there are also a few other minor element variations. SCRY-83 is often referred to as "first generation" while SCRY-4 is a "second generation" nickel superalloy [112].

The slabs, cast by Howmet, were then cut into small samples (typically 52 mm x 15 mm x 1.5 mm) with an electro discharge machine (EDM) with the length aligned approximately in the <001> direction and the width with <010> (see orientation in Figure 4.9).

The use of thin strips means that the side areas of the sample were small in comparison to the top and bottom surfaces. For instance, for a sample 52 mm long, 15 mm wide and 1.4 mm thick:

$$\mathcal{A}_{sides} = 0.122\,\mathcal{A}_{top\,\&\,bottom}$$

The side areas were therefore not accounted for the calculation of specific mass gain. It was also noted that these surfaces were oxidised during the EDM cut.

The sample was then ground to 320 grit. This differs from most work in which samples are often polished. The main objective is to reproduce the failure environment, and a polished surface is not representative of typical turbine blade surface roughness. The mass of the sample was then measured.

## 4.2 Determination of test conditions and contaminants characterisation

### 4.2.1 Selection and characterisation of relevant environment

An approach of sequential increase in the complexity of exposure was adopted to understand the effect of the environment, see Figure 4.2 (a). For example, the characterisation in air helped explain the scale formed when sample were exposed to air+$SO_2$/$SO_3$. The same approach was then repeated with superimposed force.

As seen in Chapter 3, temperature and time significantly affect the kinetic and the stability of species forming. It was also thought that solid deposit (NaCl or $Na_2SO_4$ salt) would behave differently in the case of pre-oxidation. Gravimetric investigation of these effects was performed, with a detailed characterisation of the reaction layer performed at 700 °C see Figure 4.2 (b). This temperature was selected with the help from literature [113] and experiments performed.
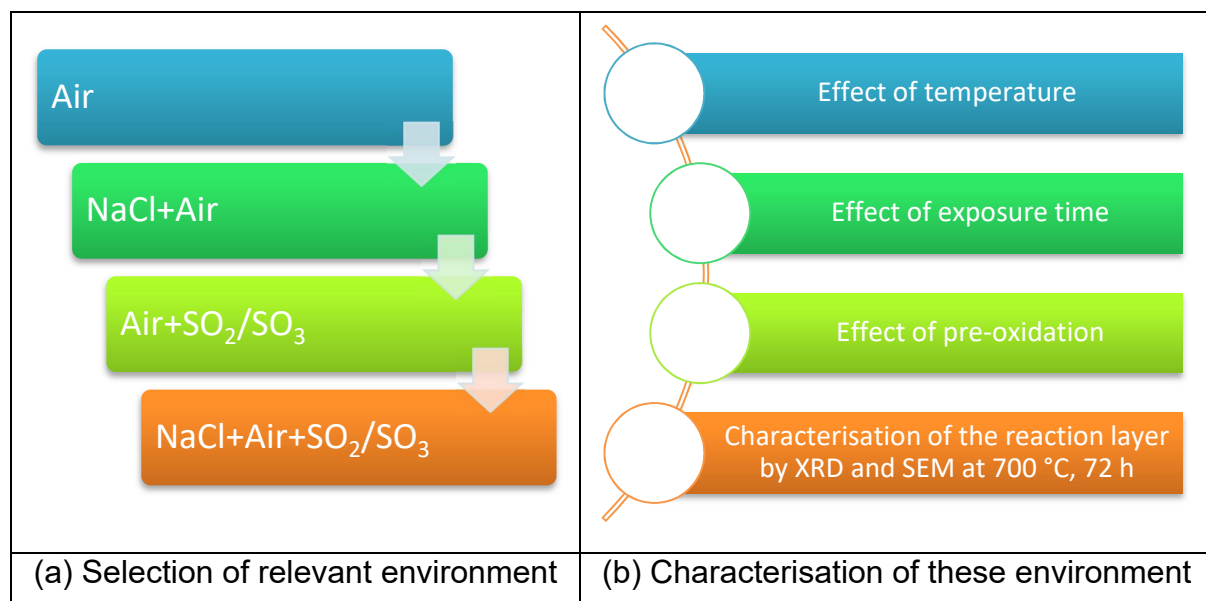


| (a) Selection of relevant environment | (b) Characterisation of these environment |
| --- | --- |

Figure 4.2: Selection of key environment and their characterisation

## 4.2.2 Effect of temperature

To ensure repeatability, the same furnace was use, hence any deviation in temperature would be repeated. Care was taken not to mix the salts in the same furnace, therefore the experiment was repeated three times (once for air only, once for samples sprayed with sodium chloride and one last time for samples sprayed with sodium sulphate).

### *4.2.2.1.1*     *Air only*

The first experiment was aimed at measuring the mass gain in air. One thin strip[2] of SCRY-4, one of SCRY-83 and one of recrystallised Alumina (99.8% purity) were inserted in a furnace (Carbolite CWF1100 controlled by a Eurotherm 91e, approximate dimensions 280 mm x 140 mm x 140 mm). Alumina strip was selected, since relatively few interactions are expected to occur with the NaCl or $Na_2SO_4$ under 850°C.

The gritted strips (see 4.1) were inserted in the furnace and left for approximately 1 h, before being withdrawn cooled down, and weighed. The strips were then inserted again at an increasing temperature. This allowed measurement of the mass gain due to oxidation at different temperatures occurring on two surfaces.

### *4.2.2.1.2*     *Air and NaCl*

This second test was very similar to the first test, except that NaCl was sprayed on one side only. To do so, a synthetic sea salt solution was prepared by mixing distilled water and ordinary table sea salt. The ordinary table sea salt was characterised in the SEM and the results are shown in Figure 4.3.

---

[2] The thin strip geometry allows to neglect the side of the sample (see § 0 for more details)

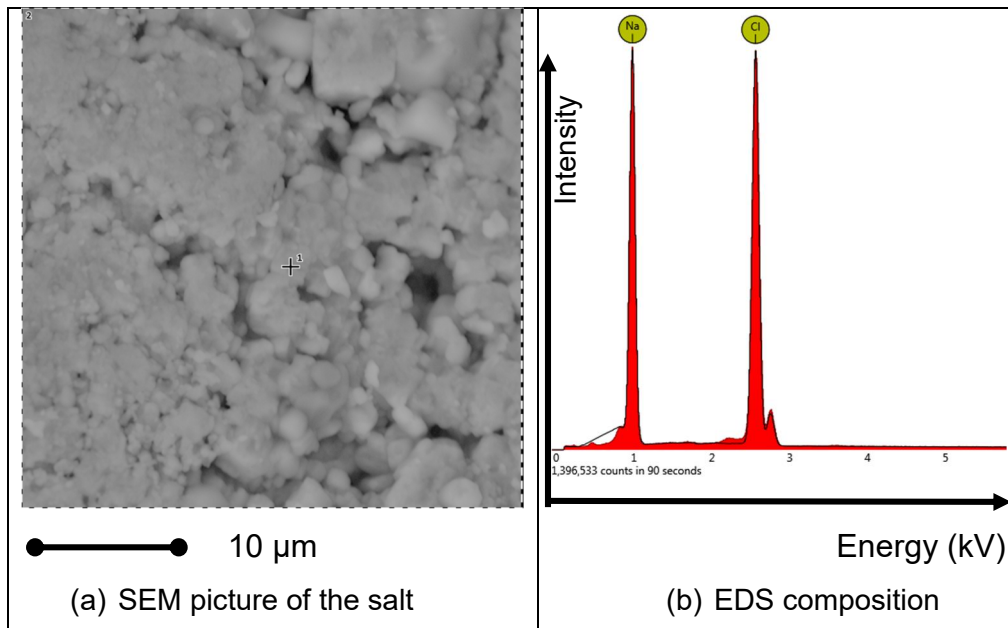|  |  |
|---|---|
| (a) SEM picture of the salt | (b) EDS composition |

Figure 4.3: Sea salt SEM picture and EDS spectrum

After each release of the solution, the water was made to evaporate by holding a hot air gun close to the sample (estimated hot air temperature around 350 °C). When the water evaporated, another release was performed until the target concentration of 25 g m$^{-2}$ was reached. This concentration was taken from Luthra [114] (equivalent to 2.5 mg cm$^{-2}$) and ensured the salt would be in excess. It was noted that the spraying varied with the nozzle setting, which was held constant throughout the different tests. The distance to the specimen was also held constant at around 30 cm. The mass of the sample was measured again.

The spraying was repeated on three strips (made of SCRY-4, SCRY-83 and Alumina). It was decided on one side only, to ensure that no salt would drop during weighing and transfer to the furnace.

The alumina strip had a different emissivity than the nickel superalloys, but this was neglected (since convection was assumed to be the dominant heat transfer mechanism at 700 °C). The strips were placed next to each other in the furnace. The mass gain from the first test (in air only) was used to offset the mass change on the bottom uncoated surface (on the two metallic strips), so the mass change on the top coated surface could be calculated.

#### 4.2.2.1.3    *Air and sodium sulphate*

The third test was similar to the second test, with the use of sodium sulphate instead of sodium chloride. The sodium sulphate solution was made by mixing distilled water with Glauber's salt ($Na_2SO_4$-$10H_2O$  CAS 7727-73-3) sold by Sigma-Aldrich with a purity ≥ 99.0 %. The same technique of spraying was used, with also a target of 25 g m$^{-2}$.

### 4.2.3 Effect of pre-oxidation

#### 4.2.3.1    *On samples coated with NaCl*

The tests above, with one hour at each temperature, are relatively quick in terms of kinetics of the chemical reaction. A second test was designed to investigate the long-term effects of salts and to assess the interaction of the salts (NaCl & $Na_2SO_4$) with the oxide.

In this test, a strip of SCRY-4, also gritted to 320, was treated in air at 700 °C during 24 h. The mass gain was divided by two to reflect the change on the two surfaces. This sample was referred to as "pre-oxidised".

After being cooled down, the strip was coated with NaCl at a target concentration of 25 g m$^{-2}$ on one face only, similarly to a reference sample (that was previously gritted to 320). The two strips were then inserted in the furnace for 24 h.

The mass change of the reference sample was offset to account for the oxidation of the bottom surface. The mass change would therefore be only related to the top coated surface.

Upon cooling, the salt coated side was removed "by hand" with distilled water. The samples were then dried and their mass was measured again.

To assess the integrity of the oxide, the samples were returned to the furnace in air only for 24 h and weighed again.

#### 4.2.3.2    *On samples coated with sodium sulphate*

A second version of this 24 h test pre-oxidation test (§ 4.2.3.1) was performed with $Na_2SO_4$ instead of NaCl.

## 4.3 Testing under controlled environment

The objective of hot corrosion testing is to be as close as possible to a real engine environment. A series of options are possible and presented in Table 4.1. A Dean furnace rig was employed in this set-up.

Table 4.1: Various possibility for hot corrosion testing

| Environment | Sample immersed in salt in a crucible | Dean furnace Rig | Burner rig | In service test |
|---|---|---|---|---|
| Operating conditions | Total or partial immersion in a fused salts bath of known composition in a controlled atmosphere (SO$_3$, SO$_2$, air) | Specimen at test temperature in a controlled atmosphere (with continuous salt or not) | Combustion of product with a mixed % of sulphur with or without thermal cycling | Turbine rotor made of different alloy. Borescope inspection to assess damage. Preventive replacement of blade every 5000 hours |
| Advantage | Helpful to understand the mechanisms | Compromise between burner rig and crucible test | The flame reproduces an environment (kinetic) close to the engine | Ideal place of testing |
| Drawbacks | High concentration of salts | Not as close as GT | Expensive to run | Very expensive in case of failure |

## 4.3.1 Description of the rig

A rig was purposely built to be able to perform the testing under a sulphur dioxide/trioxide environment and under varying load. This rig was made of several components that will be presented here.

### *4.3.1.1    Furnace*

The temperature in the vertical tube furnace was controlled by a smaller eccentric tube equipped with a type K thermocouple. A computer installed in the rig communicated with the Eurotherm 3216 furnace controller (to adjust set point).

### *4.3.1.2    Mechanical loading of the rig*

The numbers in the text refer to the numbers in Figure 4.4. A stepper-motor was vertically driving the rod of the actuator (2). This rod was mechanically connected to a load cell (4), itself connected to the "fork-shape" ceramic containing a thermocouple (8) exerting a bending moment to the specimen (9). A linear displacement transducer (3), held onto the rig frame, measured the displacement.

A computer connected to the data acquisition system, recorded the actuator force, the temperature, the displacement, the various gas measurement and piloted the motor and the solenoid valves (detailed below). This computer had software written specifically for this application (in visual basic). Part of the software modules were written by Keith Page (from the MSM electronic department).
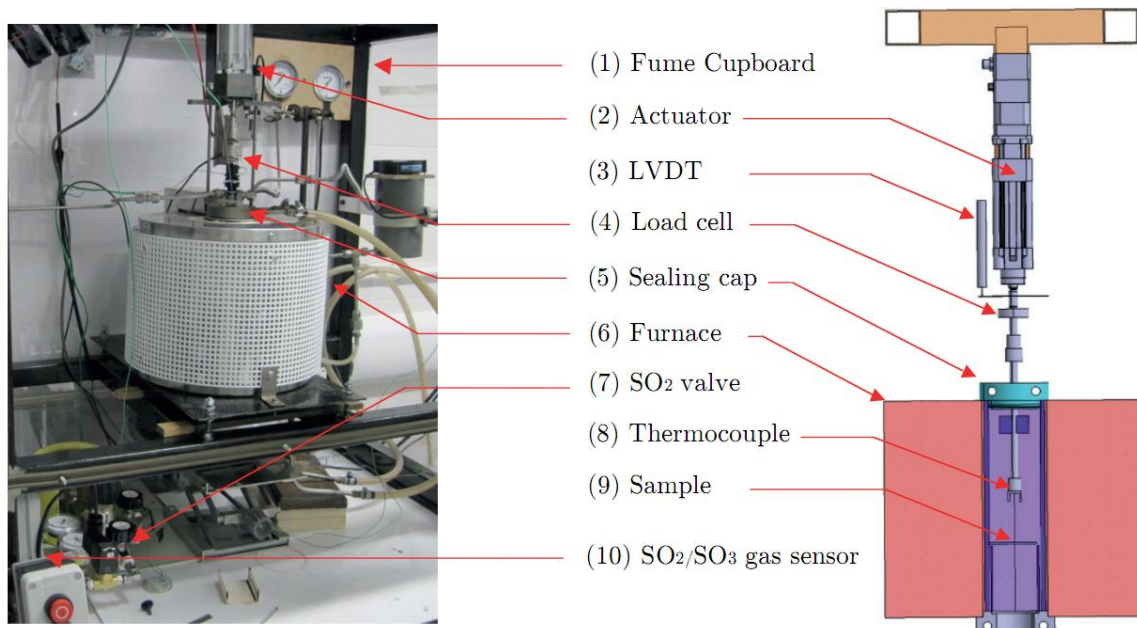
Figure 4.4: Photograph and schematic diagram of the rig

| | |
|---|---|
| (1) | Fume Cupboard |
| (2) | Actuator |
| (3) | LVDT |
| (4) | Load cell |
| (5) | Sealing cap |
| (6) | Furnace |
| (7) | $SO_2$ valve |
| (8) | Thermocouple |
| (9) | Sample |
| (10) | $SO_2/SO_3$ gas sensor |

### *4.3.1.3    Sulphur rich environment*

The vertical tube furnace was sealed by an upper (5) and lower cap that were hold in compression to maintain pressure on the flat seals. The seals used were made of silicon rubber able to withstand a maximum temperature of 230°C. Since the furnace was running at 700°C, the caps were water-cooled to ensure the seals would not overheat.

A closed loop circuit equipped with a diaphragm pump (a) in Figure 4.5, circulated the sulphur dioxide/trioxide + air.  The diaphragm pump, able to flow between 4 to 2 L/min, depending on the pressure, was manufactured by Boxer-it model 11K. With a tube volume of 0.7 L, the gas would be circulated through the line equipped with sensors ($O_2$ and $SO_2$) approximately 3 times per minute, ensuring a reliable measurement.
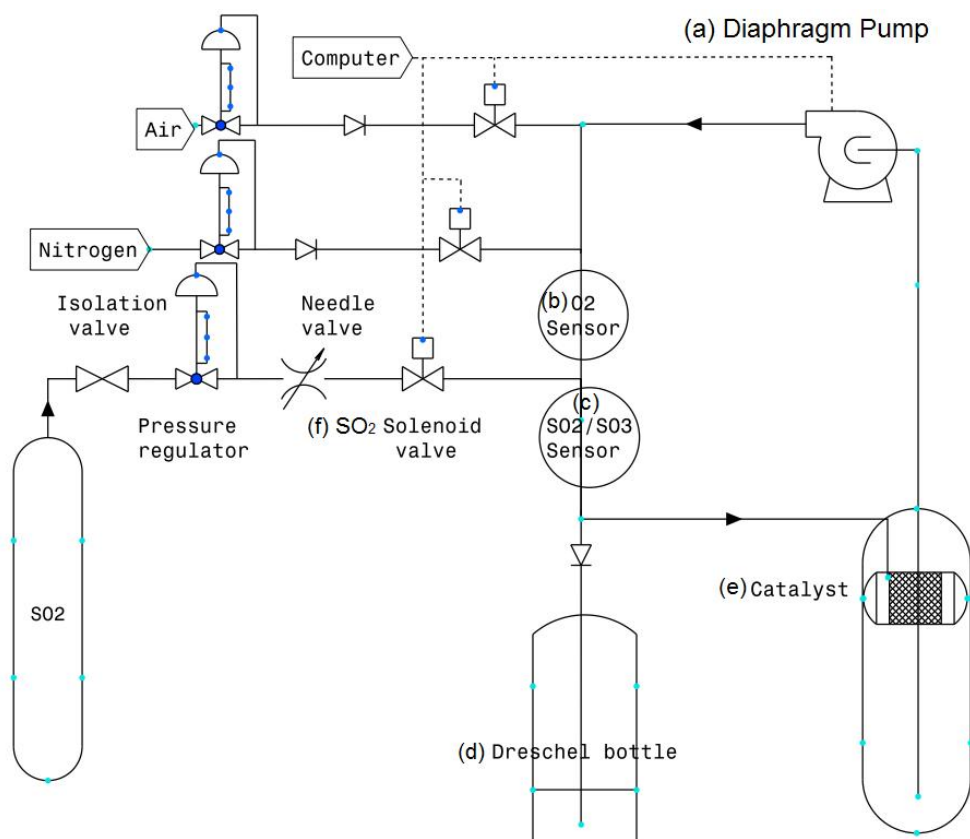
Figure 4.5: Closed loop of the testing rig

A $SO_2$ (c) and $O_2$ (b) gas sensors were fitted in the loop and used to control the injection of sulphur dioxide, air or nitrogen through solenoid valves (f). The $O_2$ sensor had a 0–25%vol range, while the $SO_2$ sensor had 0–10,000 ppmv range; both sensors were manufactured by Alphasense Ltd. It may be important to mention that the $SO_2$ electrochemical sensor also picks up the $SO_3$, so the denomination $SO_2/SO_3$ is used (to denote the sum of $SO_2$ and $SO_3$ concentrations)

The gas bottle contained (99.9%[3]) pure $SO_2$. Due to the discrete behaviour of the solenoid (on-off) and despite the needle valve, spikes of high concentration sulphur were observed, as seen in Figure 4.6. However, the mixing in the furnace is expected to smooth these out, so the $SO_x$ concentration to which the samples were exposed would have been constant. The $SO_x$ value recorded for each test was time averaged throughout the test duration (typically 1 value per second averaged across 72 h).

---

[3] Uncertified value
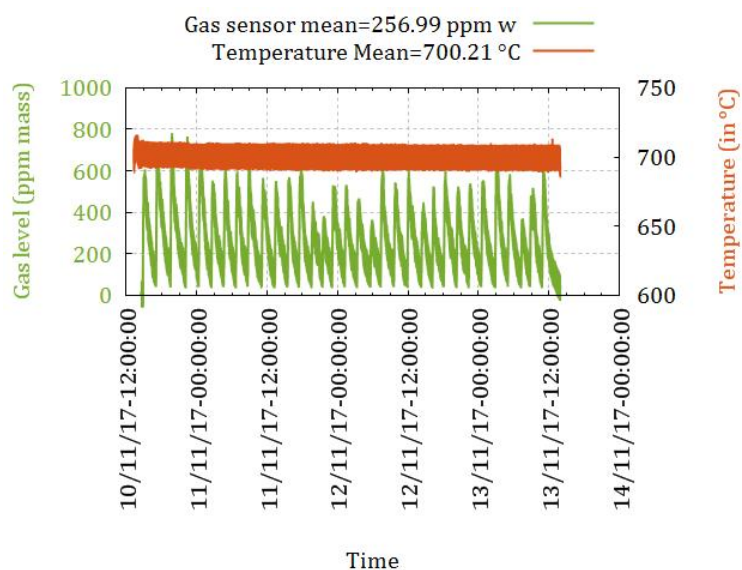
Figure 4.6: Example of measurement of the $SO_2$+$SO_3$ and temperature against time for sample C35

A catalyst (e) located in the cold zone of the furnace accelerated the sluggish reaction of $SO_2$ oxidation (Equation 3.28). Its composition is important, since, as pointed out by Garcia-Herrera et al. [87], a catalyst rich in selenium (installed on diesel cars) impedes the $SO_3$ reaction, while those made of platinum (and installed on petrol cars) promote the production of $SO_3$. To characterise the catalyst, a small amount was ground to powder and an X-ray diffraction spectrum was collected, see Figure 4.7 (a). High intensity peaks are matching the cordierite (which is often used as base material for catalysts). In addition, smaller peaks matching the Cd-Pd phase and the Pt-Te phase are seen with a lower intensity (due to small amounts of active material). The EDX spectrum of the same catalyst (collected by Colin Saunders from Techemet company) is also displayed (b), confirming that platinum and palladium are the active materials.
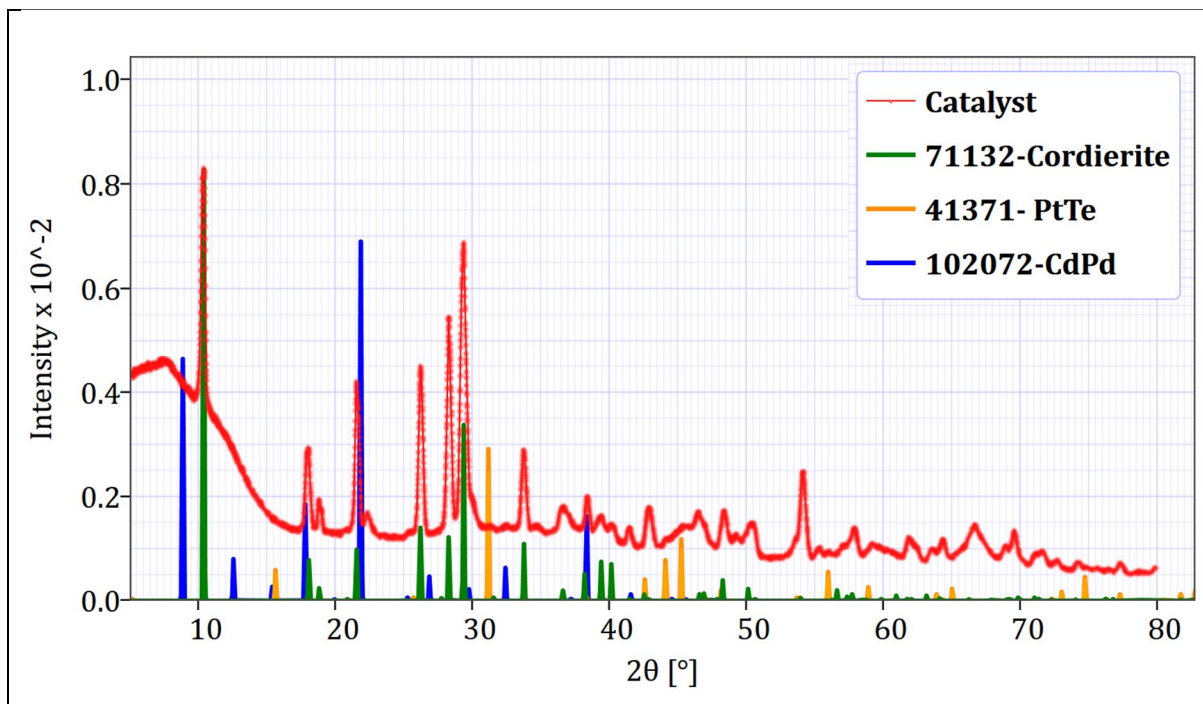
(a) X-ray diffraction spectrum of catalyst ground to powder
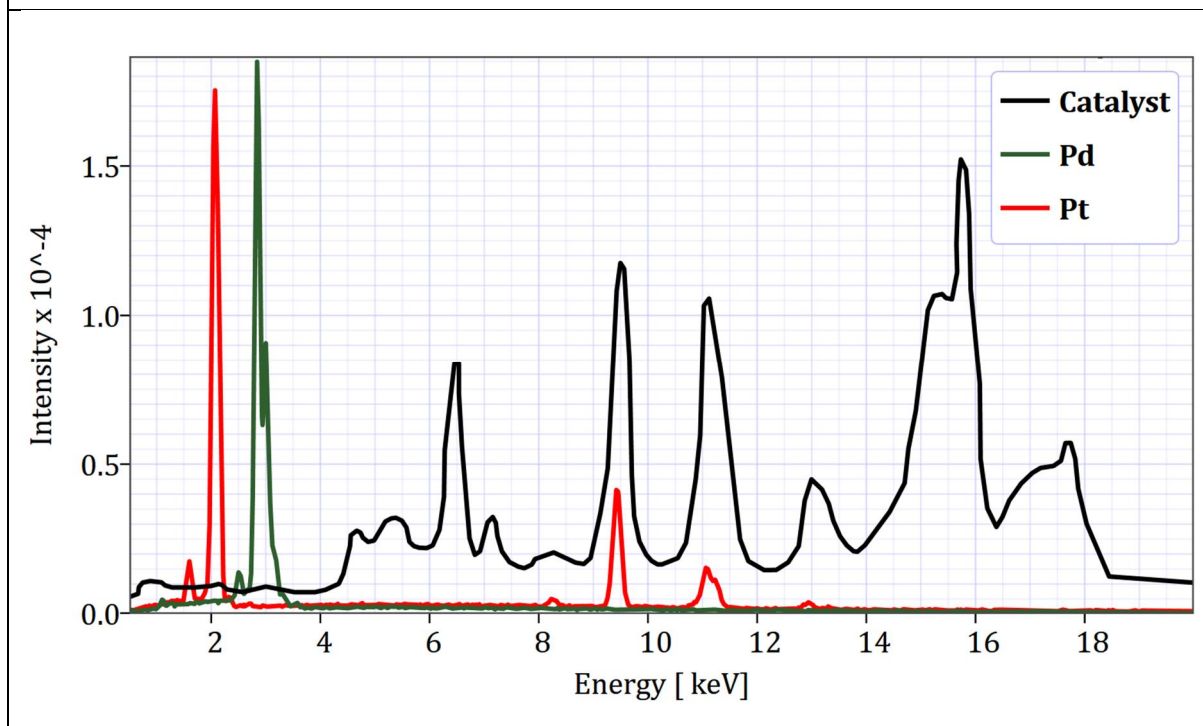


(b) EDX spectrum of active material catalyst, showing platinum and palladium peaks. Reproduced from the spectrum collected by Colin Saunders, from Techemet company

Figure 4.7: Characterisation of the catalyst material with XRD and EDS

Since the gas bled from the experiment could be reacting with other material, a Dreschel bottle (d), with an aqueous solution of sodium hydroxide, recycled the exhaust gases, see Equation 4.1. The sodium hydroxide was added to avoid formation of sulfuric acid. Sodium

hydrogen sulphate is used in the food industry [115] (food additive E514ii) and is much safer than sulphuric acid.

$$SO_3 + NaOH + H_2O \rightarrow NaHSO_4 + H_2O \qquad \text{Equation 4.1}$$
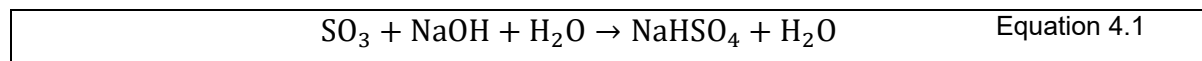
## 4.3.2 Fume cupboard

A fume cupboard (1) in Figure 4.4 was designed around the apparatus, to contain any potential $SO_2/SO_3$ leak. The extraction was located in the bottom part, since sulphur dioxide and trioxide gases are heavier than air. An additional $SO_2$ gas sensor (0–10 ppmv) connected to a red strobe was also placed in the fume cupboard.

It may be noted that the recommended maximum time-weighted average exposure to sulphur dioxide is 2 ppmv, while the maximum short-term exposure level is 5 ppmv [116].

## 4.3.3 Loading the sample in the rig

To mount the sample in the furnace, the bottom cap was removed. The support and the sample were stacked on the bottom cap and inserted into the furnace. The bottom seal was replaced after each test, while the top seal was subjected to less movement and could hold for a couple of tests. The furnace was then switched on to reach a sample temperature of 700°C. During the ramp up, the diaphragm pump was switched on and a purge with nitrogen was carried out. This ensured that any trapped and condensed gas would be flushed away. Once the temperature was stable, the required force for the test concerned was applied. To accommodate any thermal dilatation in the loading train, the force was held for at least 12 h (sometimes 24 h) before the beginning of the test. The data for this stabilisation is usually omitted, since the environment would be of air only and little effect would be expected.

### *4.3.3.1 Calculation for gas measurement*

The $SO_2$ and $O_2$ sensors gave a concentration in volume; this was converted to mass using the following formula:

$$V_{N_2} = 1 - V_{O_2} - V_{CO_2} - V_{Ar} - V_{SO_2} \qquad \text{Equation 4.2}$$

$$\sum V_i M_i = V_{O_2} M_{O_2} + V_{N_2} M_{N_2} + V_{CO_2} M_{CO_2} + V_{Ar} M_{Ar} + V_{SO_2} M_{SO_2} \qquad \text{Equation 4.3}$$

$$X_{SO_2} = \frac{V_{SO_2} \mathrm{M}_{SO_2}}{\sum V_i M_i} \qquad \text{Equation 4.4}$$

$$X_{O_2} = \frac{V_{O_2} \mathrm{M}_{O_2}}{\sum V_i M_i} \qquad \text{Equation 4.5}$$

With $V_{O_2}$ %vol and $V_{SO_2}$ (ppm vol) being measured by the sensor.

The values in Table 4.2 were assumed as constant.

Table 4.2: Constants values assumed for gas composition

| | | |
|---|---|---|
| $V_{CO_2}$ | 0.0003 | %m |
| $V_{Ar}$ | 0.0093 | %m |

### 4.3.3.2    Camera studying the surface of the sample

An ordinary digital camera focused on the lower (tension) surface of the sample, looked inside the furnace through a circular quartz window installed on the bottom cap. This camera had a specific script able to adjust the focus and take a photograph every hour.

The photos were then rotated and cropped, using a Matlab script, to include only the sample surface. Changes occurring in the furnace were seen by the eye on the post-treated images. A script identifying the number of pixels within a specific range of colours (RGB code) was therefore coded.

### 4.3.3.3    Beam stiffness acquisition

During the tests, and on a set of samples, the force, was decreased by 100 N and re-increased to the test level. During this unloading/loading the actuator force ($F_{act}$ in N) and displacement data ($\delta$ in mm) were recorded allowing the calculation of equivalent beam stiffness ($\Sigma$ in N mm$^{-1}$).

$$\Sigma = \frac{F_{act}}{\delta} \qquad \text{Equation 4.6}$$

## 4.3.4 Unloading of the sample

Once the test was completed, the furnace was cooled down to 200 °C, the bottom cap was removed and the sample extracted. The data from the test were saved and the rig was restored to its initial state.

## 4.3.5 Test conditions

Test were performed in static and then with superimposed force.

### *4.3.5.1    Static conditions*

Table 4.3: Static testing conditions

| Furnace | Sample # | Material | Treatment | Temp (°C) | Time (h) | Comments |
|---------|----------|----------|-----------|-----------|----------|----------|
| C | C23 | SCRY-4 | Air | 700 | 72 | - |
| C | C22 | | Air + NaCl | | | NaCl*: 24.6 & 25.1 g.m$^{-2}$ |
| R | C35 | | Air + SO$_2$/SO$_3$ | | | SO$_x$**: 257 ppmw |
| R | C34 | | Air + NaCl + SO$_2$/SO$_3$ | | | SOx**: 357 ppmw NaCl*: 26.1 & 24.1 g.m$^{-2}$ |
| C | E10 | SCRY-83 | Air | | | - |
| C | E11 | | Air + NaCl | | | NaCl*: 24.5 & 26.6 g.m$^{-2}$ |
| R | E16 | | Air + SO$_2$/SO$_3$ | | | SO$_x$**: 1127 ppmw |
| R | E17 | | Air + NaCl + SO$_2$/SO$_3$ | | | SOx**: 652 ppmw NaCl*: 24.4 & 27.7 g.m$^{-2}$ |

C: Performed in Carbolite furnace (see description § 4.2.2.1.1)

R: Rig (see § 4.3.1)

*The target values of NaCl coating are explained above (see § 4.2.2.1.2).

**The SO$_2$/SO$_3$ value fluctuated due to the limitations mentioned also above (see § 4.3.1.3). In addition, experience on SCRY-4 from previous samples and from literature [94], [97] shows that a target concentration of 300 ppmw ~ 150 ppmv would create detectable damage. Since the Cr content in SCRY-83 is twice the one of SCRY-4, the SO$_2$/SO$_3$ concentration was also doubled. Chemical equilibrium data shows that SO$_2$ has the same concentration as SO$_3$ at 709 °C and become predominant above that temperature (as shown in Figure 3.17) [8].

### 4.3.5.2    Superimposed force

The load was set to a prescribed level (load control). The test conditions are reported below.

Table 4.4: Superimposed force testing conditions

| Sample # | Material | Treatment | Force (N) | Temp (°C) | Time (h) | Comments |
|---|---|---|---|---|---|---|
| C36 | SCRY-4 | Air + NaCl | 200 | 700 | 12*+72 | NaCl: 24.3 & 24.6 g.m$^{-2}$ |
| C37 | | Air + SO$_2$/SO$_3$ | 303 | | 10*+72 | SO$_x$: 1167 ppmw |
| C33 | | Air + NaCl + SO$_2$/SO$_3$ | 310 | | 7*+72 | NaCl: 24.5 & 26.2 g.m$^{-2}$ |
| | | | | | | SO$_x$: 369 ppmw |
| E14 | SCRY-83 | Air + NaCl | 191 | | 12*+72 | NaCl: 25.7 & 25.2 g.m$^{-2}$ |
| E12 | | Air + SO$_2$/SO$_3$ | 282 | | 19*+72 | SO$_x$: 633 ppmw |
| E18 | | Air + NaCl + SO$_2$/SO$_3$ | 320 | | 3*+72 | NaCl: 25.7 & 27.1 g.m$^{-2}$ |
| | | | | | | SO$_x$: 1232 ppmw |

* The extra-time included in the testing was to reach thermal equilibrium (in air only) allowing detection of displacement caused by the environment.

## 4.4   Post-treatment characterisation of damage

### 4.4.1 Mass change

Mass change was measured with a micro-balance (Metler-Toledo XP 105DR) to a precision of 0.01 mg. Specific mass change (in g.m$^{-2}$) was calculated; see Equation 4.7 below (neglecting the sides as explained in § 4.1).

$$\Delta m = \frac{m_{t=7\ 2h} - m_{t=0h}}{2\mathcal{A}} \qquad \text{Equation 4.7}$$

When only one face was coated, Equation 4.8 was used to offset the oxidation of the bottom layer (if applicable). The correction factor originates from a previous sample (of area $\mathcal{A}^*$) treated in the same condition for similar amount of time.

$$\Delta m = \frac{m_{t=7\ 2h} - m_{t=0h}}{\mathcal{A}} - \frac{\Delta m_{ox}}{\mathcal{A}^*}\mathcal{A} \qquad \text{Equation 4.8}$$

## 4.4.2 X-Ray diffraction

### *4.4.2.1 Spectrum acquisition*

Since the reaction layer could spall off easily, the first task was to acquire the X-ray spectrum. A Philips PW1820 was used (Gen 3) to carry out a Gonio analysis. On the incident beam path, the divergence slit was set at 1/2°, with a mask of 15 mm. The Soller slit remained fixed at 0.04 rad. On the diffracted beam path, the anti-scatter slit was the same as the divergence slit (1/2°) and the receiving slit was set at 0.2°. The diffracted Soller slit had the same angle as the incident one (0.04 rad). The proportional detector (model PW1711) included a curved graphite monochromator (PW1752). These settings were selected to maintain a high number of counts per second, to be able to detect small peaks, whilst avoiding saturation of the detector from the underlying single crystal substrate.

The 2θ angle range was chosen to carry out phase identification (from 8° to 80°). The X-ray tube had a Cu anode, set at 40 kV and 40 mA without any filters. The radius of the goniometer was 173 mm and the distance focus divergence slit was 100 mm. Overnight scans were done, to improve the signal to noise ratio, with a step size of 0.03 ° and a step time of 20 s. Figure 4.8 shows the orientation of the sample and the angles of the sample and detector.

When the load was applied in the rig, the tension side of the specimen was scanned.
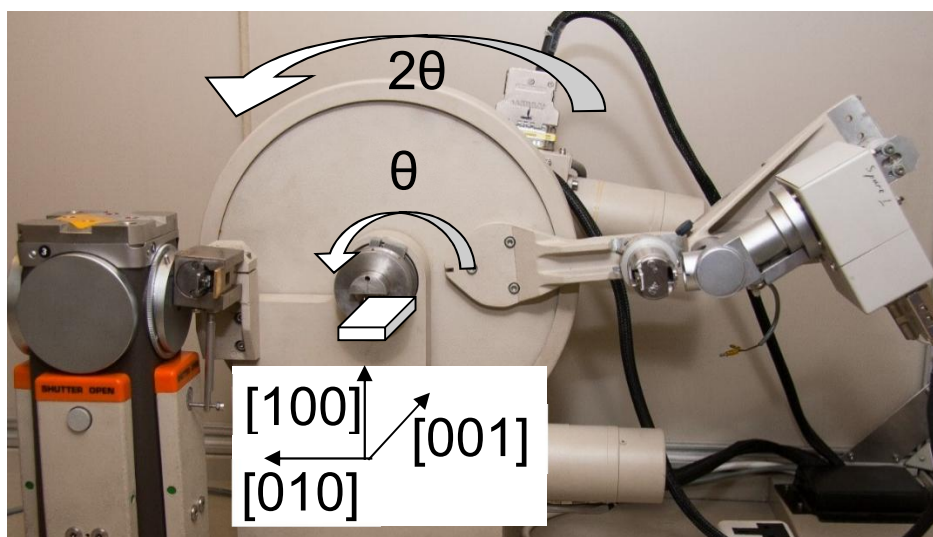
Figure 4.8: Orientation of the sample in the XRD machine

### 4.4.2.2    Post-processing

The post processing and identification of the species was done on High Score+. The XRD spectra were plotted with Crystal diffract (v6.7.1.). All the presented curved are smoothed with a radius of 3. That was found to adequately decrease the noise and preserve the shape of the peaks. The cif files of the compounds used were obtained from the Inorganic Crystal Structure Database (ICSD) and the crystal works database. The number before each species refers to their database number. Finally, for both samples, log scale was found to adequately show small peaks matching newly formed compounds and large peaks of the single crystal substrate. Offset in the *y-axis* was applied, not exceeding 200 counts to help the comparison by superposing the curves.

Exact composition of the layers, through Rietveld analysis, was not successful for several reasons. First, corrosion compounds identified on the spectrum had their coordinates missing, for example $Na_6Ni(SO_4)_4$ {ICSD: 412972} and $Na_6Co(SO_4)_4$ {ICSD: 434464}. Second, some newly formed compounds were matching only the first part of the spectrum ($Na_2SO_4$), and others matching only the high angle $Ni_2Ni(SO_4)_2$ (see Figure 5.28).

### 4.4.2.3    Linear attenuation coefficient and penetration depth

The procedure for calculating the linear attenuation coefficient for nickel is detailed by Chantler [117] and was calculated on the NIST website [118].

$$\mu_{40\ kV}^{Nickel} = 41.807\ cm^{-1}$$  Equation 4.9

57

This coefficient was used to estimate the X-ray penetration depth calculated using a Matlab routine written by Capek and Pala [119].

## 4.4.3 Cold mounting resin

After the XRD spectrum acquisition, and to maintain the delicate reaction layers, the sample was mounted on to a cold mounting conductive resin. The resin was manufactured by Demotec (model 70) and is a 2-component resin (methyl methacrylate) with conductive carbon embedded.

Once the resin was cured, the sample was cut along its length in the Secotom (feed rate of 0.25 mm s$^{-1}$ with spin speed above 3,000 rpm with $Al_2O_3$ blade) per the Z-X plane (shown below in Figure 4.9). This avoided the reaction layer being washed away by the cutting fluid.
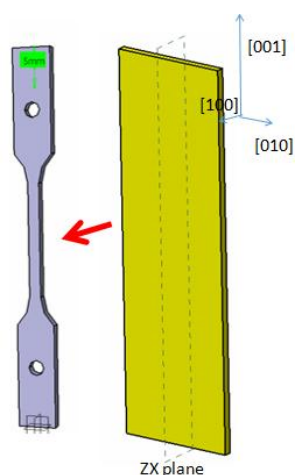


Figure 4.9: The strip exposed to the environment in the furnace is then cut in two in the ZX plane: one side for the dog-bone specimen (cut by EDM), while the other side is used for the cross-section examination under SEM

## 4.4.4 SEM characterisation

### *4.4.4.1    Sample preparation for the SEM*

The cross-section surface was ground and polished conventionally. The final polishing was done with an OPS disc and a mixture of silica and water (at a 1:1 ratio) for approximately 4 min. This polishing was selected to reveal the γ/γ' structure.

Some publications [97], [114] reports the use of kerosene or oil-based polishing liquid, to avoid sulphur being washed out. Although this was attempted, the sample was left stained and dirty. Water was found to be the most suitable.

### *4.4.4.2      SEM specifications and settings*

The Camscan MX2600 FEGSEM was used for the SEM and EDX (with Be-window X-ray detector, BSE and SE detectors) with INCA software. When the Camscan was replaced (on 13th September 2017) the ZEISS GeminiSEM 300 was then used with AZtec 3.4 software. Generally, an acceleration voltage above 20 keV was used with EDS and low acceleration voltage (3 keV) was used for high magnification pictures. The coordinates at the corner of each sample was recorded, so when a crack was found, its position along the length of the beam would be known.

### *4.4.4.3      X-Ray energy bands overlap*

It was noted that two bands overlap each other and could cause an issue in the element identification. The K-alpha emission line of sulphur (K$\alpha$=2.307 keV) is close to molybdenum (L$\alpha$ 1=2.293 keV), as shown in Figure 4.11 (a) and (b). The use of different energy bands for molybdenum requires a much higher acceleration voltage, which was, at that time, not available (Figure 4.11 (c)). The deconvolution of peaks is shown in Figure 4.11, and was checked for various samples, but this is a limitation that should be kept in mind in the following section.

Other secondary peaks overlap occurred for Cr and O and for Hf and Ta (see Figure 4.10).
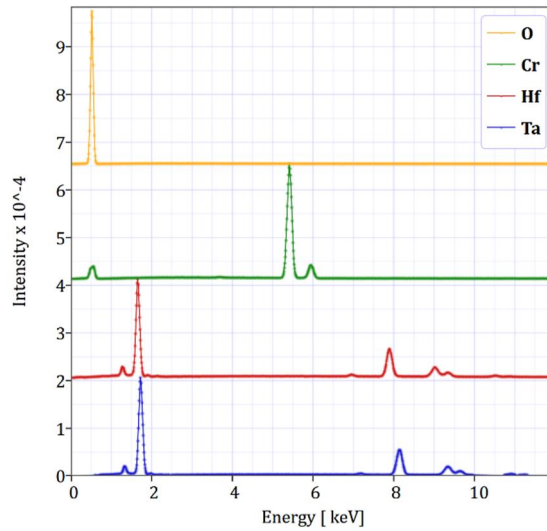
Figure 4.10: Simulated spectra (for an acceleration voltage of 30 kV, 15 mm working distance, detector area 10 mm² and a probe current of 100 nA) showing secondary peaks overlap between oxygen and chromium, and primary peaks overlap between hafnium and tantalum
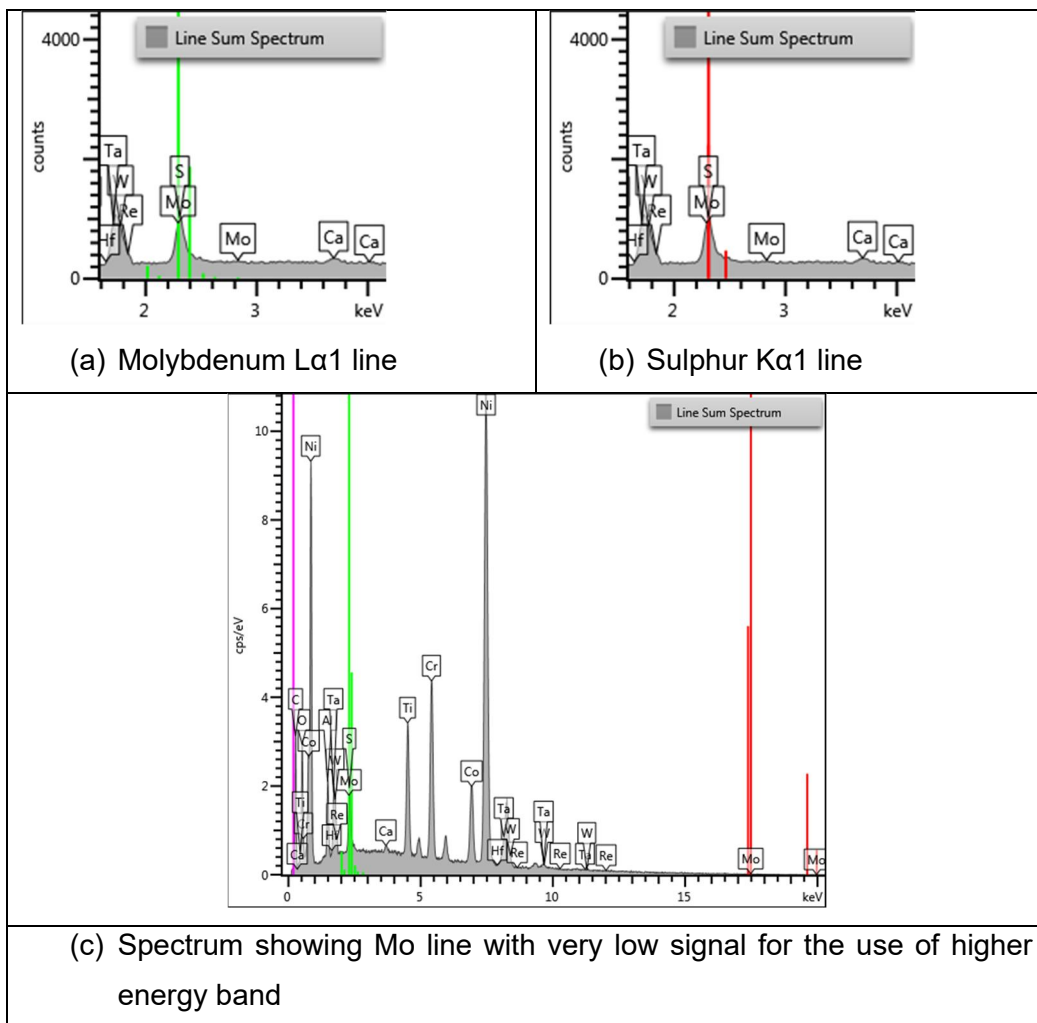


(a) Molybdenum Lα1 line

(b) Sulphur Kα1 line

(c) Spectrum showing Mo line with very low signal for the use of higher energy band

Figure 4.11: XRD spectra showing emission line of sulphur and molybdenum

### 4.4.4.4  Presentation of results

EDS maps were acquired from the region of interest (typically around cracks and reaction layers). It was found that line profiles (extracted from a map) are simpler and easier to explain than maps. The raw % weight was found to be quite noisy and was therefore smoothed out using the Bezier line as demonstrated in Figure 4.12. This specific smoothing function was found to be the most representative of the change.
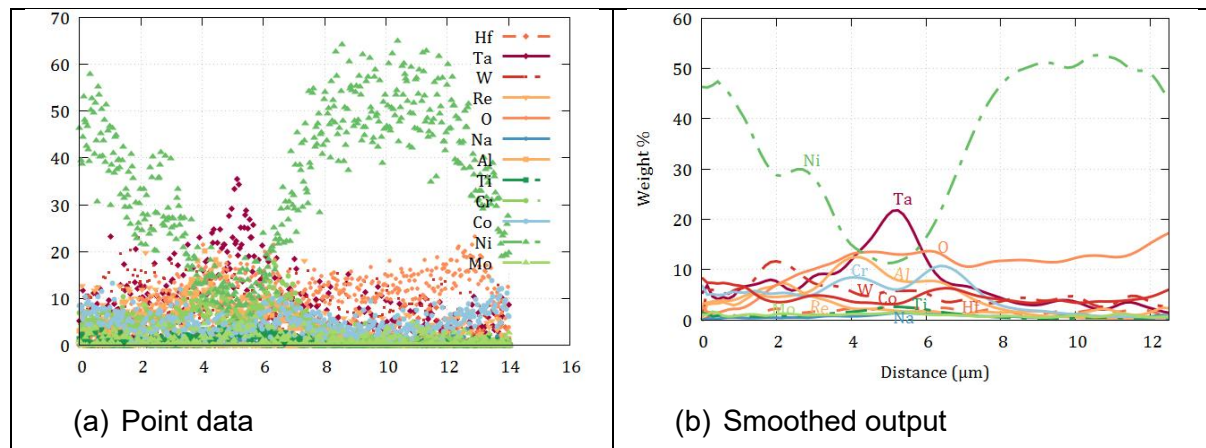


Figure 4.12: Raw output and smoothed Bezier line for sample C22

## 4.4.5 Scan with micro-computed tomograph

### 4.4.5.1  Characterisation of as-prepared sample

One as-prepared sample of SCRY-4 and one as-prepared sample of SCRY-83 were scanned using micro-computed tomography (μ-CT). A Bruker Skyscan EVA 1272 was used. The best result was obtained with an overnight scan, using a pixel size of 2 μm and a resolution size of 4,032 x 2,638. The exposure was at the maximum at 9.9 seconds and the scan was made at 360° to maximise intensity. The drawback of such a setting was that, due to the high density of superalloys, the sample had to be thin (0.7 mm x 0.7 mm). The volume was then reconstructed using NRecon. ScanIP software was used to threshold dark regions identified as pores.

### 4.4.5.2  μ-CT on exposed sample

The same technique was used to investigate the crack network that developed on corroded samples. After several attempts, a much larger sample section was selected, requiring a larger pixel size to generate sufficient intensity, resulting in some detail being lost. Nonetheless, this proved a promising non-destructive technique.

## 4.4.6 Post-exposure tensile testing

To assess the damage made by different environments, selected samples were tensile tested. To do so, the sample was cut into a dog-bone shape (seen in left part of Figure 4.9 and dimensions provided in appendix § 9.6.1) and mounted into an Instron tensile machine model 3367 with a 30 kN load cell (Manufacturer ref: 2530-444). At first, a LVDT was used to acquire the strain for test C32. Due to the grips slipping, a clip gauge (manufactured by Instron model 2620-601) was used for the remaining tests. The tensile stress was obtained by dividing the force measured by the load cell, by the section measured before the test, ie: both stress and strain are nominal ("engineering") values.

## 4.4.7 Misorientation measurements

Variability was found in the stress-strain test and required measurement of the misorientation.

### *4.4.7.1    Samples preparation*

Selected failed dog-bone shaped specimens were mounted in Bakelite in the Buehler Simpliment 2000 mounting press with the {010} plane flat on the cylinder.

The Bakelite sides were chamfer at 45° and then 3 samples were mounted onto the carousel in the automatic polisher with the following settings.

Table 4.5: EBSD automatic polishing settings

| Paper | Fluid | Time | Force | Speed |
|-------|-------|------|-------|-------|
| 600 | water | 2:00 | 20N | Working wheel: 150 rpm<br><br>Sample holder: 75 rpm |
| 1200 | | 2:00 | | |
| 2500 | | 2:00 | | |
| 6 µm | 6 µm | 2:00 | | |
| 3 µm | 3 µm | 2:00 | | |
| 1 µm | 1 µm | 2:00 | | |
| OPS | 0.25 µm | 10:00 | | |
| OPS | water | 2:00 | | |
| OPS | Silco 1:5 $H_2O$ | 5:00 | | |

Samples were then ultrasonically cleaned in water for 10 min.

### *4.4.7.2    EBSD acquisition*

Samples were then inserted into the EBSD clamp and in the Gemini 300 SEM with the following settings.

Table 4.6: SEM/EBSD settings

| Aperture | 120 μm | Tilt | 70° |
|---|---|---|---|
| Acceleration voltage | 20 kV | Working distance | 15–20 mm |
| Current | 200 nA | Optimised pattern | Mode 2 resolution |

The dog-bone length was aligned with CS1 (acquisition). An EBSD lines scan was then acquired from the region of interest. The γ and γ' phases have different composition but the same FCC crystal structure (Laue group m3m: a = b = c and α =β =γ = 90°). Therefore, both can be indexed with the FCC Ni phase.

Table 4.7: Lattice parameters from Mishima et al. [120]

| Phase | Lattice parameters (nm) |
|---|---|
| γ' | 0.587 |
| γ | 0.357 |
| Carbides | 1.06 |

### *4.4.7.3    Post-treatment*

The first orientation was defined with Euler angles (following Bunge's convention: ZXZ) between the acquisition system (CS1) and the sample coordinate system (CS0: aligned visually).

The second orientation was defined with Euler angles between the acquisition system (CS1) and the sample orientation (tensile axis visually aligned).

The misorientation was the difference between the two orientations (considering the cubic crystal symmetry). A script, inspired from the MTEX toolbox [121],  was written in Matlab to calculate the misorientation.

## 4.5   Finite Element Analysis

A finite element model of the sample, in the furnace, was created to model the stress field in the experiment. Several iterations of this model were done. The model presented here is the simplest.

### 4.5.1 Geometry of the sample

To save on computing time, two symmetry planes were used (see in Figure 4.13 (b)). The 3D model was found easier to visualise than 2D plane strain.



| (a) Dimension (in mm) of the model | (b) Isometric view showing the assembly: blue the fork, orange the support, and green the beam. The ZX symmetry plane is shown in red, and the ZY symmetry plane in purple |
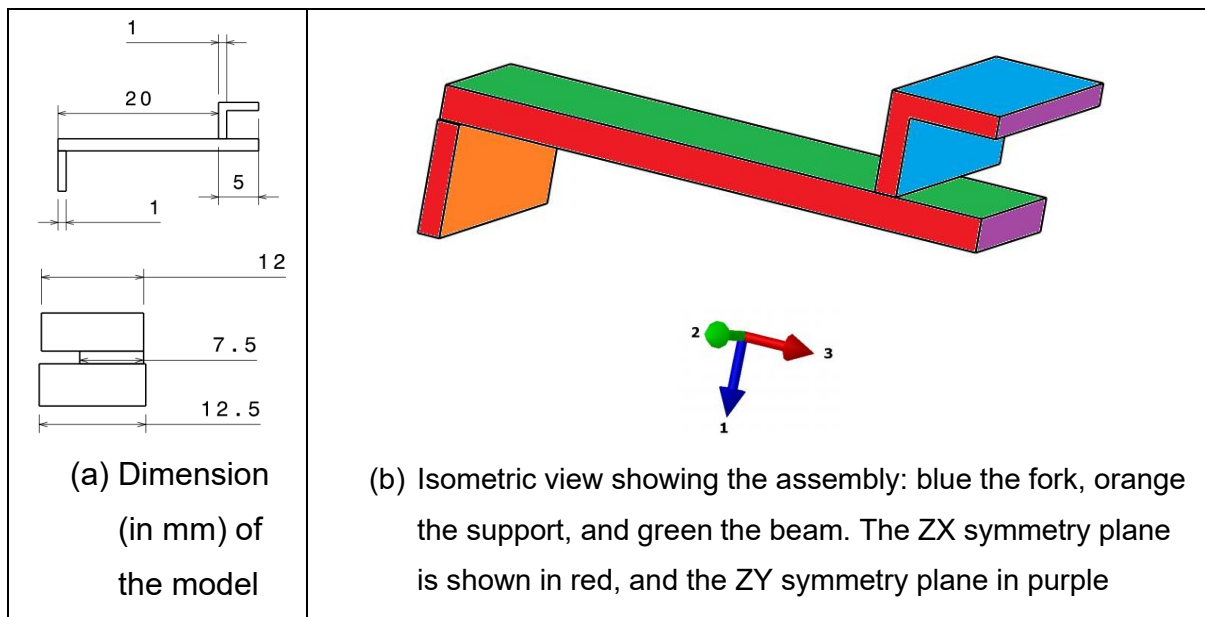
Figure 4.13: Geometry of the FE model

### 4.5.2 Values inputted in the Model

The input file is available in appendix (§ 9.1). The choice of the values is detailed in this section.

Table 4.8: Finite element analysis units

| Mass | Length | Time | Force | Stress | Energy | Gravity | Temperature |
|------|--------|------|-------|--------|--------|---------|-------------|
| g | mm | ms | N | MPa | N-mm | 9.81E-03 | K |

The two sets of surface-to-surface contacts were created. A first between the beam (master) and the fork (slave), and the second defined between the beam (master) and the support (slave). The default contact properties were used (with no adjustment of overclosure).

The fork and support were modelled as an elastic homogenous solid section with a Young's modulus of 300 GPa, which is typical of ceramic.

As mentioned above (§ 2.4), the mechanical properties of single crystal are anisotropic (Young's modulus, UTS…). When the actuator exerts a force of 400 N, the maximum stress on the beam is below 700 MPa (see Figure 6.3). Since the yield point of SCRY-4 and SCRY-83 is around 900 MPa (see Figure 6.16 and Figure 6.17), the actuator generates elastic deformation. An orthotropic elastic (only) model was therefore built on Abaqus (per formula shown in Figure 4.14) with the data taken from Shi et al. [122]. Their work focused on directionally solidified alloy DZ-4 that was assumed to be close enough to SCRY-4 and SCRY-83 (this assumption will be confirmed during the stress-strain test § 6.5.2). The orientation of the beam was defined in the model, as per Figure 4.9.

$$\begin{Bmatrix} \varepsilon_{11} \\ \varepsilon_{22} \\ \varepsilon_{33} \\ \gamma_{12} \\ \gamma_{13} \\ \gamma_{23} \end{Bmatrix} = \begin{bmatrix} 1/E_1 & -\nu_{21}/E_2 & -\nu_{31}/E_3 & 0 & 0 & 0 \\ -\nu_{12}/E_1 & 1/E_2 & -\nu_{32}/E_3 & 0 & 0 & 0 \\ -\nu_{13}/E_1 & -\nu_{23}/E_2 & 1/E_3 & 0 & 0 & 0 \\ 0 & 0 & 0 & 1/G_{12} & 0 & 0 \\ 0 & 0 & 0 & 0 & 1/G_{13} & 0 \\ 0 & 0 & 0 & 0 & 0 & 1/G_{23} \end{bmatrix} \begin{Bmatrix} \sigma_{11} \\ \sigma_{22} \\ \sigma_{33} \\ \sigma_{12} \\ \sigma_{13} \\ \sigma_{23} \end{Bmatrix}.$$

Figure 4.14: Linear elasticity in an orthotropic material from Abaqus [123]

Table 4.9: Elastic value of the orthotropic model taken from Shi et al. [122]

| T | E1=E2 | E3 | G12 | G13=G23 | v12 | v13=v23 |
|---|---|---|---|---|---|---|
| °C | GPa | GPa | GPa | GPa | - | - |
| 20 | 181 | 128 | 61.6 | 36.7 | 0.470 | 0.325 |
| 600 | 147 | 109 | 49.5 | 30.8 | 0.485 | 0.344 |
| 720 | 141 | 105 | 47.7 | 29.6 | 0.487 | 0.352 |

Finally, the boundary conditions were defined as follows:
- an encastre boundary condition was applied to the lower part of the support
- a vertical movement was prescribed to the fork (no rotation)
- the two symmetry planes were defined as per Figure 4.13 (b)
- the temperature was set constant at 973 °K

The load was applied to the top surface of the fork as a pressure, equivalent to the 400 N actuator. The time period of the model was set to 4.0 and the pressure set to ramp, allowing investigation at different levels of actuator force in one model.

The mesh was made of element C3D8R with an approximate size of 0.2. This resulted in a model containing 41,160 nodes with 34,550 elements that took less than 5 min to run.

The results of this model will be commented in Chapter 6.

# Chapter 5    The effect of Cr on static environmental exposures

The objective of this chapter is to investigate the behaviour of two single crystal nickel superalloys exposed to harsh environments. Four environments were studied: (a) air, (b) air and $SO_2/SO_3$, (c) air and sodium chloride and (d) sodium chloride, air and $SO_2/SO_3$. These tests were performed under static conditions (without superimposed mechanical load).

## 5.1    Characterisation of "as-prepared" substrates

Undamaged samples were characterised before exposure to various environments.

### 5.1.1 XRD spectra and phase identification

XRD spectra of "as-prepared" SCRY-83 and SCRY-4 samples are displayed in Figure 5.1 (a). As expected, both samples show γ and γ' peaks. SCRY-83 shows more γ' than SCRY-4. The orientation of the samples is indicated in Figure 4.8.
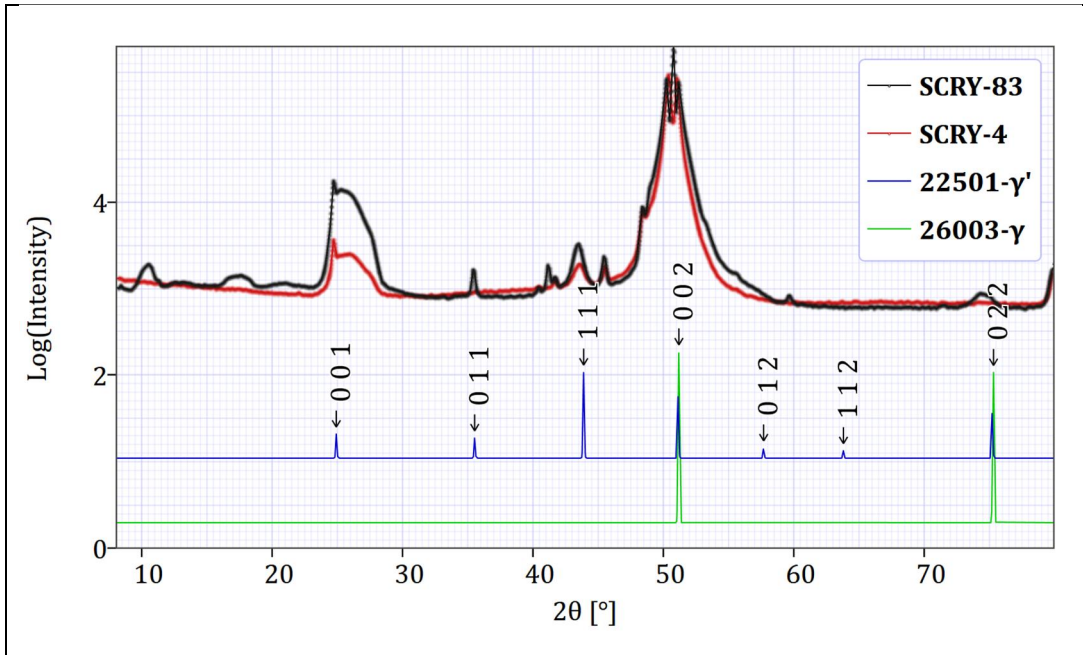
(a) XRD spectra of "as-prepared" samples (before furnace exposure)
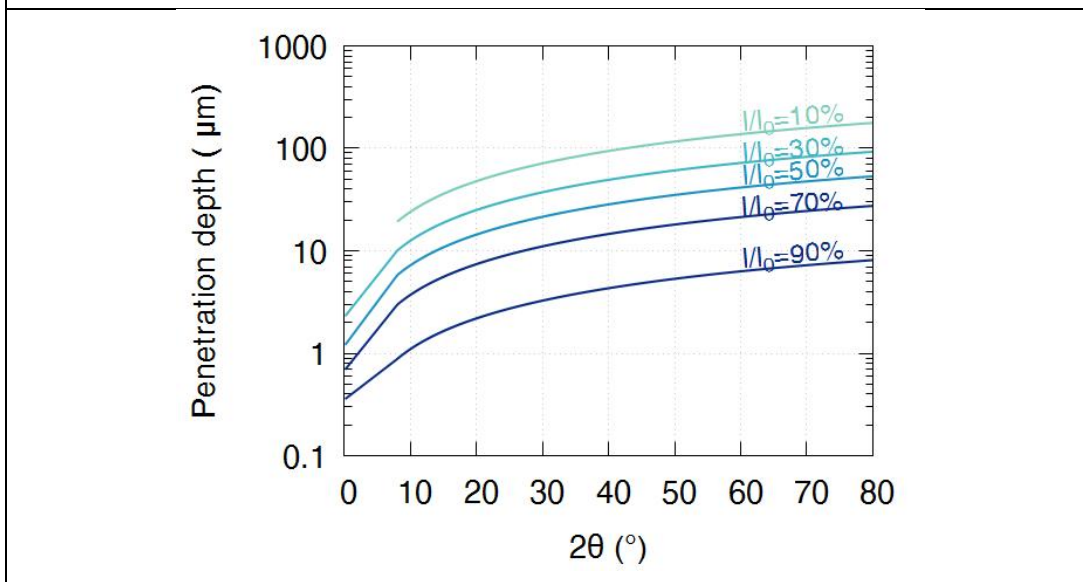


(b) XRD penetration depth as a function of 2θ

Figure 5.1: XRD characterisation and penetration depth

An estimation of the volume interrogated by XRD was performed using the procedure described in § 4.4.2.3. Figure 5.1 (b) indicates how thick the surface layer must be to diffract 10–90% of the initial intensity, as a function of 2θ. This is clearly an estimation, since the attenuation coefficient (taken here for nickel) will vary with the different alloying elements (ie: Co, Re). This figure is useful to correlate XRD spectra with microstructural information (see below).

### 5.1.2 Porosity content

In Chapter 3, it was explained the possible formation of liquids (one example is $NiSO_4$-$Na_2SO_4$). The (inter-dendritic) porosity was thought to have the potential for these liquids to flow and accelerate their progression. Micro computed tomography (µ-CT) was therefore performed to estimate the pore volume fraction and distribution. The outcome is shown in Figure 5.2.



| Pore volume fraction: 0.055% | Pore volume fraction: 0.1 % |
|---|---|
| a) SCRY-4 | b) SCRY-83 |
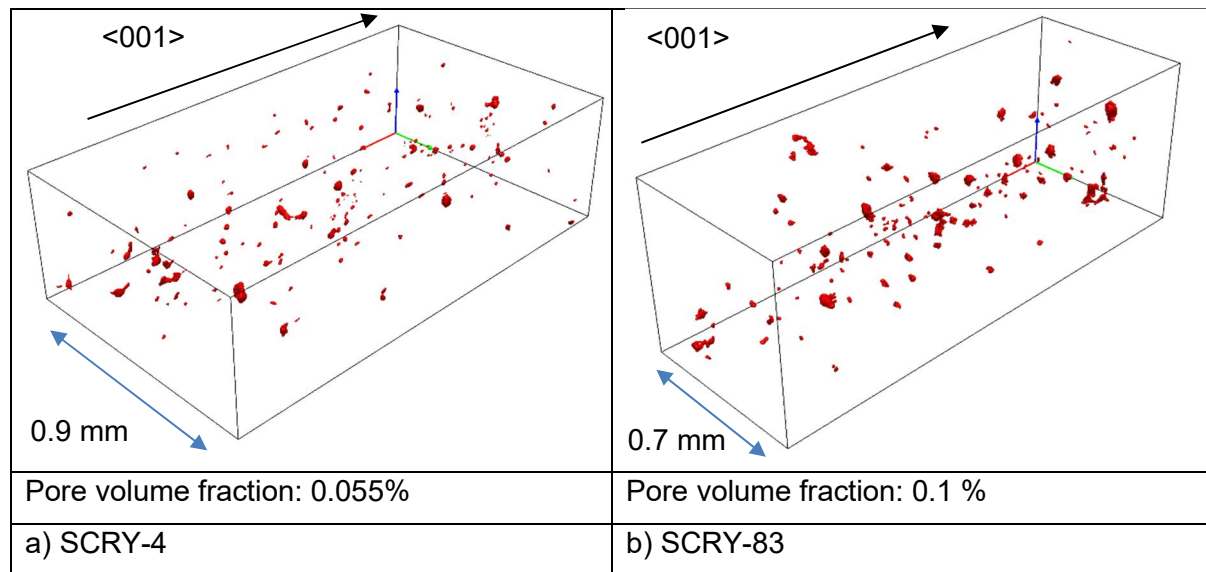
Figure 5.2: Isometric view of the pore fraction of as-prepared samples (before furnace exposure)

The pore fraction of SCRY-4 is lower than that of SCRY-83. This will be kept in mind when analysing the results. These values are probably an underestimate, since some fine porosity is likely to be missed by the resolution of 2 µm.pixel$^{-1}$ (chosen to maximize intensity).

## 5.2 Samples exposed to air

### 5.2.1 Mass change

#### 5.2.1.1 Increasing temperature test

Figure 5.3 was obtained by following the test procedure detailed in § 4.2.2.1.1. The same three samples were held for 1 h, at a series of increasing temperatures. After each 1 h period, the samples were cooled down, weighed, and re-inserted in the furnace at a higher temperature.
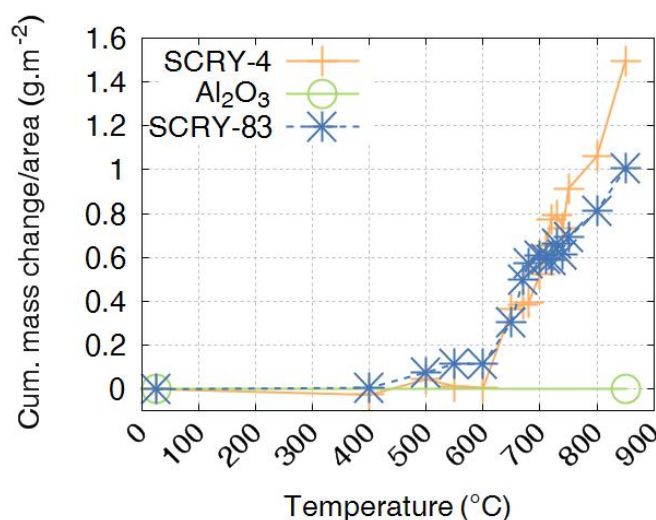
Figure 5.3: Samples exposed to air at a series of increasing temperatures. Each point represents 1 h in the furnace

Mass gains are observed due to the uptake of oxygen at the free surface of the metallic samples. At higher temperature, faster kinetic explains larger mass gain. It is noted that below 600 °C mass changes are difficult to detect. At 700 °C however, cumulative mass gains (after 1 h) attained ~0.6 g m$^{-2}$ for SCRY-4 and SCRY-83. Finally, as expected, no mass change occurred to the $Al_2O_3$ strip. To ensure detection of mass change during the environmental exposure, a temperature of 700 °C was selected for the long exposure test.

### *5.2.1.2    72 h isothermal exposure*

To allow XRD and micrograph examination of the layer, a prolonged exposure (of 72 h) was carried out on two samples at 700°C (test conditions in Table 4.3). The mass change are presented in Table 5.1.

Table 5.1: Mass change in air for 72 h at 700°C

| Material | Sample | Spec. mass gain (g.m$^{-2}$) |
|:---:|:---:|:---:|
| SCRY-4 | C23 | 0.444 |
| SCRY-83 | E10 | 0.609 |

The type of oxides formed were investigated with SEM and XRD.

## 5.2.2 Reaction layer microstructure
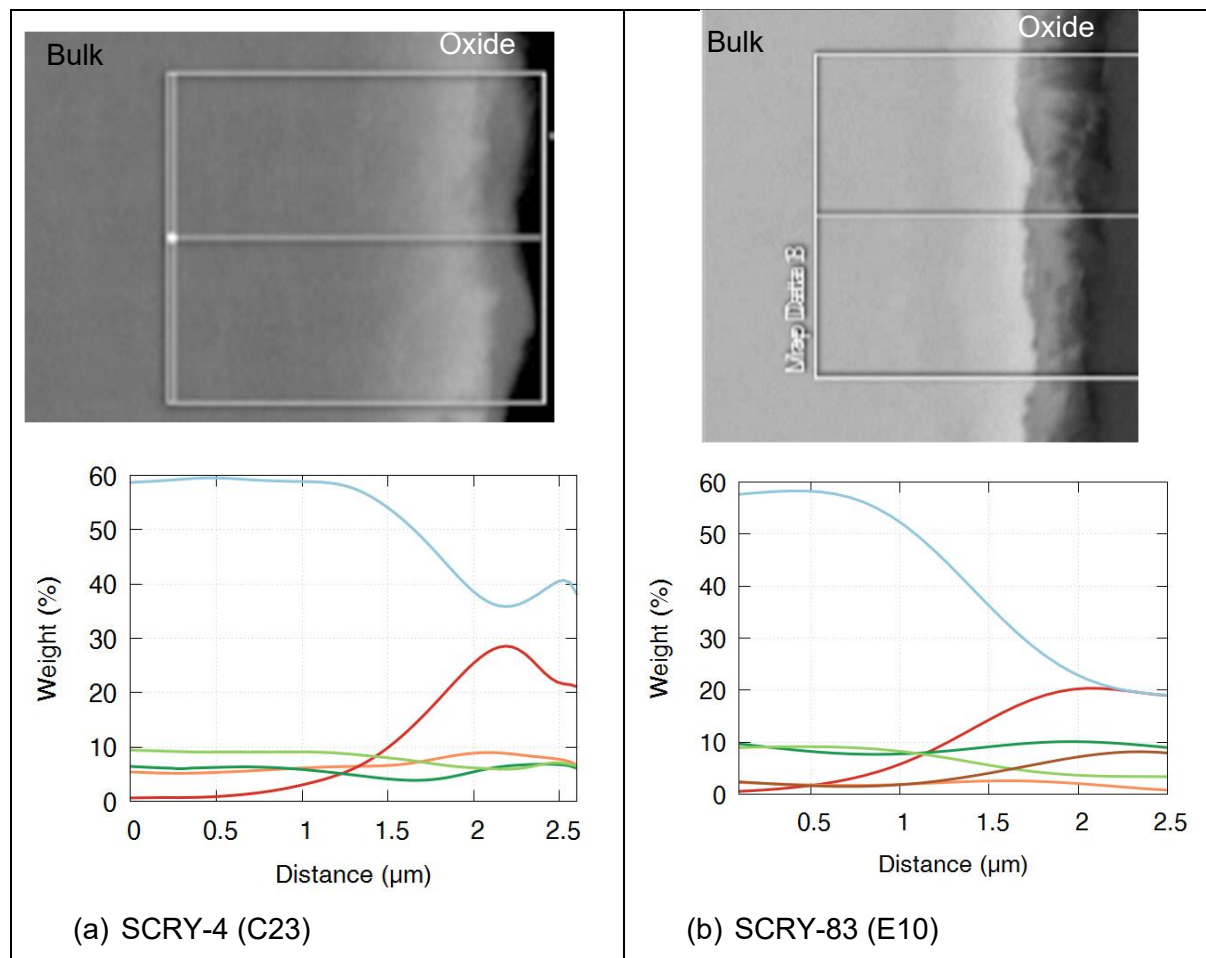


Figure 5.4: EDX composition profiles of samples treated in air for 72h at 700°C

For the $Al_2O_3$-former, in Figure 5.4 (a), the oxygen-rich layer has a thickness of about 2 μm. An inner region is seen depleted in Ni, but rich in Al and Cr, then followed by an outer layer rich in Ni.

For the $Cr_2O_3$-former, in Figure 5.4 (b), the oxygen-rich layer is also approximately 2 μm. Contrary to the previous case, there is no clear separation between inner and outer layer. Nonetheless, there is a first region rich in Cr, with a second region also rich in Ti.

## 5.2.3 XRD spectra and phase identification



(a) SCRY-4 (C23)

(b) SCRY-83 (E10)
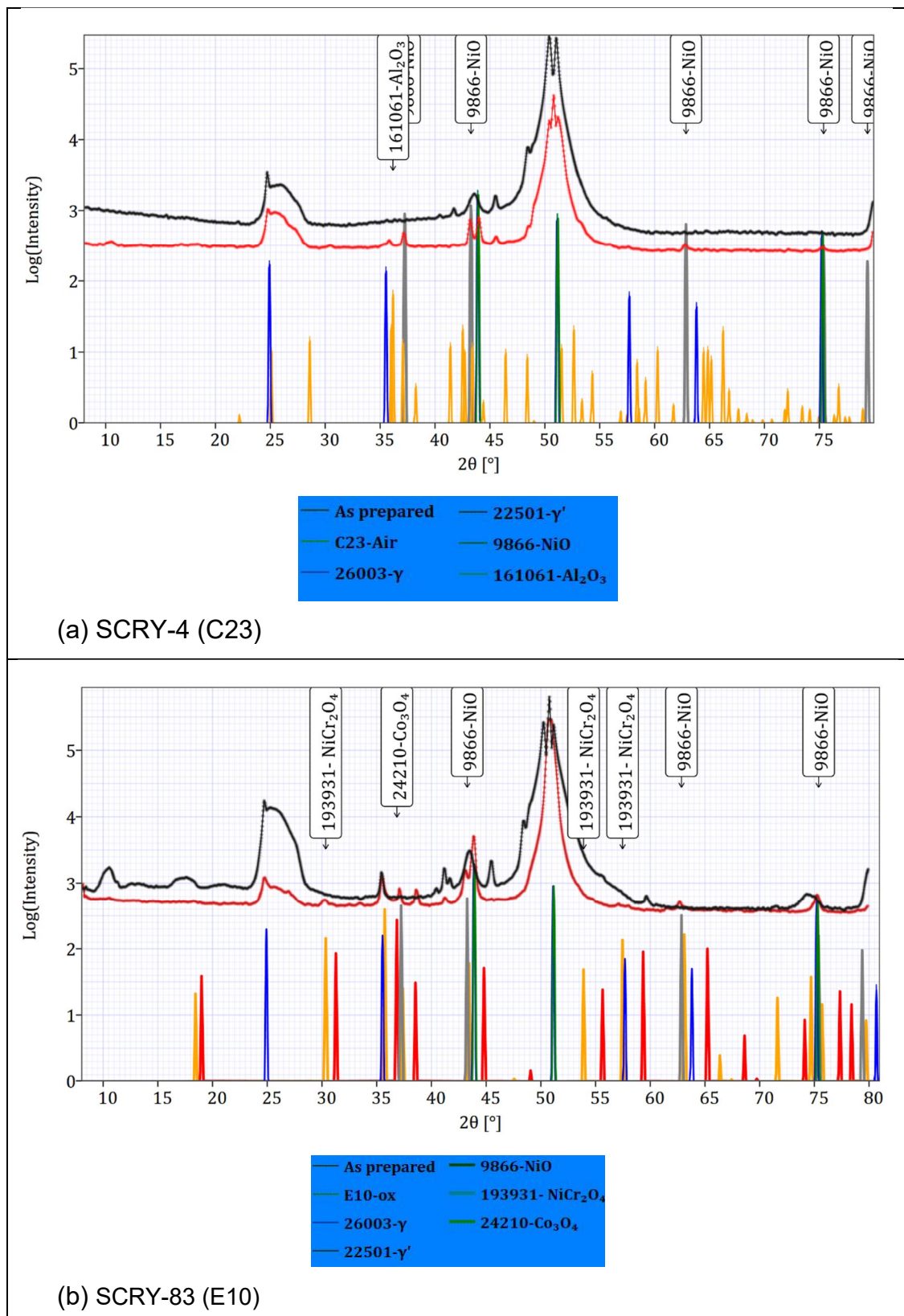
Figure 5.5: Phase identification with XRD spectra for samples exposed to air at 700°C for 72 h

Nickel oxide is detected on both alloys. While NiO formation is slow compared to other oxides, its activity (chemical potential) is high due to the abundance in the substrate (>60 wt%).

For the $Al_2O_3$-former (SCRY-4), in Figure 5.5 (a), a small aluminium oxide peak is detected. It is thought that a higher activation energy is required to form a thick layer of alumina. Nonetheless, with the EDX composition profile and the XRD, three distinct layers have formed at 700 °C and are represented in Figure 5.6.

For the $Cr_2O_3$-former (SCRY-83), in Figure 5.5 (b), nickel dichromate and cobalt oxide were detected. It is thought that also a higher activation energy (temperature) is required to form $Cr_2O_3$ in quantity detectable by XRD. Since NiO was detected via XRD, but not on EDX, it was thought that the oxide could have spalled off during the cold mounting process.

## 5.2.4 Schematic representation of the reaction layers

The XRD and micrographs results were used to produce a representation of the layers in Figure 5.6.
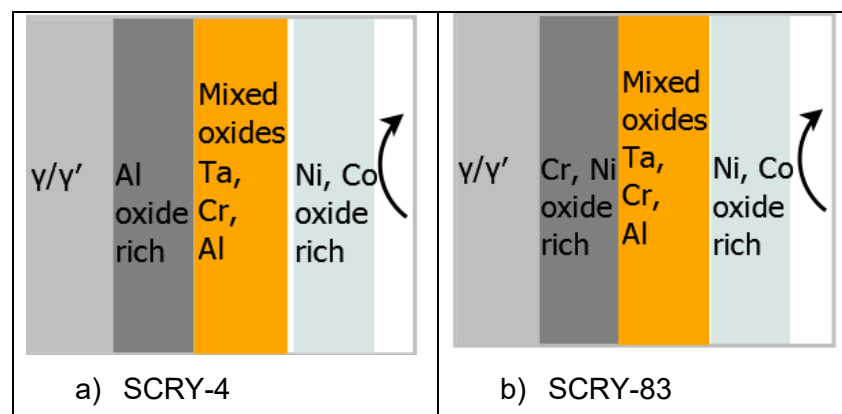


Figure 5.6: Schematic of the oxidation of SCRY-4 and SCRY-83

## 5.2.5 Weight gains kinetic of oxidation

The data from the increasing temperature test (1 h), the isothermal 24 h pre-oxidation test (from Figure 5.10), and the 72 h isothermal mass gain were merged and compared to a polycrystalline Ni-based alloy used for disk (RR1000) in Figure 5.7.
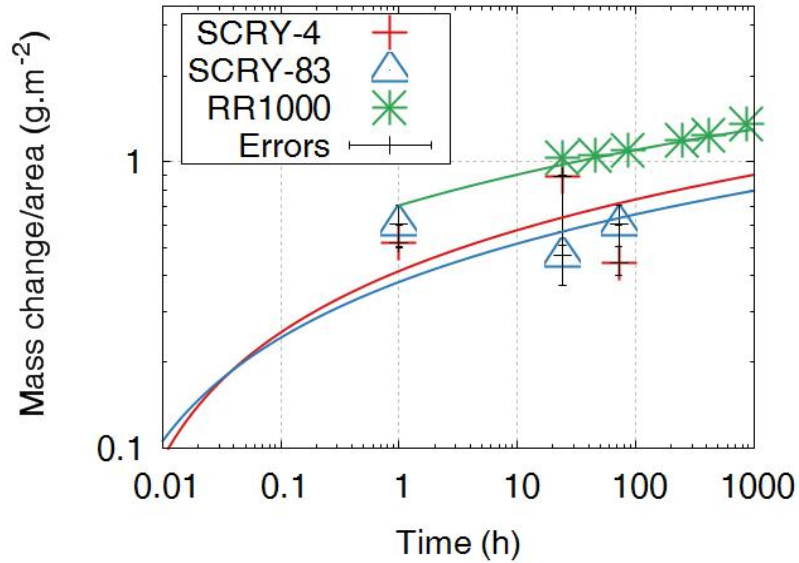
Figure 5.7: Mass change against time for SCRY-4, SCRY-83 and RR1000 exposed to air at 700 °C. RR1000 data is taken from Cruchley et al [124].

It is noted that the fitted curves share the same slope as the RR1000, albeit both blade alloys experienced a lower mass gain. This also shows that the weight gain kinetic can be approximated to a parabolic behaviour (Equation 3.4 with n=0.5).

## 5.3   Samples sprayed with NaCl

### 5.3.1 Mass change

#### 5.3.1.1      *Increasing temperature test*

Sea salt addition was found to be predominantly NaCl (see Figure 4.3) and is referred to as such. The test procedure for obtaining Figure 5.8 is detailed in § 4.2.2.1.2.
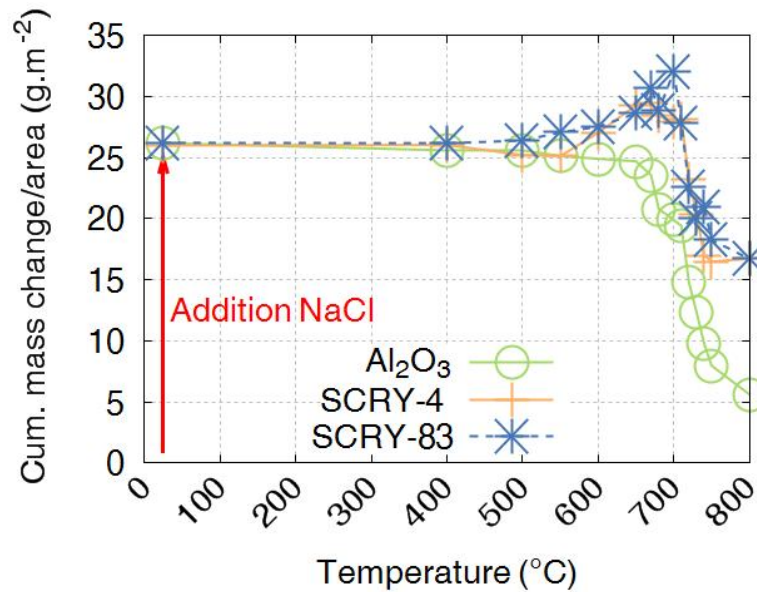
Figure 5.8: Sample coated with NaCl and exposed to air at increasing temperature; each point is 1 h in furnace

In Figure 5.8, on the $Al_2O_3$, the vaporisation of NaCl causes a decrease in mass seen at temperatures above 600°C. As indicated in (Chapter 3) Table 3.1, NaCl melts at 801°C (at atmospheric pressure) and its vapour pressure is shown in Figure 3.9.

For the SCRY-4 and SCRY-83, the mass loss is also caused by the formation of volatile chloride ($AlCl_2$, $NiCl_2$...). However, this loss is counter-balanced by the formation of oxides. The mass increase with NaCl coated, at 700 °C, for both superalloy ($\Delta m = 5$ g m$^{-2}$) is much larger than in air only (Figure 5.3 $\Delta m = 0.6$ g m$^{-2}$). This is discussed further below.

Finally, at the end of the test, a small residue of NaCl remained on the $Al_2O_3$ at 800°C ($\Delta m = 5$ g m$^{-2}$). A higher temperature or longer time may be needed to vaporise it all.

### *5.3.1.2    Effect of pre-oxidation on the degradation caused by NaCl*

After NaCl deposition and air exposure at 700°C for 24 h, the free surfaces of the samples were observed via SEM.

| (a) SCRY-4 sample (Cµ) | (b) SCRY-83 sample (Eµ) |
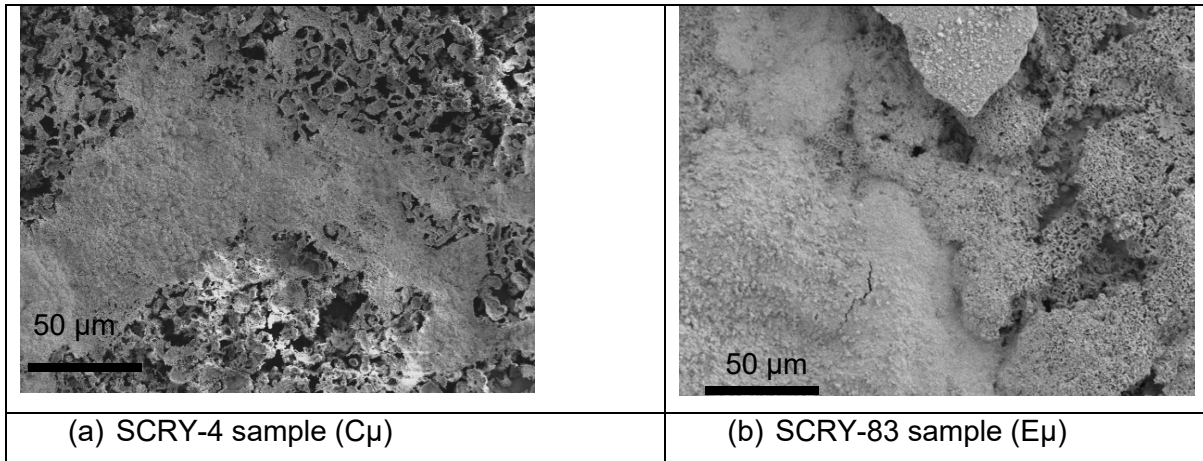
Figure 5.9: SE micrograph of free surface of sample coated with NaCl and exposed to 700 °C in air for 24 h (no water used in the surface preparation)

The free surfaces were found extremely porous and very fragile. A method was therefore created to quantify the amount of porous oxide (the method is described in § 4.2.3.1 and consist in measuring the weight of the sample before and after the removal of the porous layer with distilled water). The porous layer did not require a large force to be removed.

For the samples that were pre-oxidized and sprayed with NaCl in Figure 5.10 (b), SCRY-83 suffered a minor mass loss in the furnace ($\Delta mC'''D'''$=-7.48 g m$^{-2}$ compared to $Al_2O_3$-former $\Delta mC'D'$=-18.56 g m$^{-2}$). The SCRY-4 mass loss in the furnace is almost the same as the vaporisation of NaCl on $Al_2O_3$ strip. To explain this mass loss, Gibbs free energy comparison suggests $AlCl_3$ would form readily compared to other chlorine compounds ($\Delta G_0$ is very negative see Figure 3.8). However, since $AlCl_3$ has a very high vapor pressure (see Figure 3.9), it caused a large mass loss.
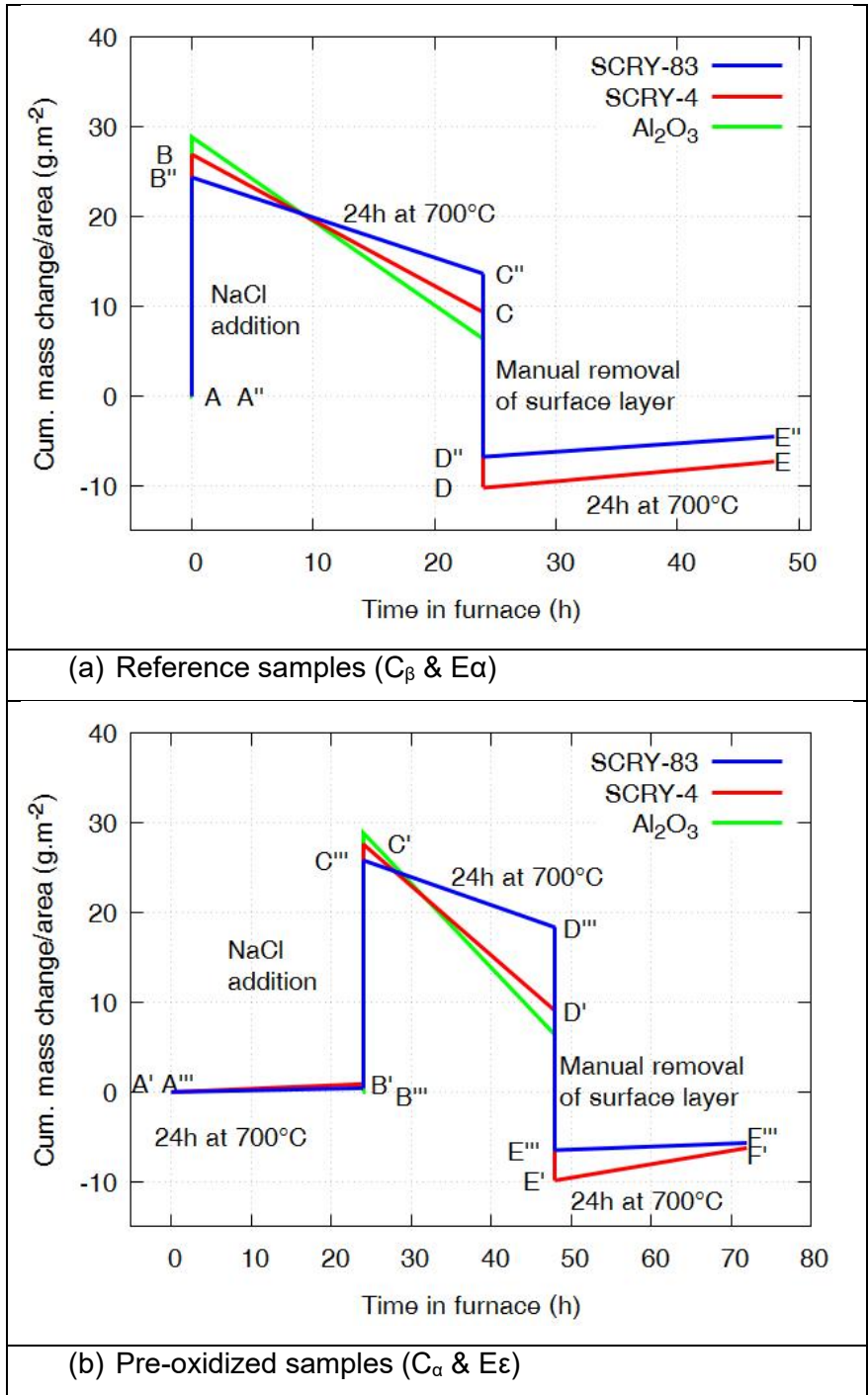
Figure 5.10: Effect of pre-oxidation on SCRY-4 and SCRY-83 samples coated with NaCl and exposed at 700°C

To verify that hypothesis a sample was coated with NaCl and exposed to air at 700 °C for 24 h. The scale developed on the $Al_2O_3$-former was then observed via SEM without the use of water (see Figure 5.11). The Al weight percent of the bulk substrate is indicated with a solid black line. An Al-rich layer is present on the outermost part of the oxide confirming its volatility. In addition, a large internal layer (measuring ~ 60 μm) is depleted in Al.
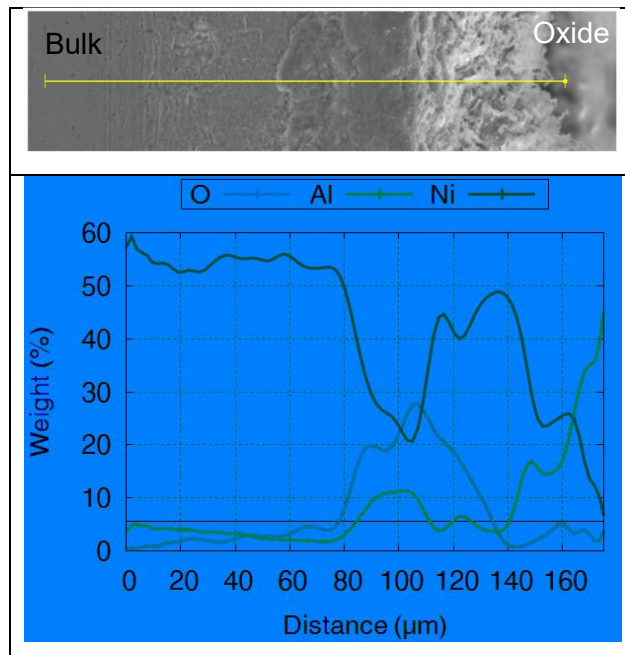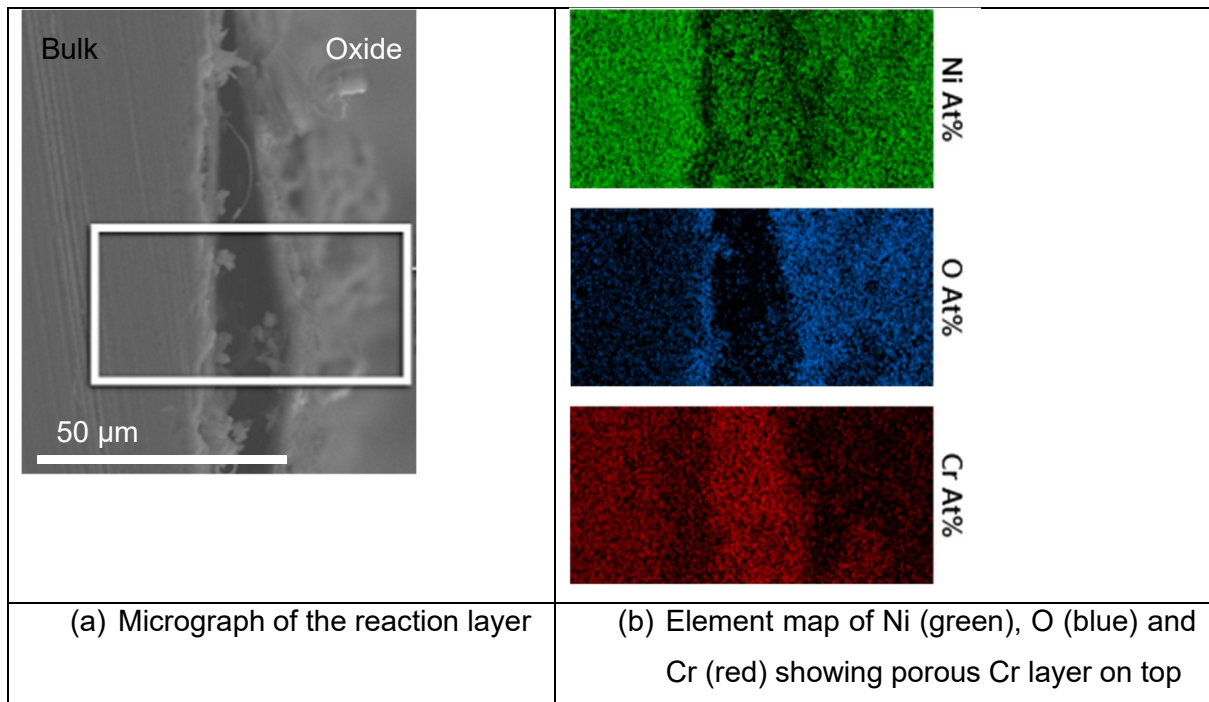
Figure 5.11: SE micrograph and EDX composition profiles of SCRY-4 sample (Cµ) coated with NaCl and exposed to 700 °C in air for 24 h (preparation: dry grinding perpendicular to surface)

In the non-pre-oxidized (reference cases), in Figure 5.10 (a), the difference in mass loss is smaller ($\Delta mB''C''$=-10.73 g m$^{-2}$ vs Al$_2$O$_3$-former $\Delta mBC$=-17.57 g m$^{-2}$). This agrees with the previous explanation of chloride formation, however, since the elements are in their bulk concentration, the mechanism is less pronounced.

The amount of porous oxides measured on the pre-oxidized samples in Figure 5.10 (b) (by washing the reaction layer) was slightly larger for the Cr$_2$O$_3$-former ($\Delta mD'''E'''$=24.809 g m$^{-2}$ against Al$_2$O$_3$-former $\Delta mD'E'$=18.88 g m$^{-2}$). This is possibly caused by the "activated oxidation" that sees CrCl$_3$/CrCl$_2$ oxidizing at the gas/oxide scale interface (due to a higher oxygen partial pressure) releasing the chlorine back into the cycle [7].

In agreement with this explanation, a lower amount of porous material was measured in the reference case in Figure 5.10 (a) ($\Delta mC''D''$=20.39 g m$^{-2}$ against Al$_2$O$_3$-former $\Delta mCD$=19.52 g m$^{-2}$). This is because, like above, the mixed Cr oxide was not formed when the NaCl was deposited. Evidence of the "activated oxidation" can be seen in Figure 5.12 (b) on the O map, where the large Cr layer has not stopped the diffusion of the oxygen.

|                                        |                                        |
| :------------------------------------: | :------------------------------------: |
| (a) Micrograph of the reaction layer   | (b) Element map of Ni (green), O (blue) and Cr (red) showing porous Cr layer on top |

Figure 5.12: SE micrographs and EDX composition maps of SCRY-83 sample (Eµ) coated with NaCl and exposed to 700 °C for 24 h in air (preparation: dry grinding perpendicular to surface)

Finally, during the last furnace exposure, the $Al_2O_3$-former experienced a larger mass gain (than the $Cr_2O_3$-former). The observation of the reaction layer, after exposure (displayed in Figure 5.13 (a)) shows a relatively large reaction layer, and more importantly very low Al concentration throughout. It was concluded that the previously formed oxide scale was disturbed during the washing of the deposit, and formation of new oxide was impaired by the internal depletion of Al.

The $Cr_2O_3$-former was less affected by the washing of the reaction layer. EDX maps shown in Figure 5.13 (b) highlights the disappearance of Ni oxides while the internal Cr layer remained at the surface. It is also noted an irregular surface.

(a) SE micrographs and EDX profile composition of SCRY-4 (Cβ, point E) showing distinctive layers with a relatively low Al content



(b) SE micrograph and element maps (wt %) of SCRY-83 sample (Eε, point F''') pre-oxidized showing rough surface and pits and evidence of a protective oxide layer
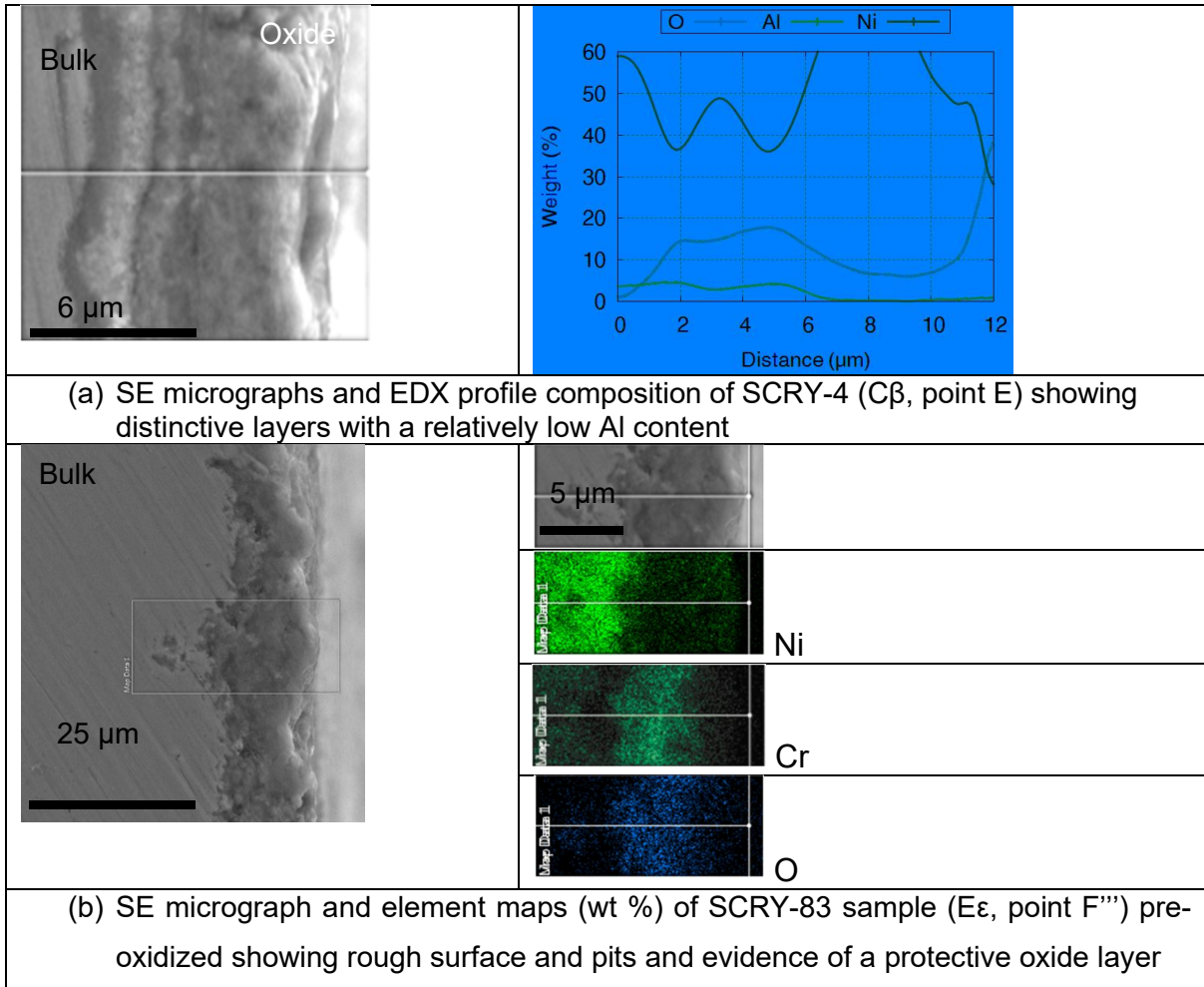
Figure 5.13: Samples coated with NaCl, exposed to 700 °C for 24 h, with their porous layer removed and a second exposure in air at 700°C for 24 h

One may ask how the Cl migrated to the substrate. Is it as a gas ($Cl_2$), or as ion ($Cl^-$) or as a liquid? Two known liquid could be formed at 700 °C ($CoCl_2$/NaCl mixture is liquid above 380 °C or NaCl/$NiCl_2$ is also liquid above 600 °C). To help answer this question, the free surfaces were observed via SEM at the end of the different steps and are shown in Figure 5.14.
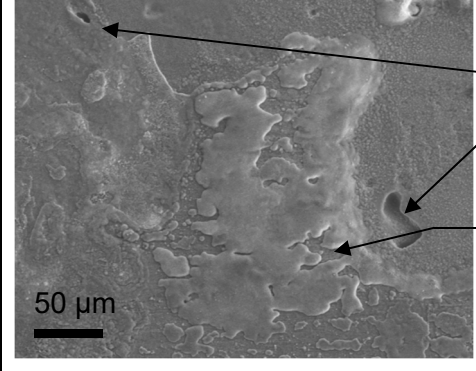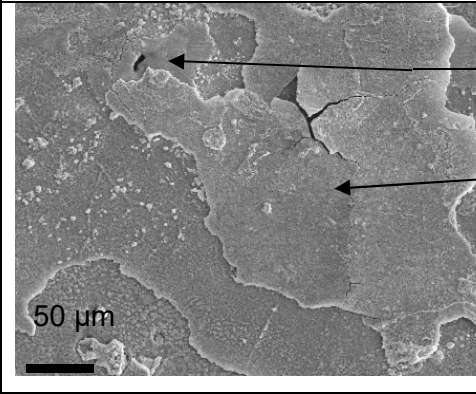
|  | Open porosity |
| | Solidified liquid |

(a) SE micrographs of the free surface of SCRY-4 sample ($C_\beta$) showing evidence of open porosity and liquid formation at the free surface

|  | Open porosity |
| | Layer spalling off |

(b) SE micrographs of the free surface of SCRY-83 sample ($E\varepsilon$ point F''') showing open porosity and stratified layers with the top one ready to spall

Figure 5.14: Free surfaces of samples coated with NaCl, exposed to air at 700 °C for 24 h, with their porous layer removed and a second exposure in air at 700°C for 24 h.

Open porosities were found at the surface of the two samples (unseen on virgin sample in §5.1.2). It was thought these pores could be vent holes where volatile compounds escaped. (EDS was not performed on these layers since layers were relatively thin in comparison to the beam interaction volume).

In addition, solidified liquid was seen on the SCRY-4, while stratified layers were seen on the SCRY-83. It is thought the spalling off (seen above) was caused by misfit strain, itself caused by different expansion coefficient, showing heterogeneity in these layers.

### 5.3.1.3    72h isothermal test

To assist comparison with previous tests, the mass change in Table 5.2 includes the initial NaCl coating (24.85 and 25.55 g.m$^{-2}$ for SCRY-4 and for SCRY-83 respectively). Also, to help comparison with air only test, the test duration was extended to 72 h. In the same way as with the progressively heated samples test above (see Figure 5.8), the mass change is made up of two components. First, the mass of the sample is increased due to the formation of a thicker

81

oxide (than in air only case). Second, a decrease in mass is experienced due to the vaporisation of NaCl and volatilisation of $AlCl_3$, $CrCl_2$, $CrCl_3$ and $NiCl_2$.

Table 5.2: Mass change of samples sprayed with NaCl and exposed to air for 72 h at 700°C

| Material | Sample# | Coating (g.m⁻²) | Specific mass change (g.m⁻²) |
|---|---|---|---|
| SCRY-4 | C22 | 24.85 | 6.93 |
| SCRY-83 | E11 | 25.55 | 19.67 |

Table 5.2 shows that SCRY-4 exhibited a large mass loss ($\Delta m$ =-17.92 g m⁻²), while SCRY-83 was relatively modest ($\Delta m$ =-5.88 g m⁻²).

## 5.3.2 Reaction layer microstructures
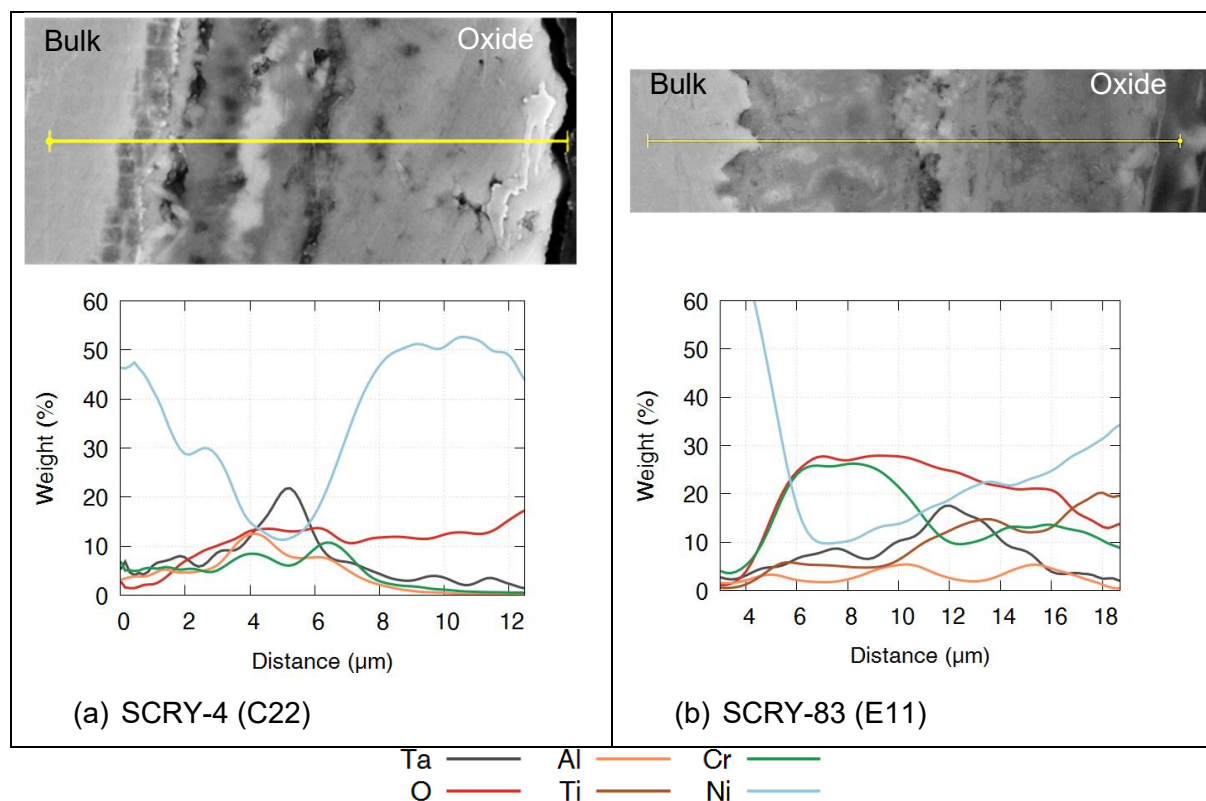


Figure 5.15: EDX composition profiles of samples sprayed with NaCl and exposed in air for 72 h at 700 °C

For the SCRY-4, in Figure 5.15 (a), a peak in Ta delimitate an inner layer depleted in Ni, but rich in Ta, Al and Cr oxides with an outer layer rich in Ni oxide. It is also noted that the reaction layer is much thicker than that observed in air only. A vertical dark line is seen at 6 µm, matching the Ta peak.

For the SCRY-83, in Figure 5.15 (b), a thick layer of Cr-rich oxide is seen (from 6 µm to 10 µm), with other Ta, Ti and Ni oxides on the outside (from 10 µm to 18 µm).

## 5.3.3 XRD spectra and phase identification



(a) SCRY-4 (C22)

(b) SCRY-83 (E11)
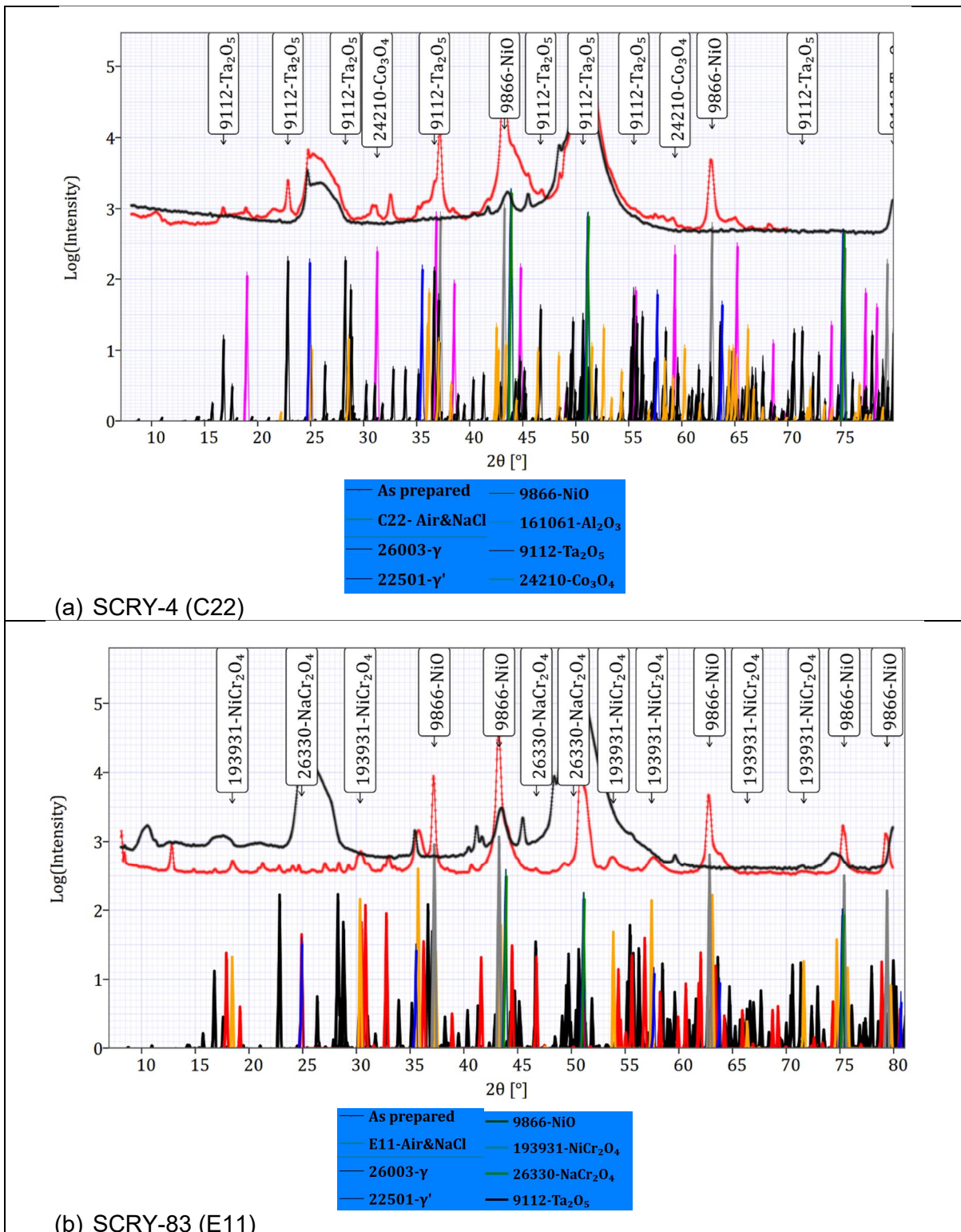
Figure 5.16: Phase identification with XRD spectra for samples sprayed with NaCl and exposed to air at 700 °C during 72 h

In Figure 5.16, a much larger difference is seen between as-prepared (black curve) and treated (red curve) than the air only case (Figure 5.5). This is consistent with a much thicker reaction layer (as seen above in § 5.3.2).

For the $Al_2O_3$-former, in Figure 5.16 (a), a large amount of nickel oxide and moderate amount of cobalt oxide are detected. $Al_2O_3$ is also detected at medium (36.1°) and high angles. Finally, $Ta_2O_5$ is detected at low and medium angle.

For SCRY-83 in Figure 5.16 (b), a large amount of nickel oxide is also detected. While $NaCr_2O_4$ and $NiCr_2O_4$ are found at low and medium angles.

## 5.3.4 Schematic representation of NaCl effect on pre-oxidised samples

| SCRY-4 | | SCRY-83 |
|---|---|---|
|  | Step 1: NaCl is deposited at the surface of pre-oxidised samples. NaCl vaporizes slowly at the surface. |  |
|  | Step 2: $NiCl_2$-NaCl liquid is formed (phase diagram § 9.4.8 with $T\epsilon$=570 °C) or $NaCl$-$CoCl_2$ (§ 9.4.7 $T\epsilon$=370°C). Chlorine compounds form and volatilize resulting in scale damage |  |
|  | Step 3: the liquid flows through pores reaching the substrate–oxide interface. High vapour pressure compounds ($AlCl_3$) continue to form, further damaging the scale | Step 3: the "activated oxidation" sees $CrCl_2$/$CrCl_3$ oxidize at higher $O_2$ partial pressure, releasing the Cl to another cycle. This form large amount of porous oxide for a small weight loss |  |
|  | Step 4: all the chlorine has been consumed, sodium has been oxidised and oxides are non-protective<br>Another oxide layer is then formed. |  |

Figure 5.17: Schematic of the effect of NaCl deposition on pre-oxidised SCRY-4 at 700 °C

## 5.3.5 Weight gains kinetics of NaCl degradation

Mass change for different exposure times is shown in Figure 5.18.
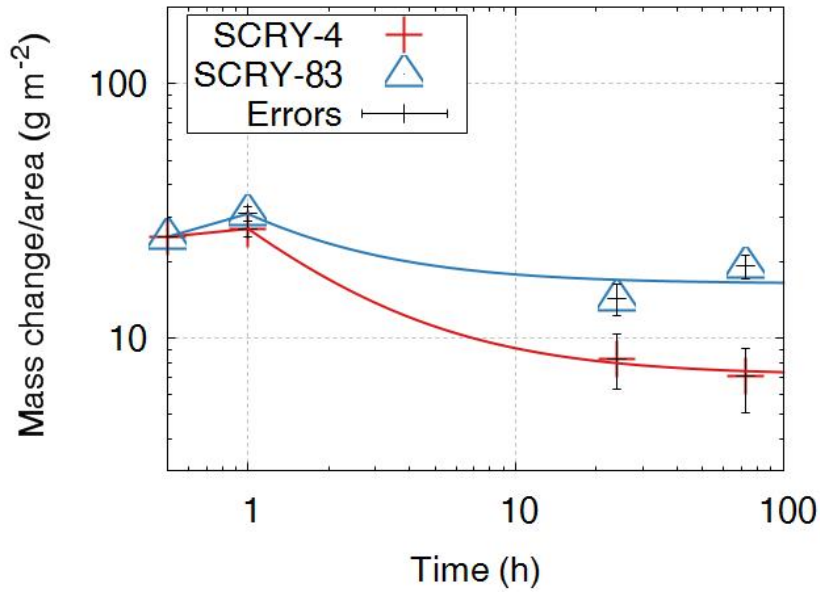
Figure 5.18: Mass change against time for samples sprayed with NaCl and exposed in air at 700 °C

A rapid mass gain is observed during the first hour, consistent with scale damage (see steps 2 and 3 above). This is followed by a slow mass loss. The mass loss originates from the vaporisation of the chloride compounds (more data points would be needed to refine this kinetic aspect).

It appears that a steady-state is reached after 24 h. The fact that no chlorine is detected, either as XRD compounds or in the EDX profiles, further confirms that it must have been vaporised.

Comparing the two superalloys, it is noted that SCRY-83 experienced a larger mass gain initially but later exhibits a smaller mass loss.

## 5.4 Samples exposed to air and $SO_2/SO_3$ gases

### 5.4.1 Mass change

Table 5.3: Mass change in air and $SO_2/SO_3$ for 72 h at 700 °C

| Material | Sample# | Specific mass gain (g m$^{-2}$) |
|----------|---------|-------------------------------|
| SCRY-4 | C35 | 3.02 |
| SCRY-83 | E16 | 0.945 |

For this environment, the furnace was brought to temperature and, after thermal equilibrium, the upper sealing cap was pressed down, followed by $SO_2$ injection into the chamber. Therefore, an oxide layer was formed before the introduction of the $SO_2/SO_3$.

The mass gain is significantly above the air only measurement (7.3 times higher for SCRY-4 and 1.5 for SCRY-83).

## 5.4.2 Reaction layer microstructure
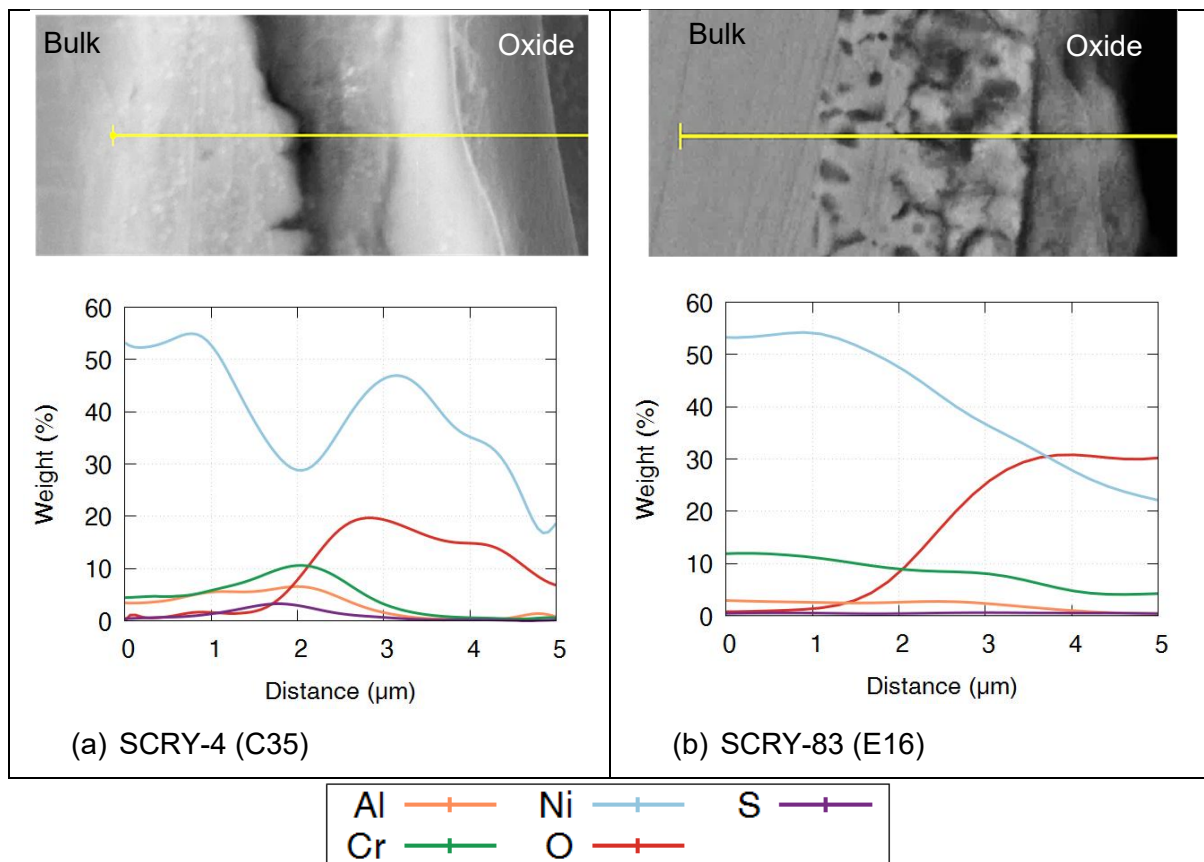


Figure 5.19: EDX composition profiles of the samples exposed to air and $SO_2/SO_3$ gases for 72 h at 700 °C

In examining Figure 5.19, it should be noted that both alloys contain molybdenum, the L$\alpha$ band of which slightly overlaps the K$\alpha$ band of sulphur (as mentioned in § 4.4.4.3).

For SCRY-4, in Figure 5.19 (a), the layout is essentially identical to air (outer region rich in nickel oxide and an inner one rich in Cr and Al) with the exception that now a sulphur-rich layer is detected in the inner region.

For SCRY-83 in Figure 5.19 (b), sulphur is undetected. However, the micrograph shows darker stains that were not seen in air only case.

## 5.4.3 XRD spectra and phase identification
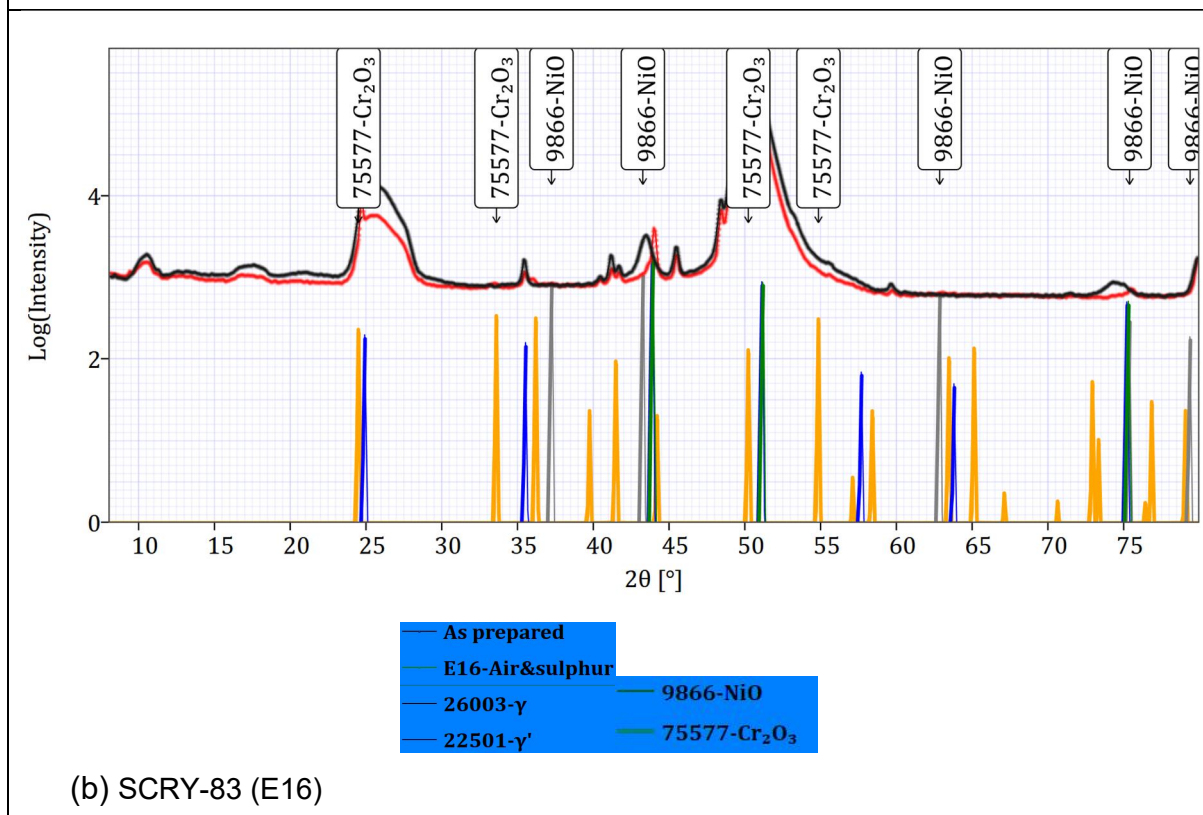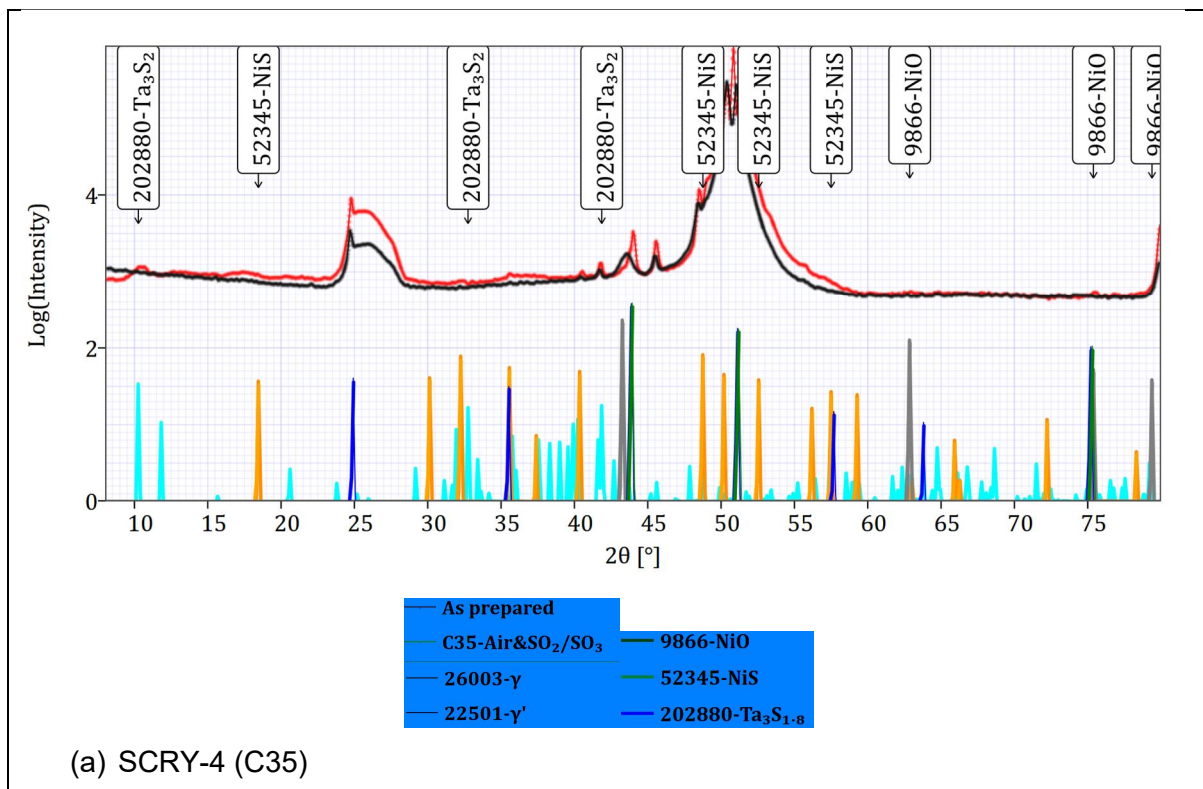


Figure 5.20: Phase identification with XRD spectra for samples exposed to air and $SO_2/SO_3$ gases at 700 °C for 72 h

In Figure 5.20, the differences between as-prepared and as-treated are very small (despite the use of log scale). This is in agreement with the reaction layers being thin, as seen in the micrographs above. Another indication of this is the remaining <001> peak of γ' (at 24.7 ° in both spectra).

For SCRY-4 in Figure 5.20 (a), nickel oxide and nickel sulphide are detected, as well as a smaller amount of tantalum sulphide.

For SCRY-83 in Figure 5.20 (b), chromium and nickel oxide are detected.

## 5.4.4 Schematic representation

A schematic representation of these mechanisms is shown in Figure 5.21.

| SCRY-4 | | SCRY-83 |
|---|---|---|
| γ/γ′ \| Al oxide rich \| Mixed oxides Ta, Cr, Al \| Ni, Co oxide rich | Step 1: oxidation of SCRY-4 (same as Figure 5.6) | γ/γ′ \| Cr, Ni oxide rich \| Mixed oxides Ta, Cr, Al \| Ni, Co oxide rich |
| γ/γ′ \| Al oxide rich \| Mix ox \| Ni, Co ox \| NiSO₄ | Step 2: upon exposure to $SO_3$, nickel oxide turns to nickel sulphate | Step 1: (same as Figure 5.6). No change to SCRY-83 |
| γ/γ′ \| Al oxide rich \| Ni₃S₂ \| Ni SO₄ \| NiO \| S \| Ni | Step 3: $NiSO_4$ dissociates to form a liquid ($Ni/Ni_3S_2$ eutectic) moving inward, while NiO moves outward. The growth of this outward scale slows the uptake of $SO_3$ | |
| γ/γ′ \| Al oxide rich \| Ni₃S₂ \| NiO \| S | Step 4: the alumina-rich layer, being non-continuous, is penetrated by sulphides. The liquid sulphides flow to the substrate–oxide interface | |

Figure 5.21: Schematic of the effect of sulphur exposure on pre-oxidised SCRY-4 and SCRY-83 at 700 °C

As explained above, sulphides can form despite being thermodynamically unfavoured (in comparison to oxides). Haflan and Kofstad [65] stated that if $NiSO_4$ is stable, then sulphidation of Ni would occur through Equation 3.11 and Equation 3.12. For SCRY-4, this is consistent with the micrograph and the XRD spectrum showing an inner layer rich in $Ni_3S_2$ (that was probably liquid at the temperature of the test) and an outer layer rich in NiO. However, for SCRY-83, the XRD and micrograph observations contradict these mechanisms. It is unclear why such a difference occurred. It is possible that despite the relatively low temperature, a dense and protective Cr oxide formed and prevented inward sulphur migration.

## 5.5 Samples sprayed with NaCl and exposed to air and SO$_2$/SO$_3$ gases

When NaCl is exposed to a mixture of air and SO$_2$/SO$_3$, it is converted into Na$_2$SO$_4$ (Equation 3.6 to Equation 3.8). Several authors [55], [60], [91], [92] have reported that hot corrosion is much worse when NaCl is added to Na$_2$SO$_4$. Investigations into the effect of Na$_2$SO$_4$ by itself was therefore carried out, followed by exposure of samples sprayed with NaCl and exposed to SO$_2$/SO$_3$.

### 5.5.1 Mass change

#### *5.5.1.1    Sodium sulphate effect at increasing temperature*

Figure 5.22 was obtained by following the test procedure detailed in § 4.2.2.1.3.
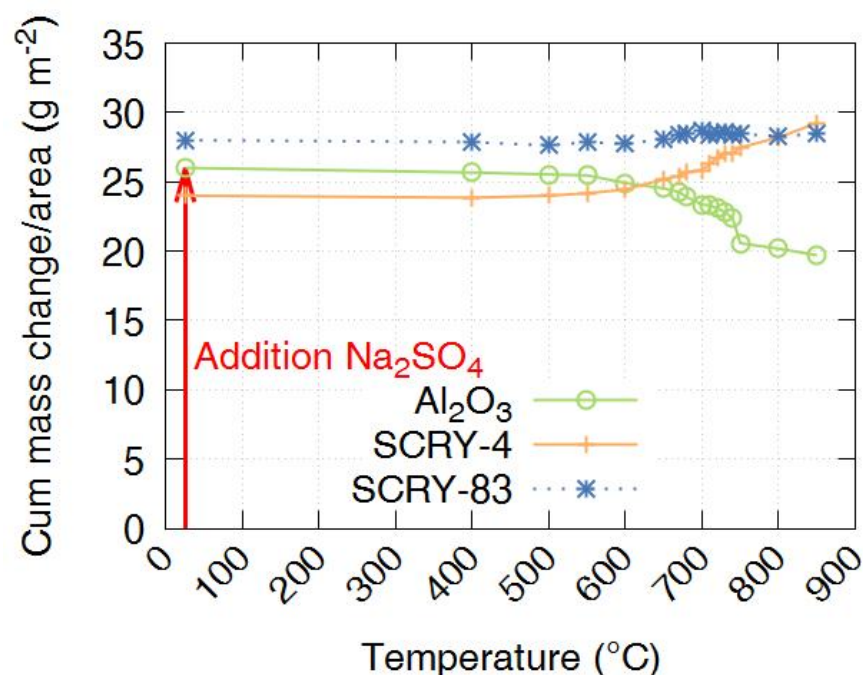


Figure 5.22: Mass change data for samples coated with Na$_2$SO$_4$ and exposed at increasing temperature. (Individual samples were weighed and returned to the furnace at higher temperatures for 1 h each time)

In Figure 5.22, a moderate decrease (less than seen in Figure 5.8) is apparent for the Al$_2$O$_3$ strip. At these temperatures, Na$_2$SO$_4$ is clearly less prone to vaporisation than NaCl (see the vapour pressure of both compounds, as a function of temperature in Figure 3.9).

For the SCRY-83, a small mass increase is seen, levelling off at around 750°C, to a value very similar to the air only case (Figure 5.3 at 750°C $\Delta m$=1.0 g m⁻²). This can be explained by the formation of a very protective oxide.

The case of SCRY-4 is very different, since increasing mass gains starts at about 550°C. This mass gain is greater than the "air only" case. This suggests that SCRY-4 is very susceptible to the degradation caused by $Na_2SO_4$ while SCRY-83 is not.

## *5.5.1.2        Effect of pre-oxidation on degradation caused by Na₂SO₄*

A very similar experiment done above with NaCl (see § 5.3.1.2) was repeated with $Na_2SO_4$ with the aim to investigate the effect of this salt and the effect of pre-oxidation. After sodium sulphate was coated, the samples were exposed to air at 700 °C during 24 h. The free surface of the two samples were observed by SEM (in Figure 5.23). Water was not used in the preparation to prevent losing soluble compounds.

|  |  |
|---|---|
|  | Feather-like salt crystal<br><br>Evidence of liquid formation<br><br>Large salt crystal |
| (a)  SCRY-4 sample (Cγ) | |
|  | Feather-like salt crystal<br><br><br><br>Large salt crystal<br><br>Evidence of liquid formation |
| (b)  SCRY-83 sample (Eρ) | |
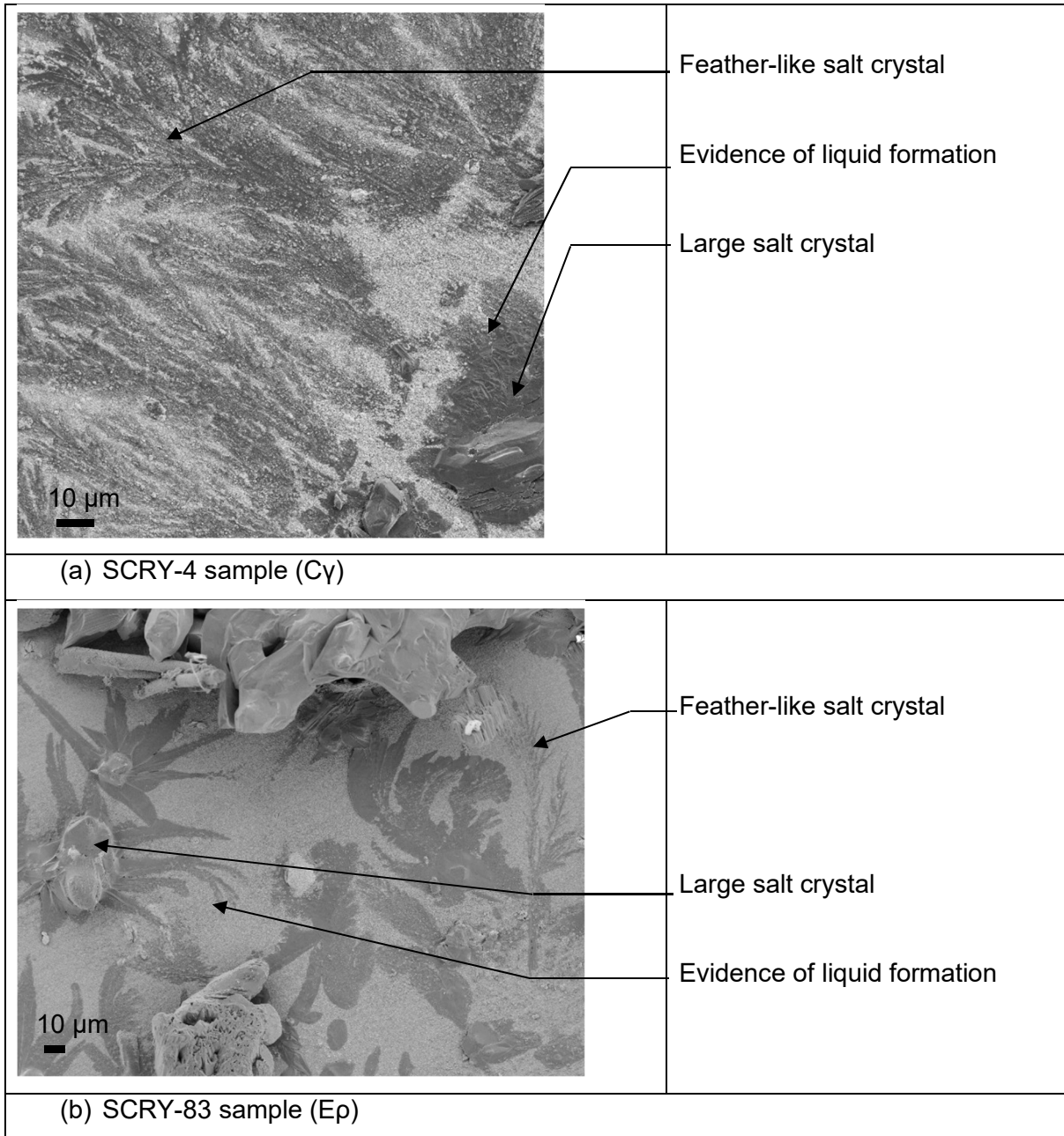
Figure 5.23: SE image of the free surface of samples coated with $Na_2SO_4$ and left for 24h at 700 °C

For both alloys, it was seen feather-like salt, large crystals (that most likely were $Na_2SO_4$) and darker regions around these crystals that was interpreted as a possible trace of liquid formation. At a macro level, white salts were seen at the surface. It was also observed dark staining on the polishing lines.

A method was created to quantify how much of liquid was formed. To that end, it was noted that $Na_2SO_4$ is soluble in water [125] while it is thought that sodium nickel sulphate (anhydrous nickelblodite) is not. Therefore, if there is no interaction with the oxide, $Na_2SO_4$ would be completely removed from the surface during the washing.

94

(a) Reference samples ($C_\gamma$ & $E_\rho$)



(b) Pre-oxidized samples ($C_\Delta$ & $E_\tau$)
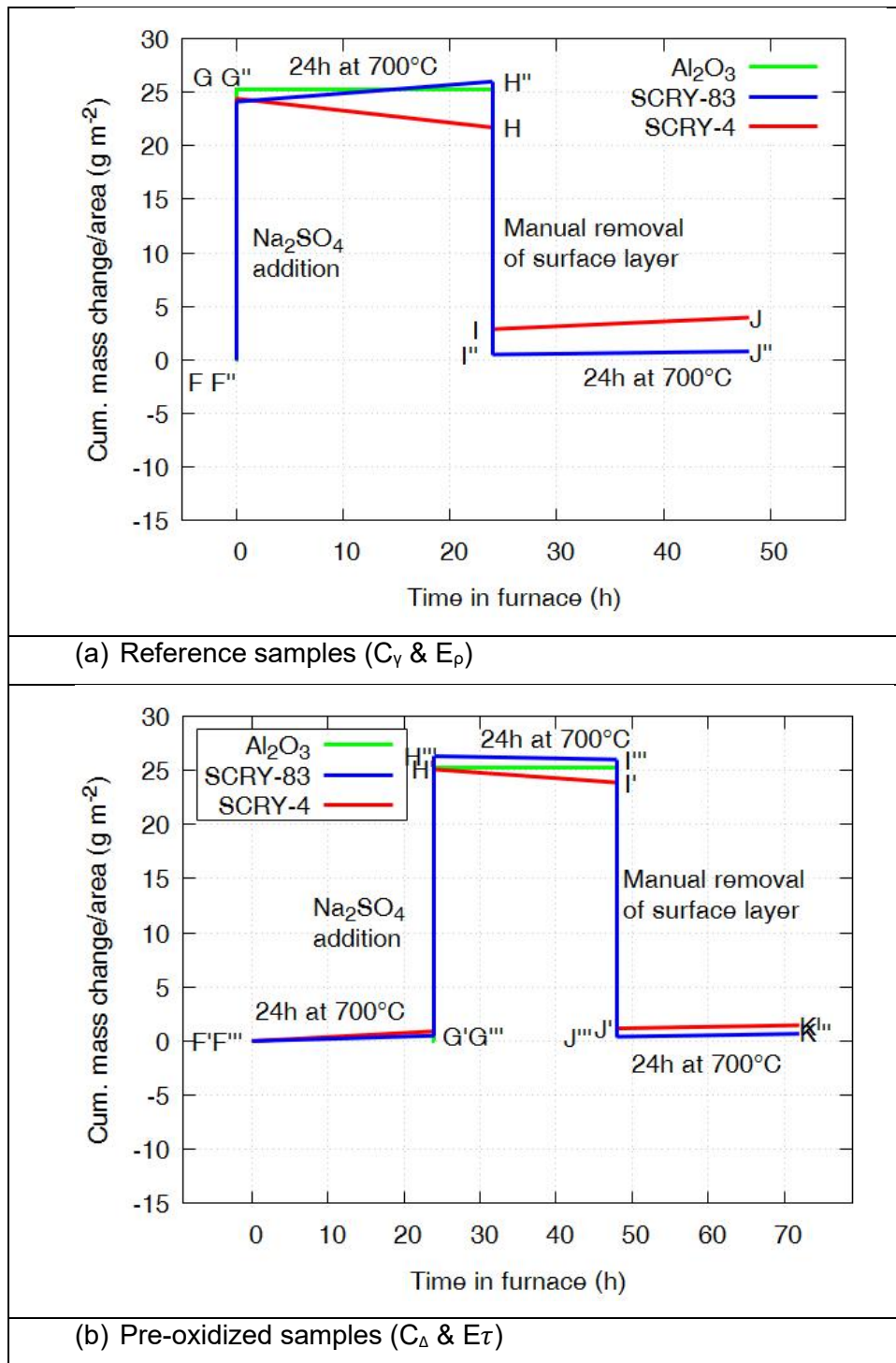
Figure 5.24: Effect of pre-oxidation on samples coated with sodium sulphate

The vaporisation of $Na_2SO_4$ (measured on the $Al_2O_3$ strip) is almost negligible at 700 °C (consistent with the small mass loss, seen in the variable temperature test, in Figure 5.22).

In the reference case, in Figure 5.24 (a), in the furnace, the mass loss experienced by SCRY-4 ($\Delta mGH=-2.68$ g.m$^{-2}$) must therefore come from the alloy. If a liquid has formed in Figure 5.23 (most likely $Na_2SO_4/NiSO_4$ although $Na_2SO_4/CoSO_4$ is also possible), it is thought that it has permitted the formation of oxides with high partial pressure (ie: $Re_2O_7$, $MoO_3$, see

95

their partial pressure in Figure 3.3). At the contrary, the $Cr_2O_3$-former experienced a minor mass gain, probably due to a protective oxide formation possible at lower temperature. A similar trend is noticed, in a smaller proportion, in the pre-oxidized case, in Figure 5.24 (b), proving that the oxide has decreased the formation of volatile compounds.

During washing of the deposit, it was noted that both SCRY-83 samples returned to a cumulative mass change (subtracting the oxide formation) of ~0.0 g.m$^{-2}$. This indicates that the $Na_2SO_4$ has hardly interfered with the alloy and was almost completely dissolved and removed by the distilled water. On the contrary, the $Al_2O_3$-former sees a significant $Na_2SO_4$ conversion into sodium nickel sulphate in the reference case ($\Delta mFl=2.87$ g.m$^{-2}$). Such conversion significantly decreases when the sample was pre-oxidized ($\Delta mG'J'=0.26$ g.m$^{-2}$). This is reflected in the reaction layer thickness shown in Figure 5.26. Both sample have a thin scale, but the reference sample also show darker γ/γ' beneath the scale.



| (a) Reference sample ($C_γ$) | (b) Pre-oxidized sample ($C_Δ$) |
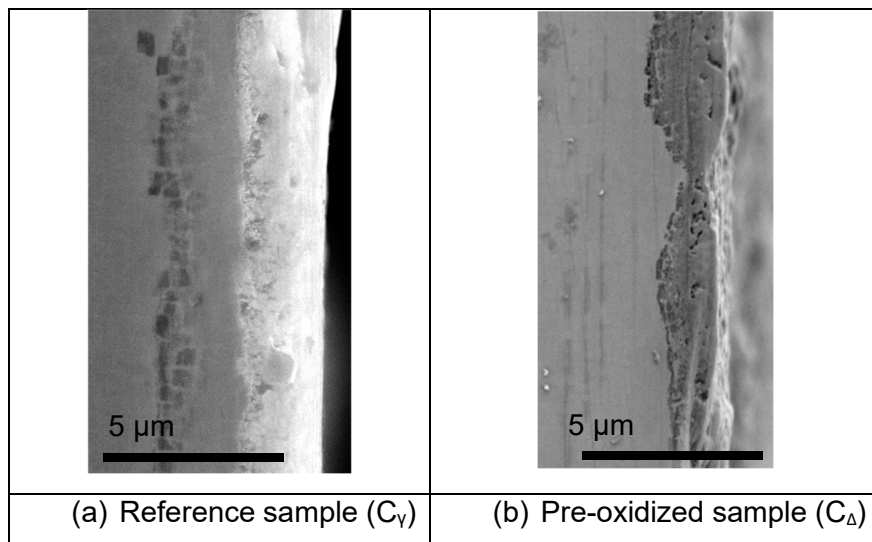
Figure 5.25: SE image of SCRY-4 sample after the final furnace exposure

Figure 5.26 provides a schematic representation of the differences noted between the reference and the pre-oxidized samples.
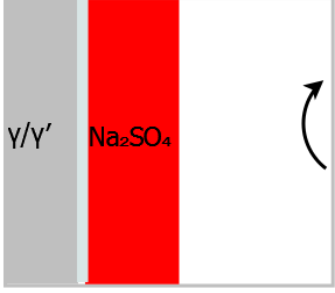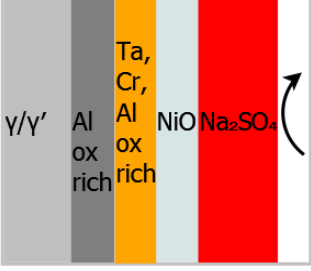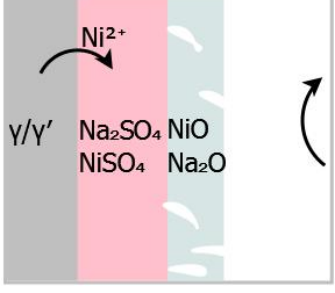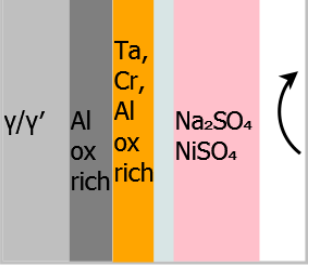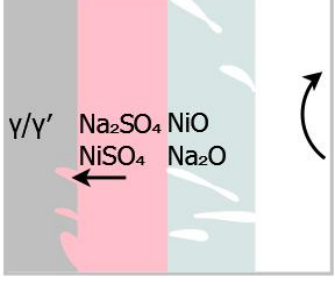
| SCRY-4 reference sample | | SCRY-4 pre-oxidized sample | |
|---|---|---|---|
| Step 1: not applicable to this sample | | Step 1: pre-oxidation step | |
|  | Step 2: deposition of $Na_2SO_4$. (Thin native NiO layer present) |  | Step 2: same as reference sample with thicker oxide |
|  | Step 3: formation of a liquid ($Na_2SO_4$/ $NiSO_4$ eutectic) moving inward. Accessing blade constituent permits synergistic dissolution of oxides |  | Step 3: formation of a eutectic $Na_2SO_4$/ $NiSO_4$, with no further changes |
|  | Step 4: porous NiO is re-precipitating at the oxide/eutectic interface, while eutectic is flowing in the γ channels (explained below) | | |

Figure 5.26: Schematic of the effect of $Na_2SO_4$ deposition on pre-oxidised and non-pre-oxidised SCRY-4 at 700 °C

## 5.5.1.3 72h isothermal test

Once again, to compare the tests with one another, a standard 72 h exposure was carried out. The chamber cap was secured after reaching thermal equilibrium, resulting in a sodium chloride effect (see § 5.3), followed by $SO_2$ injection, causing conversion of NaCl to $Na_2SO_4$ (see the effect in § 5.5.1.1).

Table 5.4: Mass change of sample sprayed with NaCl and exposed to air and $SO_2/SO_3$ at 700 °C for 72 h

| Material | Sample# | Coating (g m$^{-2}$) | Specific mass gain (g m$^{-2}$) [4] |
|----------|---------|----------------------|-------------------------------------|
| SCRY-4   | C34     | 25.1                 | 55.91                               |
| SCRY-83  | E17     | 26.1                 | 25.03                               |

Table 5.5 is useful to explain the mass change recorded in Table 5.4. Line 1 shows mass change mechanisms common with samples sprayed with NaCl.

Table 5.5: Mechanisms causing mass loss and mass gain

|   | (a) Mechanisms causing mass loss | (b) Mechanisms causing mass gain |
|---|----------------------------------|----------------------------------|
| 1 | - Vaporisation of NaCl | + Uptake of $O_2$ (due to non-protective oxide) |
| 2 | - Vaporization of $Na_2SO_4$ | + Uptake of $SO_2/SO_3$ |
| 3 | - Formation of high vapour pressure compounds ($AlCl_3$...) | + Uptake of $SO_3$ and conversion of NaCl to $Na_2SO_4$ |

For SCRY-4, a comparison between the (modest) mass change experienced by the sample sprayed with NaCl (Table 5.2 Δm=6.93 g m$^{-2}$), and the (large) mass gain experienced here highlights a major effect of lines 2 and 3 side (b) of Table 5.5.

For SCRY-83, the mass change (Table 5.2 Δm=19.67 g m$^{-2}$) is much closer to this case. The test above (see Figure 5.24) confirms that SCRY-83 is less susceptible to the effect of NaCl deposits associated with environment of air+$SO_2/SO_3$.

---

[4] Similarly to the sample sprayed with NaCl, the mass at t=0h includes the NaCl weight.

## 5.5.2 Reaction layer microstructure
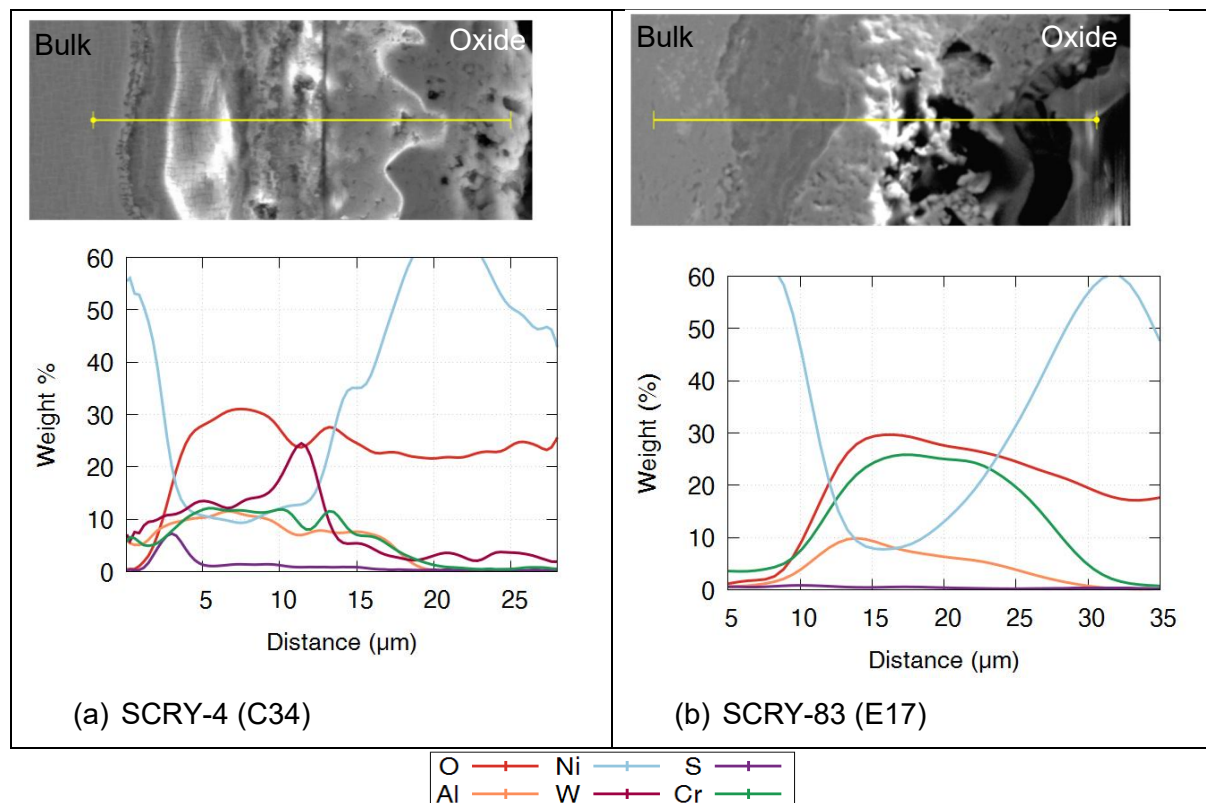


Figure 5.27: EDX composition profiles of samples sprayed with NaCl and exposed in air and SO$_2$/SO$_3$ for 72 h at 700 °C

For SCRY-4 in Figure 5.27 (a), an inner region depleted in Ni but rich in W, Cr, Al is followed by an Ni-rich oxide layer. An unusual S peak is seen at the innermost O-rich layer, close to the substrate–oxide interface. Also, a sharp W peak is detected between the two regions which was not seen in previous environments exposure. This reaction layer is the thickest which is consistent with the large mass gain recorded.

For SCRY-83 in Figure 5.27 (b), an inner region also depleted in Ni but rich in Cr and Al is then followed by a Ni-rich oxide. Sulphur is almost undetected suggesting that the thick Al and Cr oxides were very protective. (Note that W was not plotted since it remains constant and it did not add value to the explanations).

## 5.5.3 XRD spectra and phase identification
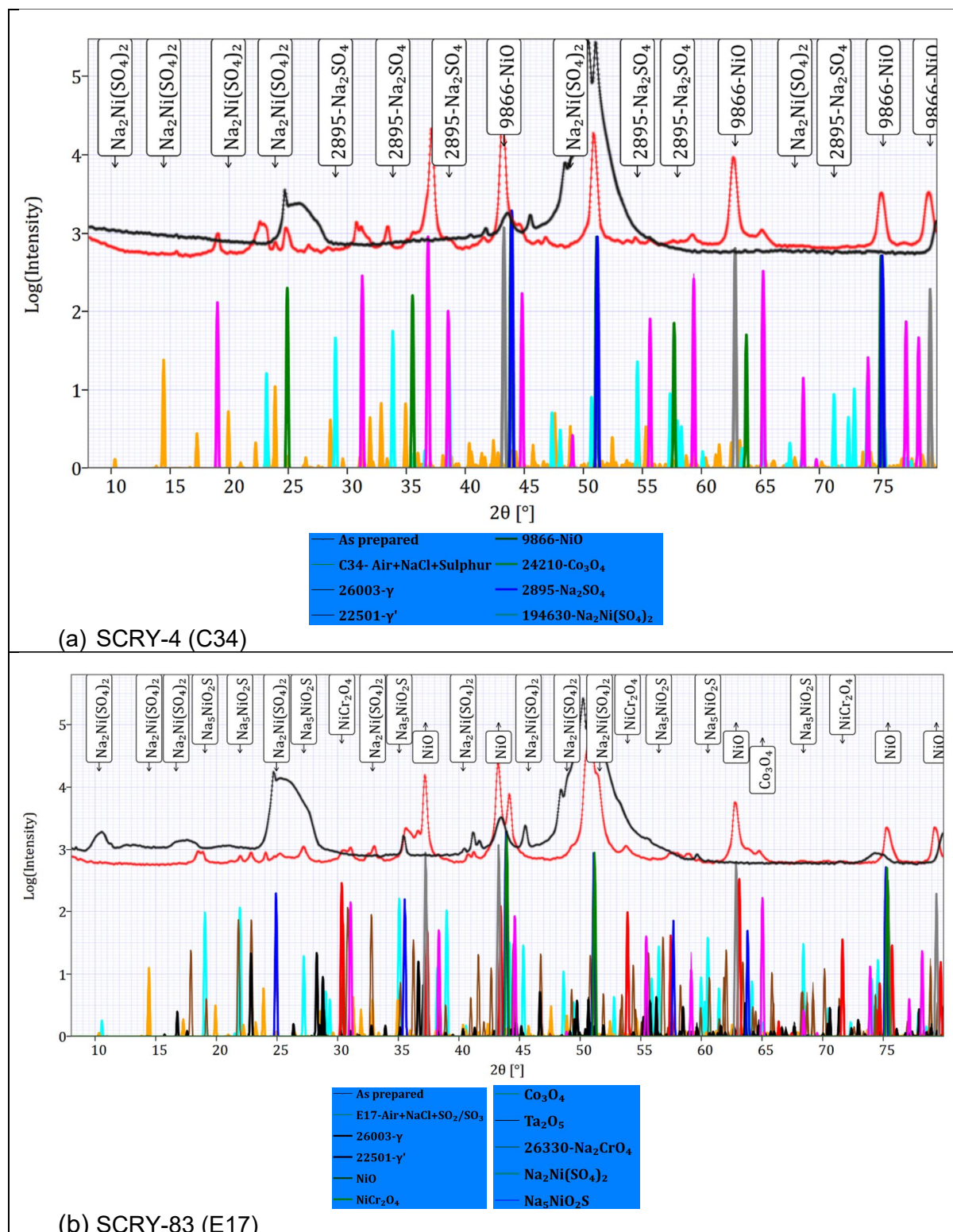


Figure 5.28: Phase identification with XRD spectra for samples sprayed with NaCl and exposed to air and sulphur at 700 °C during 72 h

For both alloys, in Figure 5.28, the {001} γ' peaks have almost disappeared, while the {002} γ' peaks are considerably weakened, this further confirms a thick reaction layer has formed.

For the SCRY-4 in Figure 5.28 (a), $Co_3O_4$ peaks are detected throughout the entire $2\theta$ range. This is at the contrary of $Na_2SO_4$ and $Na_2Ni(SO_4)_2$ for which peaks are matched only at low and medium angles. This information can be correlated with Figure 5.1 (b) that shows that 90 % of the incoming X-ray intensity is scattered by a layer of 9 μm at high angle ($2\theta=80°$), whilst only 3 μm is interrogated at low angle ($2\theta=30°$). $Na_2SO_4$ and $Na_2Ni(SO_4)_2$ are therefore present superficially.

For SCRY-83 in Figure 5.28 (b), the oxides $NiCr_2O_4$, $Co_3O_4$, $Ta_2O_5$ and $NiO$ are detected. The corrosion products $Na_2Ni(SO_4)_2$, $Na_5NiO_2S$ and $Na_2CrO_4$ are also detected. The $Na_2Ni(SO_4)_2$ (anhydrous nickelblodite) was also found superficially (matching only the low $2\theta$ angle). The discovery of $Na_5NiO_2S$ permits two deductions: first, comparing against $Na_2Ni(SO_4)_2$, $Na_5NiO_2S$ has a higher Na to Ni ratio, positioning it further away from the eutectic point on the $NiSO_4$-$Na_2SO_4$ phase diagram (§ 9.4.4). This means that this compound is probably not liquid at the temperature of the test. Second, $Na_5NiO_2S$ has less sulphate, which could be a consequence of the $Na_2CrO_4$ formation. Indeed, when $Cr_2O_3$ dissolved in the melt and forms $Na_2CrO_4$ superficially, it consumed $Na_2O$ (from Equation 3.21) and rendered the melt more acidic, limiting the ingress of $SO_3$. Moreover, formation of $Na_2CrO_4$, via dissolution of $Cr_2O_3$, helps protecting the oxide by forming a positive solubility gradient (see § 3.3.6).

## 5.5.4 Schematic representation of the effect of NaCl deposits exposed to air with $SO_2/SO_3$

The 72 h test can be divided into three periods represented schematically in Figure 5.29. At the beginning, during thermal equilibrium (since no $SO_2$ is injected), NaCl is present (region I). Upon injection of $SO_2/SO_3$, a small amount of NaCl is converted to $Na_2SO_4$ (region II). Finally, as can be seen on the XRD (Figure 5.16), at the end of the test, all the NaCl has been converted to $Na_2SO_4$ or has been vaporised.
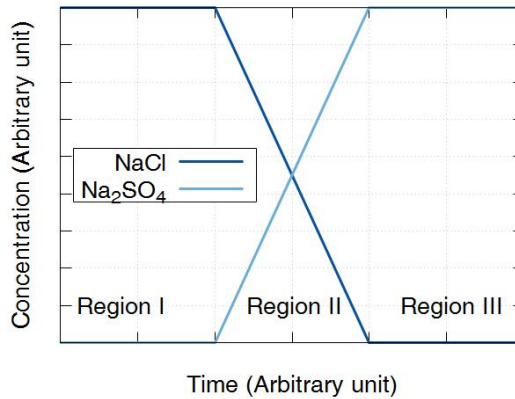
Figure 5.29: Concentration of NaCl and $Na_2SO_4$ against time during the 72 h test at 700 °C

The effect of this environment is therefore a combined effect of the NaCl environment and the $Na_2SO_4$ deposition.
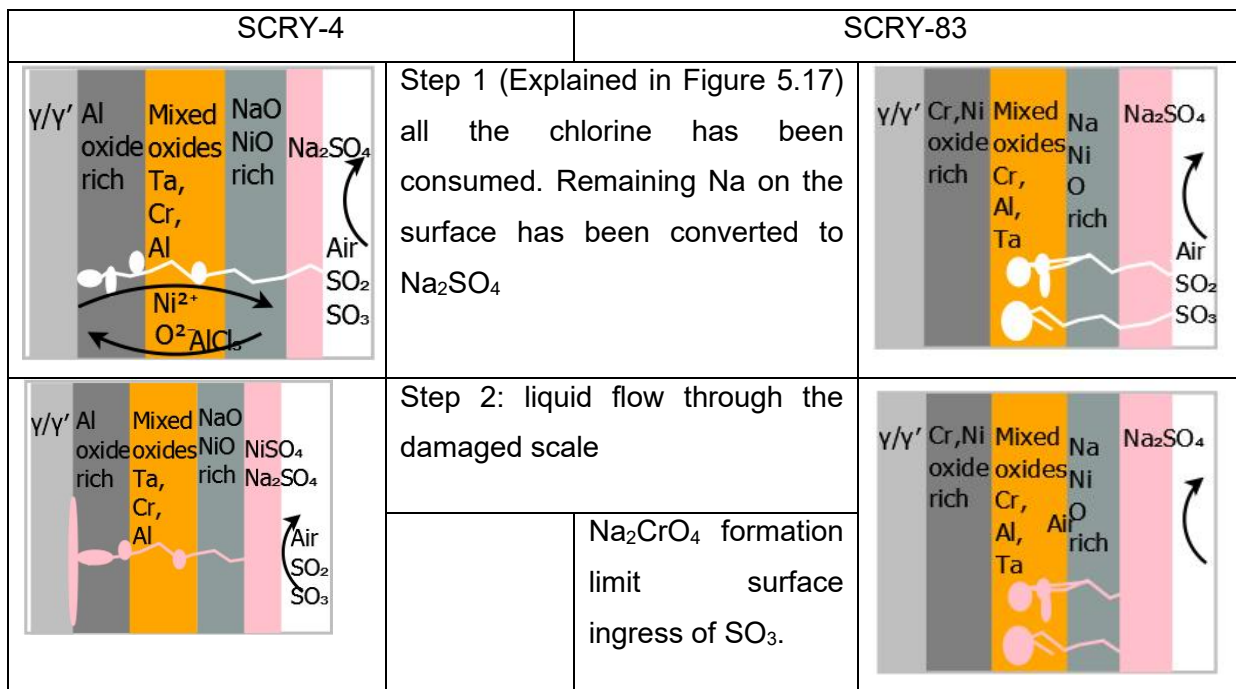
| SCRY-4 | | SCRY-83 |
|---|---|---|
|  | Step 1 (Explained in Figure 5.17) all the chlorine has been consumed. Remaining Na on the surface has been converted to $Na_2SO_4$ |  |
|  | Step 2: liquid flow through the damaged scale |  |
| | $Na_2CrO_4$ formation limit surface ingress of $SO_3$. | |

Figure 5.30: Schematic representation of the effect of samples coated with NaCl and exposed to air and $SO_2/SO_3$ for 72 h at 700 °C

Several authors [55], [60], [91] have reported that NaCl significantly accelerates the corrosion induced by $Na_2SO_4$. This is consistent with the explanation above, in region II the Cl breaks down the scale, promoting the flow of liquid ($Na_2SO_4/NiSO_4$) near the substrate.

Figure 5.31 shows a micrograph from sample C34, indicating preferential attack of the γ channels. This preferential attack was also reported by Lortrakul et al. [94]. Since the γ

channels are rich in refractory elements, this is in-line with the synergistic dissolution explained above.
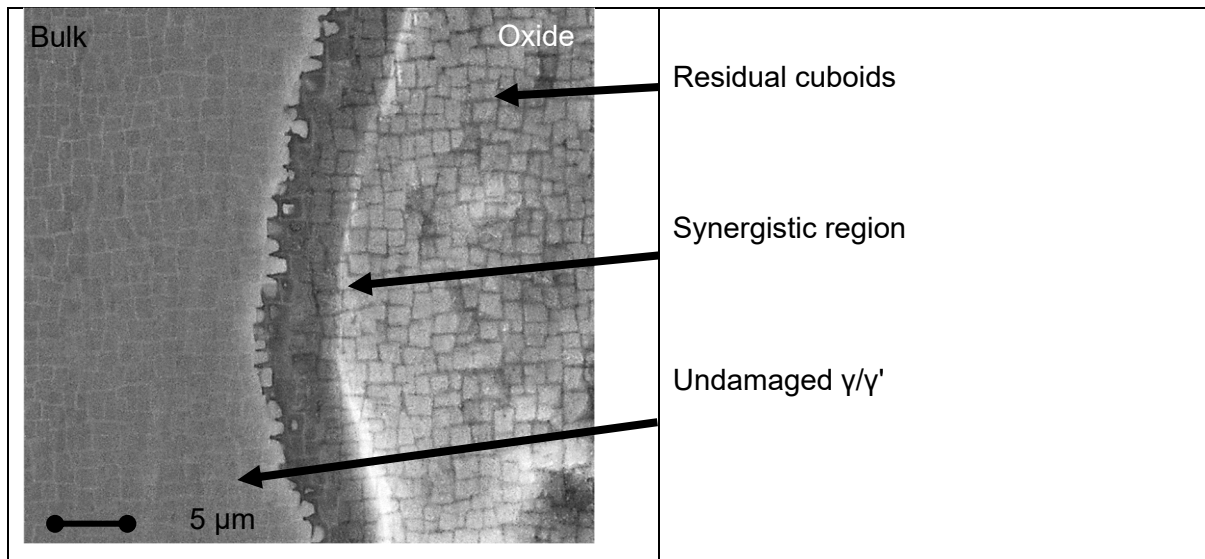


Figure 5.31: Micrograph of the attack of the γ channels on sample C34

## 5.6 Reaction layer thickness and sample mass change

Reaction layer thickness and sample mass change are often used to assess damage in different environment. However, Figure 5.32 shows that there is no correlation between the two parameters. Table 5.5 lists the numerous mechanisms at play in these environments.
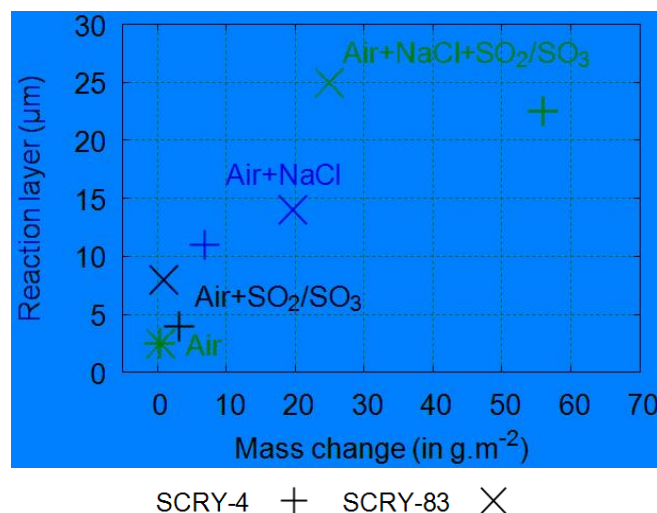


Figure 5.32: Mass change against reaction layer thickness

Mass change measurements are easy and quick to make. However, the complex behaviour when NaCl and $Na_2SO_4$ are present (ie: vaporisation as a function of time temperature and concentration, conversion of NaCl into $Na_2SO_4$) exposes limitations of such measurements.

## 5.7 Summary of the effect of Cr on static environmental exposure

o **As-produced samples**

The XRD spectra of as-produced samples will be used as a reference for the subsequent environments. Porosity was measured with micro-CT (with a resolution of 2 μm / pixel) and a slightly larger porosity was detected for SCRY-83 (compared to SCRY-4), but was found to be very low. It was thought that connected porosity could promote liquid migration.

o **Air**

Both 24 and 72 hours test data show that mass gained by both blade alloys can be approximated to a parabolic behaviour (at 700 °C) and was much lower than a typical disk alloy (RR1000). After 72 h, an oxide-rich layer measuring approximately 2 μm, was formed on both alloys, with NiO detected at the outer-most surfaces. This is in agreement with NiO being a p-type conductor that promotes outward diffusion of cations [27]. In addition, SCRY-4 had an inner-rich Al layer with a small $Al_2O_3$ peak detected via XRD. On the other hand, SCRY-83, had a rich Cr and Ti layer with a mixed oxide ($NiCr_2O_4$) picked-up by XRD.

o **Samples sprayed with NaCl and exposed to air**

Gravimetric study of NaCl is complex since significant vaporisation of the salt occurs above 600 °C. Vapour Cl can also form HCl or $Cl_2$ that further reacts with the alloy to form high partial pressure compounds, such as $AlCl_3$, $NiCl_2$ or $CrCl_2/CrCl_3$.

Formation and evaporation of $AlCl_3$ particularly affected SCRY-4, causing a mass loss. This was accompanied by scale damage, giving open porosities. Not only does this increase the surface area of the alloy (which in turns increased the mass gain), but it also significantly lowers the Al content. The reaction layer displayed two regions, separated by a $Ta_2O_5$ peak, with NiO and $Co_3O_4$ on the outside, and a small amount of $Al_2O_3$ on the inside.

The $Cr_2O_3$-former was affected by the "activated oxidation" that displaced the chromium chloride to the surface, where the higher $O_2$ partial pressure caused Cr to oxidize, thus releasing the Cl. The same Cl was then able to start another cycle, which resulted in increased amount of porous chromium oxide at the surface. Judging solely on the mass loss, it seems the $Cr_2O_3$-former displayed better resistance, however, the depth of scale damaged was equivalent to the SCRY-4. Large amount of NiO and $NiCr_2O_4$ were picked up by XRD with

trace of $NaCr_2O_4$ and $Ta_2O_5$. SEM micrograph showed that a thick Cr layer was formed in the proximity of the substrate.

Finally, traces of liquid were found on the free surface of SCRY-4 and possibly on SCRY-83 that could be a mixture of $NaCl/NiCl_2$, which is liquid above 600 °C (or $CoCl_2/NaCl$, liquid above 380 °C). It is thought that volatile chlorides could damage the scale, allowing liquid phase to flow through, explaining the fast progression of NaCl into the substrate.

○ **Samples exposed to $SO_2/SO_3$**

For the third environment, samples were first exposed to air, and a few hours later to a mixture of air and $SO_2/SO_3$. When removed from the furnace, both samples were indistinguishable from the samples exposed to air only.

However, on the SCRY-4, a large S peak was detected beneath the oxide, and a large mass gain was also measured. This was explained theoretically [65] by the NiO being sulphated to $NiSO_4$, which in turn formed $Ni_3S_2$ (liquid at 700 °C), with an outer layer of NiO.

The $Cr_2O_3$-former alloy had a mass gain nearly identical to air, and S was almost undetected. It is proposed that SCRY-83 formed a dense oxide that prevented the diffusion of S.

○ **Sample sprayed with NaCl and exposed to $SO_2/SO_3$**

In this last synthetic environment, samples were sprayed with NaCl, exposed to air and, a few hours later, to a mixture of air and $SO_2/SO_3$. This environment was therefore initially very similar to the NaCl environment (see above), but with the introduction of $SO_2/SO_3$, typical of hot corrosion Type 2, with the formation of $Na_2SO_4$.

To understand the mechanisms of $Na_2SO_4$ salt, two succinct experiments were realised. In the temperature increasing test, it was found that $Na_2SO_4$ was not very volatile (compared to NaCl) and caused mass increase starting at 550 °C, on the $Al_2O_3$-former. The SCRY-83, in contrast, only displayed mass gain typical of oxide formation. Observation of the free-surface, (after exposure for 24 h at 700 °C) showed evidence of liquid formation on both samples. In conformity with the alloy-induced acidic fluxing theory (§ 3.4.2.2), it was found that pre-oxidation of the $Al_2O_3$-former, prevented the liquid melt from accessing refractories which decreased substantially the interaction with $Na_2SO_4$.

During the 72 h exposure test, the largest weight gain was recorded on the $Al_2O_3$-former. The severity of this environment is explained by the oxide scale breached by NaCl (see above), then followed by $Na_2SO_4$ conversion and liquid formation, identified via XRD as

Na$_2$Ni(SO$_4$)$_2$ (see phase diagram § 9.4.4). The liquid migration was detected by EDX, where a S peak was seen at the edge of the affected γ/γ', beneath the oxide. In agreement with literature [94], it was found that γ channels were attacked first. This is consistent with "synergistic dissolution" and the alloy induced acidification theory, since the γ channels are rich in refractories.

    o   **Reaction layer thickness and sample mass change**

Mass change and reaction layer thickness are often used to assess hot corrosion damage. It was nevertheless found that there is no correlation between the two parameters, and mass change may not be representative of damage (ie: SCRY-83 coated with NaCl).

Now that the static conditions have been reviewed, it follows to investigate the effect of the stress on such environments.

# Chapter 6   Effect of stress and Cr content in environmental exposure of superalloys

The objective of this chapter is to explore whether superimposed mechanical loading affects the degradation reported in Chapter 5.

## 6.1   Induced stress field in the sample

An orthotropic elastic finite element model was built in Abaqus to investigate the stress field experienced by the sample, as a function of the applied force.

### 6.1.1 FE model

The model parameters are provided in § 4.5. Figure 6.1 shows the full-beam, modelled with the two symmetry planes. As can be seen, only a quarter of the beam was modelled.
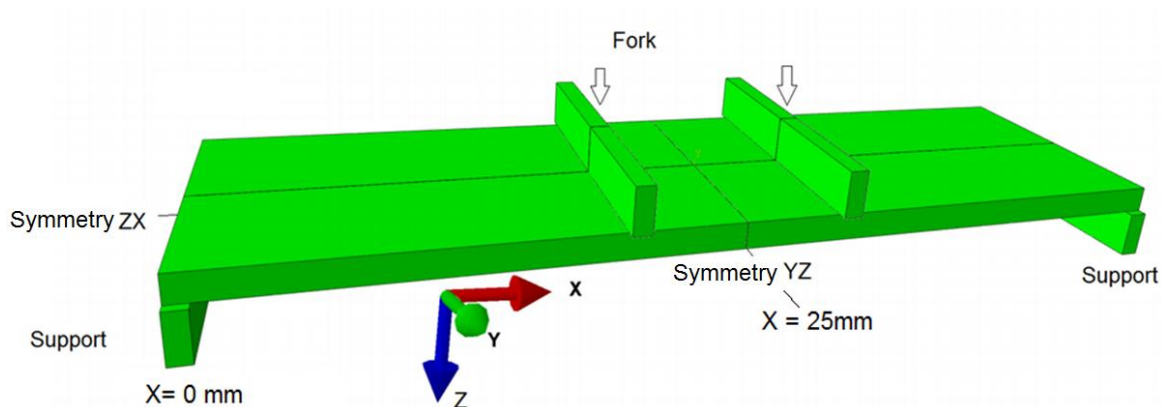


Figure 6.1: Geometry of the FE model

The material orientation was specified with <001> parallel to the X, Y and Z axes (although, as seen later a small misorientation was noted).

## 6.1.2 FE results



(a) View ZX showing $\sigma_{xx}$

(b) Isometric view showing $\sigma_{VM}$ (with mesh visible)

(c1) Bottom view of loading point (onset with support) showing $\sigma_{xz}$

(c2) Top view of the beam loading point (onset with fork) showing $\sigma_{xz}$

(d1) Bottom view of support/beam interface showing $\sigma_{zz}$

(d2) Top view of fork/beam interface showing $\sigma_{zz}$
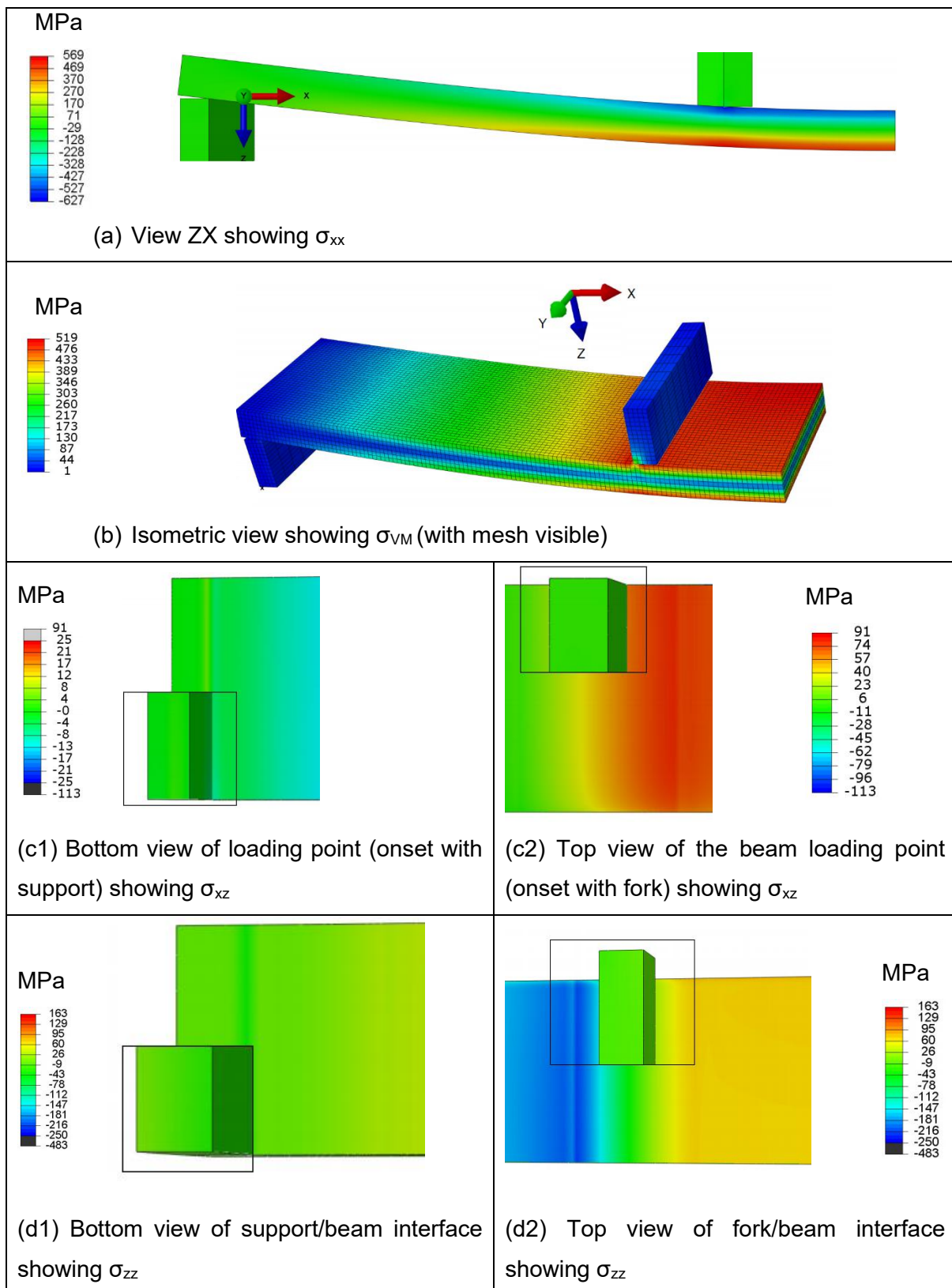
Figure 6.2: Visualisation of FEM predicted stress fields, for an applied force of 300N

The effect of a change in vertical force was also investigated and the results are displayed in Figure 6.3.
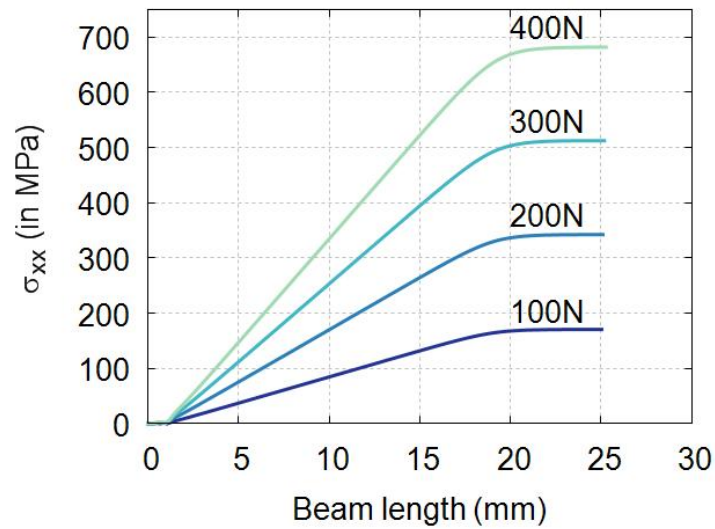


Figure 6.3: Tensile stress on the bottom surface of the sample as a function of actuator force for a beam of 1.5 mm thick

With these FE results in hands, an investigation of the effect of the environment on samples under stress can be performed.

## 6.2 Sample sprayed with NaCl and exposed to air

The test conditions are summarised in Table 4.4.

### 6.2.1 Mass change

Table 6.1: Mass change of samples sprayed with NaCl and exposed to air at 700 °C for 72 h with an applied load of 200 N

| Material | Sample# | NaCl coating (g.m$^{-2}$) | Specific mass change (g.m$^{-2}$) |
|----------|---------|---------------------------|-----------------------------------|
| SCRY-4 | C36 | 24.5 | 27.53 |
| SCRY-83 | E14 | 25.5 | 21.21 |

For the $Al_2O_3$-former, the sample suffered a mass increase instead of losing mass like the case without force ($\Delta m$=-17.92 g m$^{-2}$). This may be caused by a larger oxidized area.

For the SCRY-83, a lower mass loss is recorded in the case with force but remains very close (§ 5.3.1.3  $\Delta m$=19.67 g m$^{-2}$ compared with $\Delta m$=21.21 g m$^{-2}$).

## 6.2.2 Reaction layer microstructure
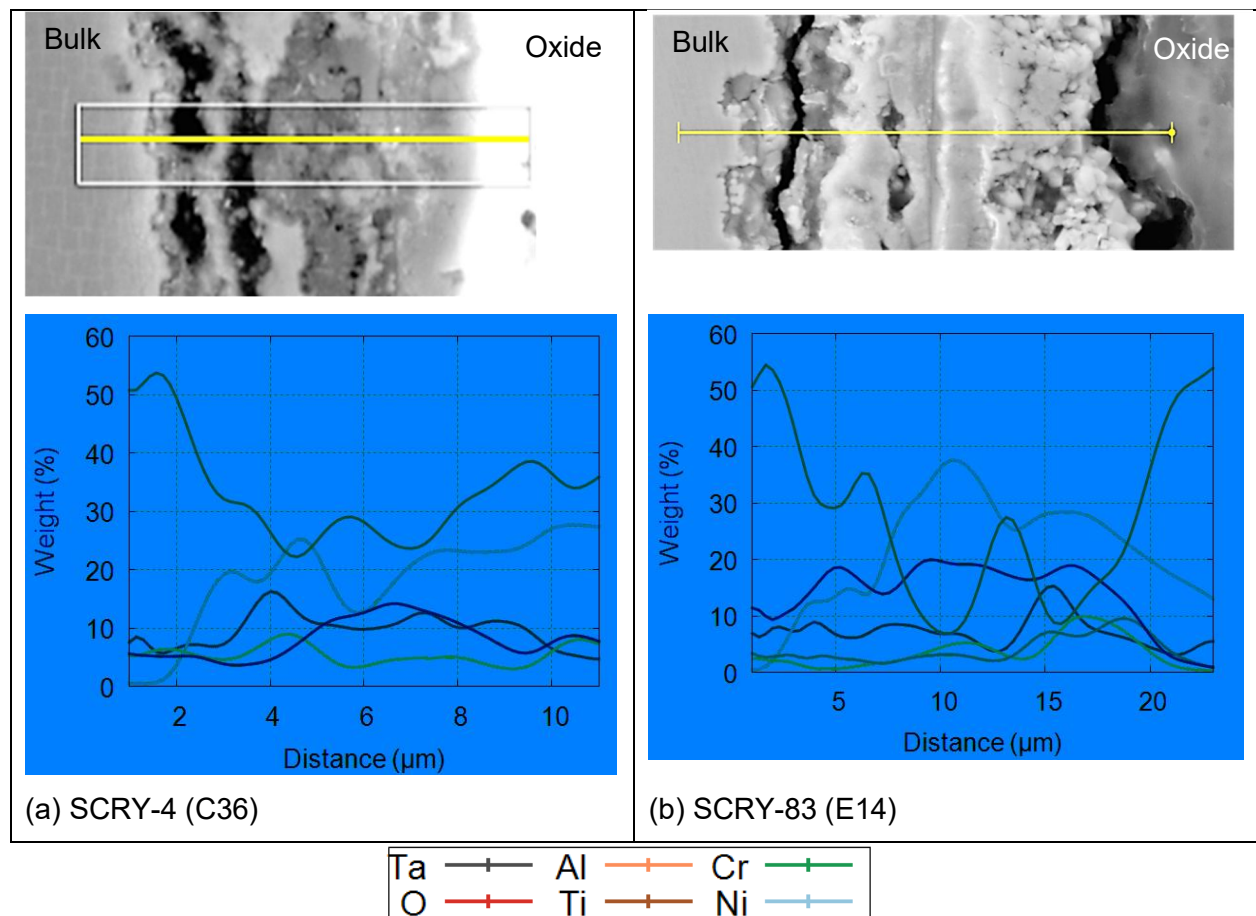


Figure 6.4: EDX composition profiles of samples sprayed with NaCl and exposed to air with superimposed force

The effect of force can be examined by comparing Figure 6.4 with Figure 5.15 (no load).

Figure 6.4 (a) also presents a Ta peak delimitating an inner region depleted in Ni, and an outer region rich in Ni. Contrary to the case without force, more alloying elements are found in the outer region. The large Cr peak has not stopped the diffusion of O throughout the scale and it is possible that the mechanism of "activated oxidation" has taken place. The Al concentration remains low (below 10 wt %) throughout the scale, also attesting the volatilisation as $AlCl_3$. Visually, the micrograph shows a heterogeneous layer that seems crumbly.

Figure 6.4 (b) also displays two regions that can be separated by the Ta peak. The inner region has O-rich peak, matching with the initial sample surface, seen on the micrograph above. Compared with the case without force, the scale is slightly thicker, but more importantly delamination from the substrate (at 5 μm) is seen.

## 6.2.3 XRD Spectra and phase identification
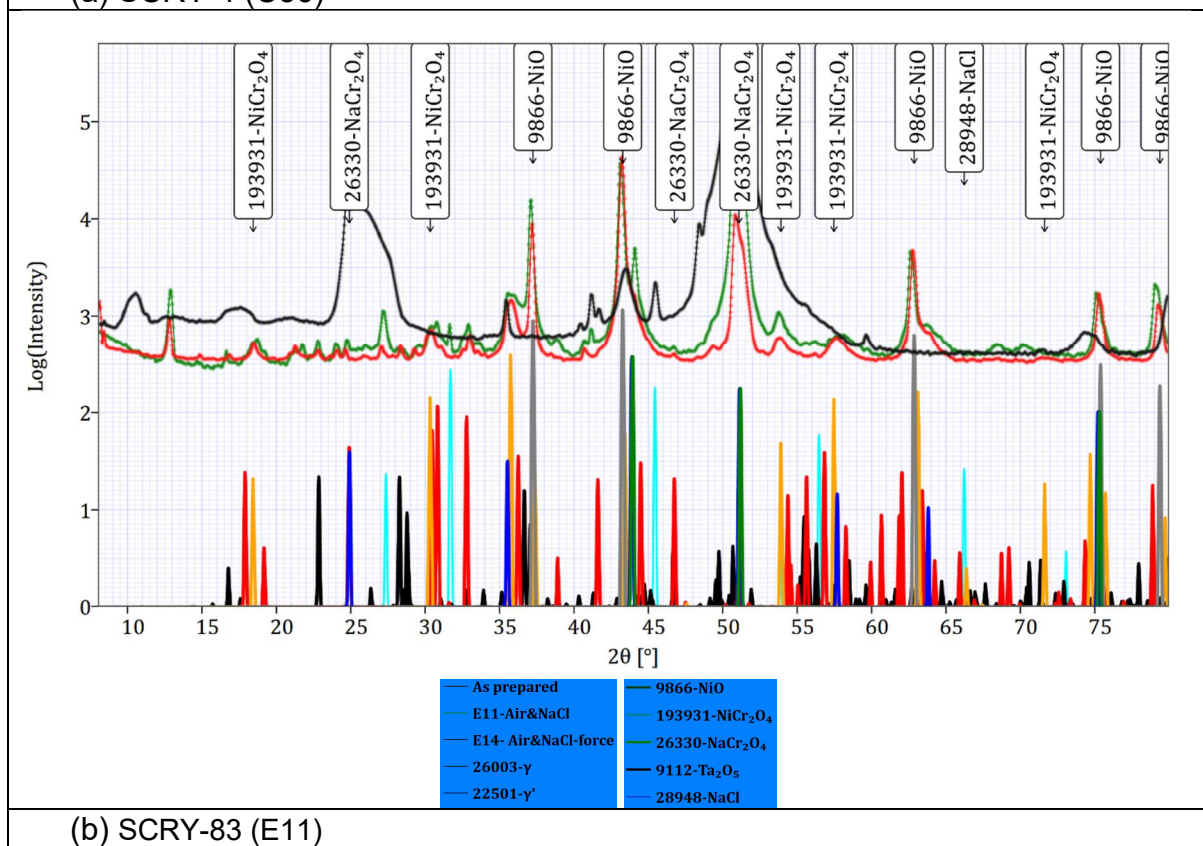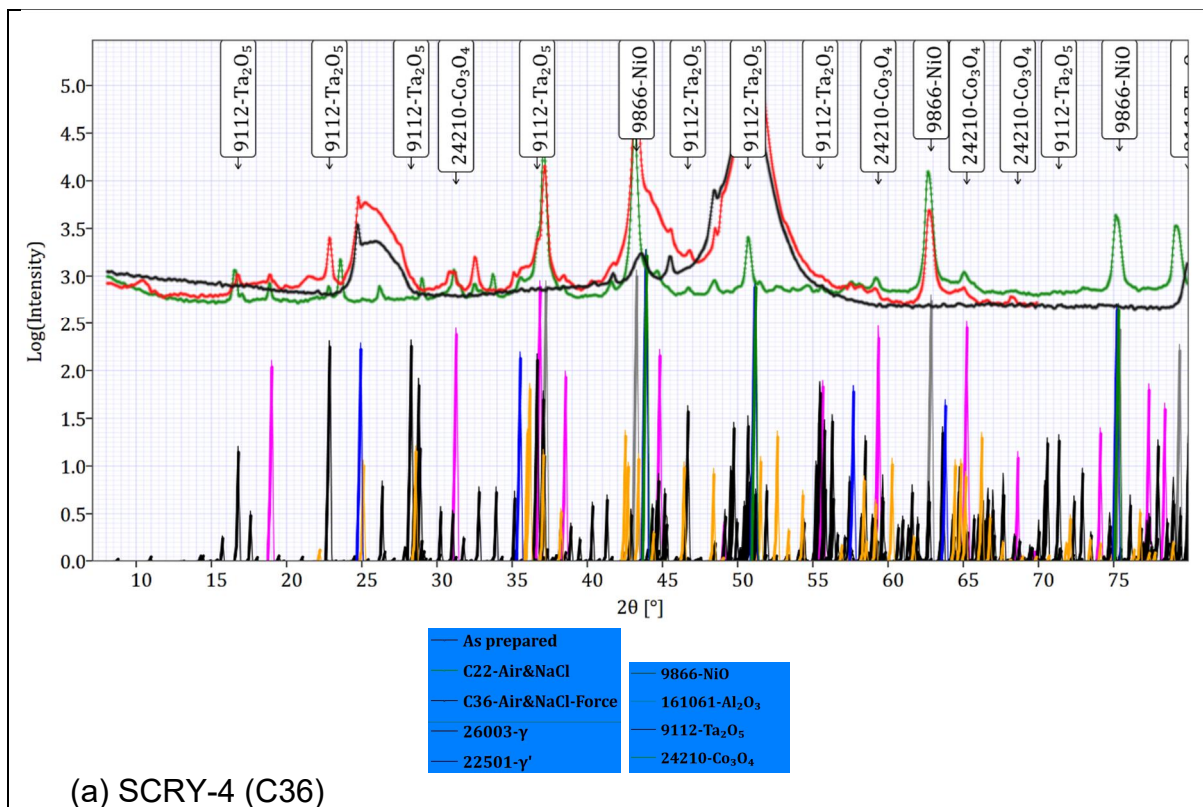


Figure 6.5: Phase identification with XRD spectra for samples sprayed with NaCl and exposed to air, at 700 °C, for 72 h

To facilitate the comparison, XRD spectra with load (green curves) and no load (red curves) are shown in Figure 6.5.

For SCRY-4, the two XRD spectra share the same peaks, however the intensity of the [001] and [002] γ' peaks have decreased substantially with the superimposed force.

For SCRY-83, surprisingly, NaCl was detected at the surface (matching low and medium angle), except that, the two spectra are very similar both in peaks and intensity.

## 6.3 Sample exposed to air and $SO_2/SO_3$ gases

### 6.3.1 Mass change

Table 6.2: Weight change of samples exposed to air and $SO_2/SO_3$ gases at 700 °C for 72 h with force of ~300 N

| Material | Sample# | Specific weight gain (g.m$^{-2}$) |
|----------|---------|-----------------------------------|
| SCRY-4   | C37     | 3.87                              |
| SCRY-83  | E12     | 3.53                              |

By comparing the sample exposed in similar environments with and without load, it highlights a minor increase for SCRY-4 (§ 5.4.1 Δm=3.02 g m$^{-2}$ compared with Δm=3.87 g m$^{-2}$) and a substantial increase for SCRY-83, (§ 5.4.1 Δm=0.945 g m$^{-2}$ compared with Δm=3.53 g m$^{-2}$).

## 6.3.2 Reaction layer microstructure
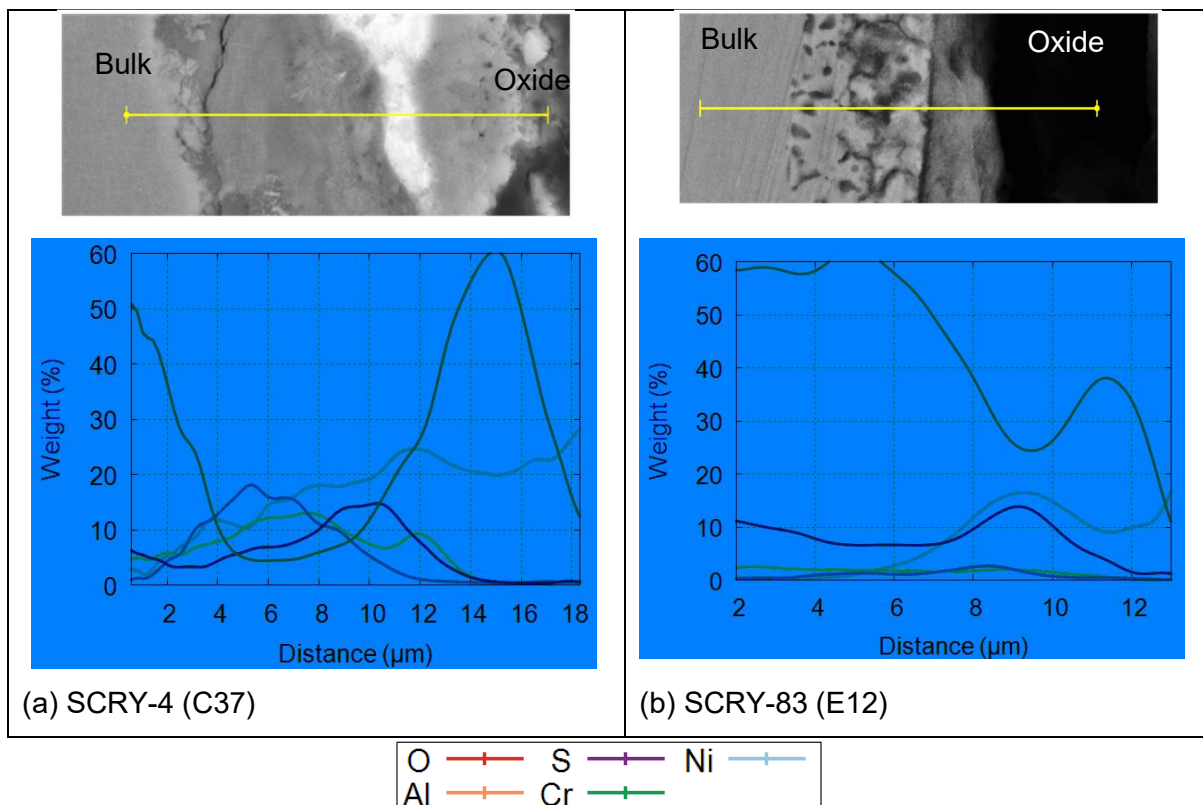


Figure 6.6: EDX composition profiles of samples exposed to air and sulphur with superimposed force

Similarly to the comparison above, the effect of force can be examined by comparing Figure 6.6 with Figure 5.19 (no load).

For SCRY-4, in Figure 6.6 (a), beneath the Al and Cr oxides peaks are found an astounding amount of ~ 20 wt % of S. It is thought that the Cr and Al oxides were not protective and did not stop the migration of S. In addition, the reaction layer is much thicker (5 μm against 18 μm with force).

For SCRY-83, the large Cr and O peaks are preceded by a S peak. The scale is also thicker in the case with force, probably explaining the larger mass gain of Table 6.2.

## 6.3.3 XRD Spectra and phase identification



(a) SCRY-4 (C37)



(b) SCRY-83 (E12)
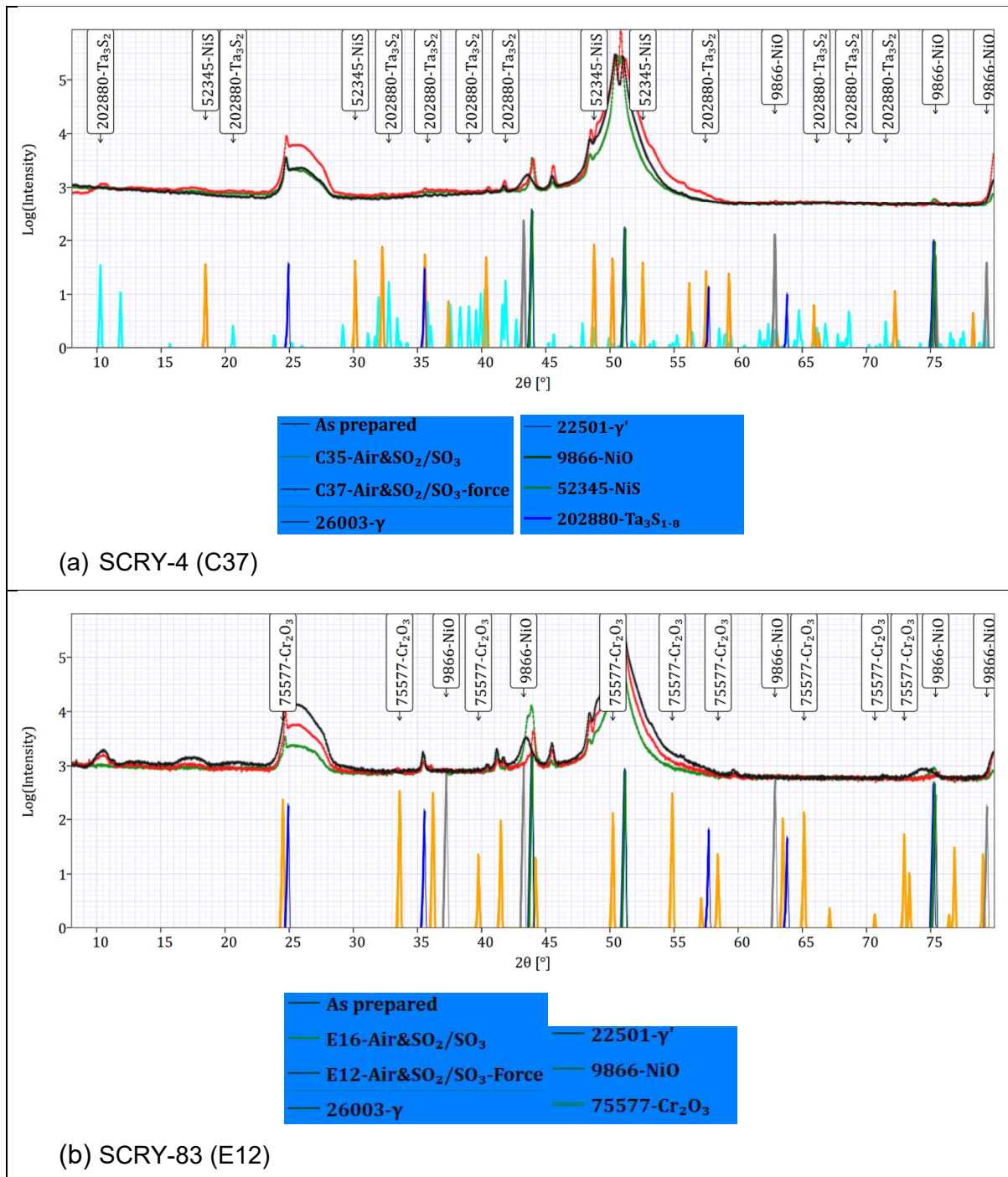
Figure 6.7: Phase identification with XRD spectra for samples exposed to air and $SO_2/SO_3$ at 700°C, for 72h with superimposed force

The comparison between the cases with and without force (green and red curves respectively) shows identical location of peaks with similar intensity.

# 6.4 Sample sprayed with NaCl and exposed to air and SO$_2$/SO$_3$ gases

## 6.4.1 Mass change

Table 6.3: Weight change of NaCl sprayed samples exposed to air and SO$_2$/SO$_3$ gases at 700 °C for 72 h with force of ~300 N

| Material | Sample# | NaCl coating (g.m$^{-2}$) | Specific weight gain (g.m$^{-2}$) |
|---|---|---|---|
| SCRY-4 | C33 | 25.4 | 48.9 |
| SCRY-83 | E18 | 26.4 | 37.2 |

The comparison of mass change with and without force (Table 6.3 vs Table 5.4) shows a slightly lower mass change for SCRY-4 ($\Delta m$=55.91 g m$^{-2}$ without force) and a slightly larger one for SCRY-83 ($\Delta m$=25.03 g m$^{-2}$ without force). These changes remain of the same magnitude, and variability in the tests may have created small differences.

## 6.4.2 Reaction layer microstructure
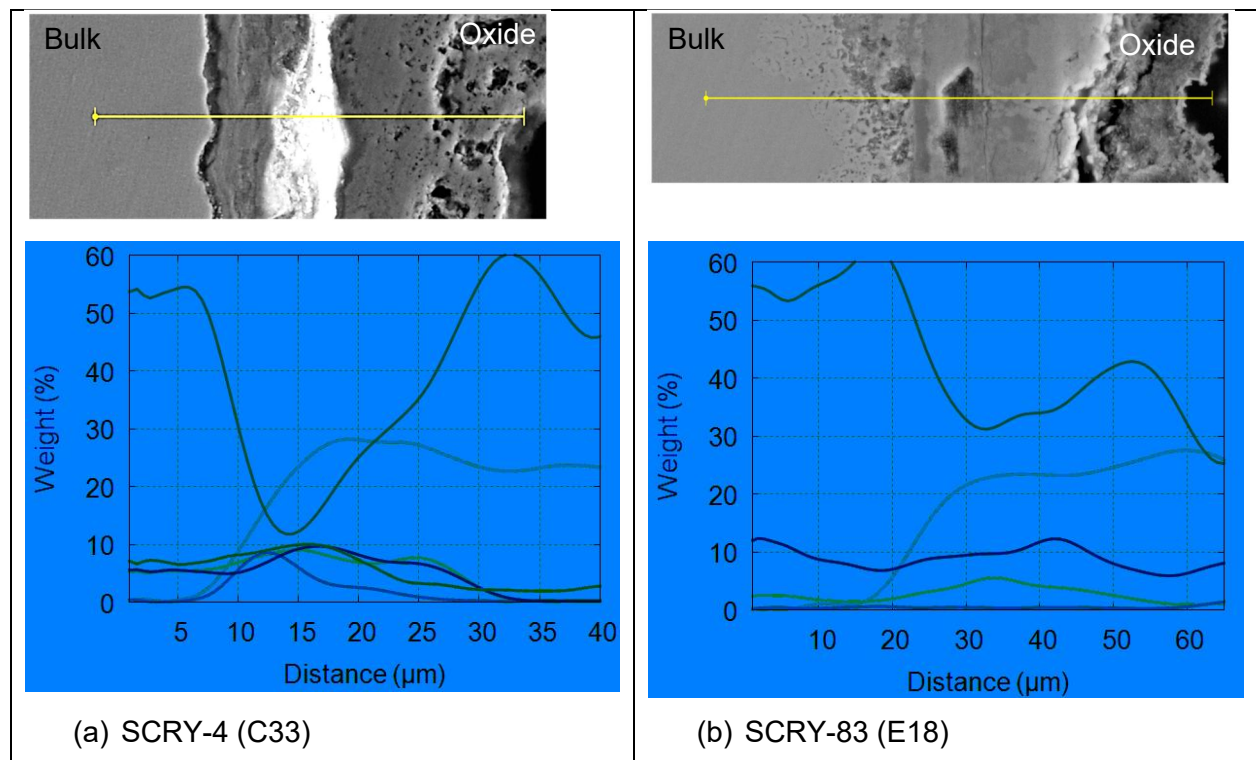


Figure 6.8: EDX composition profiles of samples sprayed with NaCl and exposed to air and $SO_2/SO_3$, with superimposed force of 300 N

Similarly to the comparison above, the effect of force can be examined by comparing Figure 6.8 with Figure 5.27 (no load).

The EDX profile composition in Figure 6.8 (a) shows an identical arrangement of the layers to the one without force. The differences between the two cases are a larger region containing S and a scale which is thicker than without force. Tensile regions were also screened for cracks and pits. Two cracks were found in the sample C33 (displayed in Figure 6.9). Cracks were located 5 mm away from the mid-section of the beam, with one crack measuring 57 μm, and one measuring 8 μm.
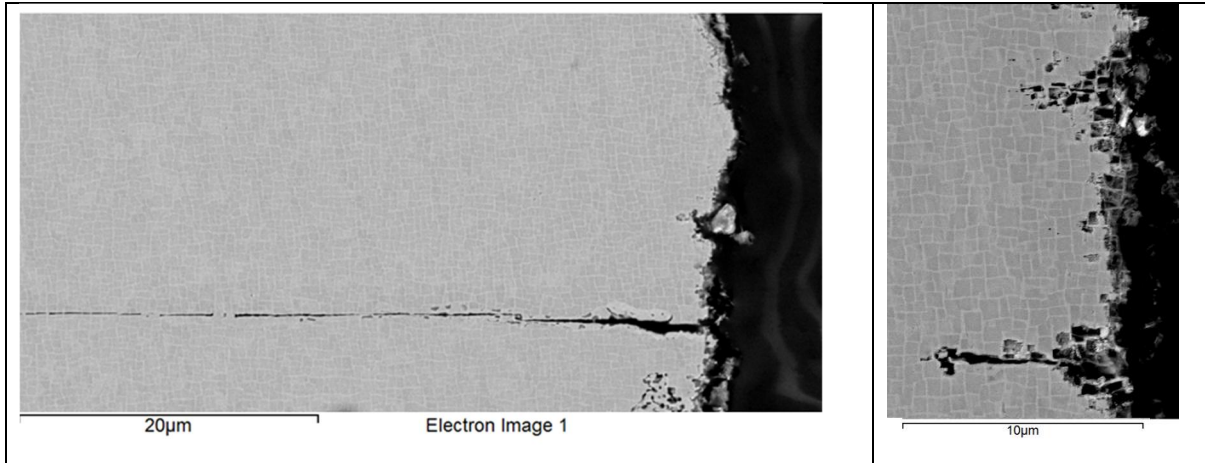
Figure 6.9: Back scatter image of cracks found on sample made of SCRY-4 (C33) sprayed with NaCl and exposed to air+$SO_2$/$SO_3$ with $SO_x$ average concentration: 369 ppmw, 72 h, 700 °C with a maximum tensile stress of 528 MPa. (SEM Acceleration Voltage 10kV dwell 10 μs)

The EDX composition profile in Figure 6.8 (b) was found also equivalent to the one without force. Differences between the two cases arise once again, on the thickness and on the Cr concentration which is almost halved in the case with force. In addition, an inner region, located at the interface of the substrate/oxide was found with voids (see Figure 6.10). No cracks and only trace of sulphur was found (<1 wt%), but these changes are likely to cause some impairment in the load-bearing capability of the alloy.
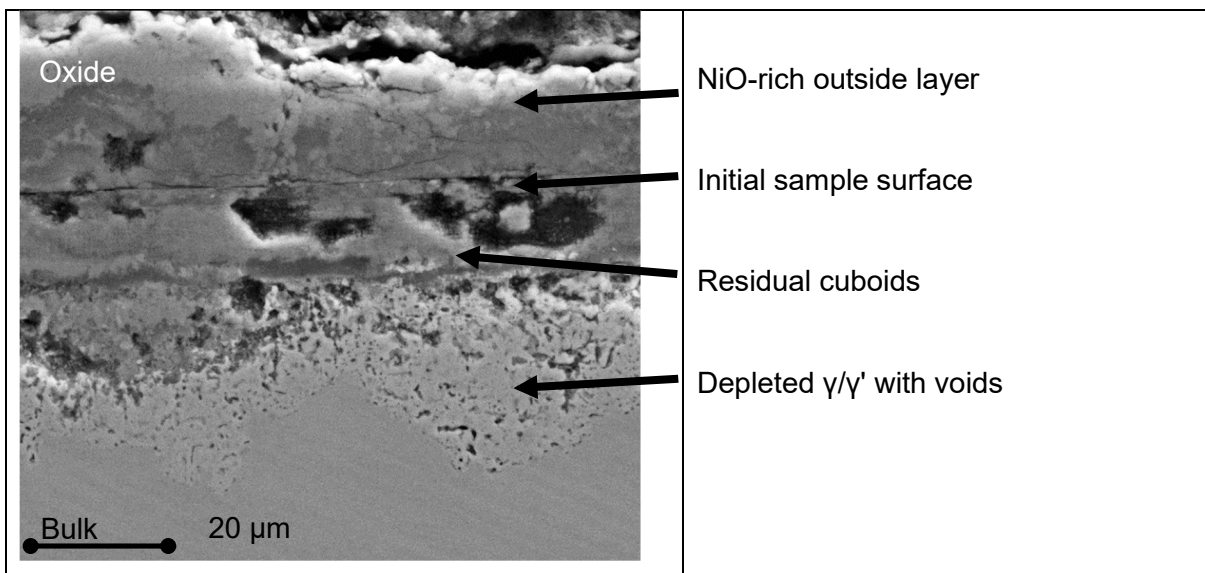


Figure 6.10: Secondary electron image of sample E18, made of SCRY-83 and sprayed with NaCl and exposed to air+$SO_2$/$SO_3$ with $SO_x$ average concentration:1232 ppmw, 72 h, 700 °C with a maximum tensile stress of 545 MPa. (SEM Acceleration Voltage 10kV dwell 10 μs)

## 6.4.3 XRD Spectra and phase identification



(a) SCRY-4 (C33)

(b) SCRY-83 (E18)
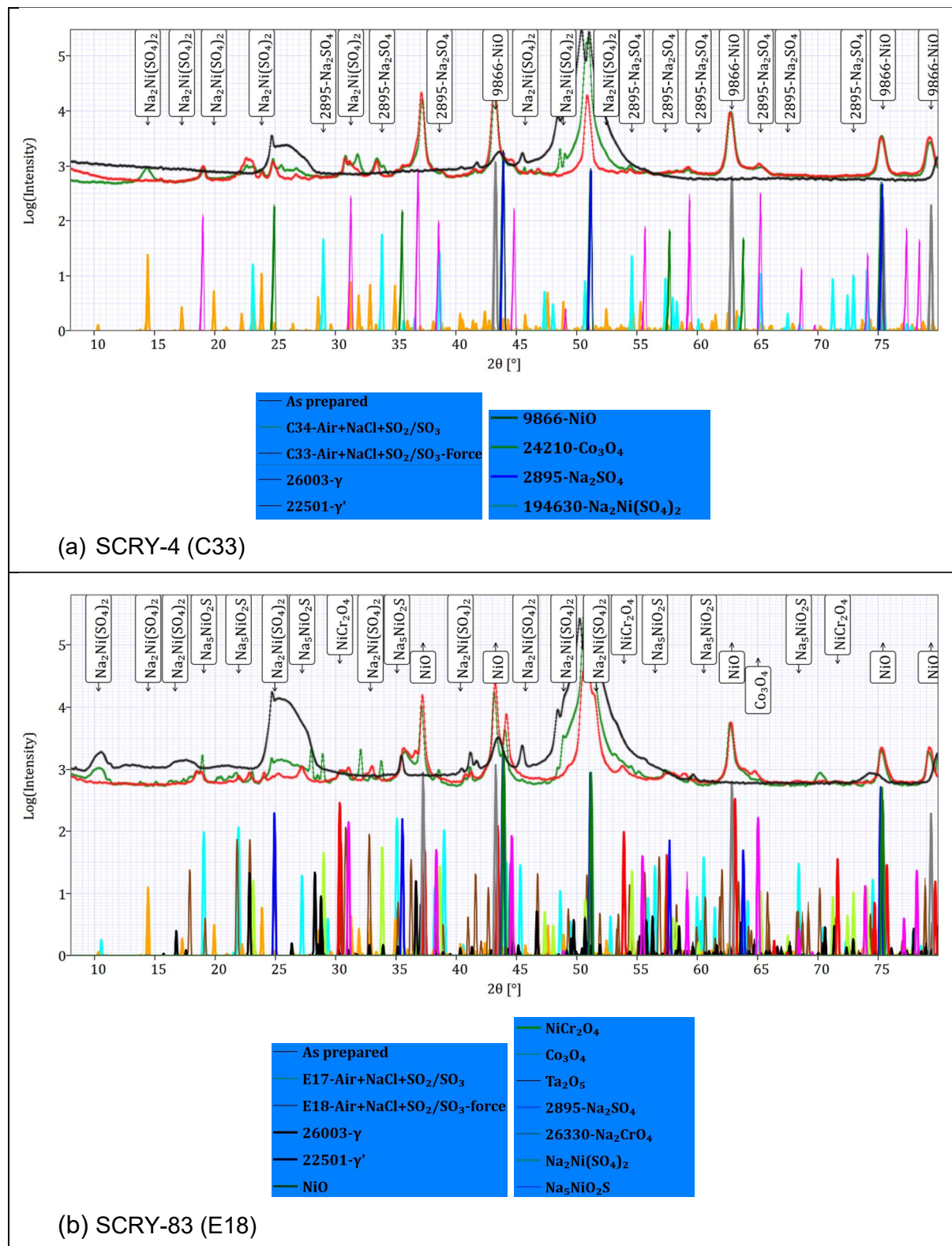
Figure 6.11: Phase identification with XRD spectra for samples sprayed with NaCl and exposed to air and $SO_2/SO_3$ at 700 °C, for 72 h with superimposed force

Comparison between spectra with and without force (green and red curves respectively) in Figure 6.11 reveals some changes at low angle, but almost identical peaks above $2\theta=35°$.

For SCRY-4, in Figure 6.11 (a), the sample with force has peaks of higher intensity matching the $Na_2Ni(SO_4)_2$ compound. Undeniably, the introduction of force has helped the flow of liquid species propagate.

For SCRY-83, in Figure 6.11 (b), at low angle, the sample with force has peaks matching $Na_5NiO_2S$ with higher intensity than without force ($2\theta=18.9°$). As explained in § 5.5.3, the ratio of Na to Ni for this compound is further away from the eutectic point. Moreover, $Na_2SO_4$ has also peaks of high intensity ($2\theta=29.0°$). Both points suggest that liquid phase did not occur superficially. However, the presence of a major peak of $Na_2Ni(SO_4)_2$ at $2\theta=32.0°$ confirms the presence of the liquid close to the substrate.

## 6.5 Alternative and novel methods to assess environment damage with superimposed force

### 6.5.1 In-situ degradation

The assessment of the degradation, caused by the environment is valuable since it can lead to removal of rotating components prior to failure. A distinction can be made between surface degradation and through-thickness degradation.

#### *6.5.1.1 Surface degradation*

Vasantasree and Hocking [96] observed corrosion microstructures and cross-checked using electron probe microanalysis. When they exposed a Ni-20%Cr alloy to a 2:1 mixture of $SO_2/O_2$ at 705 °C [95], they found a range of light and dark grey layers, which were identify as NiO-NiS eutectic. They also identified a green-tinted layer as being nickel oxide.

An approach focused on surface changes during the test was used. This was done using a digital camera, programmed to take a picture every hour (as explained in § 4.3.3.2). Figure 6.12 show the pictures of the first and last hour of the test (95 h for (a) & (b) and 72 h for (c). Obvious visual changes are noted.
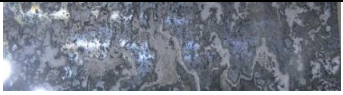
| 1st hour | | | |
|---|---|---|---|
| End of test picture | | | |
| 1 mm ▬ | (a) SCRY-4 NaCl +71ppmw $SO_2/SO_3$ and 300 N at 613 °C (C18) | (b) SCRY-83 NaCl +711ppmw $SO_2/SO_3$ and 333 N at 640 °C (E8) | (c) SCRY-4 NaCl and 300 N at 613 °C (C5) |

Figure 6.12: Picture of first and 95 h of the sample surface

Green and dark grey pixels were automatically counted in the pictures. Figure 6.13 shows the count against time. It is observed that, when the $SO_2/SO_3$ was injected, NaCl (white) became converted to $Na_2SO_4$, which is much darker (grey), and consequently the NiO, already formed also became much darker, confirming the formation of eutectic (previously described, see Figure 5.26).

For the control sample (c), a rapid surface change occurred between 0–3 h, which remained stable (small decrease is due to the condensation on the quartz windows).

Although this technique remains in its infancy, it allows an evaluation of the surface kinetic that were found to be rather quick (between 5 and 10h for a 5 cm strip). The condensation and the LED reflection on the quartz windows were sometimes found to affect the pixel count, and more reliable technique may be needed.
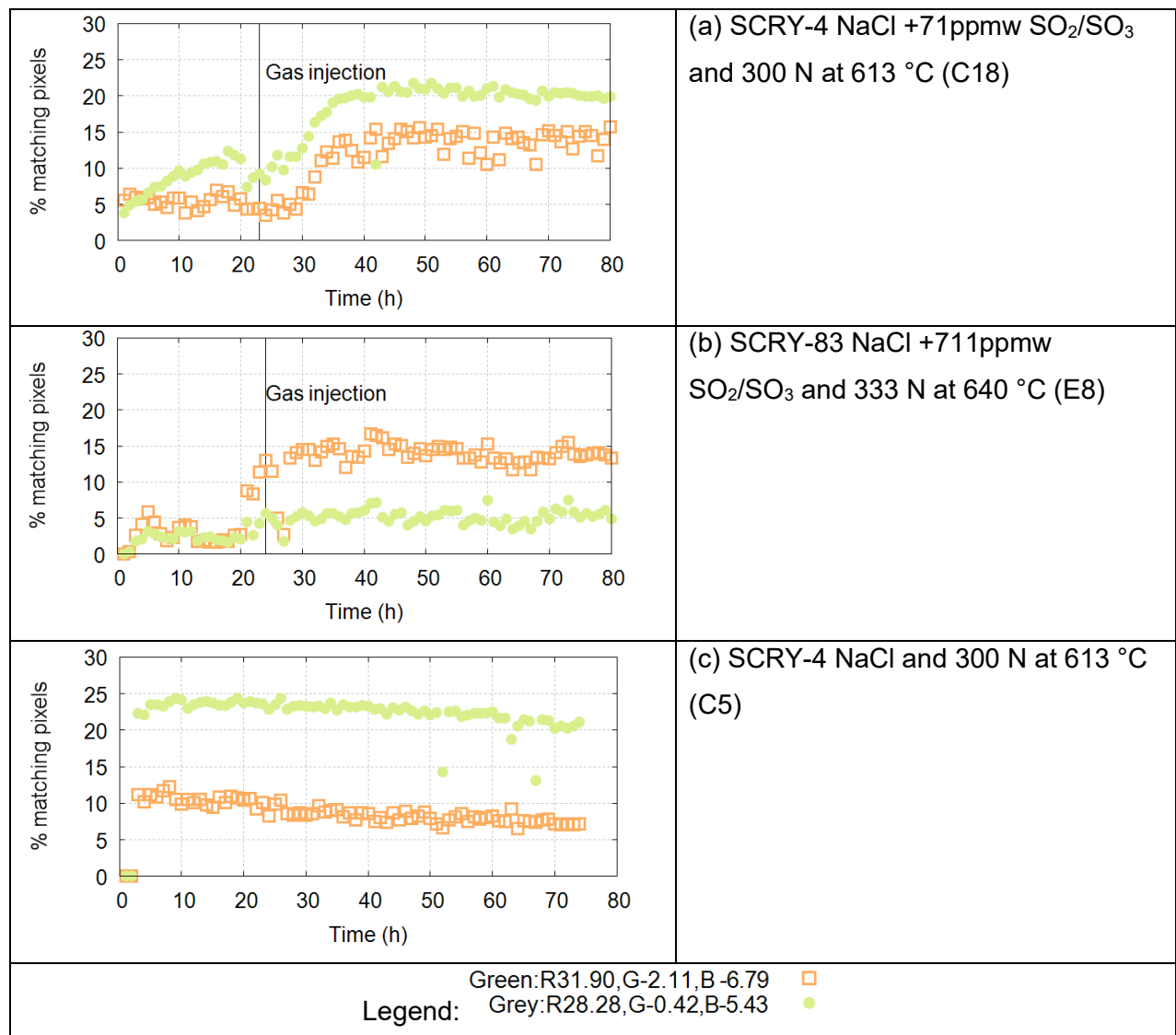


Figure 6.13: Identification of green and grey pixel across different sample at 700 °C

## 6.5.1.2 Through-thickness degradation rate

The degradation rate of the beam was assessed through changes in the displacement during the test (since the load was constant) and through beam compliance (by loading/unloading).

### 6.5.1.2.1 _Displacement in load control set-up_

Only samples exposed to aggressive environments (sprayed with NaCl and exposed to $SO_2/SO_3$) for a long time, had cracked sufficiently to cause a change in vertical displacement. Details on the test condition are copied in Table 6.4. The displacement with time are shown in Figure 6.14.

Table 6.4: Test conditions for the samples assessed with displacement monitoring method

| Name | Sample temp (°C) | SO₂+SO₃ (ppmw) | Force (N) | Sea salt (mg/cm²) | Time (h) | Specific weight change (g/m²) |
|------|------------------|----------------|-----------|-------------------|----------|-------------------------------|
| C42 | 700 | 362.8 | 277 | 2.65&2.54 | 168 | 89.69 |
| C11 |  | ~400 | 300 | ~2.5&2.5 | 120 | ? |

The rate of displacement was fitted to a linear relationship (starting after the incubation period, determined graphically: 28h for C11 and 75h for C42). C11 had a displacement rate of 3.76 μm h$^{-1}$, while C42 had one of 0.81 μm h$^{-1}$. Sample C11 had a higher concentration of $SO_2/SO_3$, which explains the higher displacement rate.
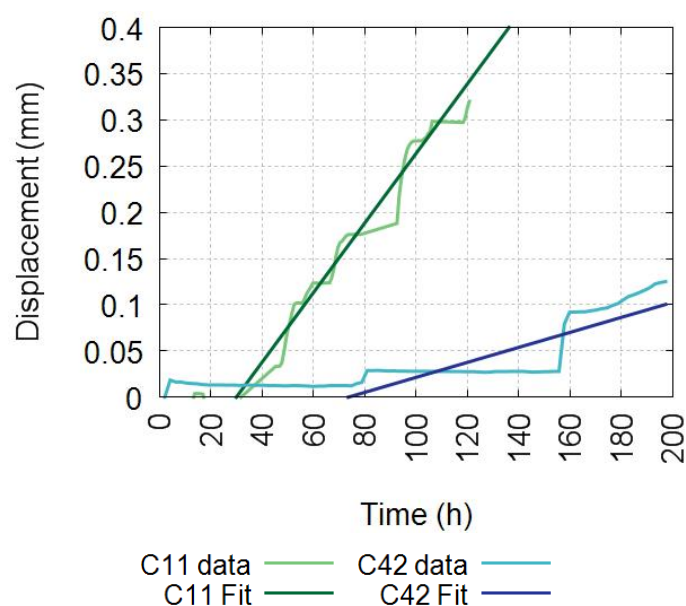


Figure 6.14: Displacement (δ) data against time for 2 samples sprayed with salt and exposed to air and $SO_2/SO_3$ at 700 °C

For aggressive environments, the displacement monitoring technique (which does not require any specific loading/unloading) provided some information indicative of the integrity of the sample.

### 6.5.1.2.2 *Beam stiffness change*

The measurement of beam stiffness during the test (of which the procedure is detailed in § 4.3.3.3) provided another source of in-situ data, relating to the subsurface integrity of the sample. For this application, a set of samples sprayed with NaCl had a varying amount of $SO_2/SO_3$.

The beam stiffness value $\Sigma$ (measured in N mm$^{-1}$) was calculated with Equation 4.6. The values were compared to the first measurement (initial stiffness) and the evolution with time is displayed in Figure 6.15.



$\times$ SCRY-4 613°C 511MPa SO$_x$=72 ppmw (C18)

$\ast$ SCRY-4 645°C 341MPa SO$_x$=267 ppmw (C25)

$\square$ SCRY-4 692°C 682MPa SO$_x$=0 ppmw (C13)

$\triangle$ SCRY-83 645°C 341MPa SO$_x$=375 ppmw (E4)
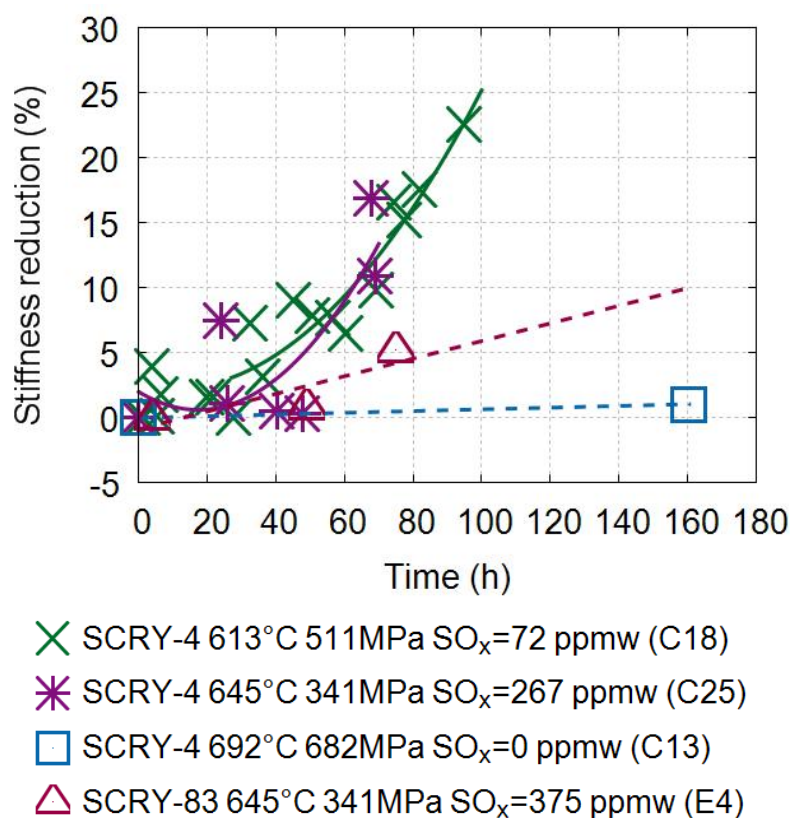
Figure 6.15: Change in beam stiffness against time for samples sprayed with salt and exposed to air and SO$_2$/SO$_3$ at 700 °C

In the absence of SO$_2$/SO$_3$ gases (C13), or for the high Cr material and a relatively low concentration (E4), a relatively small change of compliance was observed. On the other hand, with low Cr content and high SO$_2$/SO$_3$ values, the compliance changed quickly.

The observation of the beam cross-section under SEM (§ 6.5.3) confirmed that samples C18 and C25 had many cracks. Samples E4 and C13 did not suffer any cracks.

A drawback of this method is that loading/unloading cycles were found to promote further degradation. Sample C18 had several stiffness measurements taken (3 for each point) and

this was found to increase significantly the number of cracks (compared to a sample under the same conditions, without stiffness measurement).

## 6.5.2 Post-test mechanical testing

After XRD acquisition, samples were cut in two (longitudinally) and mounted in conductive cold mount resin (for cross-section observation with SEM, discussed below in § 6.5.3). The remaining half was cut into a dog-bone shaped specimen (see procedure § 4.4.6). These were then mounted in grips (drawing available in appendix § 9.6.2) and tensile tested at ambient temperature.

### *6.5.2.1     Tensile tests results for SCRY-4 samples*

Unfortunately, when testing the sample exposed to air and $SO_2/SO_3$ without force (C35), it failed inside the grip (because the axial pin was too close from the sample edge). A second sample was made and tested to replace it (C38).

The shapes of the stress-strain curves, shown in Figure 6.16, need explanation. After the yield point, it first exhibits a region that is relatively flat, followed by a second region, with a much higher work-hardening rate. This is, in fact, typical of single crystals, within the first region, the activation of just a single slip system with the highest Schmid factor. Dislocations glide solely on the slip plane and in the slip direction concerned ("easy-glide"). However, this deformation causes rotation of the crystal relative to the tensile axis and eventually the Schmid factor for at least one other slip system reaches that of the primary system. In the second region, dislocations on different slip systems interact with each other, creating jogs and tangles requiring increasing levels of applied stress for deformation to continue.
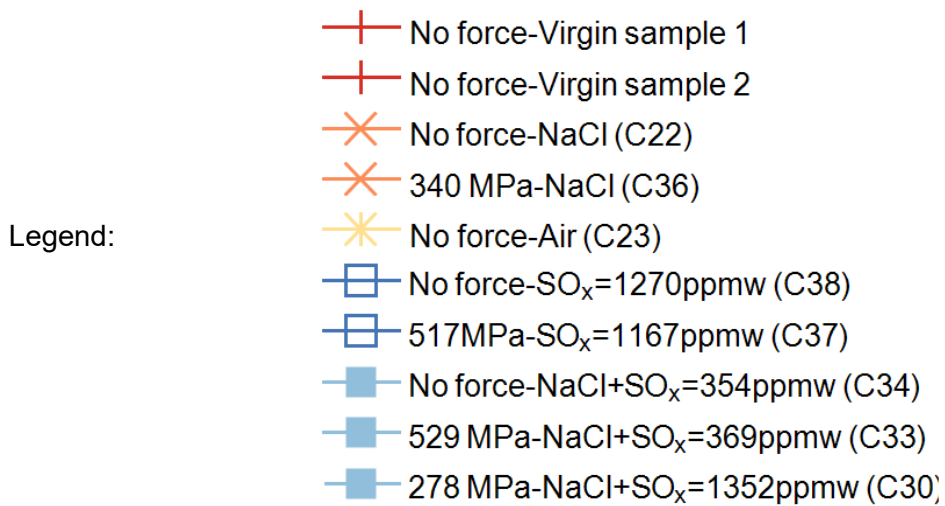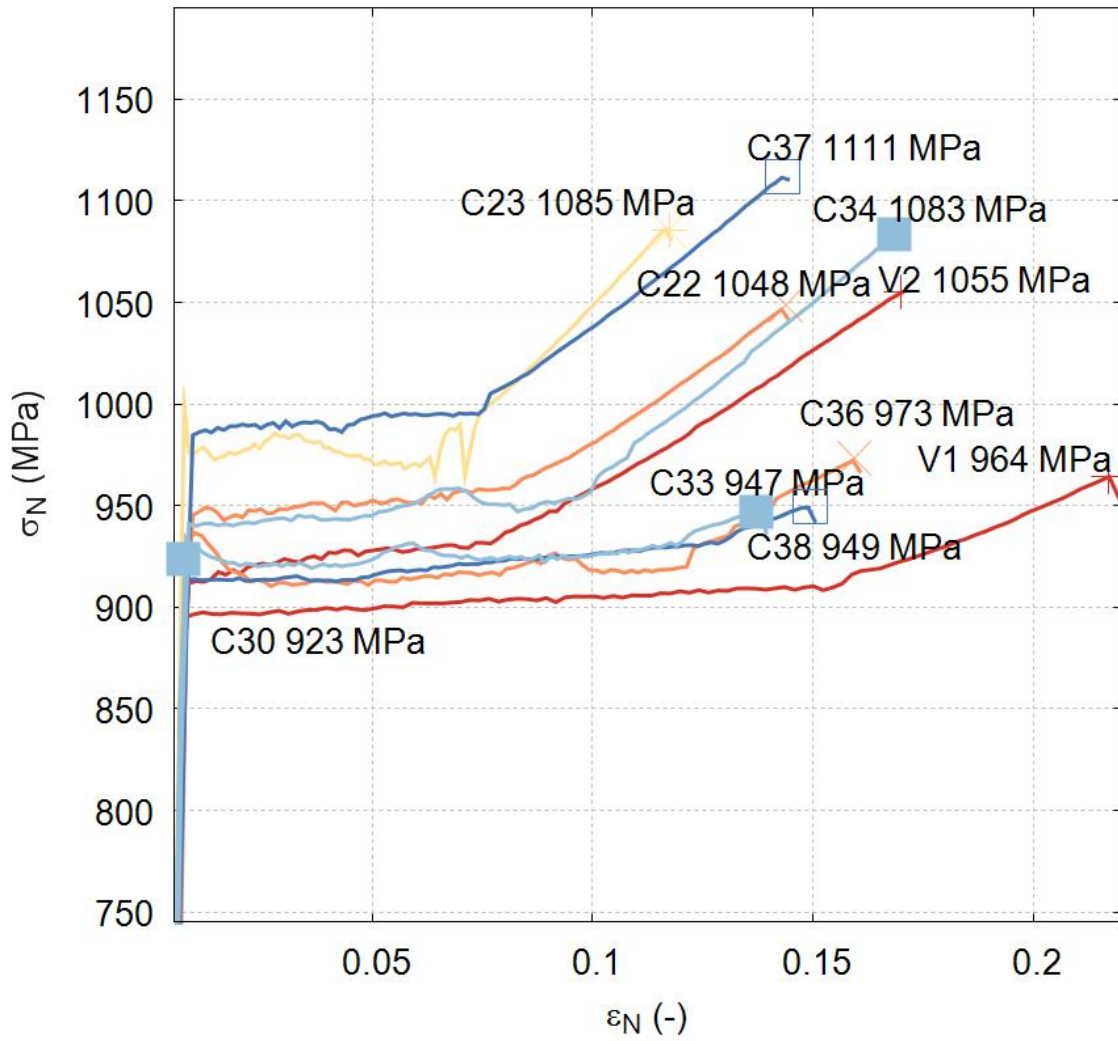
Figure 6.16: SCRY-4 tensile test stress-strain curves

### 6.5.2.2 Stress-strain data for SCRY-4 samples

Table 6.5 was extracted from Figure 6.16. The misorientation was measured by EBSD using the procedure explained in § 4.4.7. Due to time constrain EBSD was measured only on a handful of samples.

Table 6.5: Tensile test result of SCRY-4 samples

| Environment | Stress | Name | $\sigma_{0.2\%\ yield}$ | $\sigma_{UTS}$ | Ductility | Mis-orientation |
|---|---|---|---|---|---|---|
| Units | MPa | - | MPa | MPa | % | ° |
| Air | – | C23 | 974.8 | 1085 | 10.8 | – |
| Virgin | – | V1 | 895.4 | 964.6 | 20.9 | 4.09 |
| Air+SO$_2$/SO$_3$ | – | C38 | 913 | 949.5 | 14.0 | – |
| Air+NaCl+SO$_2$/SO$_3$ | – | C34 | 940.5 | 1084.0 | 16.0 | 3.70 |
| Air+NaCl+SO$_2$/SO$_3$ | 529 | C33 | 929.1 | 947.1 | 12.8 | – |
| Virgin | – | V2 | 913 | 1055.3 | 16.1 | 2.48 |
| Air+NaCl | – | C22 | 945.8 | 1048.4 | 13.4 | – |
| Air+NaCl | 340 | C36 | 936.3 | 973.1 | 15.0 | 4.70 |
| Air+SO$_2$/SO$_3$ | 517 | C37 | 983.6 | 1111.7 | 13.2 | 2.11 |
| Air+SO$_2$/SO$_3$ | 278 | C30 | 923.9 | 923.6 | 0 | - |

### 6.5.2.3 Tensile tests result for SCRY-83 samples

The tensile test data of samples E16 and E17 (exposed to air and SO$_2$/SO$_3$ and sprayed with NaCl and exposed to air and SO$_2$/SO$_3$, both without force) were not comparable to the other curves due to different gauge lengths. The data was therefore omitted.

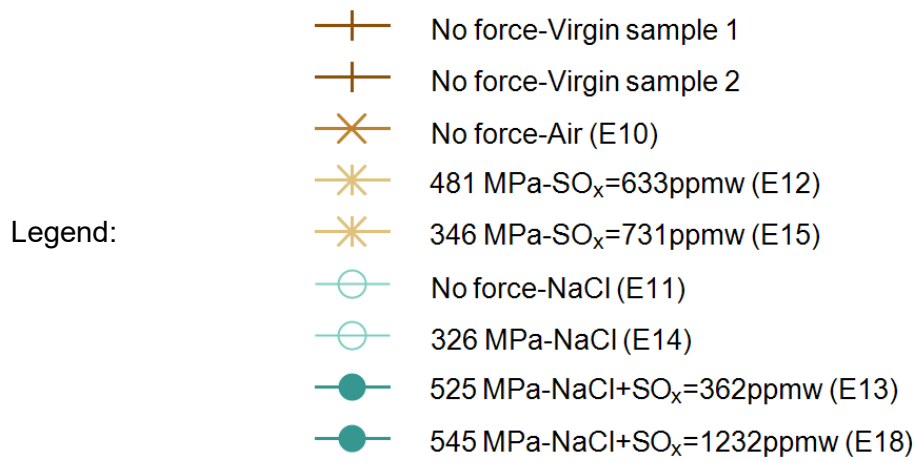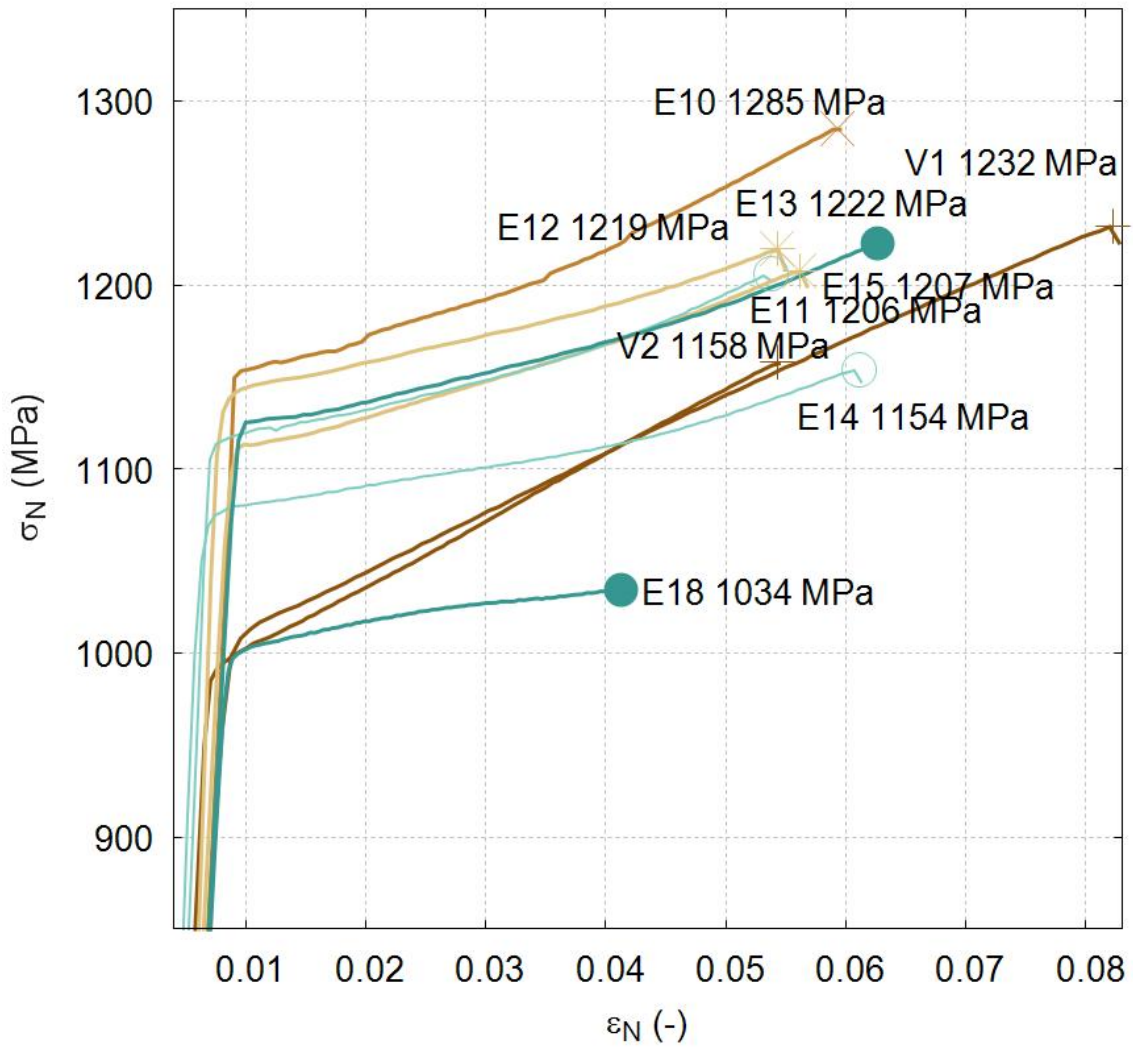The stress-strain curves of SCRY-83 samples are displayed in Figure 6.17.

Figure 6.17: SCRY-83 tensile test stress-strain curves

### 6.5.2.4 Stress-strain data for SCRY-83 samples

As done earlier with SCRY-4, the data of Table 6.6 was extracted from Figure 6.17. Similarly, only a handful of sample had their EBSD data taken.

Table 6.6: Tensile test result of SCRY-83 samples

| Environment | Force | Name | $\sigma_{0.2\%\,yield}$ | $\sigma_{UTS}$ | Ductility | Mis-orient |
|---|---|---|---|---|---|---|
| Unit | N | – | MPa | MPa | % | ° |
| Air | – | E10 | 1156.7 | 1285.7 | 4.8 | 1.4 |
| Air+SO$_2$/SO$_3$ | 282.0 | E12 | 1144.1 | 1219.5 | 4.4 | – |
| Air+NaCl+SO$_2$/SO$_3$ | 320.0 | E18 | 1002.8 | 1035.0 | 3.1 | 4.28 |
| Air+NaCl+SO$_2$/SO$_3$ | 308.0 | E13 | 1126.3 | 1223.0 | 5.2 | – |
| Air+NaCl | – | E11 | 1118.0 | 1206.2 | 4.5 | – |
| Air+SO$_2$/SO$_3$ | – | E15 | 1113.2 | 1207.6 | 4.5 | – |
| Air+NaCl | 191.0 | E14 | 1078.1 | 1154.0 | 5.3 | 3.51 |
| Virgin | – | V1 | 1013.9 | 1232.1 | 7.2 | 2.95 |
| Virgin | – | V2 | 998.1 | 1157.9 | 4.5 | – |

### 6.5.2.5 Accuracy of the tensile test results and error analysis

The objective of these tensile tests was to quantify the loss of mechanical properties caused by the environmental damage. However, this was found to be less than straightforward for several reasons.

### 6.5.2.5.1 Uncertainty on the measurements

The linearity error (0.15 %) and slip on the specimen would cause LVDT [126] measurement uncertainty translating into a ± 0.2 % uncertainty on the ductility.

The load cell (30 kN rating) would also add-up to the measurement uncertainty [127]:

$$\text{Linearity error(\%). Load cell static rating} = \pm\, 75N$$

This uncertainty translates into a stress uncertainty of ± 37 MPa (worst case).

### 6.5.2.5.2 Uncertainty on the section

There was significant scatter in the section of the samples (thickness and width) produced by EDM (In the workshop of the department of material science). Width and thickness

uncertainty was ± 0.05 mm (symmetry discrepancies were difficult to capture with a calliper and therefore ignored).

Thickness and width uncertainties were calculated to translates into stress variations of ± 87 MPa.

### 6.5.2.5.3 *Effect of the misorientation*

Despite care during sample preparation, misorientation between the tensile axis and the <001> sample axis was found (post-mortem).

This misorientation affects the Young's modulus value (see Figure 2.4 (a)) the UTS, the yield and the ductility value (same figure (b)). The higher the misorientation (away from <001>), the lower the UTS and the yield. However, a high misorientation promotes a high ductility.

For example, Shah and Cetel [22] data on PWA1483 predicted that a 5° misorientation would decrease the UTS and yield strength by 89 MPa.

A comparison between the values of SCRY-4 samples V1 (4.09°) and V2 (2.5°) shows a difference in yield of ~ 20 MPa and in UTS of ~ 90 MPa. (These two samples have not been exposed to any aggressive environment).

### 6.5.2.5.4 *Summary of errors analysis*

Table 6.7: Errors during the tensile test

|  | Stress uncertainty (MPa) | Ductility uncertainty (%) |
|---|---|---|
| Measurements uncertainty | 37 | 0.2 |
| Section uncertainty | 87 | |
| Misorientation uncertainty | 89 | |
| Total uncertainty | ± 213 | ± 0.2 |

Table 6.7 cumulates the errors occurring during the tensile test. A larger section or a repeat of the sample (2-3 tests) would greatly improve the accuracy of the results. Unfortunately, this was not possible due to time constrain.

### 6.5.2.6    Effect of the environment on SCRY-4

The relatively large errors (mentioned above) prevent precise identification of the environment effect. Despite this fact, an attempt was made, to identify the limit of sensitivity of this method.

A group of samples was found to have a UTS value below 1000 MPa (C30, C33, C38, C36, V1).

Of this group, sample C30 which was sprayed with NaCl and exposed to air with a mixture of $SO_2/SO_3$ at an average of 1352 ppmw with superimposed force, had the lowest UTS, yield and ductility. In fact, very little work-hardening had taken place, and the sample ruptured at the end of the elastic region. Observation of the sample cross-section (before tensile test) via SEM, revealed 20 cracks, distributed around the mid-span of the beam, with the largest ~ 100 μm. Such crack equates to a loss of section of 7 %.

Sample C33, also sprayed with NaCl and exposed to air and $SO_2/SO_3$ at an average of 369 ppmw with superimposed force had some work-hardening. Cross-section (see Figure 6.9) revealed 2 cracks with the largest measuring ~ 60 μm, which translates into a loss of section of 4 %.

The case of C38 is complicated since the sample treated in the same environment, but with superimposed force (sample C37), exhibited a higher UTS and yield. This result therefore casts doubt on the sensitivity of this method to assess accurately environment degradation. Unfortunately, the second sample (to check this result) failed in the grip (C35). Only suppositions can be made (ie: the sample could have a local defect caused by EDM and missed during visual inspection). In any case, this result will be discarded.

Sample C36, sprayed with NaCl with super-imposed force, displayed some work-hardening. Cross-section did not show any cracks, but the reaction layer may have contributed to the loss of mechanical properties (see Figure 6.4).

The virgin sample (V1) displayed a relatively high ductility, with a low UTS and yield values. Since this sample was virgin, it was thought this result was caused by its above average misorientation (of 4.1°).

### 6.5.2.7 Effect of the environment on SCRY-83

Using the same methodology as above, three samples had UTS value below 1200 MPa (E18, E14 and V2).

Sample E18 which was sprayed with NaCl and exposed to air rich in $SO_2/SO_3$ at an average concentration of 1232 ppmw, with superimposed force, had the lowest UTS and yield. Figure 6.10 shows a ~ 60 μm thick reaction layer with voids that explain the impairment of mechanical properties, and a 4% section loss.

Sample E14 had a second-largest ductility, and the low UTS could then be explained by an above average misorientation (3.5°).

Finally, sample V2 failed at the end of the waisted section (see appendix § 9.5.2). It is thought that a combination of low clearance in the grip and a relatively high misorientation (not measured) induced a bending force, creating a stress concentration at the extremity of the waisted section. The grips (see schematic appendix § 9.6.2) were manufactured locally, and this may be a shortcoming of this design (that should allow rotation on an axial pin).

### 6.5.2.8 Comparison between SCRY-83 and SCRY-4 properties

When samples were sprayed with NaCl and exposed to environment of air and $SO_2/SO_3$ at a concentration of ~ 300 ppmw, with an applied stress of 500 MPa, SCRY-4 suffered some damage (C33) while SCRY-83 did not (E13).

However, when the average concentration was raised to 1200 ppmw, with the same stress (~ 500 MPa), SCRY-83 starts sustaining some reduction in UTS and ductility, while the SCRY-4 sample failed immediately after the elastic region.

SCRY-83 can tolerate a higher concentration of $SO_2/SO_3$ than SCRY-4

### 6.5.2.9 Observation of the failed cross-section of the dog-bone specimens

Failed dog-bone sections were observed using an optical microscope at low magnification (and are shown in appendix § 9.5, along with location of failure) and some failed fractures surface were examined in the SEM.

When no force was applied during the test, fracture occurred just under the waisted section. As explained above, this could be caused by the grip introducing a bending force,

leading to a stress concentration. Dimple-like features were also identified (see SEM image in Figure 6.19). These were approximately orientated 45° to the view plane.
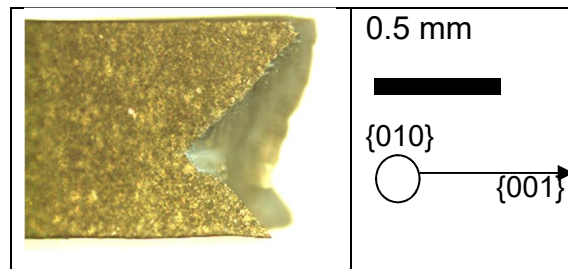


Figure 6.18: Low magnification microscope image of the failed stress strain specimen (C22) showing {111} failed plane orientated at 45° from the sample direction



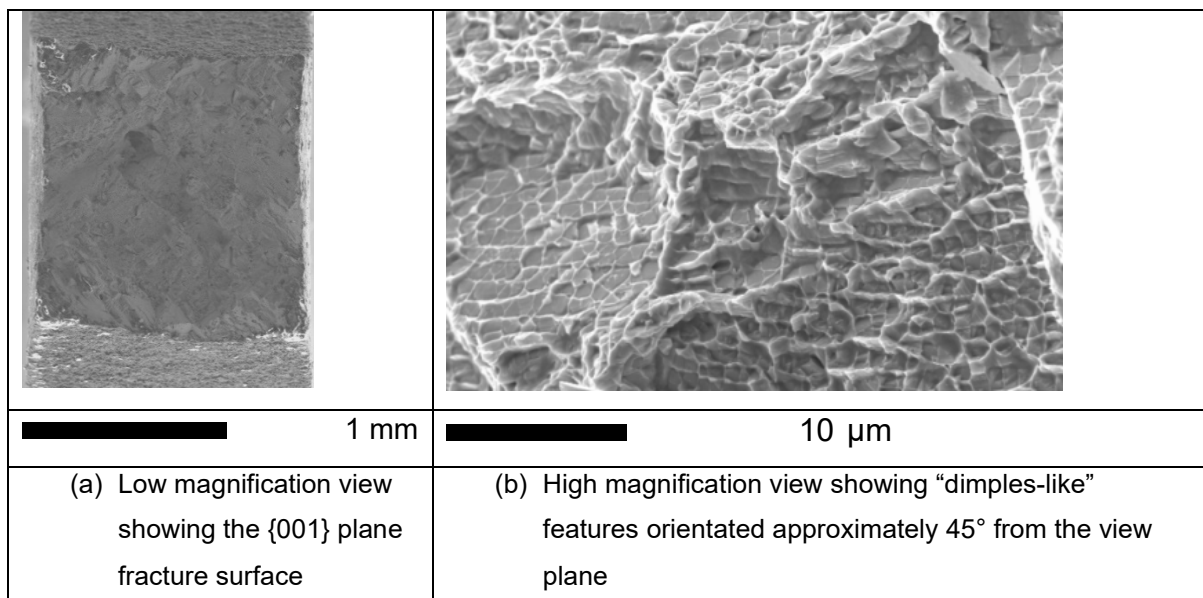| (a) Low magnification view showing the {001} plane fracture surface | (b) High magnification view showing "dimples-like" features orientated approximately 45° from the view plane |

Figure 6.19: Fracture surfaces of sample sprayed with NaCl and exposed to air (E11) without force. <001> is normal to the plane of the image

When force was applied during environmental exposure, samples tended to fail in the gauge length.

It is noted in Figure 6.20 that the cracks grown, in the aggressive environment, at 700°C are parallel to the {010} plane which is perpendicular to the highest stress direction [001].

However, the fracture plane is parallel to {110} and is thought to have developed during the tensile test at ambient room temperature.
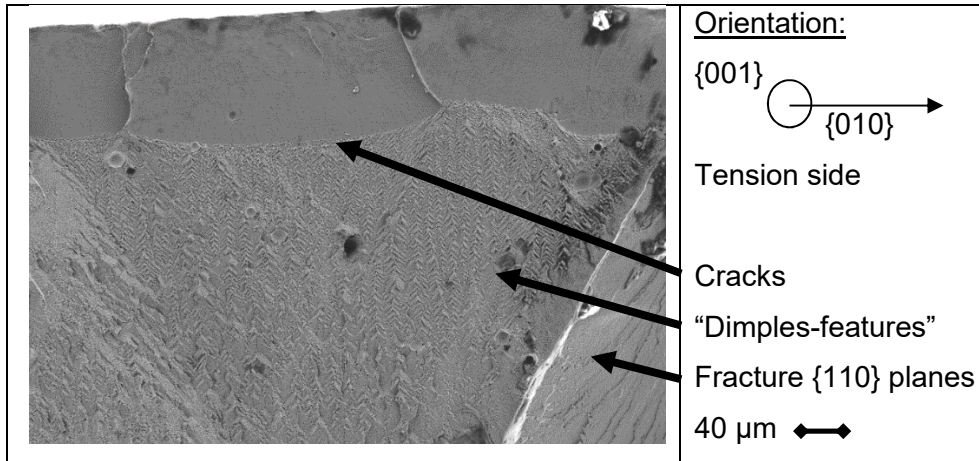
Figure 6.20: Secondary Electron image of fracture surface of sample E2

## 6.5.3 Crack position and deduction of the critical stress

A series of samples sprayed with NaCl were exposed for 72 h at 700 °C, while varying the stress and $SO_2/SO_3$ concentration. It was assumed that the cracks would be small enough, so the stress field, initially calculated, would remain unchanged. The sample was exposed to the same gas concentration however, a range of stresses occur at different locations (see Figure 6.3). The position of cracks and the critical stress was recorded and is shown in Figure 6.21 by the green line.
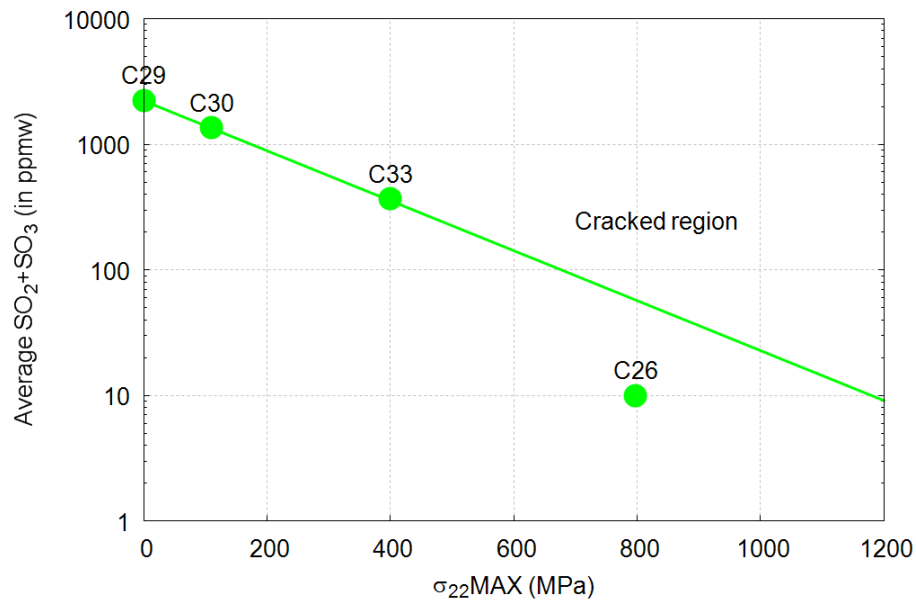


Figure 6.21: Plot of average $SO_2/SO_3$ concentration against applied tensile stress at 700 °C for SCRY-4 for 72 h showing which samples exhibited cracking

A region of high stress and relatively low sulphur concentration (ie: sample C33) can be distinguished. This is thought to be due to the protective oxides exhibiting significant cracking due to stress, facilitating the migration of corrosion product.

A second region, with low stress and high sulphur concentration is also identified (ie: sample C29). This could be explained by a much more aggressive environment (rich in $SO_3$) able to dissolve the protective oxide.

## 6.5.4 Stability of the reaction layer under superimposed stress

To assess the kinetics of the tests with superimposed stress, extended tests were performed. Once again, due to the duration of these tests, not many data points are available. Test data are available in appendix (§ 9.3).
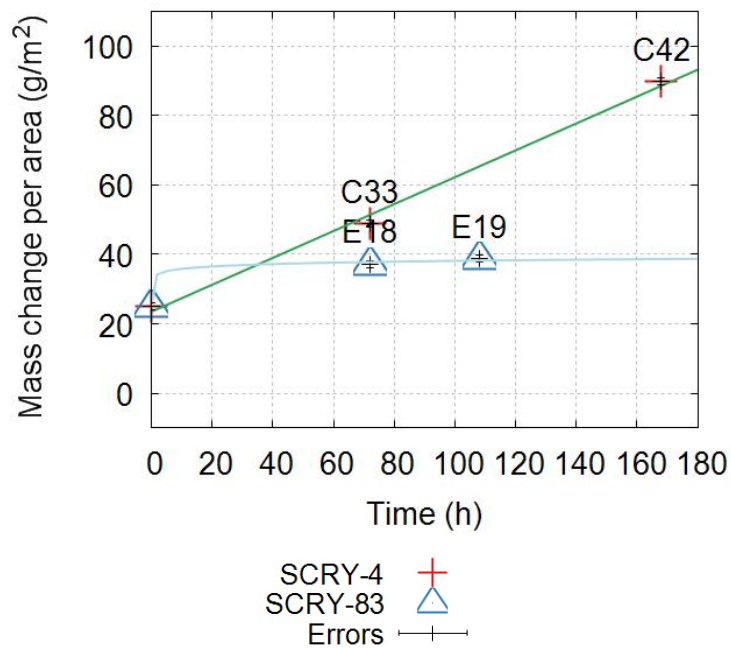


Figure 6.22: Mass change per area, as a function of time, for samples sprayed with NaCl and exposed to air and $SO_2/SO_3$ with superimposed force

Figure 6.22 shows that SCRY-4 mass gain is continuous while stabilisation of the weight gain occurs for SCRY-83 between 20 to 40 h. Nevertheless, due to the lack of data points, there is high uncertainty on this projection.

In the case of the sample C42, the sample broke at the end of the test. Data from this specific test is presented in Figure 6.23.

a)  In red, actuator force (left scale), in blue displacement (right scale)

b)  Optical image of the sample at the end of the test
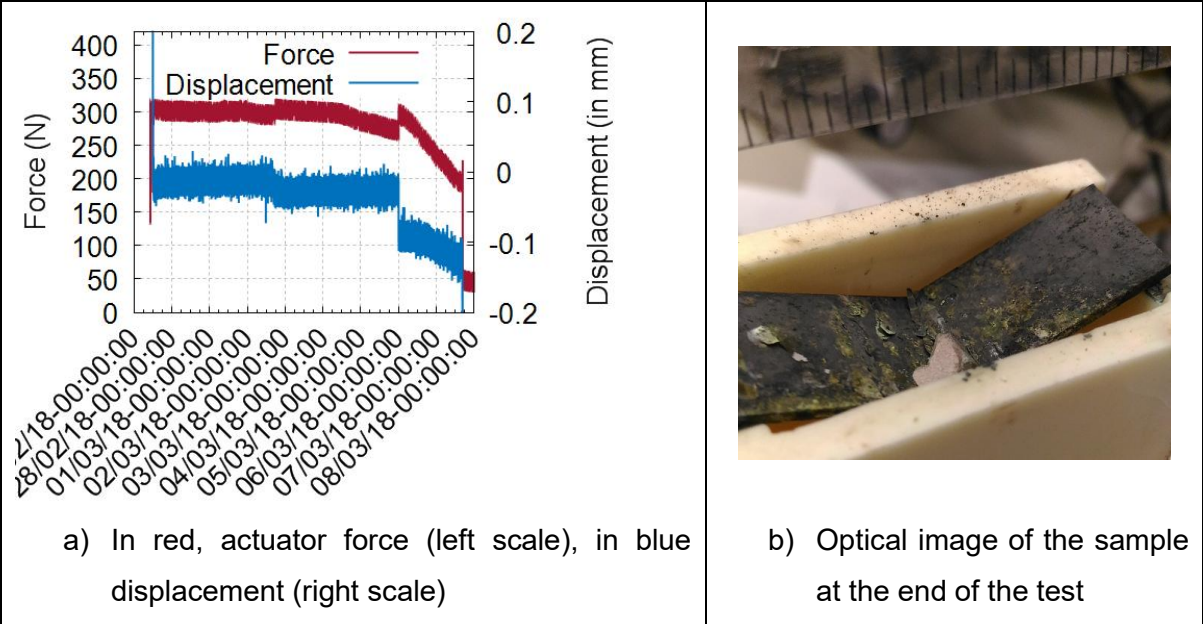
Figure 6.23: 120 h exposure test of SCRY-4, sample made of SCRY-4 (C42), sprayed with NaCl and exposed to 362 ppmw $SO_2/SO_3$, at 700 °C

# 6.6 Summary on the effect of stress and Cr content in environmental exposure

○ **Discussion of the FE results**

The comparison between the different stress fields, occurring in the beam, while exerting a vertical force on the fork, shows that $\sigma_{xx}$ is the largest component on both faces of the sample. It is also worth noting that at the temperature of interest, the maximum stress (slightly above 500 MPa for a force of 300 N) is well below the stress threshold, in which creep strain is significant (see Figure 2.5) and it will therefore be neglected.

○ **Effect of force on sample sprayed with NaCl and exposed to air**

Since the same compounds (identified in the case without force) were found on EDX and XRD, it was concluded that the superimposed force did not affect the composition of the reaction layer. However, it is thought that superimposed force promoted liquid to flow to the substrate/oxide interface (liquid was evidenced in § 5.3.1.2). This liquid and the removal of the force resulted in delamination of the reaction layers observable in Figure 6.4.

○ **Effect of superimposed force on samples exposed to air and $SO_2/SO_3$**

The introduction of force on samples exposed to air+$SO_2/SO_3$ resulted in a larger reaction layer and an increased amount of S. For the SCRY-83, the protective mixed oxide may have cracked with the force application and allowed the liquid ($Ni_3S_2$) to flow. For the $Al_2O_3$-former, since no protective oxide was found in the earlier case, the load just helped the liquid to flow deeper.

○ **Effect of force on sample sprayed with NaCl and exposed to air+$SO_2/SO_3$**

A thicker reaction layer was observed on both alloys when force was applied.

For the $Al_2O_3$-former, a larger S peak was detected, consistent with the XRD detecting also a larger intensity for the peaks of $Na_2Ni(SO_4)_2$. This compound attests the formation of a larger amount of liquid ($Na_2SO_4/NiSO_4$) close to the substrate, in which other blade constituents can dissolve. Because of this aggressive fluxing and the presence of stress, two cracks appeared, both orientated perpendicular to the highest stress direction.

For SCRY-83 however, the presence of more $Na_2SO_4$ and $Na_5NiO_2S$ seems to indicate that the amount of liquid fused salt melt ($Na_2SO_4/NiSO_4$) was limited. Coincidentally, the Cr concentration was halved (compared to the case without force). Despite a potential link

between these two results, no mechanisms were found in the literature to explain that. Structurally even though no cracks were found, a ~ 40 µm layer with damaged γ/γ' and voids was discovered at the mid-section of the beam (where the maximum stress is applied).

    ○ **Assessment of novel methods to measure environmental degradation**

Several novel methods were attempted to carry out assessment of environmental damage.

    ○ <u>Surface degradation</u>

This surface method was found sensitive enough to detect when the $SO_2/SO_3$ was injected, and it demonstrated that surfaces were quickly contaminated (within 5 to 10 h). This technique would benefit from a spectral reflectance characterisation of the compounds identified by XRD. In addition, it suffered from gas condensation on the relatively cold quartz windows.

    ○ <u>Displacement in load control set-up</u>

After an incubation time of ~ 30 to 70 h, a large vertical displacement occurred. The rate was found to increase for harsher environments. Thicker samples with larger force would permit a better characterisation.

    ○ <u>Beam stiffness change</u>

This method was found to be sensitive enough to pick-up substantial changes in equivalent beam compliance occurring in aggressive environment on the $Al_2O_3$-former. However, the requirement for loading/unloading could be a limitation in constant force tests.

    ○ <u>Post-test mechanical testing</u>

Tensile tests are advantageous at interrogating sub-surface condition. In addition, they provide additional data directly (eg: ductility, UTS) or indirectly (observation of fracture surfaces). However, in this case, large uncertainties meant that only samples that were significantly damaged could be detected as such. This could be improved by repeating experiments and/or lowering the tolerances of the EDM machining.

    ○ <u>Crack position and deduction of critical stress</u>

This technique, relying on the identification of cracks via SEM and the record of their position to determine a safe-stress threshold, was the most-suited to this work. However, for samples experiencing a large number (>10) of deep cracks (>50 µm), the stress field is

considerably changed. In contrast, samples without cracks do not provide any information. This technique requires therefore a knowledge of the approximate range of failure ($\sigma$-$SO_2$/$SO_3$).

<p style="text-align:center;">o   <u>Stability of the reaction layer and mass change</u></p>

The reaction layers of samples with applied load were found to spall much more readily than those without load, particularly during the final unloading. For this reason, the thickness of the reaction layer measured on samples tested with force tend to underestimate the damage, and should be used with care.

To elaborate on the point made above about the mass change not representing the damage (§ 5.6), Figure 6.22 shows a linear weight gain, while the sample (C42) failed catastrophically (see Figure 6.23). The weight gain data clearly needs to be interpreted carefully.

A summary of the methods tested is provided in Table 6.8.

Table 6.8: Advantages and drawbacks of different methods to assess environmental degradation

| Methods | Advantages | Drawbacks |
|---|---|---|
| In-situ or interrupted mass changes | ✓ Very easy to measure | ✗ With stress applied, spallation occurs and underestimate the damage<br>✗ Overall measurement (mass gain +mass loss) |
| (Reaction) Layers observation | ✓ Scale thickness is also easy to measure on SEM cross-section<br>✓ Cracks can be detected | ✗ With stress applied, layers tend to spall and underestimate the damage<br>✗ Destructive |
| In-situ beam displacement | ✓ Also capture subsurface change<br>✓ Does not require loading/ unloading | ✗ Requires long testing time (>100h) or aggressive environment to see degradation<br>✗ Progress very quickly |
| In-situ stiffness measurements | ✓ Capture subsurface change by modification of the beam stiffness | ✗ Necessitates loading/unloading that affects constant stress measurement<br>✗ Also Requires long testing time (>100h) or aggressive environment to see degradation |
| Post-treatment tensile test | ✓ Also capture subsurface change<br>✓ Added data (failed cross-section, E, σ, ε…)<br>✓ Ideal for low to medium harsh environment | ✗ Requires manufacturing of dog-bone specimens<br>✗ Destructive<br>✗ Time consuming<br>✗ Uncertainties best dealt with several samples (2-3)<br>✗ Requires misorientation of samples (EBSD) |
| Crack position and critical stress | ✓ Ideal for low to medium harsh environment | ✗ Need sample to crack<br>✗ But small number of cracks (so stress field is unchanged) |

# Chapter 7   Conclusions

Hot corrosion testing, in the literature, is often performed with a mixture of $Na_2SO_4$ and NaCl. However, very little is explained about the effect of each salt separately. Furthermore, exposure to $SO_2/SO_3$ has not yet been thoroughly compared to the same exposure with NaCl. Is it more aggressive? To answer these questions a testing facility was built.

- **Testing facility**

A testing rig was built to reproduce the environment experienced by the turbine blade attachment area (fir-tree). First, a furnace permitted to heat the sample to around 800 °C. Secondly, a load control set-up generated (compressive and tensile) stresses of up to about 500 MPa (for a strip of 1.5 mm thick, 15 mm wide). A closed loop, equipped with a diaphragm pump, circulated a mixture of air into which $SO_2/SO_3$ could be injected to a desired level (up to 10,000 ppmv). Several safety features were integrated to ensure the noxious gas would not be released and would be neutralized. The characterisation of the environment was then started.

- **Characterisation of the static environments**

The effect of the four environments on the samples were characterised at 700 °C for 72 h via mass change, microstructural observations and XRD. A first-generation single-crystal nickel superalloy SCRY-83 with 12.2 wt% Cr, referred to as "$Cr_2O_3$-former" was compared to a second-generation single crystal SCRY-4 with 6.5 wt% Cr, referred to as "$Al_2O_3$-former".

The first environment tested the effect of an exposure to air only. Both alloys developed a thin oxide with a three-layer arrangement. For the $Al_2O_3$-former alloy, the thin innermost layer was composed of $Al_2O_3$, while for the $Cr_2O_3$-former, only a mixed $NiCr_2O_4$ was detected. The low temperature and the short exposure time explain why the oxides were not what one would expect at full chemical equilibrium.

The second environment consisted of a NaCl coating and exposure to air. It is worth remarking that $AlCl_3$, $NiCl_2$, $CrCl_2$ and $CrCl_3$ possess much higher vapor pressure than NaCl. This point particularly affected the $Al_2O_3$-former, that suffered substantial mass loss because of the Al reacting with Cl, leaving a scale depleted in Al. On the other hand, the $Cr_2O_3$-former was affected by "activated oxidation" that sees $CrCl_2$ and $CrCl_3$ transported to the surface where the higher $O_2$ partial pressure caused $Cr_2O_3$ to form, releasing the Cl in another cycle.

Although the mass loss was lower than its low Cr counterpart, the affected region had a similar size.

The third environment involved an exposure to air and $SO_2/SO_3$. Theoretical explanations, first made by Haflan and Kofstad [65], propose that NiO can be sulphated into $NiSO_4$, which then gives an outer layer made of NiO and an inner layer made of $Ni_3S_2$ (liquid at the test temperature). The $Al_2O_3$-former displayed the phases described above, while the $Cr_2O_3$ did not. It is possible that the mixed Cr oxide played a role in stopping the S ingress even though literature was scarce on this subject.

The fourth environment consisted of NaCl coating and exposure to air and $SO_2/SO_3$. Since during this test NaCl would be converted to $Na_2SO_4$, a characterisation of sodium sulphate was first carried out. In presence of this salt, liquid was evidenced on both alloys, however, in the case of the $Al_2O_3$-former, the alloy constituents were dissolved, forming a fused salt melt, verified by the large depth of the attack, and the difficulty to form a protective oxide. This mechanism was again confirmed in the 72 hours test, with S found beneath the oxide, in the damaged substrate region. The high Cr alloy was less affected by the liquid phase, probably because of the formation of $Na_2CrO_4$ helping to develop a positive solubility gradient which limited the damage of the protective oxide.

With the static environments characterised, the effect of stress was now examined.

- **Effect of applied load on degradations**

The same methods of investigation were used in this case (mass change, microstructural investigation and XRD). (To ease referencing, the number of the environments are kept the same as the static case).

In the second environment, reactions layers on both alloys appeared delaminated from their substrate, certainly resulting from the unloading. In addition, since a liquid (possibly NaCl-$NiCl_2$ $T\epsilon$=600°C) was identified (in the static case), the applied load could have helped it to flow further explaining the thicker reaction layer.

In the third environment, the high Cr alloy also suffered, this time, an ingress of S which could be explained by the mixed oxide cracking due to the applied load. The liquid ($T\epsilon$=635°C) $Ni_3S_2$ could also have benefited from the force to flow deeper (explaining the higher S concentration recorded on the $Al_2O_3$-former).

Finally, in the fourth environment, a slight inconsistency occurred and the amount of $SO_x$ was 3 times more concentrated for the $Cr_2O_3$-former (1200 ppmw against 370 ppmw see Table

4.4). Nevertheless, the $Al_2O_3$-former experienced again a S ingress beneath the oxide, with two cracks forming perpendicular to the highest stress direction. The high-Cr alloy did not experienced cracks but had a ~ 40 µm thick region with damaged γ/γ' and voids. The cracks on the SCRY-4 and the damaged region on the SCRY-83 reflect the extreme aggressive nature of this environment.

- **Limitation of dominant and novel methods of corrosion investigation**

While proven methods were used to carry out the characterisation, novel methods were also attempted.

Mass change methods and reaction layers thickness measurement (via SEM, also named "good metal loss") are extremely prevalent in hot corrosion literature. However, both methods possess major limitations.

The major limitation of mass change, is its inability to assess the sub-surface integrity of the sample. For example, in the case where SCRY-83 was coated with NaCl, the small mass loss suggested the degradation was minimal, while the thick reaction layer suggested otherwise. Also, this method cannot predict the failure since free surfaces behave differently to internal cracks (ie: see sample C42 Figure 6.23). Lastly, the mass change is unable to distinguish the effect of mass loss and mass gain, as they are combined, and NaCl evaporation is often neglected.

Scale thickness measurement technique (via SEM) can underestimate damage when spallation events occur. This occurred more frequently when the force was applied.

An in-situ surface degradation technique, which consisted of counting pixel (of a specific RGB colour) on pictures taken every hour, resulted in finding a rapid surface contamination (within 5-10 h of $SO_2/SO_3$ injection).

In-situ displacement measurement, when the set-up was in load-control, was best suited to assess degradation of long exposure samples (>150 h). During the first part of the test, the displacement rate was nil, and increased after 30 to 70 h, indicating the end of the incubation period.

In-situ stiffness change detected variations in the most aggressive environment. However, it required the introduction of loading/unloading, which could be undesirable in constant force experiments.

Crack position and determination of safe stress level produced repeatable results. However, finding the right balance between not having an excessive number of cracks (so the initial stress field is unchanged), and having no cracks (wasting testing time) was challenging.

Post-test mechanical testing was time-consuming but produced a range of direct and indirect information. For example, study of the fracture surface brought the corrosion crack morphology to light (see Figure 6.20). The uncertainties of the method however meant that only very damaged samples were detected as such, and repeat of experiment would be extremely valuable.

# Chapter 8    Further work

- **Repeat samples in the post-test mechanical testing**

The post-test room temperature mechanical testing of the samples, previously exposed to aggressive environment, was found very valuable since it provided ductility and UTS data, that are often used for design. However, uncertainties were so large that characterisation of the damage was difficult. To increase confidence, a testing of 2 or 3 samples, each exposed to each environment would be beneficial.

- **Micro-computed tomography (μ-CT)**

Some μ-CT of exposed samples was attempted. Unfortunately, the thickness of sample (1.5 mm) meant that a 13 μm pixel size was required to maximize the intensity, resulting in the impossibility of detecting cracks. A brighter X-ray source, or a thinner sample, could permits improved resolution, that could provide insight on how cracks grow during interrupted testing.

- **Modelling**

This work constitutes the base of a mapping effort in the damage caused by hot corrosion type II. A sensibility study of the parameters would reinforce the understanding, such as, the variation of the test temperature, or the introduction of fatigue. The results above could then generate value by being integrated into a predicting life model.

- **$SO_3$ concentration**

In this work, an average $SO_2/SO_3$ concentration was quoted. However, as mentioned earlier (§ 3.4.2.1), $SO_3$ is the gas responsible for the conversion of $NaCl$ to $Na_2SO_4$, there is therefore great interest in direct sulphur trioxide measurement.

To illustrate this statement, during a test with desiccant present in the closed loop (silicon dioxide), and despite a high $SO_2/SO_3$ concentration, the degradation (measured via mass gain and reaction layer thickness) was unusually lowered. Hindiyarti et al [84] established that the presence of $H_2O$ (via OH-radical) significantly affected $SO_3$ conversion.

Regrettably, electrolytic sensors cannot distinguish between the two sulphur molecules. Thanks to a small wavelength shift in absorbance (see Figure 8.1), Fourier Transform Infra-Red spectrophotometer (FTIR) can theoretically measure the $SO_2/SO_3$ ratio. Valuably,

FTIR can also detect formation of low vapour pressure compounds. (This was done by Hiraide et al. [128] to detect $CrCl_2$ and $CrCl_3$). This is an area in which further work might be helpful.
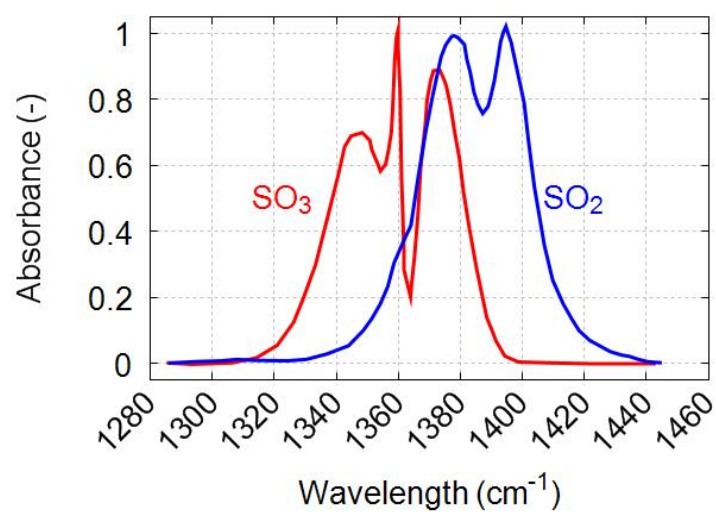


Figure 8.1: Absorbance of $SO_2$ and $SO_3$ (in blue and red respectively) showing a slight shift allowing detection via FTIR

# IX Appendix

## 9.1 Abaqus input files of orthotropic elastic model

```
*Heading
*Preprint, echo=NO, model=NO, history=NO,
contact=NO
** PARTS
*Part, name=Beam
*Node
[...]
*Element, type=C3D8R
[...]
*Nset, nset=Beam, generate
    1,  5120,      1
*Elset, elset=Beam, generate
    1,  3591,      1
*Orientation, name=Ori-1
0., 0., -1., 0., 1., 0.
1, 0.
** Section: Beam_section
*Solid Section, elset=Beam,
orientation=Ori-1, material=SCRY4
,
*End Part
*Part, name=Fork
*Node
[...]
*Element, type=C3D8R
[...]
*Nset, nset=Support, generate
    1,   924,      1
*Elset, elset=Support, generate
    1,   650,      1
** Section: Support
*Solid Section, elset=Support,
material=Support
,
*End Part
** ASSEMBLY
*Assembly, name=Assembly
*Instance, name=Fork-1, part=Fork
20., 0.75, -2.5
*End Instance
*Instance, name=Part-1-1, part=Beam
*End Instance
*Instance, name=Fork-2, part=Fork
 1., 0.75, 1.4
*End Instance
*End Assembly
** MATERIALS
*Material, name=CMSX4
*Elastic, type=ENGINEERING CONSTANTS
181000.,181000.,128000.,    0.47,
0.325,  0.325, 61600., 36700.
 36700.,   293.
147000.,147000.,109000.,   0.485,
0.344,  0.485, 49500., 30800.
 30800.,   873.
141000.,141000.,105000.,   0.487,
0.352,  0.487, 47400., 29600.
 29600.,   993.
*Material, name=Support
*Elastic
300000.,  0.2
** INTERACTION PROPERTIES
*Surface Interaction, name=IntProp-1
1.,
** BOUNDARY CONDITIONS:Fork_vertical Type:
Displacement/Rotation
*Boundary
Fork, 1, 1
Fork, 2, 2
Fork, 4, 4
Fork, 5, 5
Fork, 6, 6
** Name: Support helpd Type:Smmetry
*Boundary
Support_bot, ENCASTRE
** Name: SymetryX Type: Symmetry
*Boundary
SymetryX, XSYMM
** Name: SymmetryY Type: Symmetry
*Boundary
symetry_y, YSYMM
** INTERACTIONS
** Interaction: Interaction_Beam_Support
*Contact Pair, interaction=IntProp-1,
type=SURFACE TO SURFACE
Support_top, Beam_bot
** Interaction: Interaction_Beam_fork
*Contact Pair, interaction=IntProp-1,
type=SURFACE TO SURFACE
Fork_bot, Beam_top
** ------------------------------------------------------------
STEP: Load
*Step, name=Load, nlgeom=NO
*Static
1., 4., 4e-05, 1.
** LOADS** Name: Pressure  Type: Pressure
*Dsload
Fork_top, P, 13.3
** OUTPUT REQUESTS
*Restart, write, frequency=0
** FIELD OUTPUT: F-Output-1
*Output, field, variable=PRESELECT
** HISTORY OUTPUT: H-Output-1
*Output, history, variable=PRESELECT
*End Step
```

# 9.2 Table of material composition cited

| Weight % | Ref | Cr | Co | Mo | W | Ta | Re | Nb | Al | Ti | Hf | Ni | Si | Fe | C | Comments |
|---|---|---|---|---|---|---|---|---|---|---|---|---|---|---|---|---|
| SCRY-4/ CMSX-4 | | 6.5 | 9 | 0.6 | 6 | 6.5 | 3 | | 5.6 | 1 | 0 | 61.7 | | | | |
| SCRY-83/ IN 792 | | 12.2 | 9 | 1.9 | 3.8 | 5 | | | 3.6 | 4.1 | | 60.4 | | | | |
| Udimet 720 | [93] | 16 | 15 | 3 | 1.3 | | | | 2.5 | 5 | | 57.18 | | | 0.0 15 | B=0.015, Zr=0.035 |
| M152 | [17] | 12-15 | | 1.5 -2 | | | | | | | | 2-3 | 0.2 | bal | 0.1 - 0.2 | Mn=0.5-0.9, V=0.25-0.4, |
| IN 738 LC | [49] | 15.87 | 8.5 | 1.6 | 2.6 | 1.8 | | 0.9 | 3.52 | 3.5 | | 61.16 | | | 0.1 | |
| Nimonic 90 | [55] | 19.1 | 16 | | | | | | 1.488 | 2.5 | | 59.44 | 0.2 | 0.7 | 0.1 | B:20ppm, Zr:0.065, 0.12Cu, Mn:0.06 |
| MC2 | [102] | 8 | 5 | 2 | 8 | 6 | | | 5 | 1.5 | | 64.5 | | | | |
| IN617 | [99] | 21.48 | 12 | 8.6 | 0.1 | | | 0.1 | 1.2 | 0.4 | | 54.43 | 0.2 | 1.5 | 0.1 | Mn=0.08, Cu=0.06, v=0.01, W=0.12 |
| IN718 | [64] | 17.91 | | 3 | | | | 5.2 | 0.54 | 1 | | 53.5 | | 19 | | |
| DZ125 | [110] | 8.9 | 10 | 2 | 7 | 3.8 | | | 5.2 | 0.9 | 2 | 60.45 | | | 0.1 | B=0.015 |
| IN751 | [100] | 16.07 | | | | | | | 1.1 | 2.1 | | 72.98 93 | 0.2 | 5.7 | 0.1 | Mn=0.53,s=0 .007, Cu=0.05,Nb+ Ta=1.18 |

## 9.3  Data from extended test

| Name | Sample temp (°C) | $SO_2+SO_3$ (ppmw) | Force (N) | Sea salt (mg/cm²) | Time (h) | Specific weight change (g/m²) |
|------|------------------|---------------------|-----------|-------------------|----------|-------------------------------|
| E19 | 700 | 510 | 320 | 2.50&2.70 | 108 | 38.82 |
| C42 | | 362.8 | 277 | 2.65&2.54 | 168 | 89.69 |
| E13 | | 362 | 310 | 2.53&2.43 | 72 | 14.37 |
| C11 | | 300 | 300 | ~2.5&2.5 | 120 | ? |

## 9.4 Phases diagrams
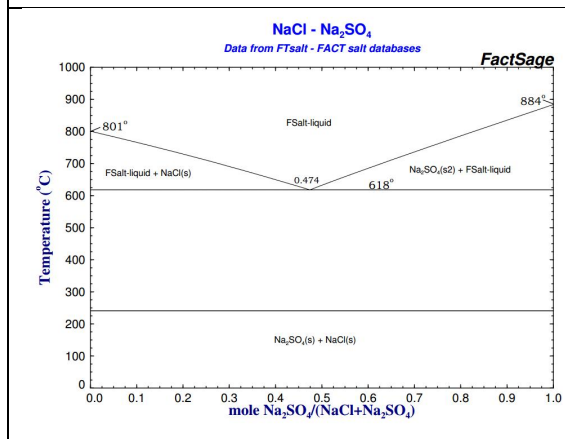
| 9.4.1 NaCl-Na₂SO₄ [69] | 9.4.2 K₂SO₄-Na₂SO₄ [69] |
|---|---|
|  |  |

| 9.4.3 CoSO₄-Na₂SO₄[129] | 9.4.4 NiSO₄-Na₂SO₄[129] |
|---|---|
|  |  |

| | |
|---|---|
| **9.4.5 Ni-S** [66] | **9.4.6 CoCl₂-NiCl₂** [69] |

| | |
|---|---|
| **9.4.7 CoCl₂-NaCl** [69] | **9.4.8 NaCl-NiCl₂** [69] |

| 9.4.9 AlCl₃-NaCl [69] | 9.4.10    NaMoO₄-MoO₃ [130] |
|---|---|
|  |  |

| 9.4.11    NaWO₄-WO₃ [130] |
|---|
|  |
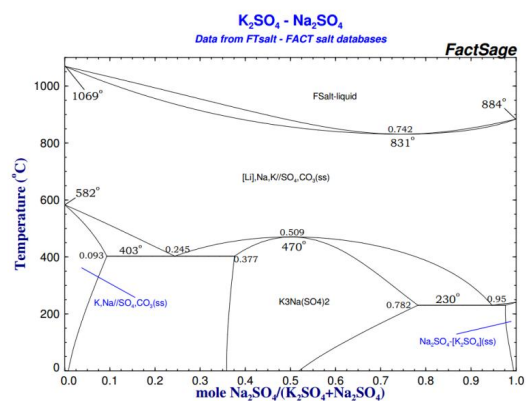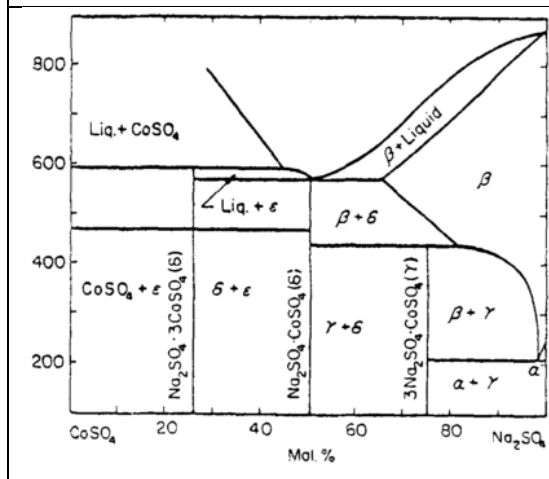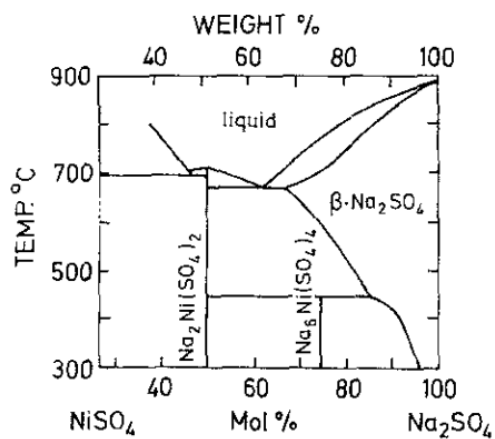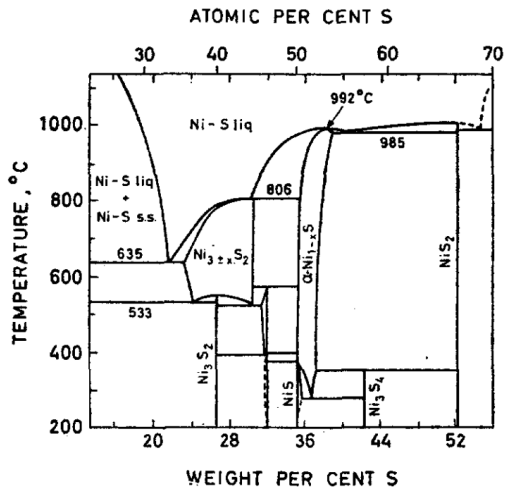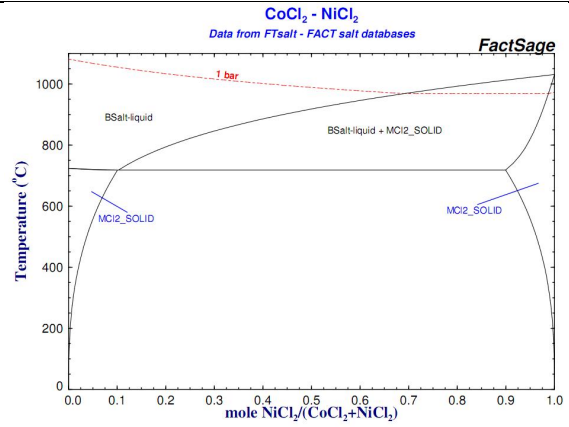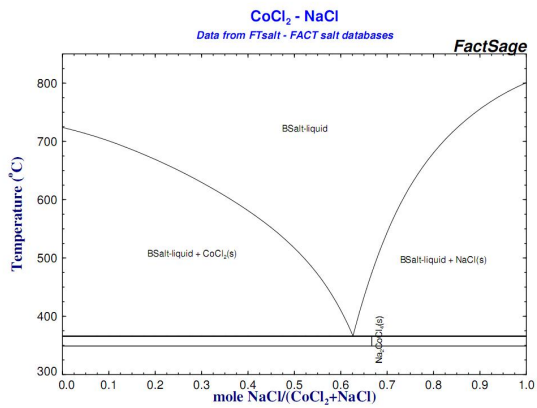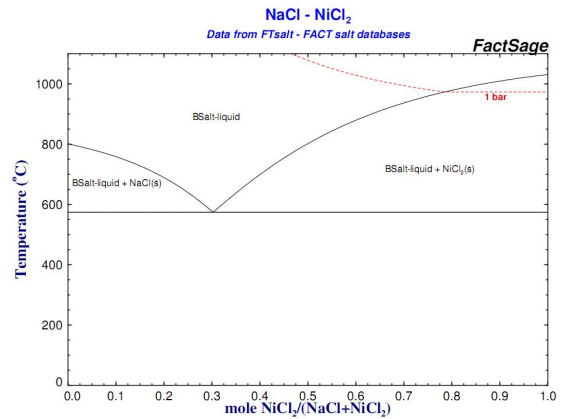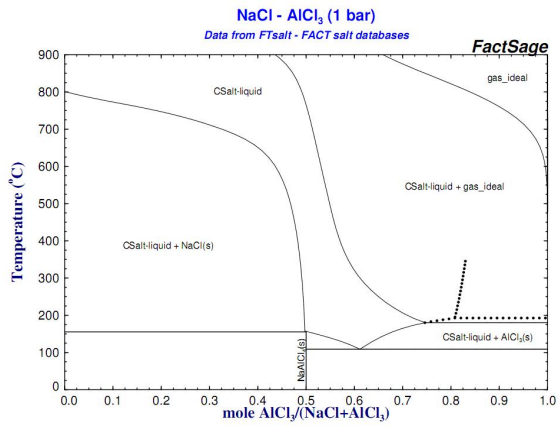
151
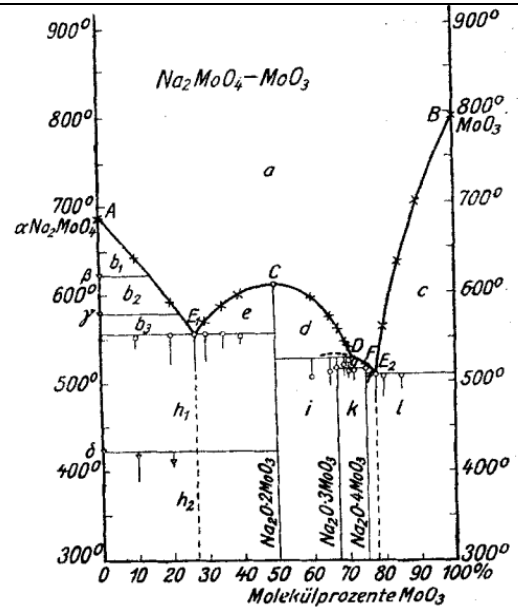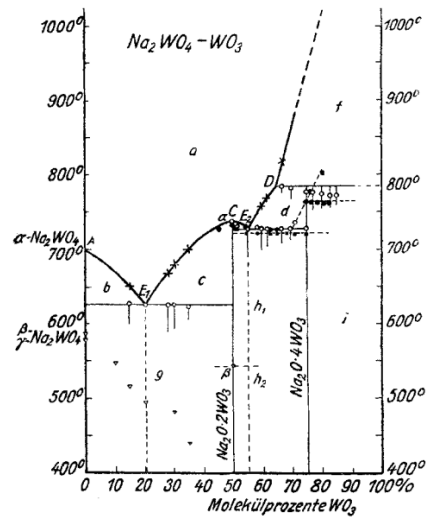
## 9.5 Fracture sections observed under visual microscope

### 9.5.1 Orientation

{001}
{010}
1.5 mm

### 9.5.2 SCRY-83 samples



E10 – waist fail



E11 – waist fail



E12 – gauge length fail



E13 - gauge length fail



E14 gauge length fail
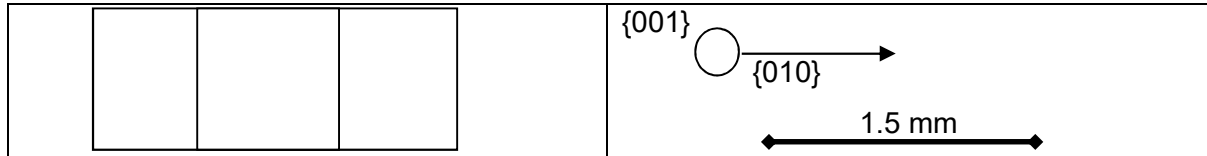


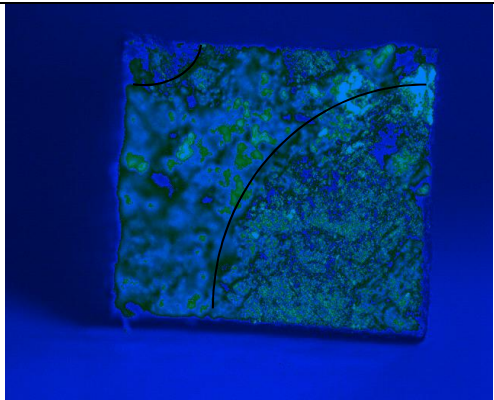E15 gauge length fail
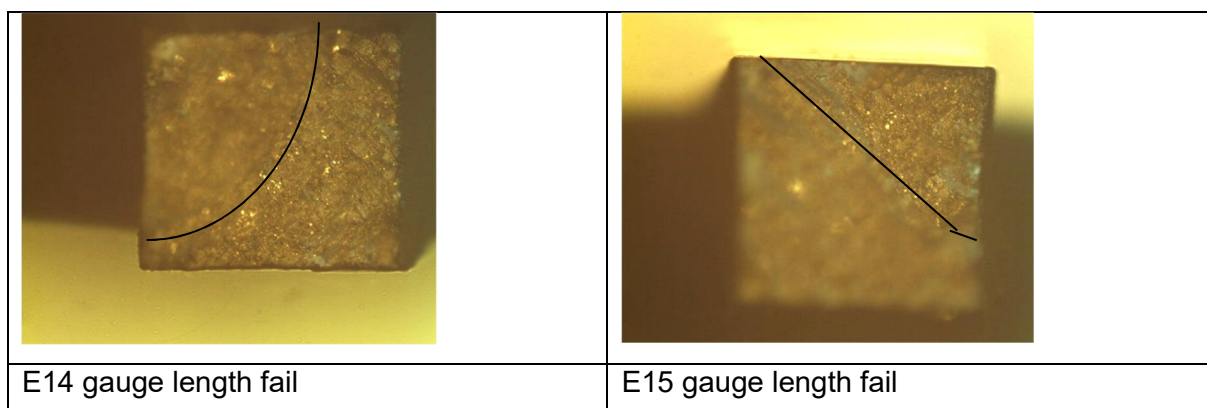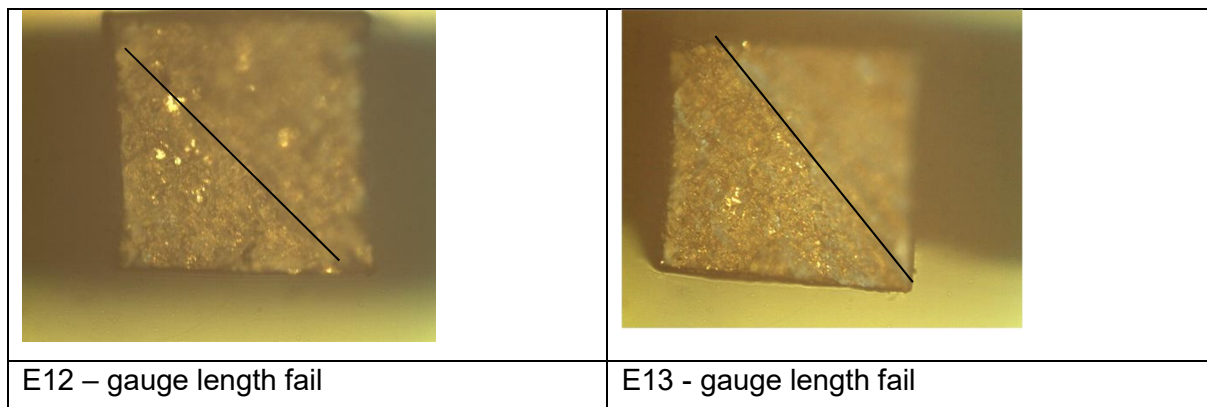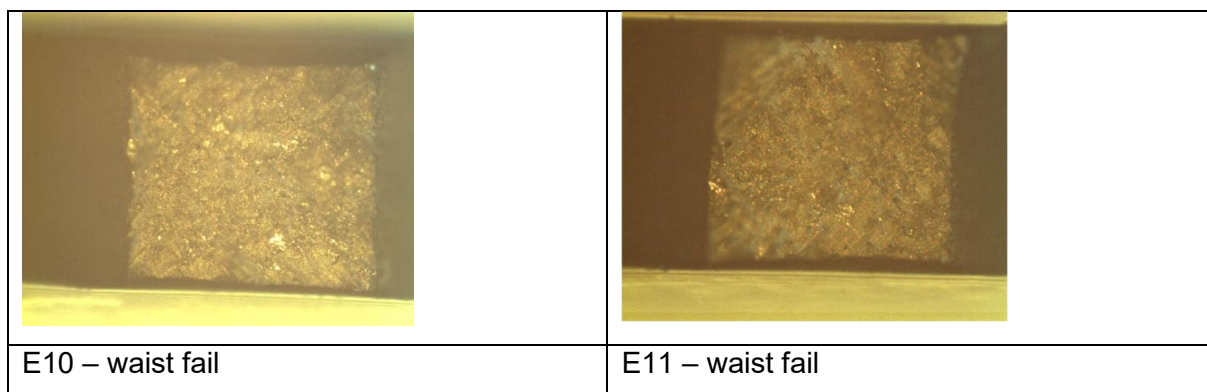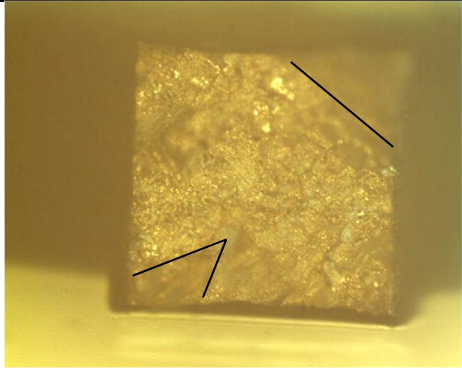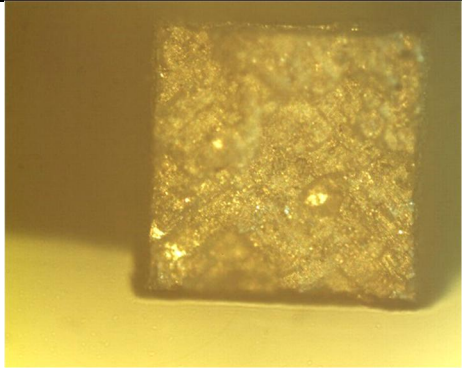
E16 – waist fail
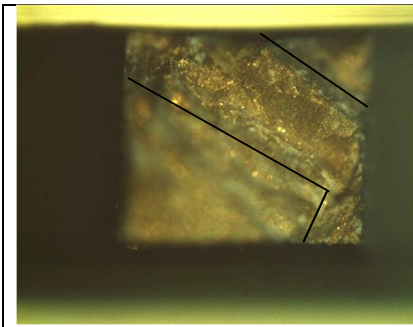

E17 – waist fail
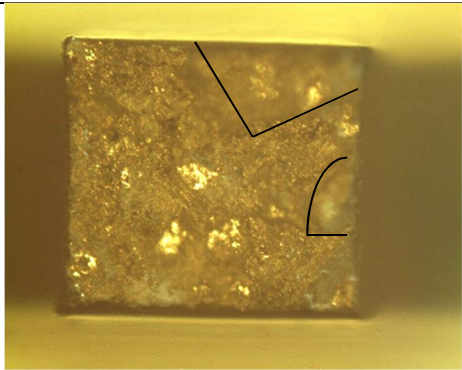

SCRY-83 Virgin 1 - gauge length fail
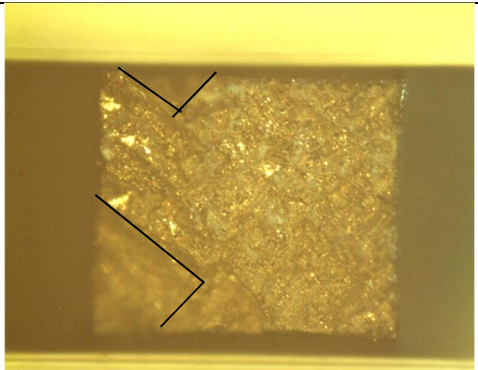

SCRY-83 Virgin 2 - waist fail


E18 - waist fail

## 9.5.3 SCRY-4 samples

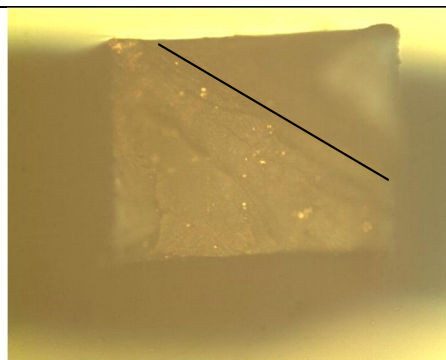| | |
|---|---|
|  |  |
| C23 – Gauge length fail | C22 – Waist fail |

| | |
|---|---|
|  |  |
| C32 – waist fail | C33 – gauge length fail |

| | |
|---|---|
|  |  |
| C34 – waist fail | C37 - gauge length fail |
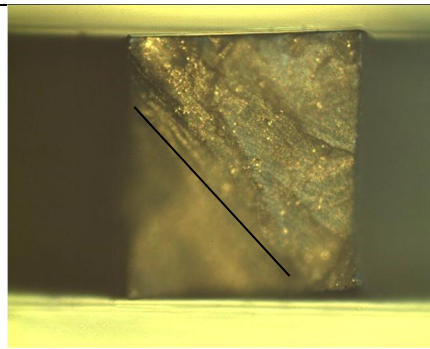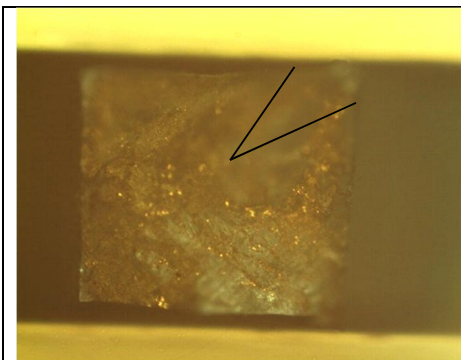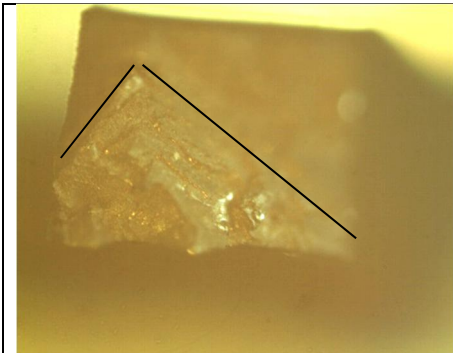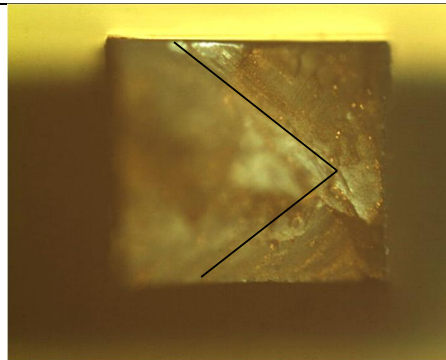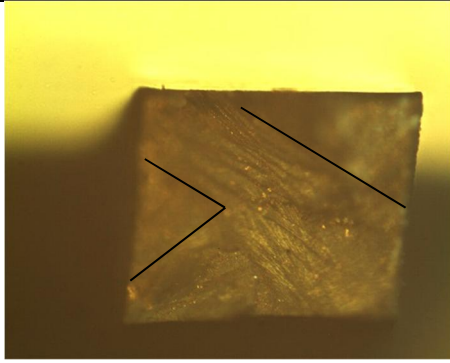
C38 - gauge length fail
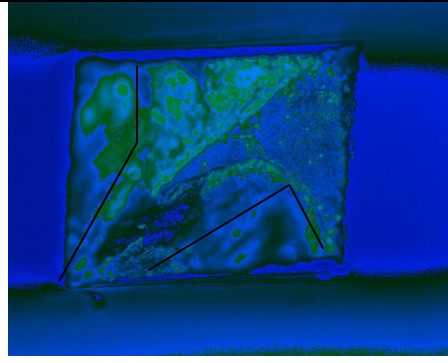


C36 - gauge length fail
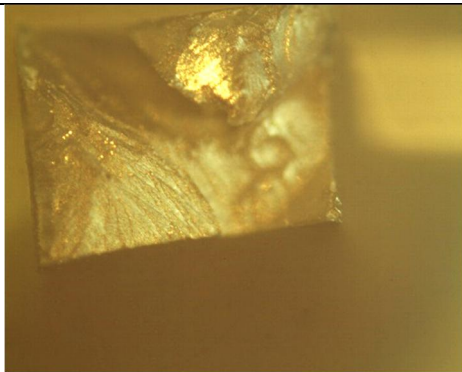


SCRY-4 virgin 2 - gauge length fail
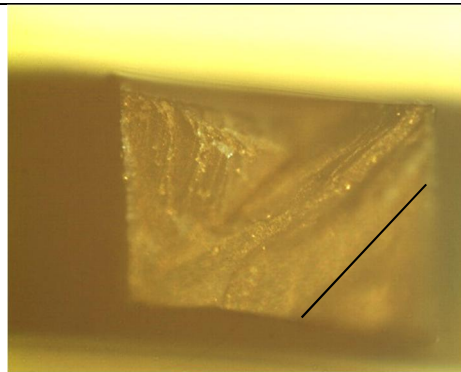


SCRY-4 virgin 1 - gauge length fail
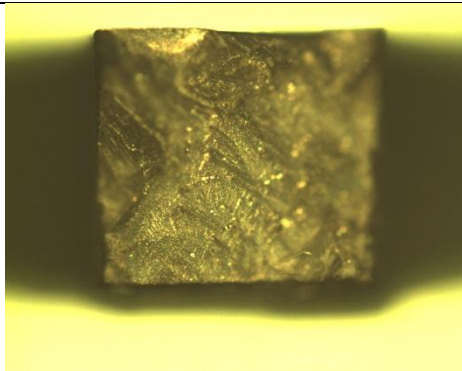


C30 - gauge length fail

# 9.6 Stress-strain tensile test

## 9.6.1 Specimen drawing and mounting
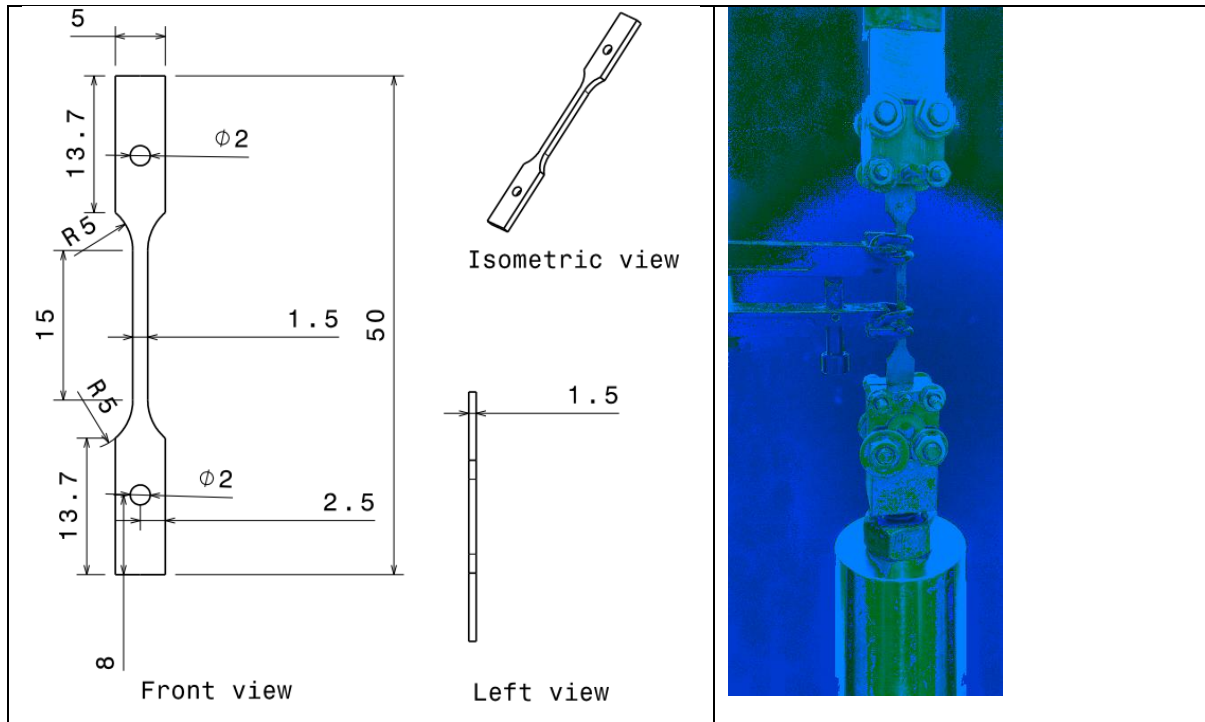


## 9.6.2 Grip drawing
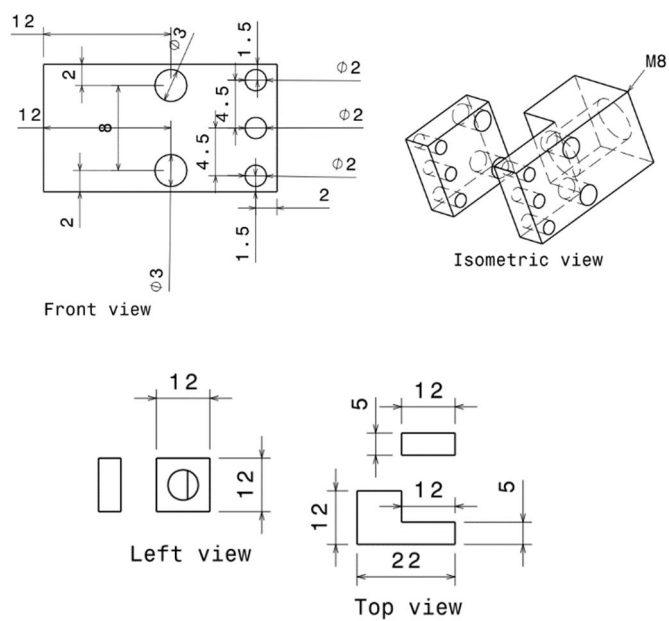
# 9.7 EBSD orientation measurement

## 9.7.1 E10 EBSD measurement

| Axial pin | Fracture |
|---|---|
|  |  |
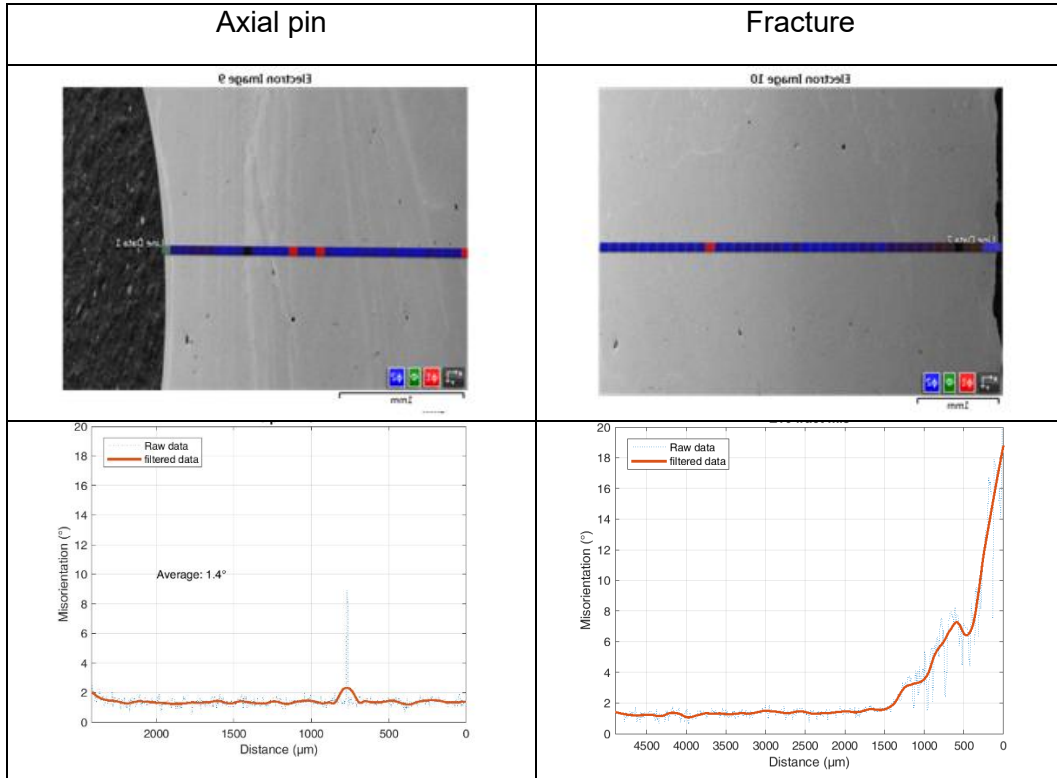
## 9.7.2 E14 EBSD measurement
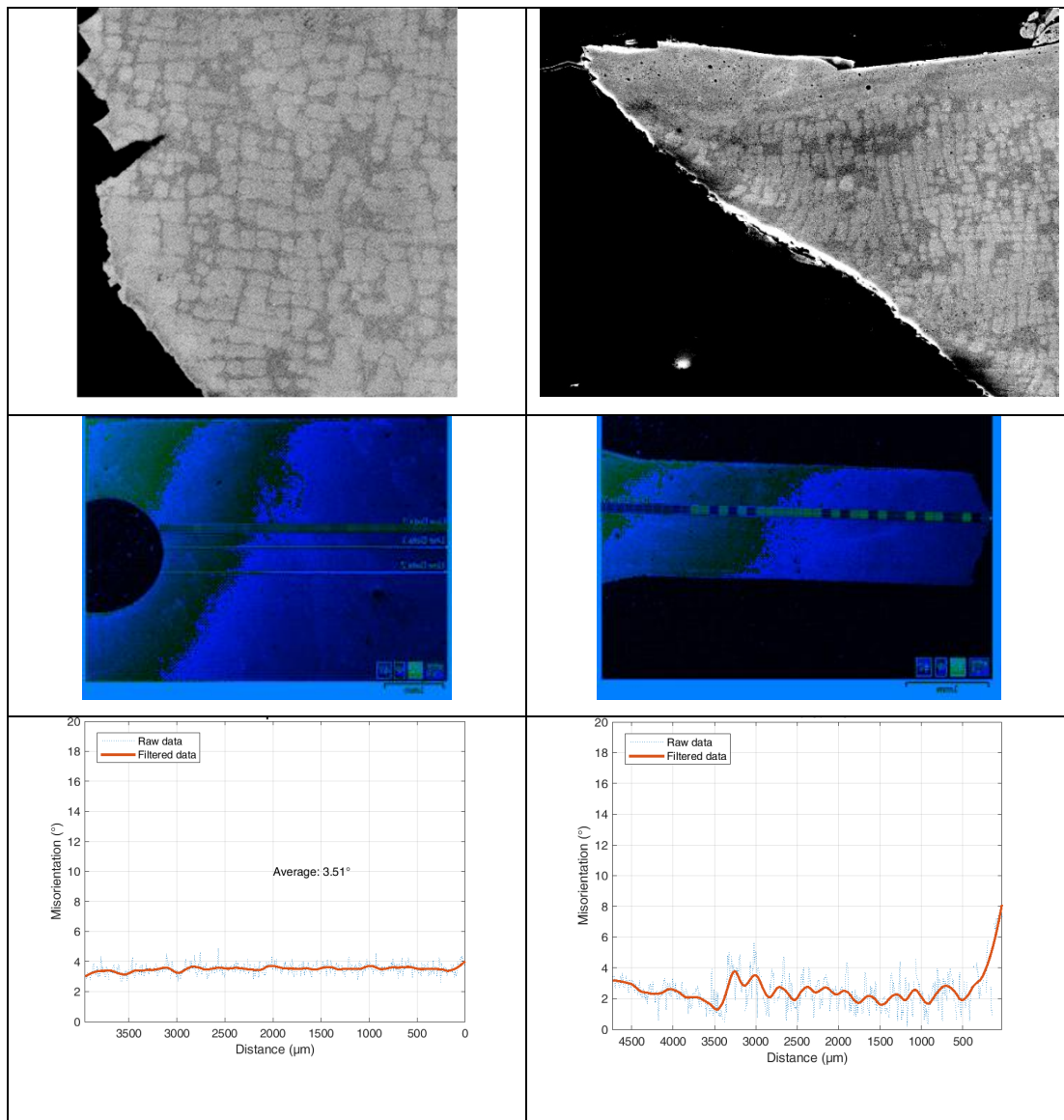
## 9.7.3 E18 EBSD measurement

| Axial Pin | Fracture |
|---|---|
|  |  |
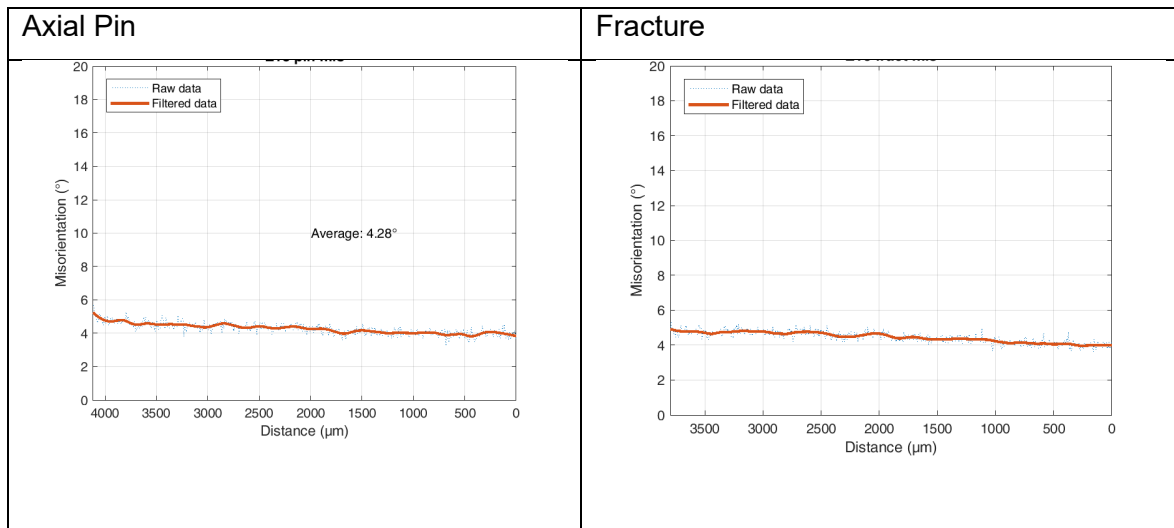
## 9.7.4 SCRY-83 – Virgin 1 EBSD measurement

| Axial Pin | Waist | Fracture |
|---|---|---|
|  |  |  |
|  |  |  |
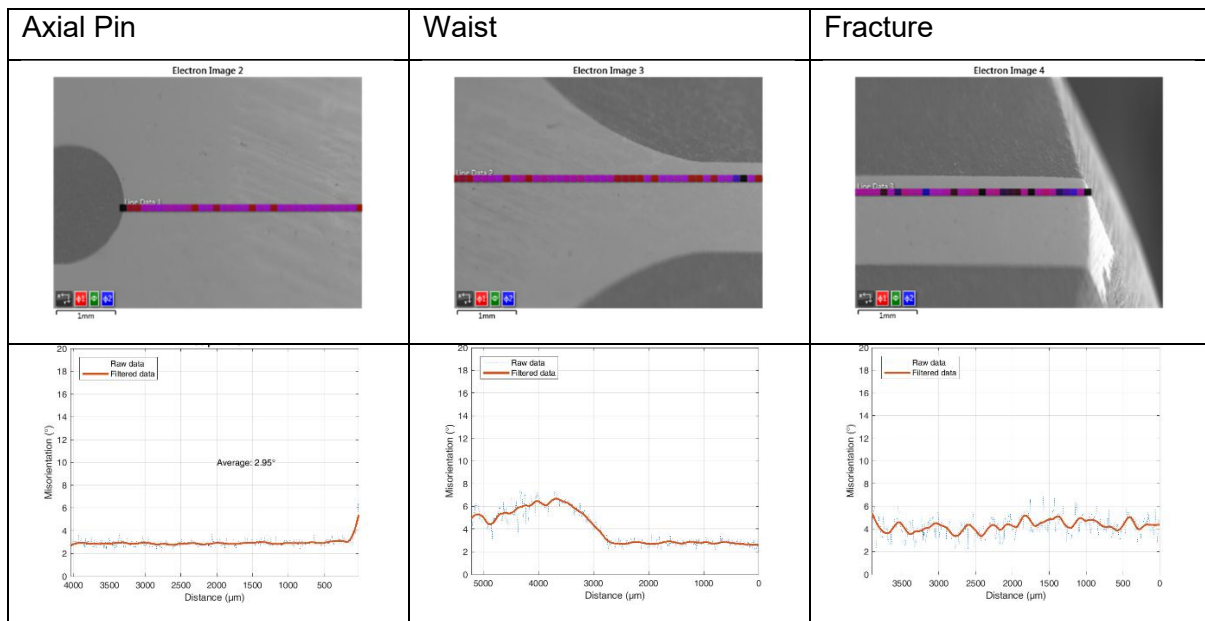
## 9.7.5 SCRY-4 Virgin 1 EBSD measurement
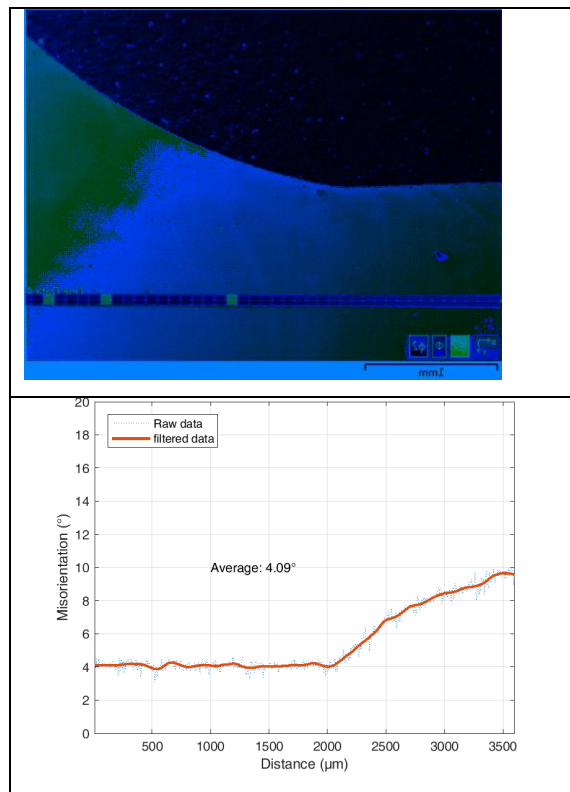


## 9.7.6 SCRY-4 Virgin 2 EBSD measurement

| Pin | Waist | Fracture |
|---|---|---|
|  |  |  |
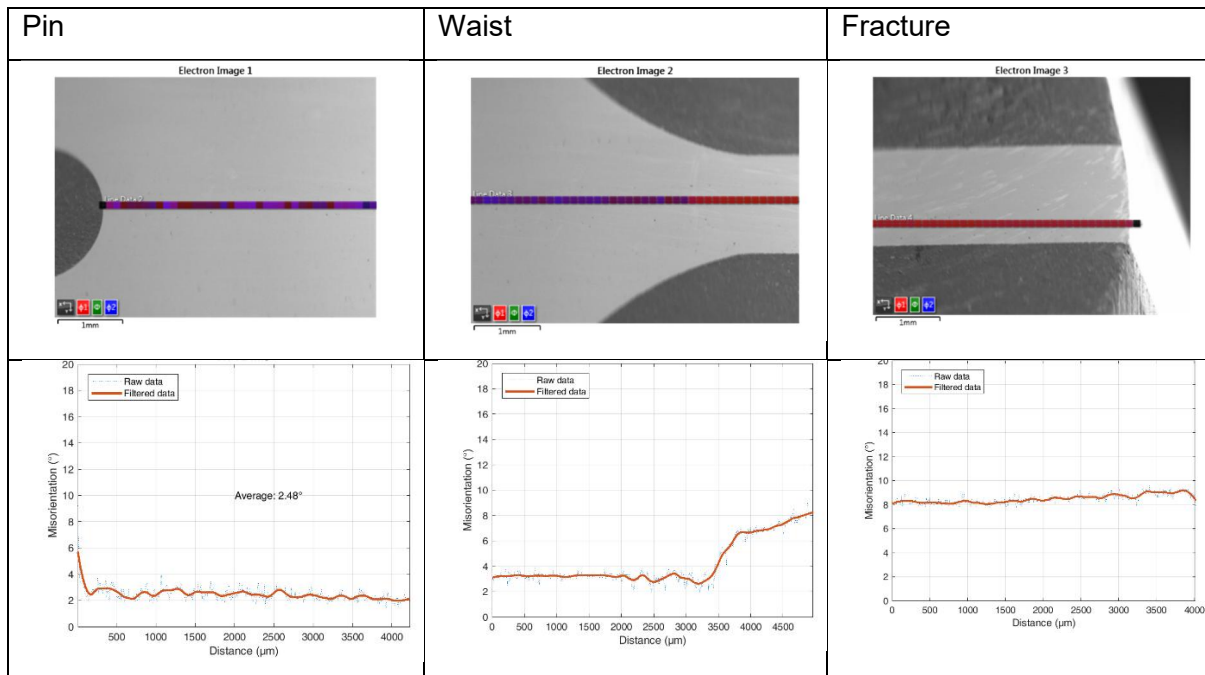
## 9.7.7 C34 EBSD measurement
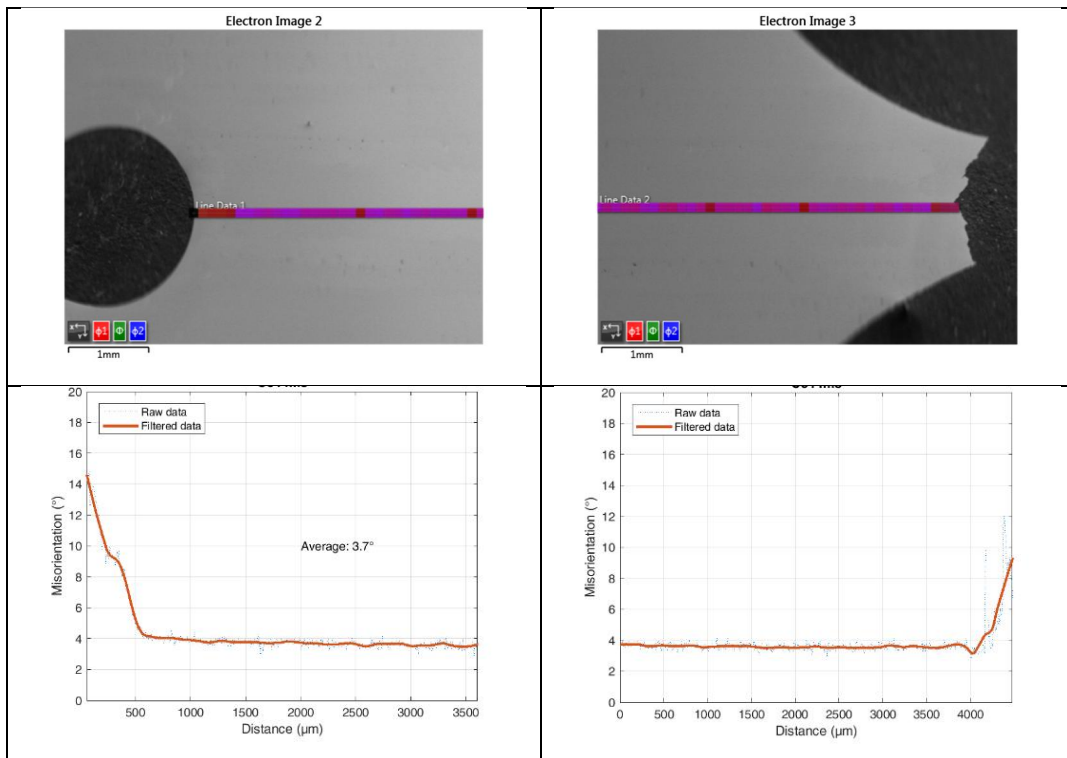
## 9.7.8 C36 EBSD measurement

| Fracture | waist | Pin |
|---|---|---|
|  |  |  |
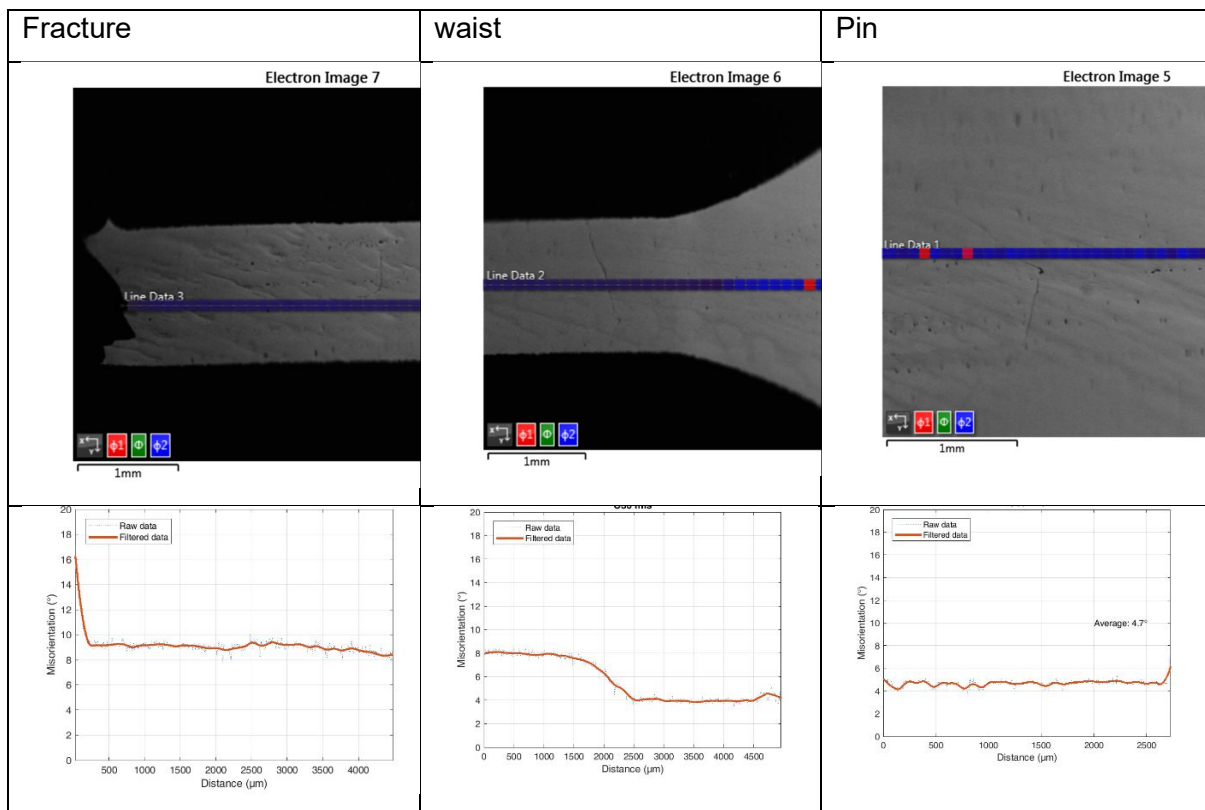
## 9.7.9 C37 EBSD measurement

| Fracture | Waist | Pin |
|---|---|---|
|  |  |  |
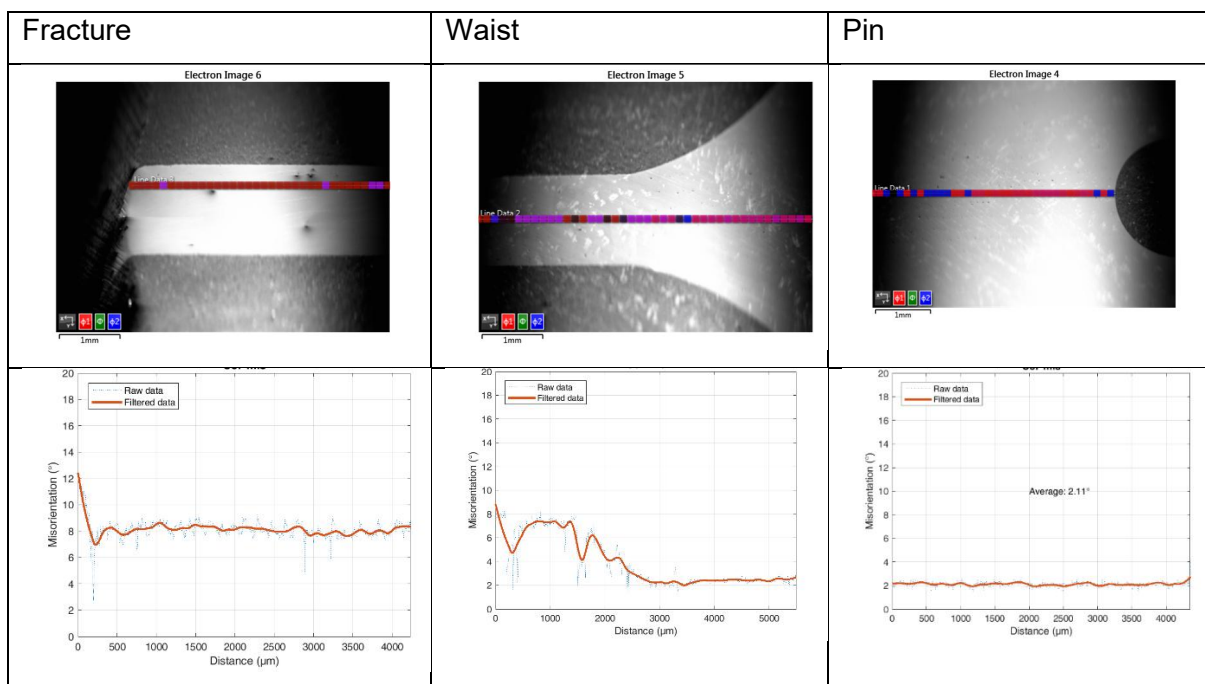
# X References

[1] International Energy Agency, "World Energy Outlook 2017," 2017. [Online]. Available: https://www.iea.org/weo2017/. [Accessed: 08-Jun-2018].

[2] L. Hindiyarti, "Gas phase sulfur, chlorine and potassium chemistry in biomass combustion," 2007.

[3] R. A. Antunes and M. C. L. de Oliveira, "Corrosion in biomass combustion: A materials selection analysis and its interaction with corrosion mechanisms and mitigation strategies," *Corros. Sci.*, vol. 76, no. 2013, pp. 6–26, 2013.

[4] A. Bradshaw, "Development of coatings for gas turbines burning biomass and waste-fuels," Cranfield University, 2009.

[5] A. Bradshaw, N. J. Simms, and J. R. Nicholls, "Passage of trace metal contaminants through hot gas paths of gas turbines burning biomass and waste-fuels," *Fuel*, vol. 87, no. 17–18, pp. 3529–3536, Dec. 2008.

[6] P. Pilidis and J. P. Palmer, "Gas turbine theory and performance." Cranfield University thermal power, Cranfield, p. 188, 2008.

[7] M. P. Boyce, *Gas turbine engineering handbook*, Third edit. Oxford: Gulf Professional Publishing, 2006.

[8] S. Gordon and B. J. McBride, "Computer program for calculation of complex chemical equilibrium compositions and applications, I. Analysis," 1994.

[9] R. C. Reed, *The superalloy fundamentals and applications*, Paperback. Cambridge: Lightning Source UK Ltd, 2006.

[10] M. A. Meyers and K. K. Chawla, *Mechanical behavior of materials*. Cambridge: Cambridge University Press, 2008.

[11] P. W. Schilke, A. D. Foster, and J. J. Pepe, "Advanced gas turbine materials and coatings (GER-3569G)," Schenectady, NY, 1991.

[12] T. M. Pollock and S. Tin, "Nickel-based superalloys for advanced turbine engines: chemistry, microstructure and properties," *J. Propuls. Power*, vol. 22, no. 2, pp. 361–374, 2006.

[13] K. Harris, G. L. Erickson, S. L. Sikkenga, W. D. Brentnall, J. M. Aurrecoechea, and K. G. Kubarych, "Development of two rhenium-containing superalloys for single-crystal Blade and directionally solidified vane applications in advanced turbine engines," *J. Mater. Eng. Perform.*, vol. 2, no. August, pp. 481–487, 1993.

[14] Rolls-Royce, *The jet engine*, 5th Ed. Derby, England: John Wiley & Sons, 2015, 2015.

[15] E. Poursaeidi, M. Aieneravaie, and M. R. Mohammadi, "Failure analysis of a second stage blade in a gas turbine engine," *Eng. Fail. Anal.*, vol. 15, no. 8, pp. 1111–1129, Dec. 2008.

[16] R. C. Reed, T. Tao, N. Warnken, and N. Rene, "Alloys-by-design: application to nickel-based single crystal superalloys," *Acta Mater.*, vol. 57, no. 19, pp. 5898–5913, 2009.

[17] N. Huc, "Thermal stress analysis of a turbine stator blade," *Comsol Multiphysic Manual*. Comsol, pp. 1–18, 2013.

[18]   R. C. Reed and C. M. F. Rae, *Physical metallurgy of the nickel-based superalloys*, Fifth Ed., vol. 1. Elsevier B.V., 2014.

[19]   Z. Liu, J. Ouyang, Y. Zhou, and S. Li, "High-temperature hot corrosion behavior of gadolinium zirconate by vanadium pentoxide and sodium sulfate in air," *J. Eur. Ceram. Soc.*, vol. 30, no. 12, pp. 2707–2713, 2010.

[20]   L. Meric, P. Poubanne, and G. Cailletaud, "Single crystal modeling for structural calculations: part 1 – model presentation," *Eng. Mater. Technol.*, vol. 113, no. January, pp. 163–170, 1991.

[21]   D. Siebörger, H. Knake, and U. Glatzel, "Temperature dependence of the elastic moduli of the nickel-base superalloy CMSX-4 and its isolated phases," *Mater. Sci. Eng. A*, vol. 298, no. 1–2, pp. 26–33, 2001.

[22]   D. M. Shah and A. Cetel, "Evaluation of PWA 1483 for large single crystal IGT blade applications," *TMS Superalloys*, pp. 295–304, 2000.

[23]   G. R. Swanson and N. K. Arakare, "Effect of crystal orientation of fatigue failure of single crystal nickel base turbine blade superalloys," in *45th ASME International Gas Turbine & Aeroengine Technical Congress*, 2000, p. 37.

[24]   N. Matan, D. C. Cox, P. Carter, M. A. Rist, C. M. F. Rae, and R. C. Reed, "Creep of CMSX-4 superalloy single crystals: Effects of rafting at high temperature," *Acta Mater.*, vol. 47, no. 12, pp. 3367–3381, 1999.

[25]   K. N. Strafford and P. K. Datta, "Progress in the design of sulphidation-resistant alloys," *Corros. Sci.*, vol. 35, pp. 1053–1063, 1993.

[26]   J. L. Smialek and G. H. Meier, "High-temperature oxidation," in *Superalloys II-High Temperature Materials for Aerospace and Industrial Power*, 1987, pp. 293–326.

[27]   D. J. Young, *High temperature oxidation and corrosion of metals*, 2nd Ed. Elsevier, 2016.

[28]   N. Jacobson, "Use of tabulated thermochemical data for pure compounds," *J. Chem. Educ.*, vol. 78, no. 6, pp. 2–7, 2001.

[29]   M. J. Zehe, S. Gordon, and B. J. McBride, "CAP: A computer code for generating tabular thermodynamic functions from NASA Lewis coefficients," Hanover, MD, 2002.

[30]   V. P. Glusko, L. V. Gurvich, G. A. Bergman, I. V. Veitz, and V. S. Medvedev, V. A.; Khachkuruzov, G. A.; Jungman, *Thermodynamic properties of pure substances, Vols. I–IV [In Russian]*, 3rd Ed. Moscow, 1982.

[31]   L. V. Gurvich, I. V. Veyts, and C. B. Alcock, *Thermodynamic properties of individual substances Volumes I and II*, 4th Ed. New-York, 1989.

[32]   D. R. Lide, *CRC handbook of chemistry and physics*, 84th Ed. Taylor & Francis, CRC Press, 2003.

[33]   C. E. Ramberg, P. Beatrice, K. Kurokawa, and W. L. Worrell, "High temperature oxidation behavior of structural silicides," in *Mat. Res. Soc. Symp. Proc.*, 1994, vol. 322, pp. 243–253.

[34]   T. A. Kircher, "Oxidation, sulfidation, and hot corrosion: mechanism and interrelationships," in *High Temperature Surface Interactions Agard No. 641*, 1989, pp. 42–49.

[35]   C. Wagner, "Beitrag zur Theorie des Anlaufvorgangs," *Zeitschrift für Physikalische Chemie*, vol. 21B. p. 25, 1933.

[36]   C. Wagner, "Theoretical Analysis of the Diffusion Processes Determining the Oxidation Rate of Alloys," *J. Electrochem. Soc.*, vol. 99, no. 10, p. 369, 2007.

[37]   H. V. Atkinson, "A review of the role of short-circuit diffusion in the oxidation of nickel,

chromium, and nickel-chromium alloys," *Oxid. Met.*, vol. 24, no. 3–4, pp. 177–197, 1985.

[38]    G. R. Wallwork and A. Z. Hed, "Some limiting factors in the use of alloys at high temperatures," *Oxid. Met.*, vol. 3, no. 2, pp. 171–184, 1971.

[39]    C. K. Sudbrack, D. L. Beckett, and R. A. MacKay, "Effect of surface preparation on the 815°C oxidation of single-crystal nickel-based superalloys," *J. Miner. Met. Mater. Soc.*, vol. 67, no. 11, pp. 2589–2598, 2015.

[40]    K. Onal, G. H. Meier, and F. S. Pettit, "The effects of water vapor on the oxidation of nickel-base superalloys and coatings at temperatures from 700 °C to 1100 °C," in *Superalloys (TMS)*, 2004, vol. 5, pp. 607–615.

[41]    M. H. Li, X. F. Sun, J. G. Li, Z. Y. Zhang, T. Jin, H. R. Guan, and Z. Q. Hu, "Oxidation behavior of a single-crystal Ni-base superalloy in air. I: At 800 and 900°C," *Oxid. Met.*, vol. 59, no. 5–6, pp. 591–605, 2003.

[42]    G. Obigodi-Ddjeng, "High temperature oxidation and electrochemical investigations on nickel-base alloys," Universität Erlangen-Nürnberg, 2011.

[43]    C. G. McCreath, "Environmental factors that determine hot corrosion in marine gas turbines rigs," *Corros. Sci.*, vol. 23, no. March, pp. 1017–1023, 1983.

[44]    N. S. Bornstein and W. P. Allen, "The chemistry of sulfidation corrosion-revisited," in *4th High Temperature Corrosion and Protection of Materials*, 1997, vol. 251–254, pp. 127–134.

[45]    P. Hancock, "The use of laboratory and rig tests to simulate gas turbine corrosion problems," *Corros. Sci.*, vol. 22, no. 1, pp. 51–65, 1982.

[46]    B. Bordenet, "High temperature corrosion in gas turbines: thermodynamic modelling and experimental results," Rheinisch-Westfälischen Technischen Hochschule Aachen, 2004.

[47]    J. Akella, S. N. Vaidya, and G. C. Kennedy, "Melting of sodium chloride at pressure to 65 kbar," *Phys. Rev.*, vol. 185, no. 3, pp. 1135–1140, 1969.

[48]    M. A. DeCrescente and N. S. Bornstein, "Formation and reactivity thermodynamics of sodium sulfate with gas turbine alloys," *Corrosion*, vol. 24, no. 5, pp. 127–133, 1968.

[49]    D. W. McKee, D. A. Shores, and K. L. Luthra, "The effect of $SO_2$ and NaCl on high temperature hot corrosion," *J. Electrochem. Soc.*, vol. 125, no. 3, p. 411, 1978.

[50]    P. Glarborg and P. Marshall, "Mechanism and modeling of the formation of gaseous alkali sulfates," *Combust. Flame*, vol. 141, no. 1–2, pp. 22–39, 2005.

[51]    W. R. Cotton, R. A. Pielke Sr., R. L. Walko, G. E. Liston, C. J. Tremback, H. Jiang, R. L. McAnelly, J. Y. Harrington, M. E. Nicholls, G. G. Carrio, and J. P. McFadden, "RAMS 2001: Current status and future directions," *Meteorol. Atmos. Phys.*, vol. 82, no. 1–4, pp. 5–29, 2003.

[52]    K. Zhang, E. Knipping, A. Wexler, P. Bhave, and G. Tonnesen, "Size distribution of sea-salt emissions as a function of relative humidity," *Atmos. Environ.*, vol. 39, no. 18, pp. 3373–3379, 2005.

[53]    T. B. Reed, *Free energy of formation of binary compounds: An atlas of charts for high-temperature chemical calculations*. Cambridge, Mass: MIT Press, 1971.

[54]    M. W. Chase, J. L. Curnutt, A. T. Hu, H. Prophet, A. N. Syverud, and L. . Walker, "JANAF thermochemical tables, 1974 supplement," *J. Phys. Chem. Ref. Data*, vol. 3, no. 2, pp. 311–480, 1974.

[55]    R. C. Hurst, J. B. Johnson, M. Davies, and P. Hancock, "Sulphate and chloride attack of nickel-

based alloys and mild steels," in *Deposition and Corrosion in Gas Turbines*, 1973, pp. 143–157.

[56]    P. A. Alexander, "Laboratory studies of the effects of sulfates and chlorides on the oxidation of superheater alloys," *The Mechanisms of Corrosion by Fuel Impurities,*. London, 1963.

[57]    P. Hancock, "Corrosion of alloys at high temperatures in atmospheres consisting of fuel combustion products and associated impurities: a critical review," HM Stationery Office, London, 1968.

[58]    H. Von Wartenberg and H. Schulz, "The vapor pressure of some salts II [from German: Der Dampfdruck einiger Salze. II]," *J. Electrochem. Appl. Phys. Chem.*, vol. 27, no. 23-24, pp. 568–573, 2018.

[59]    B. H. Zimm and J. E. Mayer, "Vapor pressures, heats of vaporization, and entropies of some alkali halides," *J. Chem. Phys.*, vol. 12, no. 9, pp. 362–369, 1944.

[60]    P. Hancock, "The role of halide in high temperature gas corrosion," in *Symposium on High Temperature Metal Halide Chemistry*, 1978, pp. 645–663.

[61]    M. G. Hocking and P. S. Sidky, "The hot corrosion of nickel-based ternary alloys and superalloys for gas turbine applications – II The mechanism of corrosion in $SO_2/O_2$ atmospheres," *Corros. Sci.*, vol. 27, no. 2, 1987.

[62]    L. Czerski, S. Mrowec, and T. Werber, "Kinetics and mechanism of nickel-sulfur reaction," *J. Electrochem. Soc.*, vol. 109, no. 4, p. 273, 1962.

[63]    P. Kofstad, *High Temperature Corrosion*. Norway: Elsevier Applied Science Publishers, 1988.

[64]    S. Floreen and R. H. Kane, "Effects of environment on high-temperature fatigue crack growth in a superalloy," *Metall. Trans. A*, vol. 10, no. 11, pp. 1745–1751, Nov. 1979.

[65]    B. Haflan and P. Kofstad, "The reaction of nickel with $SO_2+O_2/SO_3$ at 500–900 °C," *Corros. Sci.*, vol. 23, no. 12, pp. 1333–1352, Jan. 1983.

[66]    M. Seiersten and P. Kofstad, "The high temperature corrosion of nickel in $SO_2$ at 500–800 °C," *Corros. Sci.*, vol. 22, no. 5, pp. 487–506, 1982.

[67]    K. Natesan, "Oxidation–sulfidation behavior of Ni aluminide in oxygen-sulfur mixed-gas atmospheres," *Oxid. Met.*, vol. 30, no. 1–2, pp. 53–83, Aug. 1988.

[68]    V. Krishnan, S. Bharani, J. S. Kapat, Y. H. Sohn, and V. H. Desai, "A simplistic model to study the influence of film cooling on low temperature hot corrosion rate in coal gas/syngas fired gas turbines," *Int. J. Heat Mass Transf.*, vol. 51, no. 5–6, pp. 1049–1060, Mar. 2008.

[69]    C. W. Bale and D. Pelton, "FactSage." GTT & CRTT, Montreal, 2013.

[70]    K. L. Luthra and D. A. Shores, "Mechanism of $Na_2SO_4$ induced corrosion at 600–900 °C," *J. Electrochem. Soc.*, vol. 127, pp. 2202–2210, 1980.

[71]    M. D. Dolan, A. Y. Ilyushechkin, K. G. Mclennan, and S. D. Sharma, "Alkali, boron and phosphorous removal from coal-derived syngas: Review and thermodynamic considerations," *Asia-Pacific J. Chem. Eng.*, vol. 7, no. October 2011, pp. 317–327, 2012.

[72]    R. A. Rapp, "Hot corrosion of materials," *Pure Appl. Chem.*, vol. 62, no. 1, pp. 113–122, 1990.

[73]    R. A. Rapp, "Hot corrosion of materials: a Fluxing mechanism?," *Corros. Sci.*, vol. 44, pp. 209–221, 2002.

[74]    K. L. Luthra, "Low temperature hot corrosion of cobalt-base alloys: Part II. Reaction mechanism," *Metall. Trans. A*, vol. 13, no. 10, pp. 1843–1852, Oct. 1982.

[75] N. Otsuka and R. A. Rapp, "Hot corrosion of preoxidized Ni by a thin fused $Na_2SO_4$ film at 900 °C," *J. Electrochem. Soc.*, vol. 137, no. 1, p. 46, 1990.

[76] J. A. Goebel and F. S. Pettit, "$Na_2SO_4$-induced accelerated oxidation (hot corrosion) of nickel," *Metall. Trans.*, vol. 1, no. July, pp. 1943–1954, 1970.

[77] J. M. Alvarado-Orozco, J. E. Garcia-Herrera, B. Gleeson, F. S. Pettit, and G. H. Meier, "Reinterpretation of Type II hot corrosion of Co-base alloys incorporating synergistic fluxing," *Oxid. Met.*, no. 225, 2018.

[78] R. A. Rapp and K. S. Goto, "The hot corrosion of metals by molten salts," in *The Electrochemical Society Inc.*, 1981, vol. 81, pp. 159–177.

[79] D. A. Shores, "New perspective on hot corrosion mechanisms," in *High Temperature Corrosion NACE-6*, 1983, p. 493.

[80] J. Sumner, A. Encinas-Oropesa, N. J. Simms, and J. R. Nicholls, "Type II hot corrosion: Behavior of CMSX-4 and IN738LC as a function of corrosion environment," *Mater. Corros.*, vol. 65, no. 2, pp. 188–196, 2014.

[81] M. Levy, R. Huie, and F. Pettit, "Oxidation and hot corrosion of some advanced superalloys at 1300 to 2000°F (704 to 1093°C)," *Corrosion*, vol. 45, no. 8, pp. 661–674, Aug. 1989.

[82] K. P. Lillerud and P. Kofstad, "Sulfate-induced hot corrosion of nickel," *Oxid. Met.*, vol. 21, no. 5–6, pp. 233–270, Jun. 1984.

[83] N. Eliaz, G. Shemesh, and R. M. Latanision, "Hot corrosion in gas turbine components," *Eng. Fail. Anal.*, vol. 9, pp. 31–43, 2002.

[84] L. Hindiyarti, P. Glarborg, and P. Marshall, "Reactions of $SO_3$ with the O/H radical pool under combustion conditions," *J. Phys. Chem. A*, vol. 111, pp. 3984–3991, 2007.

[85] D. Fleig, "Experimental and modeling studies of sulfur-based reactions in oxy-fuel combustion," Chalmers University of Technology, 2012.

[86] D. Fleig, E. Vainio, K. Andersson, A. Brink, F. Johnsson, and M. Hupa, "Evaluation of $SO_3$ measurement techniques in air and oxy-fuel combustion," *Energy & fuels*, vol. 26, no. 9, pp. 5537–5549, 2012.

[87] J. E. Garcia-Herrera, J. M. Alvarado-Orozco, J. Munoz-Saldana, L. Garcia-Fresnillo, and G. H. Meier, "The effect of different $SO_2$/$SO_3$ catalytic media on high-temperature corrosion processes," *Oxid. Met.*, vol. 84, no. 3, pp. 233–240, 2015.

[88] M. Durand-Charre, *The microstructure of superalloys*, 1st Ed. London: Gordon and breach Science Publishers, 1997.

[89] A. Hendry and D. J. Lees, "Corrosion of austenitic steels in molten sulphate deposits," *Corros. Sci.*, vol. 20, no. 3, pp. 383–404, 1980.

[90] R. L. Jones, C. E. Williams, and S. R. Jones, "Reaction of vanadium compounds with ceramic oxides," *J. Electrochem. Soc.*, vol. 133, no. 1, pp. 227–230, 1986.

[91] J. Stringer, V. Nagarajan, and D. P. Whittle, "The role of chloride in the hot corrosion of cobalt-base alloys," in *Symposium on High Temperature Metal Halide Chemistry*, 1978, pp. 123–140.

[92] R. Barkalow and F. Pettit, "The effect of sodium chloride on the sodium sulfate-induced hot corrosion of alloys," in *Symposium on High Temperature Metal Halide Chemistry*, 1978, vol. 78–1, pp. 617–633.

[93] H. Rosier, K. Perkins, A. Girling, J. Leggett, and G. Gibson, "Factors affecting the corrosion

fatigue life in nickel based superalloys for disc applications," *MATEC Web Conf.*, vol. 14, no. 2014, p. 03001, 2014.

[94]    P. Lortrakul, R. W. Trice, K. P. Trumble, and M. A. Dayananda, "Investigation of the mechanisms of Type-II hot corrosion of superalloy CMSX-4," *Corros. Sci.*, vol. 80, pp. 408–415, Mar. 2014.

[95]    M. G. Hocking and V. Vasantasree, "Hot corrosion of Ni-Cr alloys in $SO_2/O_2$ atmospheres—II. Visual observations, analyses and mechanisms," *Corros. Sci.*, vol. 16, no. March 1975, pp. 279–295, 1976.

[96]    V. Vasantasree and M. G. Hocking, "Hot corrosion of Ni-Cr alloys in $SO_2+O_2$ atmospheres—I. Corrosion kinetics," *Corros. Sci.*, vol. 16, no. March 1975, pp. 261–277, 1976.

[97]    L. Brooking, J. Sumner, S. Gray, and N. J. Simms, "Stress corrosion of Ni-based superalloys," *Mater. High Temp.*, vol. 3409, pp. 1–10, 2017.

[98]    L. Brooking, S. Gray, J. Sumner, J. R. Nicholls, G. Marchant, and N. J. Simms, "Effect of stress state and simultaneous hot corrosion on the crack propagation and fatigue life of single crystal superalloy CMSX-4," *Int. J. Fatigue*, vol. 116, no. March, pp. 106–117, 2018.

[99]    A. Homaeian and M. Alizadeh, "Interaction of hot corrosion and creep in Alloy 617," *Eng. Fail. Anal.*, vol. 66, pp. 373–384, 2016.

[100]   M. Yoshiba, O. Miyagawa, and T. Hamanaka, "Strength and fracture of a nickel-base superalloy subjected to different waveforms of loadings in hot corrosion environment [In Japanese]," *Boshoku Gijutsu*, vol. 39, pp. 132–140, 1990.

[101]   C. Leyens, L. G. Wright, B. A. Pin, and P. F. Tortorelli, "Significance of experimental procedures on the hot corrosion behavior of nickel-base alloys under cyclic conditions," Oak Ridge, Tennessee, 1999.

[102]   A. Raffaitin, F. Crabos, E. Andrieu, and D. Monceau, "Advanced burner-rig test for oxidation–corrosion resistance evaluation of MCrAlY/superalloys systems," *Surf. Coatings Technol.*, vol. 201, no. 7, pp. 3829–3835, Dec. 2006.

[103]   M. A. Harper, J. E. Barnes, and C. Regan, "Hot corrosion burner rig testing of various commercial alloys," *Corrosion*, no. 67, 1999.

[104]   P. Elliott and S. K. Vermai, "Burner rig trials with nickel –and cobalt– base alloys," *Corros. Sci.*, vol. 16, no. May 1975, pp. 1–7, 1976.

[105]   D. J. Wortman, R. E. Fryxell, K. L. Luthra, and P. A. Bergman, "Mechanism of low temperature hot corrosion: Burner rig studies," *Thin Solid Films*, vol. 64, pp. 281–288, 1979.

[106]   D. L. Deadmore, C. E. Lowell, and F. J. Kohl, "The effect of fuel-to-air ratio on burner rig hot corrosion," *Corros. Sci.*, vol. 19, no. August 1978, 1979.

[107]   D. A. Shifter, "Alloy and coatings parameters that may contribute to the performance behavior of high temperature materials," *Corrosion*, no. 02385, pp. 1–13, 2002.

[108]   S. R. J. Saunders, "Correlation between corrosion rig testing and service experience," vol. 2, no. March, pp. 282–289, 1986.

[109]   G. S. Mahobia, N. Paulose, S. L. Mannan, R. G. Sudhakar, K. Chattopadhyay, and N. C. S. Srinivas, "Effect of hot corrosion on low cycle fatigue behavior of superalloy IN718," *Int. J. Fatigue*, vol. 59, no. 2014, pp. 272–281.

[110]   X. Yang, S. Li, and H. Qi, "Effect of high-temperature hot corrosion on the low cycle fatigue behavior of a directionally solidified nickel-base superalloy," *Int. J. Fatigue*, vol. 70, pp. 106–113, 2015.

[111]  L. Brooking, S. Gray, J. Sumner, J. R. Nicholls, and N. J. Simms, "Interaction of hot corrosion fatigue and load dwell periods on a nickel-base single crystal superalloy," *Int. J. Fatigue*, vol. 117, no. July, pp. 13–20, 2018.

[112]  J. B. Wahl and K. Harris, "New Single Crystal Superalloys, CMSX®-7 and CMSX®-8," *Superalloys 2012*, pp. 177–188, 2012.

[113]  F. Pettit, "Hot corrosion of metals and alloys," *Oxid. Met.*, vol. 76, no. 1–2, pp. 1–21, 2011.

[114]  K. L. Luthra, "Low temperature hot corrosion of cobalt-base alloys: Part I. Morphology of the reaction product," *Metall. Trans. A*, vol. 13, no. 10, pp. 1843–1852, Oct. 1982.

[115]  National Center for Biotechnology Information. PubChem Compound Database, "Sodium bisulfate | NaHSO4 –PubChem," *CID=516919*. [Online]. Available: https://pubchem.ncbi.nlm.nih.gov/compound/516919. [Accessed: 15-May-2018].

[116]  "Safety data sheet Sulphur dioxide," BOC Industrial Gases, Guildford, 2011.

[117]  C. T. Chantler, "Detailed tabulation of atomic form factors, photoelectric absorption and scattering cross section, and mass attenuation coefficients in the vicinity of absorption edges in the soft X-Ray (Z=30–36, Z=60–89, E=0.1 keV–10 keV), addressing convergence issues," *J. Phys. Chem. Ref. Data*, vol. 29, no. 4, p. 597, 2000.

[118]  "NIST: X-ray form factor, attenuation and scattering tables." [Online]. Available: http://physics.nist.gov/PhysRefData/FFast/html/form.html. [Accessed: 15-Jun-2018].

[119]  J. Čapek and Pala Z, "Auxiliary programs for diffraction experiments," *Mater. Struct.*, vol. 22, pp. 78–81, 2015.

[120]  Y. Mishima, S. Ochiai, and T. Suzuki, "Lattice parameters of Ni(γ), Ni₃Al(γ') and Ni₃Ga(γ') solid solutions with additions of transition and B-subgroup elements," *Acta Metall.*, vol. 33, no. 6, pp. 1161–1169, Jun. 1985.

[121]  R. Hielscher and F. Bachmann, "MTEX Toolbox." Chemnitz, Germany, 2018.

[122]  D. Shi, C. Wang, X. Yang, and S. Li, "Failure assessment of the first stage high-pressure turbine blades in an aero-engine turbine," *Fatigue Fract. Eng. Mater. Struct.*, vol. 40, no. 12, pp. 2092–2106, 2017.

[123]  M. Smith, "ABAQUS/Standard User's Manual, Version 6.14," 2014.

[124]  S. Cruchley, H. E. Evans, M. P. Taylor, M. C. Hardy, and S. Stekovic, "Chromia layer growth on a Ni-based superalloy: Sub-parabolic kinetics and the role of titanium," *Corros. Sci.*, vol. 75, pp. 58–66, 2013.

[125]  P. Marliacy, R. Solimando, M. Bouroukba, and L. Schuffenecker, "Thermodynamics of crystallization of sodium sulfate decahydrate in H2O-NaCl-Na2SO4: Application to Na2SO4·10H2O-based latent heat storage materials," *Thermochim. Acta*, vol. 344, no. 1–2, pp. 85–94, 2000.

[126]  Instron inc, "Dynamic Strain Gauge Extensometer- 2620 series," 2012. [Online]. Available: https://www.instron.us/-/media/literature-library/products/2005/01/2620-series-dynamic-strain-gauge-extensometer.pdf?la=en-US.

[127]  Instron inc, "2530-400 Series Load Cells," 2007. [Online]. Available: https://www.instron.com/~/media/literature-library/products/2003/08/2530-400-series-load-cells.pdf?la=en.

[128]  N. Hiraide, T. Muneno, and H. Kajimura, "Reaction of Cr and Cr oxide with NaCl at elevated temperature [from Japanese]," *Mater. Environ.*, vol. 58, p. 348－355, 2009.

[129] E. M. Levin, C. R. Robbins, and H. F. McMurdie, *Phase diagrams for ceramists*. Columbus, Ohio: American Ceramic Society, 1964.

[130] F. Hoermann, "Beitrag zur Kenntnis der Molybdate und Wolframate. Die binaren Systeme," *Zeitschrift fur Anorg. und Allg. Chemie*, vol. 177, no. 1, pp. 145–186, 1929.

[131] Z. Z. Fang, "Preface: aims and scope of journal," *Int. J. Refract. Met. hard Mater.*, vol. 72, 2018.